

Universidade Federal do ABC

Programa de Pós-Graduação em Nanociências e Materiais Avançados

Mainã Portella Garcia

Influence of welding heat input on microstructure,
mechanical properties and corrosion behaviour of
high-strength steels

*Influência do aporte térmico na microestrutura, propriedades
mecânicas e comportamento de corrosão de aços de alta
resistência*

Santo André

2018

Mainã Portella Garcia

**Influence of welding heat input on microstructure,
mechanical properties and corrosion behaviour of
high-strength steels**

*Influência do aporte térmico na microestrutura,
propriedades mecânicas e comportamento de corrosão de aços
de alta resistência*

Thesis submitted in partial fulfillment of
the requirements for the degree of Doctor of
Philosophy of Nanosciences and Advanced
Materials, under the supervision of Prof. Dr.
Gerson Luiz Mantovani and co-supervision of
Prof. Dr. Renato Altobelli Antunes

*Tese apresentada como parte dos
requisitos para obtenção do título de Doutor
em Nanociências e Materiais Avançados, sob
orientação do Prof. Dr. Gerson Luiz
Mantovani e coorientação do Prof. Dr. Renato
Altobelli Antunes*

Santo André

2018

Sistema de Bibliotecas da Universidade Federal do ABC

Elaborada pelo Sistema de Geração de Ficha Catalográfica da UFABC
com os dados fornecidos pelo(a) autor(a).

Portella Garcia, Mainã

Influence of welding heat input on microstructure, mechanical properties
and corrosion behaviour of high-strength steels / Mainã Portella Garcia. —
2018.

184 fls. : il.

Orientador: Gerson Luiz Mantovani

Coorientador: Renato Altobelli Antunes

Tese (Doutorado) — Universidade Federal do ABC, Programa de Pós
Graduação em Nanociências e Materiais Avançados, Santo André, 2018.

1. Welding. 2. High-Strength Steels. 3. Advanced High-Strength Steels.
4. Heat Input. 5. SVET. I. Mantovani, Gerson Luiz. II. Altobelli Antunes,
Renato. III. Programa de Pós-Graduação em Nanociências e Materiais
Avançados, 2018. IV. Título.



MINISTÉRIO DA EDUCAÇÃO

Fundação Universidade Federal do ABC

Programa de Pós-Graduação em Nanociências e Materiais Avançados

Avenida dos Estados, 5001 – Bairro Santa Terezinha – Santo André – SP

CEP 09210-580 - Fone: (11) 4996-0017

ppg.nanomat@ufabc.edu.br

FOLHA DE ASSINATURAS

Assinaturas dos membros da Banca Examinadora que avaliou e aprovou a Defesa de Tese de Doutorado da candidata Mainã Portella Garcia, realizada em 5 de fevereiro de 2018:

Prof.(a) Dr.(a) **Gerson Luiz Mantovani** (Universidade Federal do ABC) – Presidente

Prof.(a) Dr.(a) **Sydney Ferreira Santos** (Universidade Federal do ABC) – Membro Titular

Prof.(a) Dr.(a) **Mauro Coelho dos Santos** (Universidade Federal do ABC) – Membro Titular

Prof.(a) Dr.(a) **Carlos Trivello Rios** (Universidade Federal do ABC) – Membro Titular

Prof.(a) Dr.(a) **Maurício David Martins das Neves** (Instituto de Pesquisas Energéticas e Nucleares) – Membro Titular

Prof.(a) Dr.(a) **Juliano Soyama** (Universidade Federal do ABC) – Membro Suplente

Prof.(a) Dr.(a) **Jeroen Schoenmaker** (Universidade Federal do ABC) – Membro Suplente

Prof.(a) Dr.(a) **Hercílio Gomes de Melo** (Universidade de São Paulo) – Membro Suplente

Prof.(a) Dr.(a) **Humberto Naoyuki Yoshimura** (Universidade Federal do ABC) – Membro Suplente



Universidade Federal do ABC

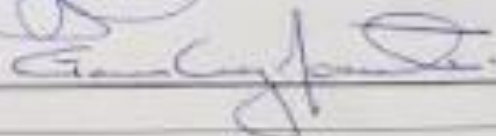
Este exemplar foi revisado e alterado em relação à versão original, de acordo com as observações levantadas pela banca no dia da defesa, sob responsabilidade única do autor e com a anuência de seu orientador.

Santo André, 20 de fevereiro de 2018.

Assinatura do autor:



Assinatura do orientador:



Preface

This thesis is submitted for the degree of Doctor of Philosophy at *Universidade Federal do ABC*. The research described herein was conducted under the supervision of Prof. Dr. Gerson Luiz Mantovani and co-supervision of Prof. Dr. Renato Altobelli Antunes in the *Nanociências e Materials Avançados*. This work is to the best of my knowledge original, expect where acknowledgement and reference is made to previous work.

Part of this work is published in the following publication:

Garcia, M.P., Mantovani, G.L., Vasant Kumar, R., Antunes, R. A.; Corrosion Behavior of Metal Active Gas Welded Joints of a High-Strength Steel for Automotive Application; Journal of Materials Engineering and Performance, 2017, 26 (10), 4718-4731.

Acknowledgements

I would like to express my sincere thanks and gratitude to my supervisor Prof. Dr. Gerson Luiz Mantovani for his support, guidance and enthusiasm.

I also want to acknowledge my co-supervisor Prof. Dr. Renato Altobelli Antunes for all support and attention.

I am greatly indebted to Prof. Dr. Vasant Kumar for the most amazing opportunity to join his group at Cambridge University.

I am grateful to Mauro Paraiso, my industrial supervisor, for initiating the project and providing direction, along with the resources necessary to successfully complete it.

Special thanks are due to Adriano Carbento, Teodolino Lemos and Daniel Falleiros, who have communally provided instruction, insight and discussion.

I express my sincere gratitude to Dorival Tecco, Erico Franca, Tadeu Carneiro, Marcos Stuart and Hugo Lemos. All of them were crucial on the achievements of my project. I believe that we do not do anything alone, we always need people to help us.

I would also like to mention Juliana Sarango, with whom I had helpful discussions.

I earnestly acknowledge CNPq for the provision of a maintenance grant for the whole period of this research work, CBMM for sponsoring my study at Cambridge University and Fronius for welding facilities.

I also thank Mercedes-Benz Brazil for all the available facilities and for accepting this collaboration with UFABC.

Last but not least, I would like to thank my family, Enir, Sálvio, Mairê, Daniel and Mateus for their assistance, devotion and understanding throughout my life. I also express my gratitude and love to my fiancé Jamie Barnett for his constant encouragement and love all the time. If were not for their dedicated care and advices, I might never have had the opportunity to pursue my studies this far.

The end of wisdom is freedom.
The end of culture is perfection.
The end of knowledge is love.
The end of education is character.

Politics without principles,
Education without character,
Science without humanity, and
Commerce without morality
Are not only useless, but positively dangerous.

Knowledge without integrity is dangerous and dreadful,
knowledge without character is a powerful evil.
Knowledge without action is useless; action without knowledge is foolishness

Sri Sathya Sai Baba

Resumo

Recentemente, a indústria automotiva tem acelerado os esforços para melhorar a economia de combustível dos automóveis. Os aços de alta resistência possibilitam a redução de peso, garantindo a segurança e desempenho. A Microestrutura, propriedades mecânicas e comportamento de corrosão de juntas soldadas de dois aços de alta resistência (LNE500 e AHSS900) foram estudados. Os aportes térmicos utilizados foram de 0,72, 0,70, 0,47 e 0,31 kJ/mm utilizando soldagem a arco elétrico. A microestrutura da junta soldada foi analisada por microscopia eletrônica de transmissão, microscopia eletrônica de varredura, microscopia óptica e difração de raios X. Os resultados confirmam a influência do aporte térmico na microestrutura, fases cristalinas, tamanho de grão, precipitados e suas distribuições. O perfil de dureza (*Vickers*) revelou uma região de amolecimento localizado na zona afetada pelo calor (ZAC) com grãos finos para as juntas soldadas do metal de base AHSS900. Os resultados do teste de tração revelaram uma variação significativa do escoamento e da resistência à tração entre o metal de base e as amostras soldadas, com a última apresentando ductilidade e resistência reduzidas. O comportamento de corrosão foi estudado utilizando impedância eletroquímica, polarização potenciodinâmica e técnica de varredura por eletrodo vibracional (SVET). A combinação dessas técnicas indicou onde e como a corrosão aconteceu. ZAC e metal de base atuaram como ânodo e o cordão de solda atuou como cátodo. SVET revelou que a corrosão iniciou no cordão de solda e se espalhou pela superfície da junta soldada. A grande quantidade de locais ativos (óxidos) e o alto teor de Si no cordão de solda podem ter sido responsáveis pelo início da corrosão nessa região. As imagens de microscopia confocal mostraram que a ZAC e o metal de base corroeram mais rápido do que o cordão de solda.

Palavras chaves: Corrosão, Aços de alta resistência, Aços avançados de alta resistência, Aporte térmico, SVET.

Abstract

Recently, automotive producers have been accelerating efforts to significantly improve vehicle fuel economy. High-strength steels have been proven to achieve weight reduction while meeting vehicle safety and performance requirements. The microstructure, mechanical properties and corrosion behaviour of gas metal arc welded joints of two high strength steels (LNE500 and AHSS900) have been studied. The welded joints were obtained using heat input of 0.72, 0.70, 0.47 and 0.31 kJ/mm. The microstructure was investigated by transmission electron microscopy, scanning electron microscopy, optical microscopy and X-ray diffraction. The results confirm the influence of heat input on the microstructure, crystalline phases, grain size, precipitates size and distribution. Vickers microhardness test revealed a softening region in the fine-grained heat affected zone (FGHAZ) for the AHSS900 welded joints. The tensile test results revealed a significant variation in the magnitude of yield and tensile strength between the base metal and welded samples, with the latter exhibiting reduced ductility and strength. Corrosion behaviour was studied using electrochemical impedance spectroscopy, potentiodynamic polarisation and scanning vibrating electrode technique (SVET). The combination of these techniques indicated that HAZ and BM acted as the anode and weld metal (WM) acted as the cathode of the galvanic couple. SVET showed that corrosion started in the WM and, then, it spread to the whole joint. The high amount of active sites (oxide inclusions) and the high Si content in the WM may be responsible for corrosion initiation. HAZ/BM corroded faster than WM, producing a depth difference, which was detected by confocal laser scanning microscope.

Key words: Corrosion, High-strength steels, Advanced High-strength Steels, heat input, SVET.

Nomenclature and Abbreviations

AHSS	advanced high-strength steel
AHSS900	advanced high-strength steel with strength of 900 MPa
BM	base metal
CCT	continuous cooling transformation
CE	carbon equivalent
CGHAZ	coarse-grained heat affected zone
CLSM	confocal laser scanning microscopy
CMT	cold metal transfer
DP	dual phase
EDS	energy dispersive X-ray spectroscopy
EIS	electrochemical impedance spectroscopy
FGHAZ	fine-grained heat affected zone
GMAW	gas metal arc welding
HAZ	heat affected zone
HI	heat input
HSLA	high-strength low-alloy
JCPDS	joint committee on powder diffraction standards
LNE500	high-strength low-alloy with strength of 500MPa
MAG	metal active gas
MIG	metal inert gas
OCP	open circuit potential
PHAZ	partially heat affected zone
QT	quenched tempered
SAW	submerged arc welding
SEM	scanning electron microscope
STEM	scanning transmission electron microscopy
SVET	scanning vibrating electrode technique
TEM	transmission electron microscopy

TMCP	thermomechanical controlled processing
TRIP	transformation induced plasticity
TTT	time temperature transformation
UFG	ultrafine grains
VEGW	vertical electro-gas welding
WE	working electrode
XRD	X-ray diffraction
WM	weld metal

Symbols

wt%	weight percent
γ	austenite
α_a	acicular ferrite
α_w	Widmanstätten ferrite
α	allotriomorphic ferrite
i_{corr}	corrosion current density / current rate
E_{corr}	corrosion potential
R_p	charge transfer resistance

Contents

1.	Introduction	25
2.	Literature Review	27
2.1.	Economic aspects	27
2.2.	Classification of High-strength steels.....	29
2.2.1.	Microalloyed steels	30
2.2.2.	Martensitic steels	32
2.3.	Arc Welding	34
2.4.	Influence of welding parameters.....	37
2.5.	Corrosion behaviour	43
2.5.1.	Corrosion techniques.....	44
2.5.2.	Corrosion behaviour of microalloyed steels (base metal)	53
2.5.3.	Corrosion behaviour at welded joints.....	57
2.6.	Scope of the work	60
3.	Materials and Experimental Techniques	63
3.1.	Introduction.....	63
3.2.	Materials	63
3.3.	Manufacturing of welded plates	64
3.4.	Optical Microscopy	69
3.5.	Scanning electron microscopy and Transmission electron microscopy.....	70
3.6.	X-ray diffraction	71
3.7.	Microhardness test	71
3.8.	Tensile test	72
3.9.	Grain size measurement and fraction of precipitates and phases ..	73
3.10.	Corrosion	73

3.10.1.	Conventional techniques	73
3.10.2.	Scanning vibrating electrode technique	74
4.	Microstructure characterization	77
4.1.	Microstructures of the base metals	77
4.1.1.	LNE500	77
4.1.2.	AHSS900.....	79
4.1.3.	Considerations of BMs microstructures	86
4.2.	Microstructure of the welded joints for the LNE500 steel.....	86
4.4.	Microstructure of the welded joint AHSS900.	96
4.5.	Discussion of the microstructure of the welded joints	107
4.6.	Grain size and Chemical composition measurement.....	110
4.7.	influence of heat input on the microstructure	117
4.8.	Conclusions	119
5.	Mechanical properties	121
5.1.	Microhardness	121
5.2.	Tensile tests	127
5.3.	Conclusions	132
6.	Corrosion behaviour	135
6.1.	Electrochemical behaviour.....	135
6.1.1.	Base metals.....	135
6.1.2.	Welded joints	138
6.2.	Confocal laser scanning microscopy (CLSM)	145
6.3.	Scanning vibrating electrode technique (SVET)	148
6.4.	Discussion	161
6.5.	Conclusions	167
7.	General Conclusions	169
8.	Future work	171
9.	References.....	173

Chapter 1

1. INTRODUCTION

Steels are the most useful materials for structural and automotive applications. In 2016, 1,515 million tonnes of finished steel products were used in different application. The amount of steel per capita in the world in 2010 was 192.6 kg whereas in 2016 it was 207.9 kg, which evidence considerable increase and the importance of this class of material (BASSON, 2017).

Because of the complexity of the iron-carbon system, steels are extremely versatile. Their versatility is mainly due to the variety of microstructures that can be obtained by transformation from austenite (γ) (BHADESHIA, 1985). Steels properties can be ranged by adding elements and by using mechanical and heat treatments.

Conventional high-strength steels obtain their strength through high alloying content and hence high carbon equivalent (CE) value. Due to their high CE, conventional high-strength steels require heating prior and post to welding to avoid hydrogen cracking, increasing manufacturing costs (ATTA-AGYEMANG et al., 2017).

Nowadays, longer and more secure usage of steel product becomes much more important and to attend the different requisites from the wide range of industries, steels properties must be improved. Weight reduction and structural durability drive research activities into high strength steels. In the 1990s the use of high-strength steel sheet accounted for only 30% whilst in 2011 it increased to 60% (USHIODA et al., 2011). A special attention is given to High-Strength Low-Alloy steels (HSLA) and Advanced high-strength steels (AHSS) due their low carbon content.

The strength of AHSS and HSLA steels does not depend on the carbon content, being associated with different strengthening mechanisms such as grain refinement, microalloying effects and precipitation strengthening (LAGNEBORG et al., 1999; NIE

et al., 2010). Combinations of controlled rolling and microalloying additions have systematically improved the mechanical properties of HSLA steels to meet the rigorous demands of various industries. Finally, the low carbon content and low CE negate the requirement for weld preheating, which leads to significant cost savings through decreased labour and energy requirements and increased productivity (CAO et al., 2011). Martensitic steels (AHSS) can provide further increase for the mechanical properties, achieving tensile strengths of up to 1,500 MPa by proper combinations of quenching and tempering procedures (ZHANG, 2011).

In the automotive industry, welding is required to join most of the vehicle's structural components. The welded area, which includes BM (base metal), HAZ (heat affected zone) and WM (weld Metal), is a crucial region as it generally becomes the weakest part of the component. Therefore, the microstructure and properties of this part must be improved (USHIODA et al., 2011). Many factors influence the microstructure of HAZ such as steel composition, austenite grain coarsening characteristics, plate thickness and the welding conditions. All parameters control the microstructure and mechanical properties. Indeed, composition and grain coarsening are related to steel hardenability (BARBARO et al., 2015).

Welding of high-strength steels is generally more challenging than that of standard ferrous alloys because of their high mechanical strength and microalloyed elements. One problem arises in the HAZ close to the fusion line, where coarse grain heat affected zone (CGHAZ) develops. The challenge is to minimize the loss of mechanical strength in the CGHAZ region. For this purpose, better quality steels and selection of proper welding parameters are important. One of the important welding parameters is the heat input. It affects the mechanical properties of the weld CGHAZ of high strength steels. Higher heat input enhances coarsening of prior austenite grain size due to slower cooling rate, thus, decreasing the strength level of the welded joint (KUMAR & NATH, 2016).

Moreover, for successful applications of high-strength steels in the automotive industry, knowledge regarding welding corrosion behaviour is of particular interest (PAGOTTO et al., 2015). The change in the microstructure and chemical composition in the welded area may lead to the formation of galvanic corrosion in this region, consequently reducing the lifetime of a welded component in service.

Chapter 2

2. LITERATURE REVIEW

2.1. ECONOMIC ASPECTS

Two major drivers for the use of newer steels in the automotive industry are fuel efficiency and increased safety performance. Fuel efficiency is mainly a function of the weight of steel parts, which in turn, is controlled by gauge and design. Safety is determined by the energy absorbing capacity of the steel used to make the part (BHATTACHARYA, 2016). As it is well-known, trucks and buses are mostly powered by diesel engines and, therefore, their emissions contain carbon monoxide CO, carbon dioxide CO₂ and nitrogen oxides (NO_x gases). Saving fuel leads to a reduction of such emissions. Many regulations have been enforced to reduce them (MAYYAS et al., 2012; SVENSSON, KARLSSON, SÖDER, 2015).

A current Mercedes-Benz bus chassis is weight up to 3,668 kg. A model is shown in Figure 1.

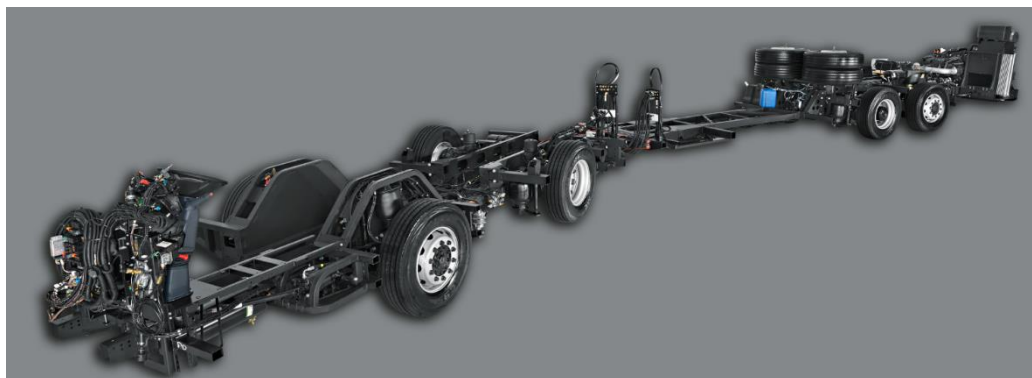


Figure 1: A current Mercedes-Benz bus chassis (MERCEDES-BENZ BRAZIL, 2016).

In average, a weight reduction of 10% of the total vehicle weight (apart from passengers and cargo) may represent an improvement of 5% in the fuel efficiency, as reported by Mayyas (MAYYAS et al., 2011).

In this context, application of high-strength steels has an effective approach to weight reduction (Kastensson, 2014), particularly for parts with thicker materials. Thus, the use of high-strength steels for heavy vehicles is a trend. Chassis are the main focus since it is by far the heaviest part (SATO et al., 2013; SVENSSON, KARLSSON, & SÖDER, 2015).

Over the recent years high-strength steels have been adopted in trucks. The combined approach of an integrated design of main and auxiliary frame allied with the application of high-strength steel (700 MPa yield strength) allowed an impressive weight reduction of approximately 800 kg. Steels with yield strength around 900 MPa is already on the horizon for Chinese truck producers (MOHRBACHER, 2015).

It should be emphasised that production costs of vehicle lightweighting are disproportionately higher than the fuel cost savings. However, vehicle lightweighting is more cost-effective for larger vehicles (KIM, KEOLEIAN, & SKERLOS, 2010). At the same time, the introduction of new steels in general industries allows reducing the self-cost of plate steel production by 20-25%. This significant reduction is claimed to be achieved by decreasing the quantity of alloying elements, reducing labour and energy consumption for installation and construction, including welding of structures and finally by reduced need for maintenance and fewer accidents (ORYSHCHENKO & KHLUSOVA, 2011). In addition, high-strength steels are claimed to be more cost-effective compared to conventional mild steels (JAVIDAN et al., 2017)

Therefore, to produce lighter vehicles, it is not only necessary to develop new alloys but also to achieve optimum strength/formability/cost balance for the various components. Among the potential materials, high-strength steels have been proven to allow weight reduction while meeting vehicle safety and performance requirements (DRILLET, VALLE, & IUNG, 2012; ORYSHCHENKO & KHLUSOVA, 2011).

2.2. CLASSIFICATION OF HIGH-STRENGTH STEELS

Steel is arguably the most important material in engineering, construction and automotive industries. It has a wide range of applications and an extensive range of attractive properties. It is well-known that steel microstructure is a direct result of the processing history and its chemistry. The microstructure dictates the final properties and performance of the alloy.

The wide range of steels is an enormous benefit to the automotive industry. Each steel fulfils some specific necessity. Figure 2 shows several types of high-strength steels and their classification in two main groups: High-Strength and Advanced High-Strength Steels (AHSS).

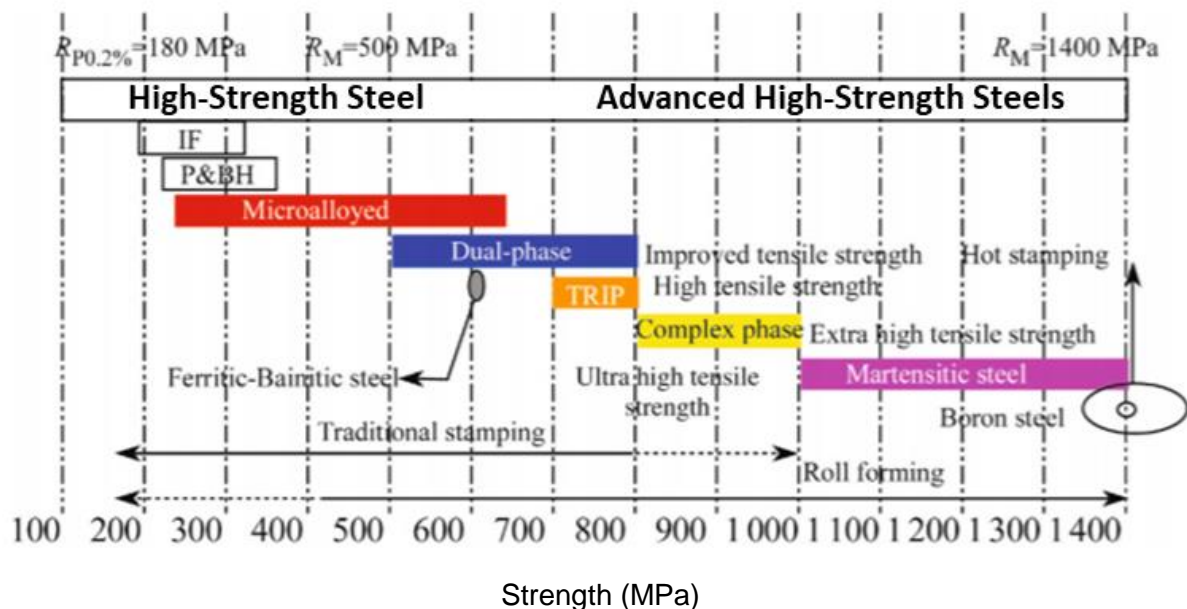


Figure 2: Steels grades and typical forming techniques as a function of strength (MOHRBACHER, 2015)

The dual-phase (DP) steels are low-alloy steels with two major phases, ferrite and martensite. The former is soft, and the latter is significantly harder. This class of steels contain manganese, silicon, some contain vanadium; additions of Cr (0.5 wt%) and Mo (0.2-0.4 wt%) are frequently used to control the microstructure. The final microstructure is achieved by annealing and air cooling (BHADESHIA & HONEYCOMBE, 2017). The mechanical properties of dual-phase steels can be improved by producing ultrafine grains (UFG) characterized by grain sizes smaller than 1-2 μm . Furthermore, the addition of some kinds of alloying elements, such as strong

carbide formers (V, Ti, Nb, etc.), would inhibit grain growth during heat treatment to result in much finer DP structure. Some disadvantages of DP steels include high alloy content, some springback issues (the elastically driven change of shape of a metal sheet during unloading and following forming which is called springback issues) (WAGONER, LIM, & LEE, 2013), potential for edge cracking and poor formability (CHO et al., 2011).

Transformation induced plasticity (TRIP)-assisted steels are a new generation of low-alloy steels that exhibit an enhanced combination of strength and ductility (VAROL et al., 2013). This combination is a result of a plastic deformation process to obtain martensite. Stress concentrations are relieved by martensitic transformation induced by local stress, which increases work-hardening rate. Their microstructure consists of allotriomorphic ferrite (major phase) with 30-40% of a mixture of bainite, martensite and carbon-enriched retained austenite (BHADESHIA & HONEYCOMBE, 2017). Mechanical properties of TRIP-assisted steels can be improved by designing heat-treatment processes (SHEN & ZUO, 2016). Table 1 summarises the advantage of TRIP and DP steels. Furthermore, it presents two other steels: HSLA and Martensitic which will be the topic of the next sub-sections.

Table 1: Advantages and disadvantages of HSLA and AHSS steels (CHO et al., 2011).

Steel type	Advantage	Disadvantage
Dual-Phase	High strength, formability acceptable, crashworthiness similar to TRIP steels No major welding issues	High alloy content, some springback issues, potential for edge cracking, formability remains a challenge
TRIP	High crash-worthiness, high strength with small forming strains	Require expensive annealing cycles, carbon equivalent can be high, limited weldability
HSLA	Familiarity, excellent weldability and widely available	Relatively low formability, variability in properties and springback issues as the yield strength increases
Martensitic	Ultra-high strength	Low formability, geometrical variability between slit coils

2.2.1. Microalloyed steels

High-strength low-alloy (HSLA) steels are also referred to as microalloyed steels. Their strength is considered 'high' compared to mild steel. HSLA steels yield

strength is in the range from 350 to 700 MPa (HULKA, 2005). The strength of HSLA steels is primarily obtained through precipitation strengthening and refinement of grain size by addition of a small amount of elements such as Nb, V, Ti and Mo. Thermomechanical rolling is the standard production route for HSLA steels. The properties are guaranteed in the as-rolled condition which avoids the need for further treatments. This process is characterised by a final deformation in the lower austenite region without recrystallisation (HULKA, 2005).

The typical microstructure of HSLA steels obtained by controlled rolling contains bands of refined equiaxed ferrite grains and lamellar pearlite (KORCZAK, 2004). The strength in ferrite-pearlite steel is often attributed to the prior austenite grain size, size of the pearlite colony, amount of elements in solid solution, dislocation density in ferrite and interlamellar pearlite spacing. Pearlite is a common constituent of steels and adds to its strength. It is composed of cementite which is rich in carbon and ferrite which can only accommodate very little carbon. The transformation of pearlite is diffusion-controlled (PANDIT, 2011). In low-carbon steels, pearlite nucleates at the austenite-ferrite interface followed by subsequent lamellar growth of a pearlite colony into austenite. The colonies of pearlite consist of alternating lamellae of ferrite and cementite (REICHERT, 2016).

New designs of microalloyed steels have been created. In a recent work, a low-cost hot rolled high strength steel was produced at a cooling rate of 13 °C/s and a coiling temperature¹ of 650 °C. The final steel microstructure consisted of 90% of 5 µm polygonal ferrite and 10% of pearlite. The yield strength was 570 MPa and tensile strength was 615 MPa. The ferrite-pearlite steel exhibited excellent bendability and Charpy impact property for the automotive application (HU et al., 2014).

There is, however, a growing need for even higher strength levels for automotive steels, leading to the development of martensitic steels. This type of AHSS is described in the next section.

¹ In modern mills the cooling process happens in two parts. Initially, after the final hot rolling passes the strip is cooled rapidly. Once a predetermined temperature is reached this rapid cooling is then stopped at a temperature known as the 'coiling temperature'. From this the hot-strip is gathered into a coil, stored, and allowed to cool to ambient temperature at a much slower rate (FACCO, 2005).

2.2.2. Martensitic steels

The yield strength of microalloyed steels are limited by their ferrite grain size. One believes that the ferrite grain size processed by heavy hot deformation is limited to 1 μm which resulted in yield strength of 800 MPa (DONG et al., 2011). For several applications, higher strength is desired. In this context, martensitic steel has to be applied as it has higher strength than HSLA steels (MOHRBACHER, 2014).

The tensile strengths of martensitic steels are normally within the range 600-1,800 MPa. The martensitic microstructure is the result of quenching from austenite, and the main factor responsible for its strength is the carbon content in solid solution. However, tempering is necessary to improve toughness, even though it reduces the martensite strength. During tempering the supersaturation of the as-quenched martensite is relieved. As a consequence, there is formation of a distribution of iron and alloy carbides (DONG et al., 2011; PODDER, 2011). Tempered martensite with a fine dispersion of alloy carbides, such as CrC_x , MoC_x and VC_x , is a base structure for high-strength steels (BHADESHIA & HONEYCOMBE, 2017).

Traditional martensitic steels have a high C content to ensure the hardenability during quenching. In addition, some expensive alloying elements such as Mo, Cr and Ni must be added. High Si content is necessary to prevent carbide precipitation while Mn and Cr promote hardenability and inhibit the formation of undesirable constituent phases. Junior et al. performed an investigation of tempering influence on the microstructure of a high carbon steel (C0.56-Mn0.58-Si1.43-Cr0.47 wt%). Multi-phase microstructures were obtained containing martensite, bainitic ferrite and retained austenite. They concluded that isothermal heat-treatment below martensite-start temperature could be used to obtain higher hardness values for steels tempered at either 400 °C or 450 °C (JUNIOR & SANTOS, 2013).

However, high C content martensitic steels are very susceptible to hydrogen embrittlement, which result in low weldability and toughness (ATTA-AGYEMANG et al., 2017; TSAY et al., 2006). Therefore, Advanced High-Strength Steels with low carbon and less expensive alloying are of great interest (DONG et al., 2011).

The combination of low carbon contents and grain refinement is a promising route to develop new high-strength steels. The rolling process has a major influence on the final microstructure of martensitic steels due to grain refinement. Han et al.

studied the influence of two different rolling temperatures (950 °C and 1100 °C) on the grain refinement and strength of a Ti microalloyed low carbon martensitic steel. They concluded that hot rolling temperature plays a significant role in the microstructure and mechanical properties of the steel as shown schematically in Figure 3 (HAN et al., 2012).

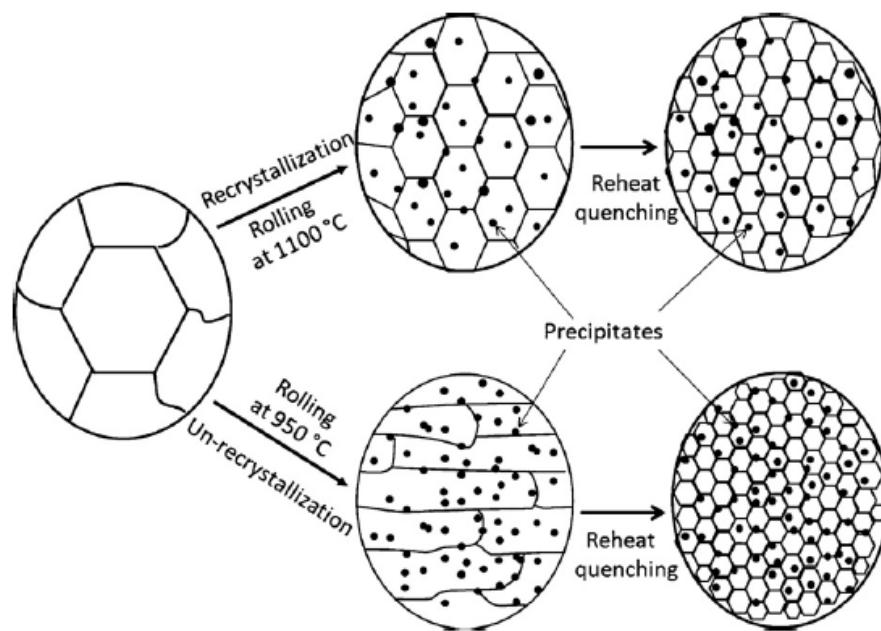


Figure 3: Schematic diagram of the grain evolution during rolling and heating process (HAN et al., 2012).

The finest microstructure was reported to be the one rolled at 950 °C (non-recrystallisation region). Deformed pancake grains were formed under deformation. TiC precipitates were detected for both conditions. However, because of the higher dislocation density and increased low angle boundaries (due the deformation energy stored in the matrix), rolling at the non-recrystallisation region was found to have finer final microstructure. The refining effect for the rolling process at the recrystallisation region was limited and part of the TiC precipitates grow to a large size rapidly (HAN et al., 2012). The dislocations resulting from rolling in the non-recrystallisation region served as nucleation sites for austenite/ferrite transformation, making ferrite grain more fine and homogeneous (WOO et al., 2013).

2.3. ARC WELDING

A variety of methods are available to join different components in the metalworking industry. The joining methods can be either permanent or temporary depending on the type and design of the product. The latter methods use parts like bolts, screws, and rivets, whereas the former usually involves welding. Welding is one of the most common permanent joining processes in the metal industry (KAH & MARTIKAINEN, 2012; PÉPE et al., 2011).

Arc welding, in particular, has been widely used because of its numerous advantages such as low cost, high welding speed, low spatter and high deposition efficiency (KAH & MARTIKAINEN, 2012; YI et al., 2015). In addition, when it is coupled to a robotic system there is a significant productivity increase (BOLMSJO, OLSSON, & CEDERBERG, 2002).

Gas metal arc welding (GMAW) is characterised by an electrical arc between a continuously fed electrode and the weld pool. The range of the arc temperature varies between 5,000 and 30,000 K, depending on the precise nature of the plasma and the amount of current flowing through it. Arc current and arc voltage are the two most important factors determining the arc characteristics affecting the weld quality (KAH et al., 2014). Because of the presence of high temperatures during fusion welding, reactions between the weld pool and its surrounding atmosphere (oxygen and nitrogen) can take place very easily if proper protection is not provided for the molten metal. To prevent oxidation the weld pool is protected by an externally administered gas (KAÇAR & KÖKEMLI, 2005; RAMOS-JAIME, LÓPEZ-JUÁREZ, & PEREZ, 2013; WONG & LING, 2014). The main purposes of shielding gas are shown in Figure 4.

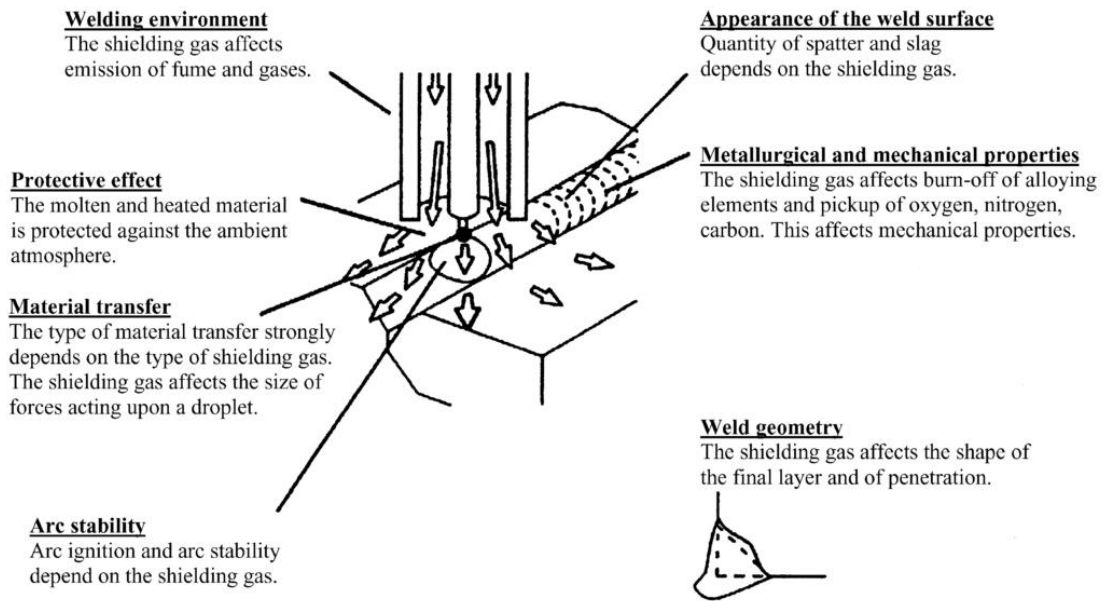


Figure 4: Influence of shielding gas in GMAW processes (SUBAN & TUSEK, 2001).

The gas can be active, a process named metal active gas (MAG), or inert, metal inert gas (MIG). The commonly used shielding gases in GMAW are carbon dioxide (CO_2), argon gas (Ar) and their combinations. The arc initiation and stability attained by using argon are better than by using CO_2 since the values of ionization potential and electric conductivity of argon gas are higher. However, CO_2 can achieve better temperature distribution within the arc welding and weld penetration due to its higher thermal conductivity and it is cheaper than argon (KAH & MARTIKAINEN, 2013; WONG & LING, 2014).

The heat input (HI), which is the energy supplied to the workpiece during the welding processes, is a crucial parameter for the quality of the welded joint. It determines the peak temperature at each location within the heat-affected region as well as the cooling rate (ALIPOORAMIRABAD et al., 2017; NOWACKI, SAJEK, & MATKOWSKI, 2016). The HI per unit length (kJ/mm) is calculated according to Equation 3 (QUINTINO et al., 2013; WAINER, BRANDI, & MELLO, 1992).

Equation 1: Heat input

$$HI = f \cdot \frac{E \cdot I}{1000 \cdot S}$$

Where f = Efficiency of heat transfer; E = arc voltage (V); I = arc current (A); and S = welding speed (mm/s). It is clear that the heat input is directly proportional to

the arc current and voltage. It also depends on the cooling time as represented in Figure 5.

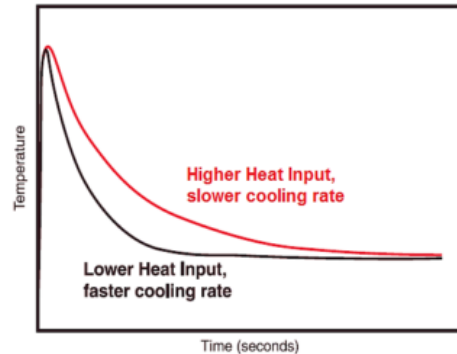


Figure 5: Heat input influences cooling rate (MOHAMMED et al., 2017)

It can be observed from Figure 5 that higher heat input leads to slower cooling rates whereas the opposite occurs for relatively lower heat inputs (HUTCHINSON et al., 2015). As the heat input increase the base metal is heated up to longer distances, forming larger HAZ. Therefore, the temperature difference between the point of heat input and the base metal decreases, thus diminishing the cooling rate (KUMAR & NATH, 2016).

The heat generated by the arc melts the base metal surface as well as the electrode tip. A droplet of the molten electrode is transferred to the workpiece through the electric arc. There are several modes to transfer the molten electrode to the workpiece. Each transfer mode depends on the welding process, the welding power supply, the filler metal and has its own distinct characteristics and applications. The choice of the transfer mode depends on several aspects such as weld position, thickness of the base metal and weld quality.

Spray transfer occurs at large currents and wire feed speeds, and involves a continuous stream of small diameter droplets. Pulsed transfer is characterised by a pulsed current waveform and each current pulse detaches a droplet of the molten material. The droplet has a similar size to that of the wire (filler) diameter. The transfer occurs when the wire dips into the weld pool and a short circuit occurs (PÉPE et al., 2011; WAINER et al., 1992). However, when the short circuit occurs (when the droplet makes contact with the workpiece) the current increases, resulting in an explosive rupture of the wire and high levels of spatter.

Short circuiting transfer occurs when the currents and voltages are generally low and the wire 'dips' into the weld pool, this transfer is also called dip transfer. The same spatter problem occurs. Controlled short arc - under market name CMT - overcomes this issue by controlling the wire motion automatically during droplet detachment. The wire is pulled back during or just after metal transfer. CMT can be used in almost all welding positions, with almost all kinds of metallic materials, and with different thicknesses (FRONIUS, 2014; KAH et al., 2014; SCHORGHUBER, 2009). Furthermore, when thin sheets are required, the GMAW process with pulsed arc is no longer suitable (KAH et al., 2014). In the case of conventional, short-circuit MAG welding, droplets separation is forced with a relatively large current value, whereas in the case of CMT, the short-circuit current is significantly reduced. Despite this, the droplets separate easily, which is facilitated by programming of the wire feed speed. The principle of the CMT process is to cause wire withdrawal with a digital control system at the moment of short circuit, which facilitates liquid metal droplets separation (GRZYBICKI & JAKUBOWSKI, 2013).

Due to its lower short-circuit current and, consequently, lower heat input, CMT is more suitable for small thickness plates when compared to pulsed transfer (BHADESHIA & HONEYCOMBE, 2017). Low heat input is advantageous for welding of high-strength steels because it maintains the fine grain structure on the HAZ.

2.4. INFLUENCE OF WELDING PARAMETERS

During welding, the base material and filler material experience high temperatures. The time-temperature profile experienced during welding changes along the distance from the fusion line creating a steep temperature gradient. The metallurgy of the welded joint can be divided into two major regions, the fusion zone and the heat affected zone (HAZ).

The HAZ is composed of different regions which are differently affected by heat. Figure 6 shows a schematic representation of the welded joint including several zones within the HAZ and also a temperature profile.

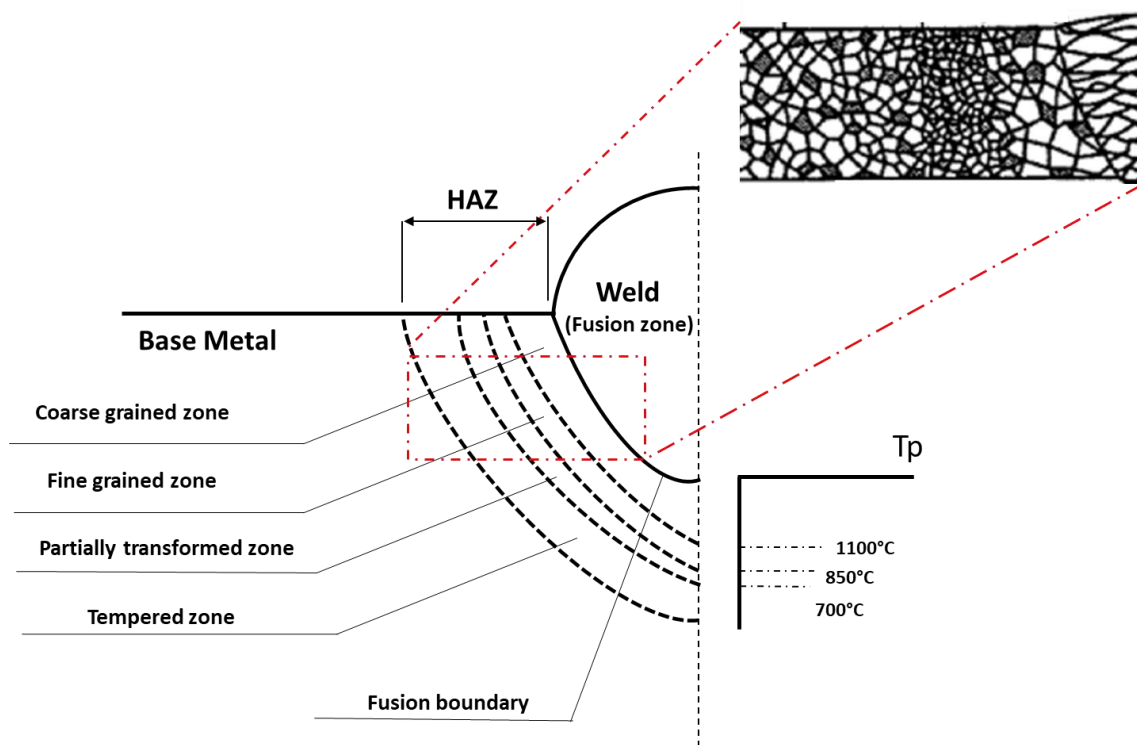


Figure 6: A schematic presentation of the different zones in the HAZ. Modified (THAULOW, PAAUW, & GUTTORMSEN, 1987)

It can be seen that each zone experiences different peak temperatures and cooling cycles in the HAZ due to the intense heat from the welding process. Cooling cycle is less sensitive to the distance away from the fusion boundary (BHADESHIA & HONEYCOMBE, 2017).

The coarse-grained austenite is the region adjacent to the fusion boundary and will be referred to as CGHAZ (coarse-grained HAZ). To have a complete formation of austenite in steels, the temperature required is about 950°C. However, in this zone, the temperature is much higher (up to 1100 °C) which leads to a rapid grain coarsening. The fine-grained austenite zone has grains of about 20-40 μm in size (BHADESHIA & HONEYCOMBE, 2017).

Partially austenitic region forms at a distant region from the fusion zone where the temperature cannot completely austenitize the microstructure. The small amount of austenite that does form has a large carbon concentration because of the higher solubility of carbon in austenite at lower temperatures (700-850 °C) (BHADESHIA & HONEYCOMBE, 2017).

A distributed heat source model to predict welding temperature distribution and variations was presented by Gery, Long and Maropoulos as shown in Figure 7 (GERY,

LONG, & MAROPOULOS, 2005). They considered welded plates and filler material as a solid body and a moving heat source model was developed to present the heat generated by the torch in the MIG welding process.

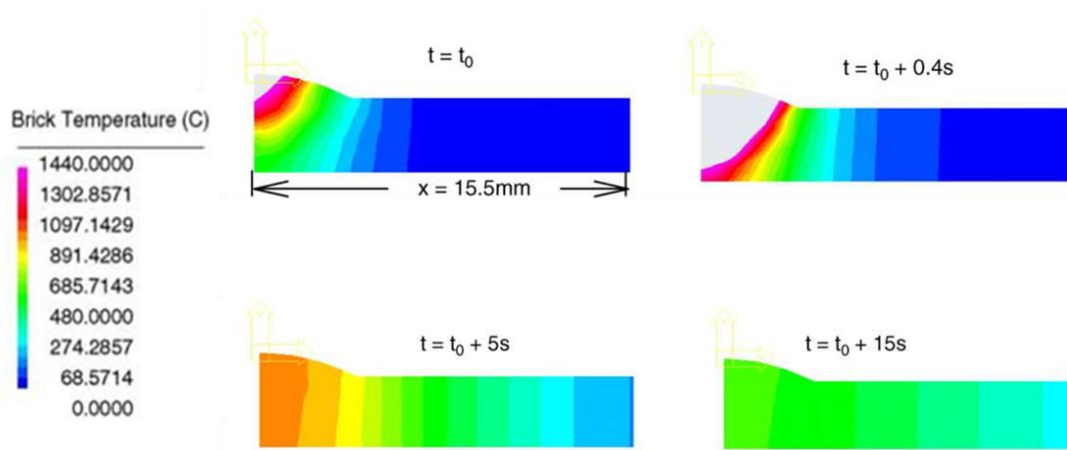


Figure 7: Temperature evolution in function on time in the welded plate (GERY, LONG, & MAROPOULOS, 2005).

Clearly the microstructure is affected even when the heat source is not present in that position anymore. On this model, a rapid heat transfer from the welding pool is observed.

Therefore, heat input influences the solidification mode and secondary metallurgical transformations. As mentioned earlier, for higher heat inputs, there is an increase of the solidification time and a reduction of the cooling time (see Figure 5). Both characteristics increase the grain sizes and, accordingly, the metal quench ability (QUINTINO et al., 2013).

The understanding of the post-weld microstructure is important as it determines the performance of the welded joint, i.e., toughness and hardness. The CGHAZ is a critical region due to the consequences of grain growth on the mechanical properties welded part such as hardness and tensile strength reduction (QUINTINO et al., 2013).

It is known that HAZs are often the most critical regions with regard to potential failures of welded parts. Some welding procedures have been shown to produce grain growth and subsequent softening in the HAZ. A wide range of studies is dedicated to understanding and avoid the coarse-grained zone where softening can occur. The addition of grain-refining additives such as aluminium, titanium, niobium or vanadium minimises the growth of austenite grains by making the grain boundary movement

more difficult which seems to be an efficient strategy to decrease HAZ-related softening (LAGNEBORG et al., 1999).

Many studies have shown the influence of microalloying elements and heat input in the HAZ (HUTCHINSON et al., 2015; MILITZER, FAZELI, & JIA, 2014; MOHANDAS, REDDY, & KUMAR, 1999; YANG & HUANG, 2014).

Mohandas et al. verified that steels with high carbon-equivalent exhibited maximum softening for high-heat input process (Gas Metal Arc Welding (GMAW)), compared with low-heat-input process (shielded metal arc welding (SMAW)). The general HAZ softening is due to decomposition of martensite to soft products due to over-tempering. Moreover, higher contents of elements that retard the martensite-start temperature such as Si contribute to a lower softening tendency (MOHANDAS et al., 1999).

Titanium nitride is a highly thermal-stable precipitate present in Ti-microalloyed steels. Due to its pinning action, TiN has an effective control of austenite grain boundary migration. Lagneborg et al. reported no measurable TiN coarsening below about 1300 °C which may prevent coarsening of the bulk of the austenite microstructure during short heating periods, such as in the HAZ of welded joints. Consequently, this would give a secure control of the grain growth inhibition (LAGNEBORG et al., 1999). However, it has been reported that, due to steelmaking controls, an optimum precipitate size distribution is required, but it can be difficult to achieve consistently. On the other hand, the addition of Nb seems to increase the control of HAZ and increase toughness (BARBARO et al., 2015). Nb importance is confirmed when welding these steels, hence its amount in solution may vary as a function of welding conditions (HUTCHINSON et al., 2015)

Nb carbonitrides are stable at low temperatures, but they dissolve at higher temperatures (YANG & HUANG, 2014). This may result in rapid coarsening of austenite grains in the HAZ adjacent to the fusion line (MILITZER, FAZELI, & JIA, 2014). The effect of Nb on steels can be enhanced by the presence of Molybdenum. Mo operates synergistically with solute niobium to promote transformation at a low temperature to give a fine lath bainitic structure having a high density of high angle boundaries (MOHRBACHER, 2014). Specifically, the results show that increased

levels of Nb in low carbon steels provide greater tolerance to increasing levels of weld heat input by controlling grain coarsening (XIA et al., 2016).

A recent report has studied simulated HAZ from two HSLA steels, one microalloyed with Nb and another one microalloyed with V and N. The HAZ structure simulation was over a range of heat input (HI) conditions, characterised by the cooling time from 800 to 500 °C ($\Delta t_{8/5}$). For the V-N steel, the toughness improved with increasingly rapid cooling (low HI conditions), whereas the HSLA steel microalloyed with Nb showed toughness decreased at slow cooling time (higher HI). The improvement in toughness for V-N steel at low HI is due to the non-coarse-grained ferrite in the HAZ. The HAZ microstructure was completely bainitic and was little affected by the heat input. A final remark was that lath boundaries in the bainite were predominantly on {110} planes of the ferrite. The lath boundaries average spacing varied depending on steel composition and cooling rate. They conclude that since {110} is also the slip plane in ferrite, the close spacing between the lath boundaries inhibits general plasticity at stress concentrations and favoured fracture initiation. The differences between the two steels are due to their transformation behaviours on cooling where precipitation of vanadium nitride in austenite accelerated ferrite formation and raised the temperature of the phase transformation in V-N steels (HUTCHINSON et al., 2015).

Yang and Huang reported the effect of Nb content (0.01, 0.02 and 0.04 wt%) on the HAZ microstructure with different heat inputs (20, 50 and 80 kJ/cm). The typical structure in a low-alloy steel HAZ is characterised by a very coarse prior austenite grain size with allotriomorphic ferrite layers formed during cooling after welding. There was found a significant difference on the microstructure in the HAZ in the steel without Nb and niobium-containing steels when the highest heat input was applied (80 kJ/cm). A large amount of pearlite colonies was found in the HAZ of the Nb-free steel, whereas the microstructure on the Nb-steels consisted mainly of secondary Widmanstätten ferrite (α_w) and retained microphases trapped between the α_w plates. The reason why pearlite colonies do not exist in the niobium-containing steels is the retardation effect of Nb for the austenite-ferrite transformation kinetics. At the low energy heat input level (20 kJ/cm), the microstructures of the CGHAZ of the niobium-containing steels were all similar and consisted mainly of interlocking ferrite plates with small amounts of bainite and Widmanstätten ferrite. The microstructure of the niobium-free steel was

comprised of α_w and martensite with a small quantity of pearlite. The results from Charpy impact tests indicated that the niobium-containing steels with a heat input of 20 kJ/cm possessed higher toughness than those welded at heat inputs of 50 and 80 kJ/cm. It is proposed that the interlocking ferrite structure, which forms in the HAZ of the niobium-containing steels after simulation of a 20 kJ/cm heat input level, improves the toughness property (YANG & HUANG, 2014).

Nevertheless, the main influence of heat input in the HAZ is the grain size. Prior-austenite grain size in the HAZ of single-pass butt welded joints of thick HSLA-100 steel plates was evaluated by Shome. For a HI of 10 kJ/cm the grain size in the coarse grain heat-affected zone was 80 μm corresponding to a peak temperature of 1450 °C. The grain size is much smaller, 40 μm within a distance of 0.5 mm from the fusion line. At a higher HI (40 kJ/cm), grain size was 130 μm for the same peak temperature and the CGHAZ zone had 1.1 mm wide (SHOME, 2007).

To elucidate the effect of heat input on geometry, microstructure and mechanical properties, a hot-rolled Nb-Ti-Mo microalloyed steel was welded using different heat inputs (3.90, 5.20 and 7.75 kJ/cm). With increased heat input, the depth/width of penetration increased, and the geometry changed to “wine cup-like” shape. In regard to the microstructural constituents, the martensite content was decreased, but granular bainite (GB) content was increased. The hardness distribution was similar for different heat inputs. Hardness in FZ, CGHAZ and mixed-grained HAZ was higher than the base metal (BM). But for the fine-grained HAZ, hardness was similar or marginally lower than that of the BM. The tensile strain was concentrated in the BM such that fracture occurred in this region. The sample exposed to the heat input of 5.20 kJ/cm presented superior geometry, microstructure, and mechanical properties (WANG et al., 2017).

It has to be emphasised that a number of problems can be caused by ultra-high strength (quenched and tempered) steel welding because of microstructural aspects. Joints of arc welded martensitic steels usually exhibit worse mechanical properties than analogous parameters for mild steels. The strength of such joints rarely turns out to be higher than the strength of the parent material, which can be best illustrated with tensile strength tests that most frequently result in the fracture of specimens at the welded joint (NOWACKI et al., 2016).

After a detailed literature review, most of the investigations are found to have focused on the effects of heat transfer/heat input on high strength steels by using various welding techniques. It is clear that irregular heat input variations of various fusion welding process on high-strength steels cause drastic changes in the phase balance, which needs to be balanced. Knowledge about the microstructural evolution of such kind of steels, as well as about its thermal history, is fundamental to achieve the expected mechanical behaviour. Moreover, the influence of welding heat input on the microstructure transformation of quenched and tempered advanced high-strength steels is fragmentarily interpreted (NOWACKI et al., 2016). Therefore, extensive research is needed to deal with the effects of heat input on HSLA and AHSS welds for an in-depth understanding of this phenomenon and for controlling and improving the weld quality.

2.5. CORROSION BEHAVIOUR

Corrosion can be defined as a simultaneous transfer of mass and charge across a metal/solution interface. It is a phenomenon characterised by metal reaction with the environment, converting metal into oxides or other corrosion products (MCCAFFERTY, 2010).

There are many forms of corrosion. Some examples are uniform attack, crevice corrosion, pitting, intergranular corrosion and galvanic corrosion. The latter occurs when two metals are in mechanical or electrical contact. In a corrosive environment, one of the metals acts as an anode and undergoes corrosion, while the second metal acts as a cathode and remains unattacked (MCCAFFERTY, 2010).

Steel corrosion will be governed by active sites present on its surface, which include, but are not limited to grain boundaries and precipitates. These imperfections are schematically represented in Figure 8.

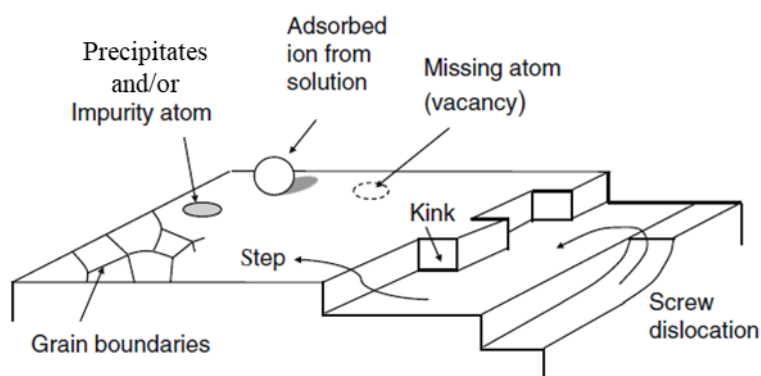


Figure 8: Possible heterogeneities on a metal surface. Adapted (MCCAFFERTY, 2010).

These active sites will take part in the redox reaction, increasing the anodic current density (LI, WANG, & LIU, 2004). The effects of such imperfections are not easy to understand due to difficulty in isolating their individual contributions to the overall corrosion process. A discussion on this subject will be provided later (section 2.5.2. and 2.5.3.).

2.5.1. Corrosion techniques

Several techniques have been used to estimate the corrosion rate of steels, such as potentiodynamic polarisation (HEMMINGSEN et al., 2002), the weight loss method (OGAWA et al., 1995; XUE et al., 2013) or Electrochemical Impedance Spectroscopy (FERNÁNDEZ-PÉREZ et al., 2014).

Potentiodynamic polarisation is accomplished by continuously changing the electrode potential at a constant rate, and simultaneously recording the current (GREENE & LEONARD, 1964). The behaviour of local corrosion couples can be greatly clarified by the two potential-current curves relating, respectively, to a reduction reaction produced in a "cathodic" region, and to an oxidation reaction produced in an "anodic" region (POURBAIX & VANDERVELDEN, 1965). These reactions can be represented by a polarization curve (see Figure 9).

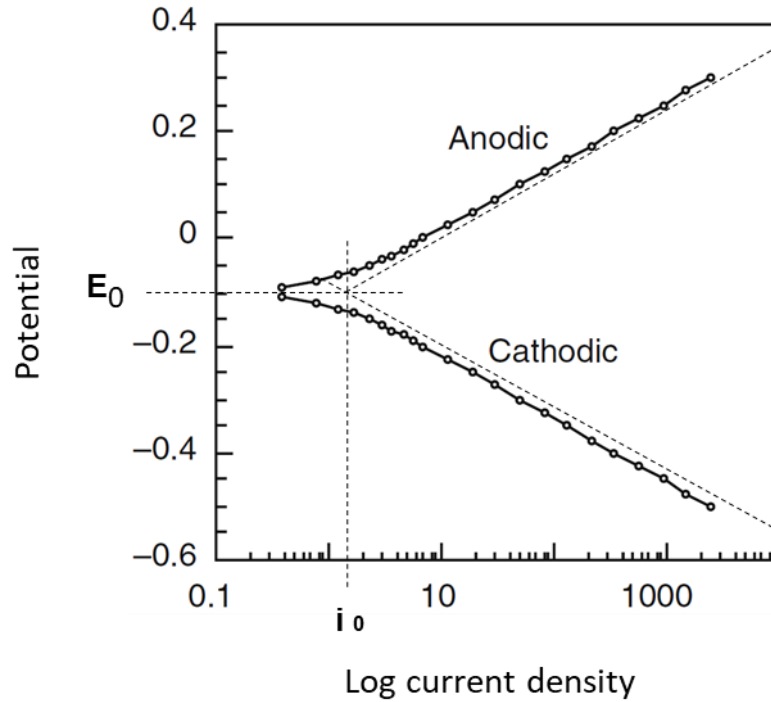


Figure 9: Polarization curve (ORAZEM & TRIBOLLET, 2008).

There is a well-defined value for the electrode potential of the metal surface at which the thermodynamic equilibrium state of the reaction is realised, called the equilibrium electrode potential E_0 . This is an equilibrium value at which the reaction cannot proceed either in the oxidation or reduction directions. At potentials that are higher than E_0 only oxidations reactions can occur, and reduction reactions predominates at potentials lower than E_0 (POURBAIX & VANDERVELDEN, 1965). Wagner and Traud postulated the “mixed potential theory”. It postulates that even without the assumption of the existence of local anodes and cathodes, one can explain corrosion reactions by assuming that cathodic and anodic partial reactions occur at the phase boundary metal/electrolyte in constant change with random distribution of location and time of the individual reaction ($I_{\text{cathodic}} = I_{\text{anodic}} = I_{\text{corr}}$) (LUMSDEN, 2006; WAGNER & TRAUD, 1938).

In 1957, Stern and Geary derived an equation that quantitatively relates the slope of a polarisation curve at the corrosion potential, E_{corr} , to the corrosion current density, i_{corr} (Equation 2) (STERN & GEARY, 1957).

Equation 2: I_{corr} – Stern-Geary relationship

$$I_{\text{corr}} = \frac{B}{R_p} = \frac{\beta_A |\beta_C|}{2.3(\beta_A + |\beta_C|)} \quad \text{or} \quad \frac{I}{E_{\text{corr}}} = \frac{2.3(\beta_A + |\beta_C|) i_{\text{corr}}}{\beta_A |\beta_C|}$$

Where β_A and β_C are the Tafel coefficients of the anodic and cathodic partial reactions and I is the applied current. The linear polarization resistance is defined as the slope of the polarization curve (Equation 3) (ANGST & BÜCHLER, 2015; STERN & GEARY, 1957).

Equation 3: Polarization resistance - Stern-Geary relationship

$$R_p = \frac{\Delta E}{\Delta I}_{E=E_{corr}}$$

The Tafel's law postulates that the logarithm of the current density in an electrochemical reaction varies linearly with the electrode potential (MCCAFFERTY, 2005). In the Tafel-extrapolation technique, the anodic or cathodic partial polarisation curves - or both - are extrapolated back to corrosion potential (E_{corr}). The intersection point corresponds to the corrosion current density (i_{corr}) or corrosion rate (KAJIMOTO, WOLYNEC, & CHAGAS, 1985). This intersection is shown in Figure 9. The Tafel constants are calculated from the anodic and cathodic slopes by using the following equations:

Equation 4: Tafel slope for anodic polarisation ($\Delta E > 0$)

$$b_a = \frac{\Delta E}{\log \frac{\Delta i}{i^*}}$$

Equation 5: Tafel slope for cathodic polarisation ($\Delta E < 0$)

$$b_c = \frac{\Delta E}{\log \frac{\Delta i}{i^*}}$$

Where, $\Delta E = E - E_{corr}$, E is the applied potential, $\Delta i = i_a - i_c$, with i_a being the anodic current density and i_c the cathodic current density and i^* is the corrosion rate. The visually interpolated Tafel lines (graphic technique) used for analysing a polarisation curve are very attractive because of their simplicity when the cathodic and anodic straight lines are well-defined. When the linearity is not well-defined, the extrapolation can be done by the region between: $E = E_{corr} - 0.06$ and $E = E_{corr} - 0.120$ for the cathodic slope. The contribution of the back reaction to the forward reaction is usually negligible for overvoltages ranging from 60 to 120 mV. That is, linear Tafel regions are usually observed for overvoltages 59-120 mV away from the open-circuit potential

(MCCAFFERTY, 2010). Extrapolation from the Tafel region typically provides a sound basis for the prediction of the rate of corrosion reactions (POORQASEMI et al., 2009).

Electrochemical Impedance Spectroscopy (EIS) is a technique that studies the interface between metal and solution. Unlike potentiodynamic polarisation, it is a non-destructive technique. Only a small signal of alternating potential (10-20 mV) with a frequency range of 0.01-100,000 Hz is applied to the electrochemical system and the response to this perturbation - current density - is measured. Figure 10 shows the current response to the input potential for different applied frequencies.

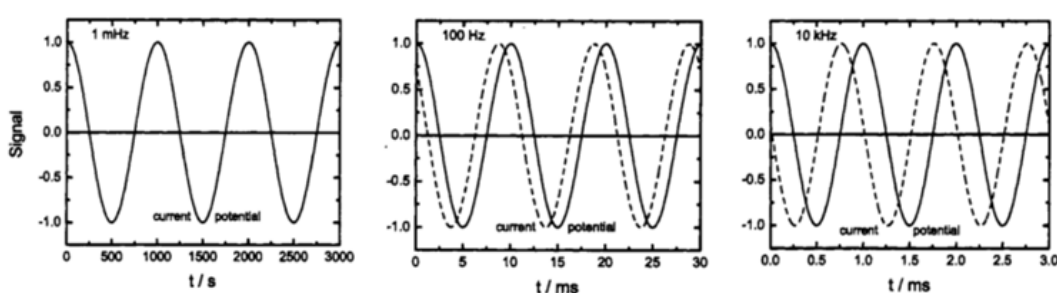


Figure 10: The current density response to a sinusoidal potential input for a system with different frequencies, 1 mHz, 100 Hz and 10 kHz. The solid line represents the potential input and the dashed line represents the resulting current density (ORAZEM & TRIBOLLET, 2008).

At low frequencies, the current density is in phase with the potential perturbation, at the characteristic frequency (100 Hz) the current signal lags the potential input by 45°, and at much higher frequency (10 kHz) current response lags the potential input by 90°.

During EIS measurements the frequencies are applied from high to low values. All responses are measured at the same time according to the arrival on the detector. Potential perturbation amplitude is kept low, so the response is linear, in other words, the applied potential cannot alter the system, it can only perturb it.

When the potential is applied, the molecules in the electrical double layer are perturbed. The double layer is a structure that appears on the surface of the metal when it is exposed to the electrolyte. A schematic representation of an electrical double layer is presented in Figure 11.

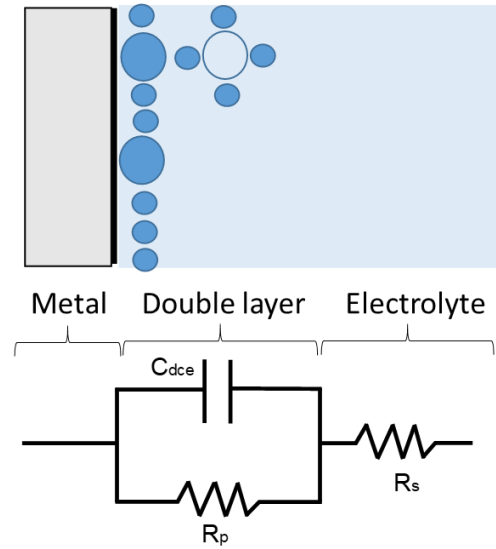


Figure 11: Schematically representation of a double layer formed between the metal and the electrolyte.

The double layer is formed as ions from the solution adsorb onto the electrode surface. The properties of this layer control the corrosion process as the ions from metal and electrolyte have to pass through this layer for corrosion to occur. As can be seen in Figure 11, the electrical properties of the double layer can be fitted into an equivalent circuit using passive circuit elements, such as capacitor, inductor and resistor. Each circuit component corresponds to each interfacial component. The element C_{dce} is the capacitance of the double layer, R_p is polarisation resistance, and R_s is the resistance of the solution.

After a perturbation of the double layer, the molecules require a time to return to their equilibrium state, and this is called time constant expressed by Equation 6.

Equation 6: Time constant

$$\tau = RC$$

Where R is resistance and C is the capacitance. The impedance is also represented by Equation 7.

Equation 7: Impedance

$$Z = \frac{1}{i\omega C}$$

Where ω is angular frequency, C is capacitance, and i is the complex variable for sinusoidal perturbations. After some mathematic calculations the impedance can be expressed by a complex number, as follows:

Equation 8: Complex impedance

$$Z = (Z') + (iZ'') = \left(R_s + \frac{R_p}{1 + \omega^2 \cdot R_p^2 \cdot C_{dce}^2} \right) + \left(- \frac{\omega \cdot R_p^2 \cdot C_{dce}}{1 + \omega^2 \cdot R_p^2 \cdot C_{dce}^2} \right)$$

Where R_p is polarisation resistance, C_{dce} is the capacitance of the double layer, R_s is the solution resistance, ω is the frequency, Z' is the real part of the impedance and Z'' is imaginary part of the impedance. The mathematical procedure will not be treated in this thesis as it is out of its scope. Equation 8 expresses the impedance of the circuit showed in Figure 11. From Equation 8 the frequency can be isolated, giving the results shown in Equation 11.

Equation 9: Semi-circle

$$\left[Z' + \left(R_s + \frac{R_p}{2} \right) \right]^2 + Z''^2 = \left(\frac{R_p}{2} \right)^2$$

The graphic representation of Equation 11 gives the semi-circle shown in Figure 12. This representation is known as Nyquist plot or Cole-Cole plot.

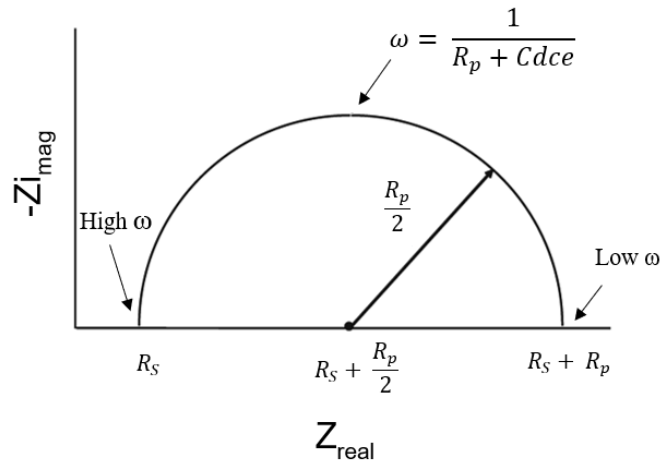


Figure 12: Nyquist diagram, imaginary part Y-axis and real part X-axis (MCCAFFERTY, 2010).

The semicircle is characteristic of one single time constant. Some systems can often contain several semicircles which are related to more than one single electrochemical process. In practical terms, corrosion rust (scale) is formed and contribute to the corrosion process, and a different equivalent circuit will represent the

electrical properties of this system (BOKATI, DEGHANIAN, & BOX, 2017). Other ways to present the EIS data are from Bode plots (Modulus of impedance and Phase plots). In $\log |Z|$ vs. $\log f$ plots, when $\omega \rightarrow 0$, then $|Z| = R_s + R_p$ and when $\omega \rightarrow \infty$, $|Z| = R_s$. Figure 13 shows an example of such plot.

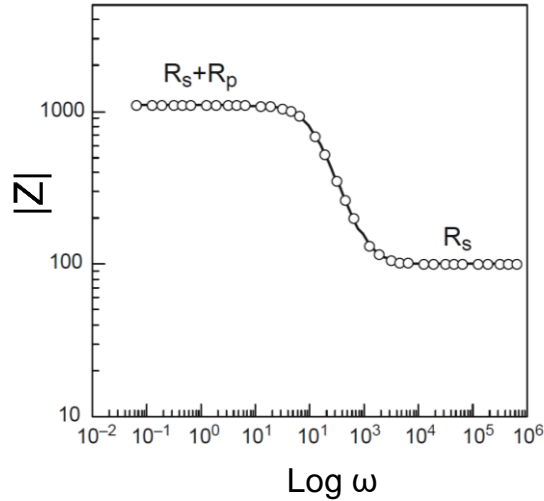


Figure 13: Bode plot (MCCAFFERTY, 2010).

In this representation, the resistances are shown by horizontal lines and capacitance by vertical lines. Unlike the Nyquist Plot, the Bode Plot does show frequency information. Figure 14 shows Phase plot representation.

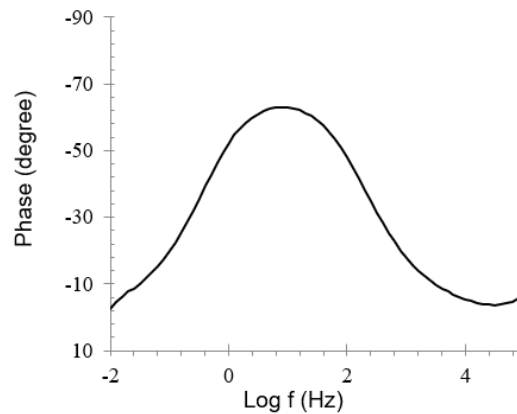


Figure 14: Phase-angle plot

The response of an ideal capacitor has a phase angle of -90° with respect to the applied perturbation signal. The phase is correlated with the delay between a signal applied and the interface reply. Therefore, it is dependent on the time constant (τ). An advantage of Bode plots is that the impedance behaviour at high frequencies is shown with equal weight, along the plot, to that at low frequencies. Whereas, in Nyquist plots,

high-frequency data tend to become bunched together towards the $\omega \rightarrow \infty$ intercept on the Z real axis. In the Phase-angle plot, a purely capacitive behaviour at low ω can usually be identified by the presence of phase-angle plateau at -90° (BARSOUKOV & MACDONALD, 2005).

Potentiodynamic polarisation and impedance may be classified as surface-average techniques in which charge-transfer reactions that take place dictates all the related parameters to be described based solely on the full impedance and polarisation data. The result from these techniques is from an average response of the whole surface immersed (relatively large surface area of the materials) in an electrolyte solution. Therefore, the traditional electrochemical measurements described above (potentiodynamic polarisation and impedance) provide only limited/average information about the system (CHANG & PARK, 2010). In addition, electrochemical systems rarely show an ideal behaviour, and this can lead to difficulties with data interpretation. For instance, in the case of localised corrosion, surface-averaged techniques cannot identify the time of initiation or even the location of a single attack considering that many single attacks are happening at the same time in the surface of the material (HUANG et al., 2011).

A non-conventional technique to evaluate corrosion is the scanning vibrating electrode technique (SVET). This localised measurement technique enables assessing the signal of a sample and obtaining information about different electrochemical responses at its surface. SVET is used to spatially resolve the magnitude of localised anodic and cathodic currents across a surface. It is based on the use of a single microelectrode which is vibrated in one or two directions across the sample surface, allowing the potential gradient to be measured accurately with a lock-in amplifier referenced to the probe-vibration frequency (HUANG et al., 2011).

The microelectrode (probe) is electroplated with a platinum black tip of 2-50 μm in diameter. The tip of the probe is vibrated vertically in the electrolyte in a sine wave. As in a capacitor, the two conductors, i.e., the specimen (working electrode) and the probe, are positioned in parallel, and the separation varies following the vertical vibration of the probe. The probe detects the potential drop, ∇_ϕ , between the two extreme vibration points which is associated with the ionic current originating from the

specimen surface into the electrolyte. The current density is then obtained using Ohm's law (ISAACS, 1988; ZOU, ISAACS, & THIERRY, 2000), as follows:

Equation 10: Current density to SVET

$$i = -\kappa \cdot \nabla_{\phi}$$

Where, ∇_{ϕ} is the potential gradient and $-\kappa$ is the electrolyte's conductivity. Current density is then processed and plotted for each scan point in the form of a current density map. Figure 15 shows different ways to present the current density maps, 2D (LIU et al., 2017) or in 3D (WANG et al., 2014).

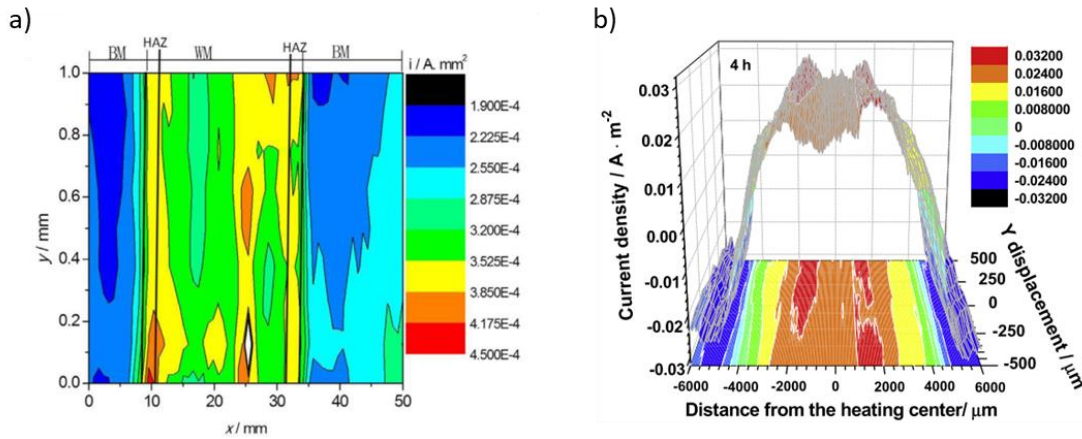


Figure 15: SVET measurements in a) 2D (LIU et al., 2017) and b) 3D (WANG et al., 2014) representation.

SVET is commonly used to map cathodic/anodic sites on metallic surfaces, leading to a better understanding of galvanic microcells.

SVET can be used at open circuit potential (OCP) in which no external potential is applied, or with an applied potential where the specimen is the working electrode, the counter electrode is a platinum reference wire, and the reference electrode is a microelectrode Ag/AgCl. A schematic representation of the probe is given in Figure 16.

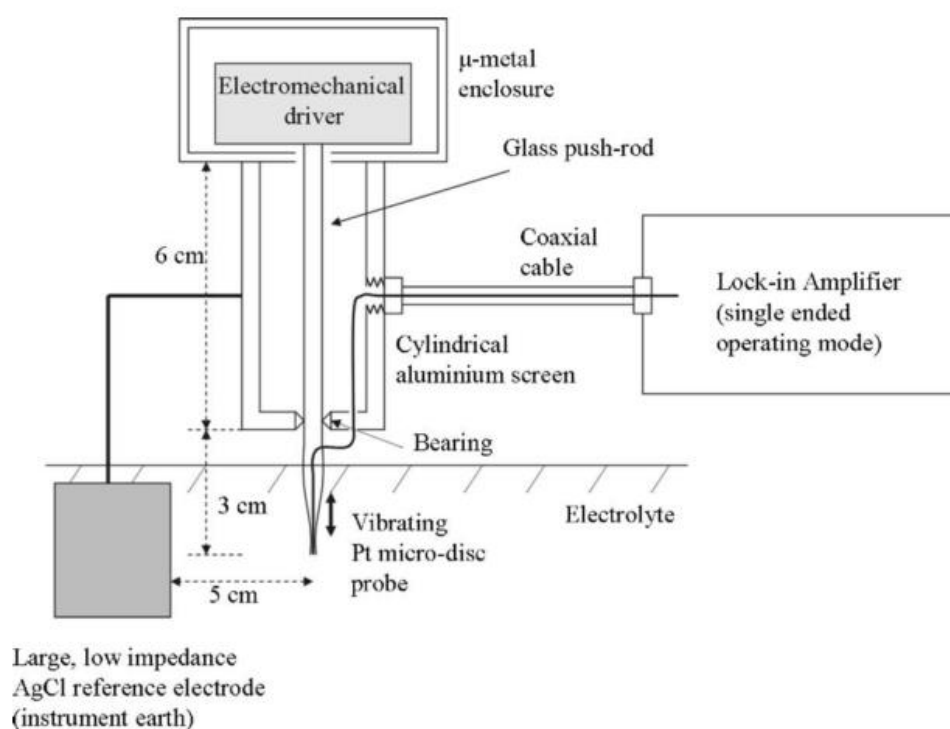


Figure 16: Schematic representations of the SVET probe/vibrator assembly (WILLIAMS & MCMURRAY, 2008)

A large-area (2.5 x 2.5 cm), low-impedance Ag/AgCl reference electrode, directly connected to the cylindrical aluminium screen and located at 5 cm distant from the vibrating probe, acted as an instrument earth.

Regarding the corrosion study of welded joints, SVET experiment provides the opportunity to quantify the time dependent evolution of localized corrosion currents across welded joints without the need for isolating the base metal and weld metal.

2.5.2. Corrosion behaviour of microalloyed steels (base metal)

Choi et al. investigated the effects of Cr, Cu, Ni and Ca on the corrosion behaviour of low carbon steel in synthetic tap water. Carbon steel and new alloy steels showed active behaviour in synthetic tap water. E_{corr} was shifted to noble direction, and i_{corr} decreased with adding alloying elements. The steel with simultaneous addition of Cr, Cu, Ni and Ca presented the lowest corrosion rate. The results of EIS measurement showed that all specimens represented one-time constant behaviour. The R_p

(polarisation resistance/charge transfer resistance) values increased by adding the alloying elements (CHOI, SHIM, & KIM, 2005).

Nam and Kim evaluated the performance of niobium-containing low alloy steels (blank steel, 0.05Nb and 0.10Nb steel) in a 10 wt% H₂SO₄ solution. All the alloys were well passivated with a low passive current density at the same potential range. The passive current density decreased with increasing Nb addition. It suggests that the decrease in current density is related to lower anodic dissolution with increasing Nb content. The addition of Nb promotes the formation of a passive film, consequently increasing the corrosion performance (NAM & KIM, 2010).

In a more recent research, Liu et al. studied the corrosion behaviour of a HSLA steel in comparison to that of a mild carbon steel. Elements such as Cr, Mo, Ni and Al helped to improve the corrosion resistance of the HSLA steel for a long time (144 h) in seawater by promoting the formation of protective corrosion scales. Because alloying elements such as Cr and Mo are less soluble than Fe, the amount of insoluble oxides (rust layer/substrate interface) in the HSLA steel is larger than the amount of soluble ones (solution/rust layer interface) in the carbon steel. The dissolution process leads to enrichment in Cr, Al and Mo in the rust layer. Accordingly, the HSLA steels with higher alloy elements can form more protective rust layers than the carbon steel in seawater. However, in the same study they also identified that for short immersion times (up to 6 h) these elements intensified galvanic corrosion on the steel surface and accelerated ferritic matrix dissolution (LIU et al., 2014).

Earlier works have shown that corrosion resistance can be improved by heat treatment conditions in which the alloying elements remain in solid solution since their beneficial influence, particularly Cr, can be expected only if these elements are in solution in the iron matrix (ALVES, BRETT, & CAVALEIRO, 2001).

The steel matrix also has a key role on the corrosion behaviour. Ferritic steels having a softer matrix can be easily and rapidly corroded depending on the immersion time. Bainitic and martensitic steels having ceramic based hard precipitates, presenting lath or plate shapes, are more resistant to corrosion (NAM & KIM, 2010; UJIRO et al., 2001). For the same composition, steels with normalised (ferritic-pearlitic) microstructure exhibit better corrosion resistance than quenched-and-tempered

martensitic microstructure. The result is correlated to the different corrosion scale formed for different microstructures. An apparent corrosion scale spallation was observed on the surface of quenched-an-tempered steels, while only slight scale spallation was seen for normalised steel (WU et al., 2013).

Atapek and Zor evaluated the effect of tempering temperature and microstructure on the corrosion behaviour of low carbon tempered steels. The sample tempered at 200°C (QT1) exhibited typical decomposed martensite due to stress relief annealing, with lath type ferrite and cementite. The sample tempered at 540°C (QT2) presented tempered martensitic matrix with massive cementite precipitation, which had an increase in the hardness due to the presence of more stable alloy carbides than cementite. The sample tempered at 600°C (QT3) exhibited a softer matrix including globular cementite phase in coarsened ferrite phase. The results of weight loss showed that the microstructure and microhardness of the steels tempered at different temperatures directly affect the corrosion rate. As the microhardness of steel matrix increases, the corrosion rate decreases. Moreover, according to their study, QT2 steel had the lowest corrosion rate and its corrosion rate was close to that of QT1. Tempering at 600°C causes softening and as a result QT3 steel was the most corroded one. This indicates that oxide layer formed on the surface of QT2 steel provides a higher protection characteristic by passivating the metal surface. The microstructural characterisation of the steel after immersion into NaCl solution as a function of immersion period showed that the grain boundaries are the regions where corrosion initiates and propagates preferentially, due to their high energy potential for a given reaction. Lath boundaries play a similar role as the grain boundaries. It is inevitable that corrosion propagates on both grain boundaries and lath boundaries due to their atomic irregularities (ATAPEK & ZOR, 2013).

Guo et al. studied the corrosion behaviour of low alloy steels having different carbon contents and compared to 09CuPCrNi under salt fog and outdoor testing. The results revealed that a selective corrosion happened on large pearlites which produced stress in the initial corrosion product films. The best uniform corrosion product film (only containing few cracks) tended to form on homogeneous microstructures such as ferrite and bainite. They concluded that homogenous microstructures, with proper amounts of carbon content, fine carbides and few large pearlite structures, were beneficial to the corrosion resistance. Uniform corrosion product film was considered an

advantageous for the formation of compact rust layers during initial corrosion (GUO et al., 2008).

The corrosion behaviour of the alloying elements Cr and Cu on low-alloy ferritic pearlitic steels was studied by Xu et al. After immersion test in simulated groundwater, all steels exhibited an inner rust layer with good corrosion protection ability. The alloying elements Cr or Cu enriched the rust on low-alloy steel. Thus, the difference between the corrosion resistance of carbon steel and low-alloy steel was related to the inner rust layer (XU et al., 2016).

The corrosion behaviour of low-alloy steel containing 1% Cr with normalised (ferritic-pearlitic-1Cr-N) and quenched-and-tempered (tempered martensitic-1Cr-QT) microstructures was investigated in CO₂ environments. V and Nb addition can form more stable carbides than Cr element, resulting in more available Cr in the matrix for forming Cr(OH)₃ enriched “passive” layer. Also, it is well-known that small amounts of Al can improve the compactness of the corrosion scale. It is expected that the addition of small amount of alloying elements (Cr, V and Nb) to carbon steel should play similar effect as Al. Therefore, the addition of small amounts of alloying elements (Cr, V, Nb and Al) to carbon steel has remarkably improved the CO₂ corrosion resistance. During the tempering process, Cr precipitates as carbides. As a result, the Cr content is depleted in the matrix. Because of insufficient Cr, electrolyte penetrated into the corrosion layer and etched the fresh surface, leading to the formation of galvanic couples between Cr-rich patches and the fresh steel surface. Compared with 1Cr-QT, a relative high Cr content can be provided in the microstructure of 1Cr-N where no chromium carbides are precipitated during heat-treating process. With the increase of Cr content in the steel matrix, the content of Cr(OH)₃ in corrosion products increases remarkably. As a result, a thinner scale with fewer defects and more uniformly dispersed FeCO₃ was obtained for 1Cr-N. The morphology of cementite also affects the corrosion. Lamellar cementite in pearlite for 1Cr-steel with normalised (ferritic-pearlitic) microstructure seems to provide a better grip for the protective scale than particulate cementite in tempered martensite, which increases the adhesion of latterly formed corrosion scale. At the initial stage of corrosion, ferrite dissolves, and the network of lamellar cementite phase remains as a cathode. The corrosion product will form in the Fe-dissolved location. Lamellar cementite in pearlite for 1Cr-N seems

to provide better adhesion for protective scale than particulate cementite in tempered martensite for 1Cr-QT (WU et al., 2013).

2.5.3. Corrosion behaviour at welded joints

Welding leads to heterogeneous microstructures. Weld metal or filler material may not have the same composition and microstructure as the parent metal/base metal (BM), and the surface of the weld metal is generally rougher. Because welding involves localised heating and cooling, residual stresses are introduced in the welded joint. Indeed, hardness and strength levels may be different from BM and filler material. The combination of these features such as difference in chemical composition, surface conditions, microstructure and mechanical stresses in the weldments make the corrosion behaviour of the welded joint different from that of the parent metal. If the composition of the weld metal differs from that of the parent metal, galvanic corrosion occurs. A severe attack on the weld metal may occur if the weld metal is anodic with respect to the BM (BALAKRISHNAN, 1994).

Corrosion behaviour of welded joints can be affected by compositional and microstructural alterations resulting from the heating cycles during welding (LÓPEZ, PÉREZ, & SIMISON, 2003; QUINTINO et al., 2013). Gradients in microstructures, chemical compositions and grain sizes can create local electrochemical potential variations, leading to galvanic corrosion (BARKER et al., 2013; HEMMINGSEN et al., 2002; KAH et al., 2014; WANG et al., 2014; WANG, MA, & LI, 2011). The corrosion behaviour of welded joints is complex due to the heterogeneous microstructure over the welding zone which impacts onto at least three adjacent regions with varying microstructures: heat-affected zone, base metal and weld metal with different corrosion rates (ELIYAN & ALFANTAZI, 2013).

Conventionally, in order to protect against welding-related corrosion, the filler material is made with nobler than the base metal (HEMMINGSEN et al., 2002).

For successful applications of high-strength steels in the automotive industry, knowledge regarding corrosion behaviour of the welded joint is of particular interest.

Localised and general corrosion reduces lifetime significantly and may cause failures (ALAWADHI et al., 2013; BARKER et al., 2013; HEMMINGSEN et al., 2002). The weld bead has a small area compared to the parent metal. Thus, a selective weld attack can take place. Preferential weld corrosion is thought to occur partially from galvanic effect.

The majority of studies in the literature is devoted to investigating the influence of heat input on corrosion behaviour and mechanical properties of stainless steels (GENG et al., 2015; MOHAMMED et al., 2017; MOURAD, KHOURSHID, & SHAREF, 2012; YOUSEFIEH, SHAMANIAN, & SAATCHI, 2011). Stainless steels are well-known to resist corrosion. Their resistance to corrosion is a consequence of chromium oxide film created on the metallic surface that forms a passive layer, isolating it from the environment. It has been reported that a low heat input decreases corrosion resistance for duplex stainless steels. Rapid cooling rate leads to a lower austenite content and enhanced chromium nitride precipitation which decrease the corrosion resistance. Higher austenite volume fractions taking more nitrogen into solid solution with a subsequent decrease in the amount of Cr_2N precipitated in ferrite may also contribute to the beneficial effect of slow cooling rates (MOHAMMED et al., 2017). Yousefieh and collaborators reported similar results, the best corrosion properties were obtained with approximately equal amounts of austenite and ferrite and the absence of third phases such as Cr_2N (YOUSEFIEH, SHAMANIAN, & SAATCHI, 2011). Mourad et al., however, asserted that the properties of welded duplex stainless steel joints are remarkably influenced by weld bead size rather than the austenite-ferrite balance (MOURAD et al., 2012).

Many other reports are exclusively devoted to HSLA steels for pipeline applications. Due to the severe influence of environment that these steels face in their final application, many studies focus on their corrosion behaviour. Zhao et al. studied the corrosion behaviour of a X80 pipeline steel in H_2S solution. The shape and amount of martensite/austenite (M/A) constituents were responsible for the lowest corrosion resistance of the intercritically reheated coarse-grained HAZ. The relatively fine grain, uniform distribution of the microstructure, and presence of a large amount of polygonal ferrite with few dislocations contributed to good corrosion resistance in the BM. In addition, the M/A presents granular, fine, low length-to-width ratio and uniform distribution making the galvanic effect between M/A constituents and matrix negligible in the BM. The poor corrosion in the CGHAZ was attributed to the relatively coarse

matrix and M/A constituents. In addition, the granular bainite presented in this region is a non-equilibrium microstructure, and the high welding residual stress, lattice distortion, and dislocations lowered the corrosion resistance in the CGHAZ. Finally, the high fraction of coarse necklace-shaped M/A constituents with relatively high carbon fraction in the intercritically reheated HAZ contributed to poor H₂S corrosion resistance. The coarse M/A constituents can be the trap for stress and hydrogen (ZHAO et al., 2016). Using a different electrolyte, Wang et al. obtained different results for the same pipeline X80 steel. In their study, the electrolyte was a solution simulating an acidic soil located in southeast China. Microstructures in the vicinity of the heating centre (fusion zone) acted as anode, while those at the edge of the heat affected zone and in the base metal acted as cathode. The microstructure of granular bainite mixed with ferrite in the HAZ showed the highest charge transfer resistance and the most positive current density value (higher cathodic current density). Acicular ferrite base metal displayed the lowest charge transfer resistance and the most negative current density. With the increase of immersion time, both the positive and negative current density peak values increased at first and then decreased due to the formation of corrosion products (WANG et al., 2014).

As mentioned before, welding induces major differences in both chemistry and metallurgy of the welded joint. SVET offers the opportunity to study these differences within the sample. Galvanic corrosion arises when two metals of different electrochemical potentials are connected and come into contact with a conducting electrolyte. When this occurs, one metal will become predominantly anodic at the expense of the other metal which becomes cathodic (AKID & MILLS, 2001). SVET has been used to the visualisation of the galvanic effects at welded joints. In chloride solution, a galvanic couple was observed after different immersion times for a carbon steel. The weld metal acted as the anode and the base metal was the cathode. Optical micrographs obtained after the SVET measurement revealed an orange film composed of iron hydroxides that are poorly protective due to its non-adherent character. After 8 h of immersion, the corrosion product covered a larger area in the anodic electrode. Due to this, the anodic and cathodic currents decreased with time. The author concluded that the corrosion process was not completed, but the non-adherent oxide hinders corrosion current measurements (PAGOTTO et al., 2015). Using similar electrolyte, the corrosion behaviour of a HSLA (crude oil storage tank) was also

studied. The specimens were welded by two different welding processes: submerged arc welding (SAW) and vertical electro-gas welding (VEGW). The SVET results showed that the VEGW joints showed small corrosion current in the welding zone (HAZ + weld metal) and the corrosion process was occurred in the HAZ, while the SAW joints exhibit high corrosion current in the welding zone and the key attack was in FZ. The VEGW joint microstructure presented coarser micro-phase and more uniform microstructure in the welding zone than the SAW joint. VEGW coarser microstructure in the welded joint is related to its higher heat input, compared with SAW (LIU et al., 2017).

To sum up, researchers have suggested that the use of autogenous welds (made without filler additions) and weldments made with matching consumables provide the best preferential welded joint corrosion resistance (PÉPE et al., 2011). However, the application of matching filler materials is not a practical option in most cases since automotive industry use steels with complex chemical compositions. Therefore, the corrosion behaviour of each combination of base metal, filler and welding parameters is a new case and must be studied to understand their influence. In addition, only few reports have attempted to understand the heat input influence on corrosion behaviour of HSLA steels used in automotive industry.

2.6. SCOPE OF THE WORK

This work aimed to study the influence of heat input of the welding process on the properties of two high-strength steels. Within the scope of this thesis two high strength steels were used: LNE500 (low carbon hot-rolled steel) and AHSS900 (low carbon quenched and tempered steel). For each high-strength steel two heat input values were applied and their influence was discussed. Arc welding - MAG (metal active gas) - was used to weld the samples.

To understand the influence of heat input the thesis presents the follow secondary aims:

1. To characterize the microstructure of the base metals and welded joints via optical microscopy, scanning and transmission electron microscopy, chemical X-ray energy dispersive spectroscopy and X-ray diffraction.

2. To evaluate the mechanical properties using microhardness and tensile tests.
3. To measure the corrosion behaviour via conventional corrosion techniques (impedance and polarisation) and localised corrosion technique (scanning vibrating electrode technique).

Chapter 3

3. MATERIALS AND EXPERIMENTAL TECHNIQUES

3.1. INTRODUCTION

This chapter details the welding processes and all experimental techniques employed on this project. All welded joints were prepared at Fronius Brazil. Chemical analysis of the high strength steels and microhardness measurements were carried out at Mercedes-Benz Brazil. TEM, SEM and XRD were carried out at Department of Materials Science and Metallurgy at Cambridge University. Corrosion tests were carried out at UFABC and in Swansea University.

3.2. MATERIALS

Two different base steels were used on this work. LNE500 is a hot-rolled steel current used in Mercedes-Benz bus chassis in Brazil. Plates with a thickness of 6 mm were provided by Mercedes-Benz Brazil. Currently, LNE500 is the steel with highest strength on Mercedes-Benz chassis.

The second steel AHSS900 (S900MC) was provided in the form of TMCP (Thermo-mechanically Controlled Processed) quenched and tempered plates with 4 mm thickness by PCP steels. The filler metal used was a 1.2 mm-diameter steel wire. The chemical compositions and nominal mechanical properties of the base metals and filler material are shown in Table 2 and Table 3, respectively.

Table 2: Chemical composition of base and filler materials (wt%)

	C	Si	Mn	Cr	Mo	P	Nb	Ti	Al	B	Others
LNE 500	0.062	0.078	1.351	0.055	0.004	0.018	0.057	0.033	0.051	0.0001	0.001 V and Sn; 0.010 Ni; 0.009 S; 0.005 Cu; 0.003 Co and W
AHSS 900	0.047	0.194	1.223	0.284	0.392	0.010	0.016	0.013	0.034	0.0028	0.040 V; 0.006 Ni; 0.002 S; 0.010 Cu; 0.002 Co; 0.004 W; 0.001 Sn
Filler	0.092	0.850	1.526	0.029	0.003	0.030	-	-	0.001	-	0.001 V; 0.017 Ni; 0.013 S; 0.141 Cu;

Table 3: Nominal mechanical properties of the base metals and filler

	Tensile strength (MPa)	Yield strength (MPa)
LNE500 BM	600	500
AHSS900 BM	950	900
Filler	650	500

For the sake of clarity, the choice of the filler material was twofold:

(1) the filler is already used at Mercedes-Benz for LNE500 so the intention was to use the same filler material for a higher strength steel, i.e. AHSS900.

(2) Many studies report that great mechanical properties of welded samples can be achieved by using filler with different strength levels, even undermatching the base metal strength (LIU & Bhole, 2013; PISARSKI & DOLBY, 2013; SAMPATH, 2006).

Therefore, these were the reasons why the same filler material was used to weld both base metals.

3.3. MANUFACTURING OF WELDED PLATES

The as-received plates presented dimensions up to 1 m². They were cut down to 100 mm x 500 mm rectangles using a hydracult Guillotine as shown in Figure 17.

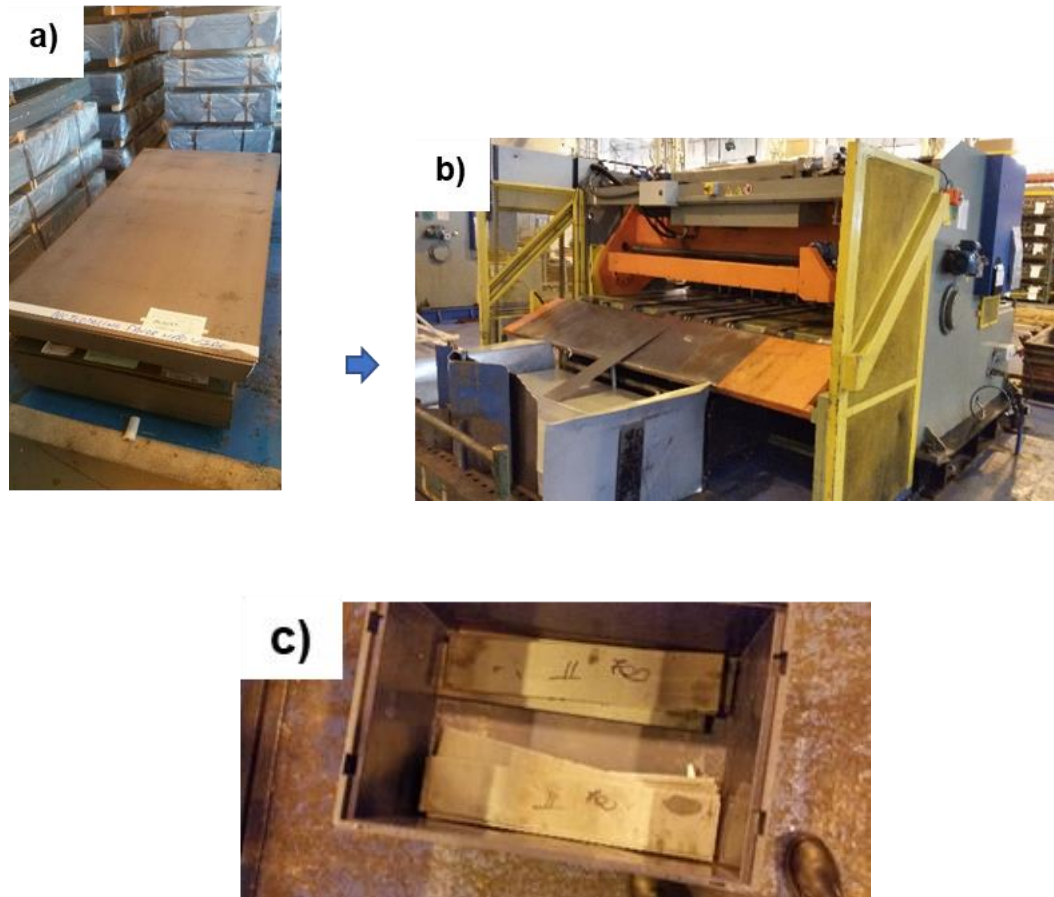


Figure 17: a) as-received plates; b) hydracult guillotine; c) final specimen ready to be welded.

The weld-joint was fabricated by single pass butt-welding from 6mm (LNE500) and 4mm (AHSS900) thick sample blanks of approximately 100mm×500mm size using metal active gas (MAG) welding process. The shielding gas was a mixture containing 20 %CO₂ and 80 %Ar. Figure 18 and Figure 19 show the robot used to weld the samples and the MAG apparatus, respectively.



Figure 18: ABB robot with a CMT (Cold Metal Transfer) Fronius® power supply.

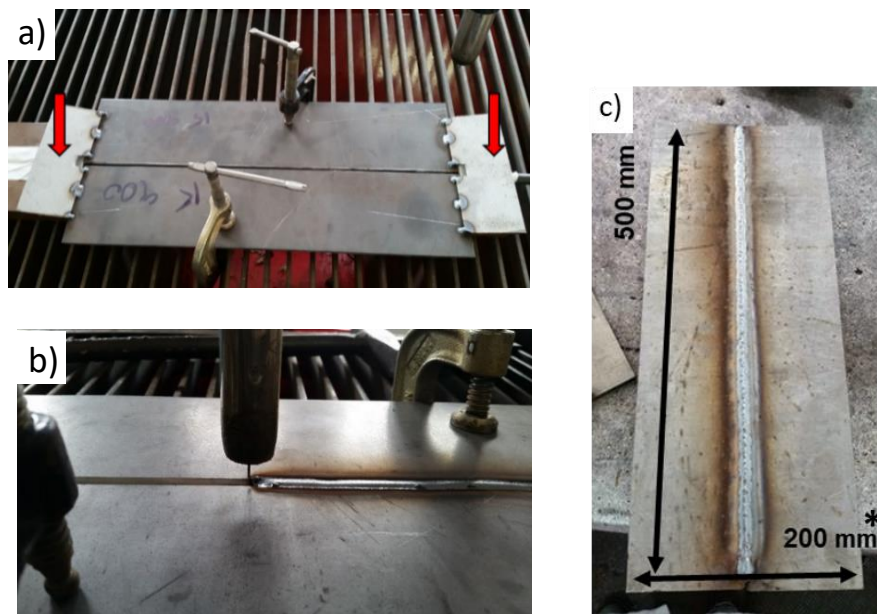


Figure 19: a) Apparatus before welding process, fixing two plates with 2 mm gap to prevent their movement during the welding process, b) during the welding and c) specimen after welding process.
*the width is 200+2mm (due the gap between the plates).

Two rectangular plates (100mmx500mm size) were firmly fixed to the bed of the arc welding machine to prevent movement, leaving a 2-mm gap between them to be filled with the filler metal during the welding process. Two different welding transfers mode were used to join the LNE500 base metal: Cold Metal transfer (CMT) (sample B) and pulsed transfer (sample A) while for the base metal AHSS900 only CMT was used. Pulsed transfer was initially used to join the BM AHSS900, however, any test succeeded. The heat was too intense that distorted the welded plate (Figure 20a) and excessive penetration was detected (see Figure 20b). These welding defects were

created due to the excessive welding heat input. These defects were detected using DIN EN ISO 5817 (GERMAN INSTITUTE FOR STANDARDIZATION, 2006).



Figure 20: Welding defects on the AHSS900 base metal welded by pulsed transfer, distortion(a) and excess penetration (b).

The welding parameters were adjusted to obtain full penetration. The parameters are shown in Table 4. It can be seen that different heat input values were achieved by changing the welding speed.

Table 4: Welding parameters of the MAG process.

Base metal	Nomenclature	Transfer mode	Current (A)	Potential (V)	Welding Speed (mm/s)	Arc %	Dynamic %	Wire speed (m/min)	Arc Efficiency* (%)	Heat Input (kJ/mm)
LNE500	Sample A 500-P-0.72	Pulsed	187	22.7	5	8	0	6	85	0.72
LNE500	Sample B 500-CMT-0.70	CMT	250	20	6	6	0	8.3	85	0.70
AHSS900	Sample C 900-CMT-0.31	CMT	150	14.6	6	-5	2	4.4	85	0.31
AHSS900	Sample D 900-CMT-0.47	CMT	150	14.6	4	-5	2	4.4	85	0.47

*Efficiency for both transfers are considered similar (PÉPE et al., 2011).

The heat input per unit length was calculated according to the Equation 3.

Equation 3: Heat Input

$$HI = f \cdot \frac{E.I}{1000.S}$$

After welding, samples were cut down in different dimensions in accordance with the need for specific tests (i.e., Tensile tests, hardness measurements and corrosion tests). Figure 21 shows an illustration of the specimen prepared for microstructural, mechanical and corrosion characterisation.

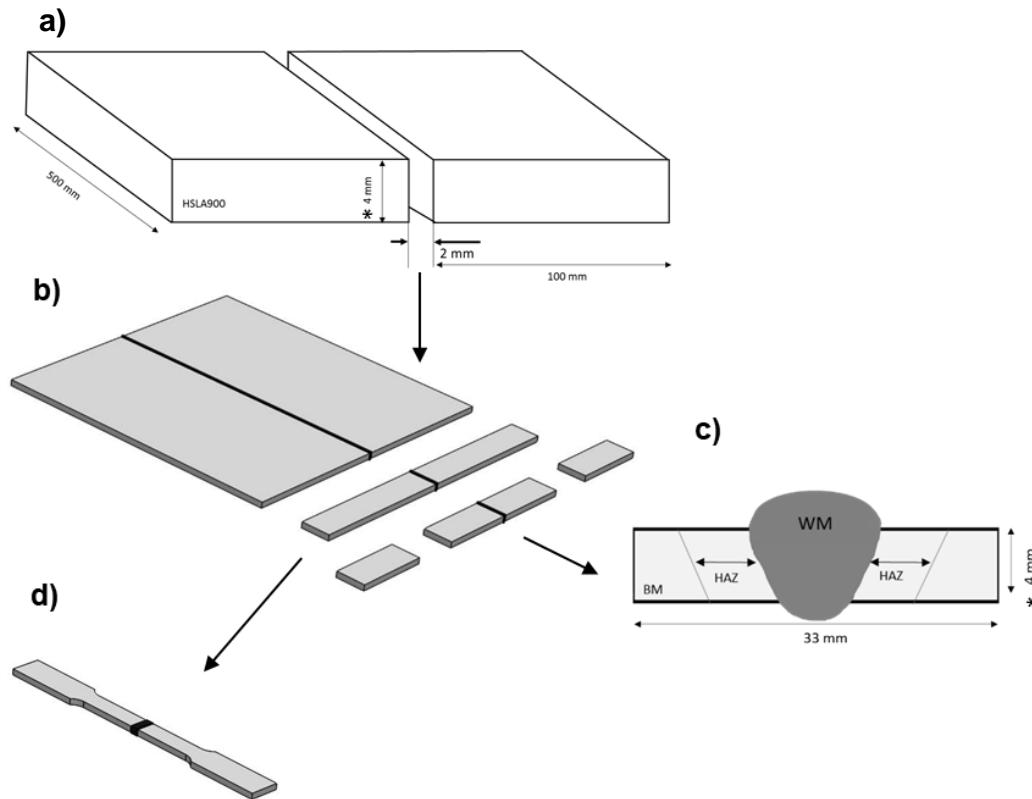




Figure 21: Illustration of specimen preparation: a) Base metal before welding; b) Bulk specimen after welding and its cutting; c) butt weld specimen for optical metallography, microhardness and corrosion tests; d) tensile specimen. *In the case of LNE500 the thickness is 6mm.

Before cutting, liquid penetrant inspection was carried out on all samples in order to detect any local surface-breaking defects. The test followed the standard ASTM E165/E165M-12 (AMERICAN SOCIETY FOR TESTING AND MATERIALS, 2012a).

Table 5 shows the welded samples prepared for this thesis. There were three specimens for each group, three specimens from sample A, three from sample B, three from sample C and three from sample D.

All the welds made showed no obvious defects in the form of bubbles, microcracks or porosity throughout their whole cross sections, which may indicate the correctness of their execution.

Table 5: Welded samples

LNE500	Sample A 500-P-0.72 0.72 kJ/mm Top surface		Sample B 500-CMT-0.70 0.70 kJ/mm Top surface	
				
	Bottom surface		Bottom surface	
				
AHSS900	Sample C 900-CMT-0.31 0.31 kJ/mm Top surface		Sample D 900-CMT-0.47 0.47 kJ/mm Top surface	
				
	Bottom surface		Bottom surface	
				

3.4. OPTICAL MICROSCOPY

The sectioned samples were cold mounted, ground using silicon carbide (SiC) abrasive papers from 600-grade to 1200-grade and were mechanically polished with 1 μm diamond paste.

2% Nital was suitable to etch all the specimens to microstructure analysis. However, picric acid solution was also used to further measurements (grain size measurements). Picric acid solution etched some of the samples. The picric acid solution was prepared by mixing of two solutions. First, a saturated picric acid solution was prepared, using a ceramic spoon and 4 grams of picric acid was put into 100 ml ethanol (solution A). Secondly, 1 gram of sodium metabisulfite was added into 100 ml deionized water (solution B). Finally, solution A was mixed with solution B in a 1:1 ratio immediately before etching. The samples were etched by 20-60s at room temperature by dipping them into the solution.

3.5. SCANNING ELECTRON MICROSCOPY AND TRANSMISSION ELECTRON MICROSCOPY.

The microstructure of the welded joint was examined using scanning electron microscopy (SEM) (FEI Nova nanoSEM) at 20 kV. Weld cross-sections were prepared following standard metallographic procedure consisting of mounting, grinding and polishing using 1 μ m diamond suspension as a last step and etching in 2% nital solution.

A scanning transmission electron microscope (STEM) (FEI Tecnai Osiris 80-200) was used for high resolution characterisation of precipitates at an accelerating voltage of 200 kV. The steps used in the preparation of thin foils are shown in Figure 22. Thin foil specimens were prepared from 0.3-0.6 mm thick slit parallelepiped using a cut-off wheel (Seccutom-10) as shown in Figure 22a. Secondly, using a spark erosion machine and a copper wire, the parallelepiped specimens were cut down into 3 mm diameter discs (see Figure 22b). The disks were subsequently mechanically ground by hand to less than 0.1 mm thickness using SiC paper. Finally, the disks were thinned in a twin electropolishing unit using 5% perchloric acid in ethanol at -20°C (see Figure 22c). The voltage was adjusted to get the best polishing effect. After polishing the specimens were cleaned in a gentle stream of alcohol.

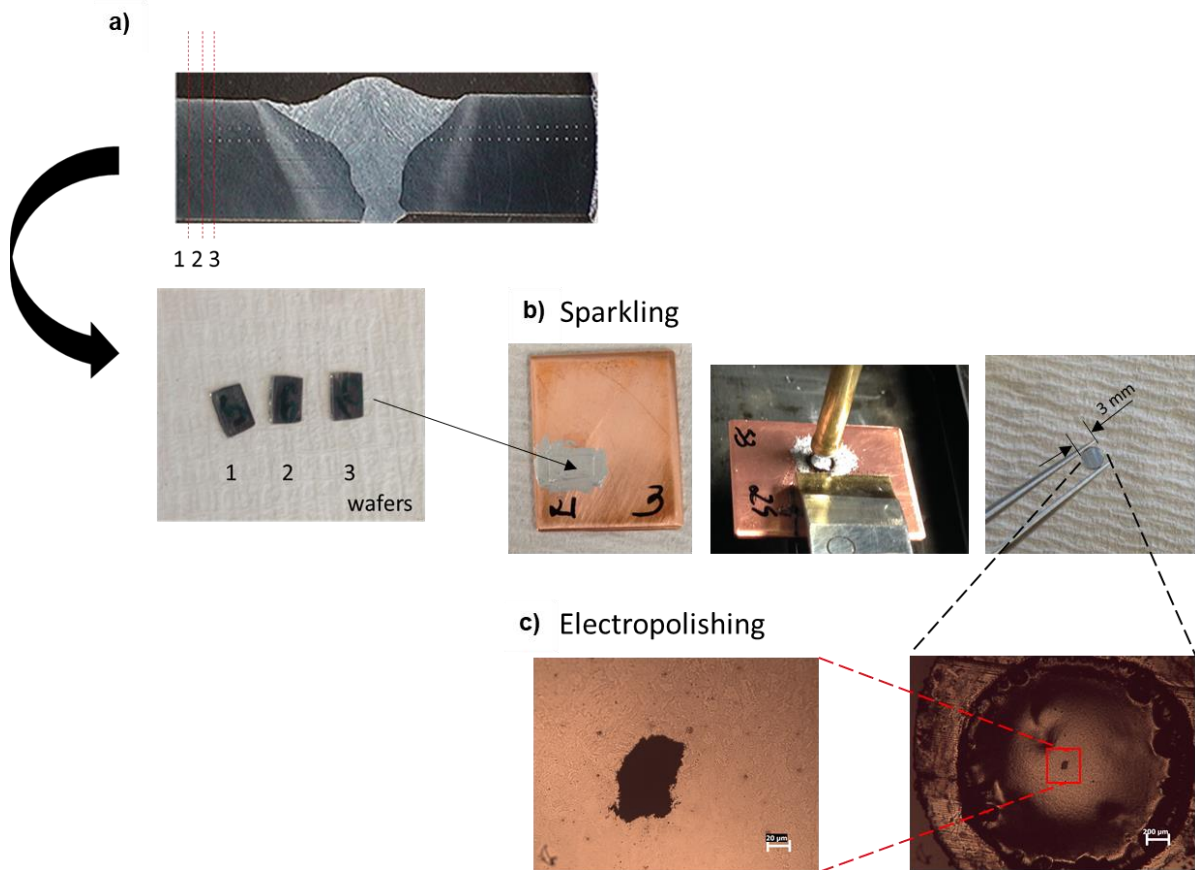


Figure 22: TEM sample preparation steps

3.6. X-RAY DIFFRACTION

Transverse sections of each region of the weld (BM, HAZ and WM) were analysed using a D8 Bruker Advance theta/theta diffractometer using Cu K-alpha radiation operated at 40 kV and 40 mA from 30° to 85°.

3.7. MICROHARDNESS TEST

Vickers microhardness (VH) survey was conducted across welded joints of LNE500 and AHSS900 employing *Future Tech Corp* FV-700 hardness testing machine. All of the hardness readings were obtained at a load of 1 kg. The full load

was held for 10 s. The distance between two consecutive indentations was in accordance with ASTM E384 (AMERICAN SOCIETY FOR TESTING AND MATERIALS, 2012b).

3.8. TENSILE TEST

Uniaxial tensile tests were carried out based on ASTM E8/E8M-13a standard test methods for tension testing of metallic materials. The specimen dimensions are shown in Figure 23. Tensile tests were performed at room temperature in a 100 kN electromechanical universal testing machine MTS (Exceed E45). A 10 mm gauge length extensometer was used in the elastic region and then it was removed to complete the tensile test (inelastic region) and 10 samples were tested to each condition (AMERICAN SOCIETY FOR TESTING AND MATERIALS, 2013b).

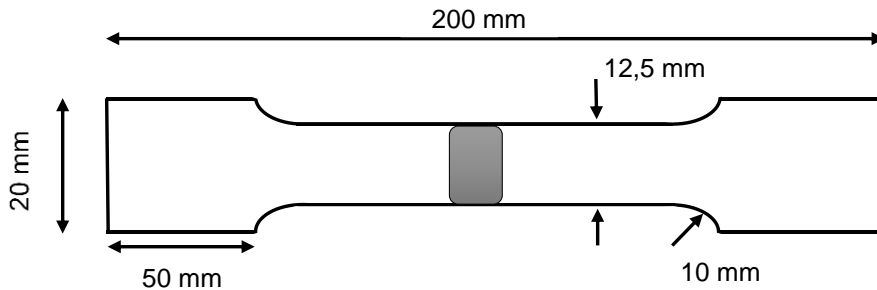


Figure 23: Tensile test specimen prepared according to ASTM E8/E8M-13a standard.

Joint efficiency (%) was calculated following the Equation 11:

Equation 11: Joint efficient

$$Effi = \frac{\text{Strenght of weld}}{\text{Strength of base metal}}$$

3.9. GRAIN SIZE MEASUREMENT AND FRACTION OF PRECIPITATES AND PHASES

The prior austenite grain size of BM and HAZ were evaluated by the linear intercept method from the optical micrographs. The average of three readings was reported (AMERICAN SOCIETY FOR TESTING AND MATERIALS, 2013a). The image analysis software ImageJ was used to determine the fraction of precipitates. The numerical images were transformed into a binary image, and a threshold was applied to highlight the constituents from the background. All samples were etched with the picric acid solution, detailed in section 3.4.

The same procedure was used to measure the fraction of pearlite in the LNE500 BM. The material was etched with Nital 2%. The average of three images was reported.

3.10. CORROSION

3.10.1. Conventional techniques

All electrochemical measurements were performed in a standard three-electrode cell with Ag/AgCl as the reference electrode, a platinum wire as the auxiliary electrode and the welded joints (consisting of base metal, HAZ and weld metal) as the working electrodes (WE). The tests were carried out in Multi Autolab 101M potentiostat/galvanostat in 3.5 wt% NaCl solution at room temperature. Firstly, the open circuit potential was monitored for 1 h and the steady state condition was noted. Next, electrochemical impedance spectroscopy (EIS) measurements were performed at the open circuit potential in the frequency range from 100 kHz to 10 mHz with an amplitude of 10 mV (rms) and acquisition of 10 points per decade. Right after the EIS tests, potentiodynamic polarisation curves were obtained by sweeping the potential from -300 mV versus the OCP up to 0.4 $V_{\text{Ag/AgCl}}$ at a scanning rate of 1 mV.s^{-1} . Figure 24 shows the specimen used. The electrochemical tests were conducted on the parent metal and over the whole welded joint, including the HAZ, BM and WM by exposing them simultaneously to the electrolyte. The electrochemical measurements were also carried only in the WM region. In this case the HAZ and BM were covered with nail

polish and solely the WM region was exposed to the electrolyte as shown in Figure 24c. In this case the intention was to study the corrosion behaviour solely from the WM and to compare with the BM.

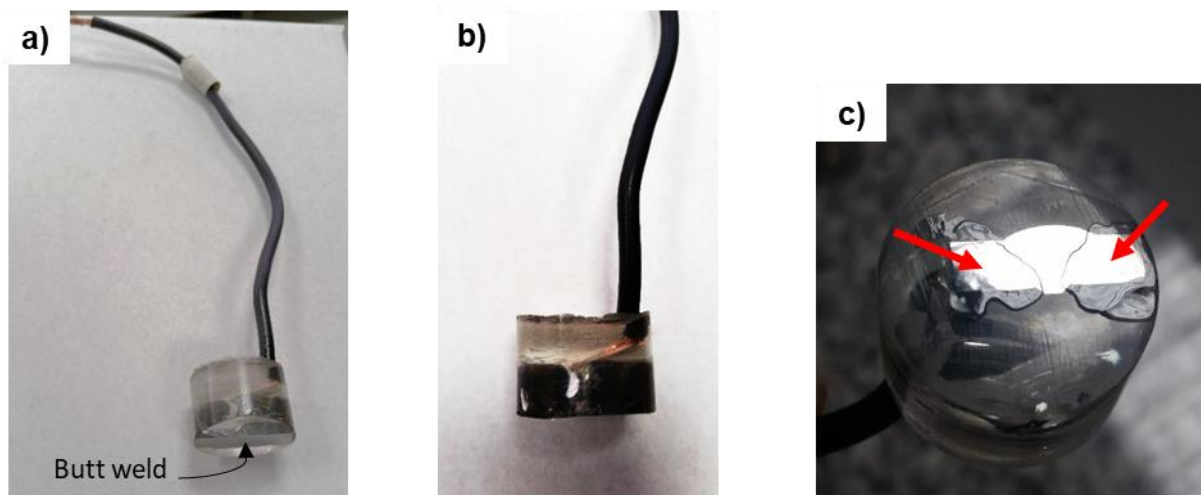


Figure 24: Electrochemical specimen a) showing the working surface; b) showing the electric connection; c) showing the arrangement of the electrochemical test only on the WM

After electrochemical tests, the corrosion product was removed by using a solution of 100 mL water and 100 mL HCl (60%) for few seconds until the corrosion product detached from the surface. Next, the specimens were analysed by confocal laser scanning microscopy (Olympus LEXT OLS 4100).

3.10.2. Scanning vibrating electrode technique

An in-situ scanning vibrating electrode technique (SVET) was used to characterise the time-dependent changes in local anodic and cathodic current density distributions measured across butt weld samples under open-circuit conditions in 0.1 wt% NaCl solution at room temperature. The apparatus is shown in Figure 25. Samples were mounted, and standard metallographic techniques were used (as described in section 3.5). The working surface was then covered with 90 μm thick extruded PTFE tape (3M 5490), leaving only a rectangular square area centred on the welded region of the specimen exposed to the electrolyte. The probe vibration frequency was 140 Hz and the peak-to-peak vibration amplitude was $30 \pm 5 \mu\text{m}$.

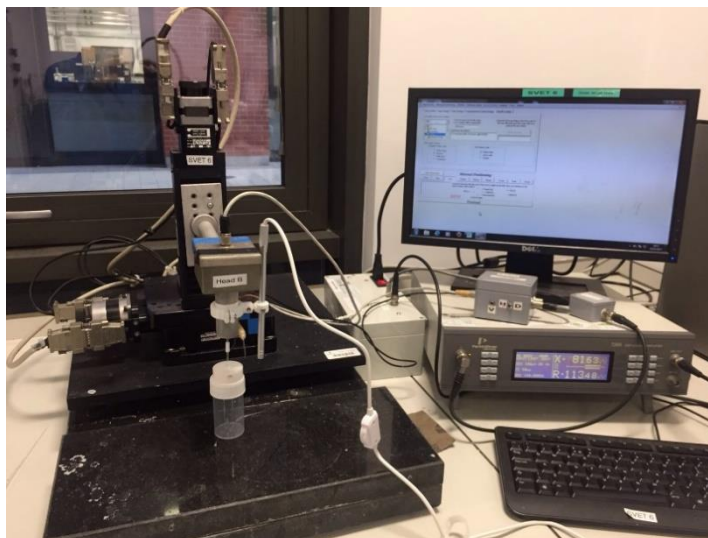


Figure 25: SVET apparatus

A preliminary test was done with 3.5 wt% NaCl solution, but corrosion happened too fast to allow a clear distinguishing between anodic and cathodic local sites as shown in Figure 26.

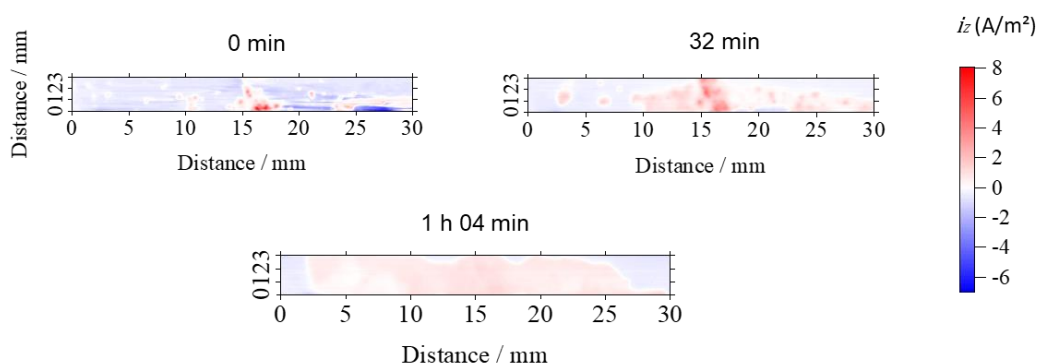


Figure 26: SVET measurements of a welded joint in 3.5 wt% NaCl aqueous solution.

Figure 26 shows three scans that were recorded consecutively. The maps show the scanned area of the sample (distance vs distance in mm). In the third map, corrosion had spread to nearly the whole surface. The red colour represents anodic current (positive current) and the blue colour represents cathodic current (negative current). For this reason, a solution with 0.1 wt% NaCl was chosen, in which corrosion proceeded slower and more information about localised attack could be obtained.

Chapter 4

4. MICROSTRUCTURE CHARACTERIZATION

4.1. MICROSTRUCTURES OF THE BASE METALS

4.1.1. LNE500

The general microstructure of the LNE500 steel is shown in Figure 27a and 27b. The microstructure is comprised of a ferritic matrix and some dark regions (arrows in Figure 35b). The ferritic grains are oriented along the rolling direction. From SEM micrographs, the dark regions were identified as pearlite due to the alternating lamellar structure of ferrite and cementite as shown in Figure 27c and 27d. The amount of pearlite is low because of the low carbon content of the steel.

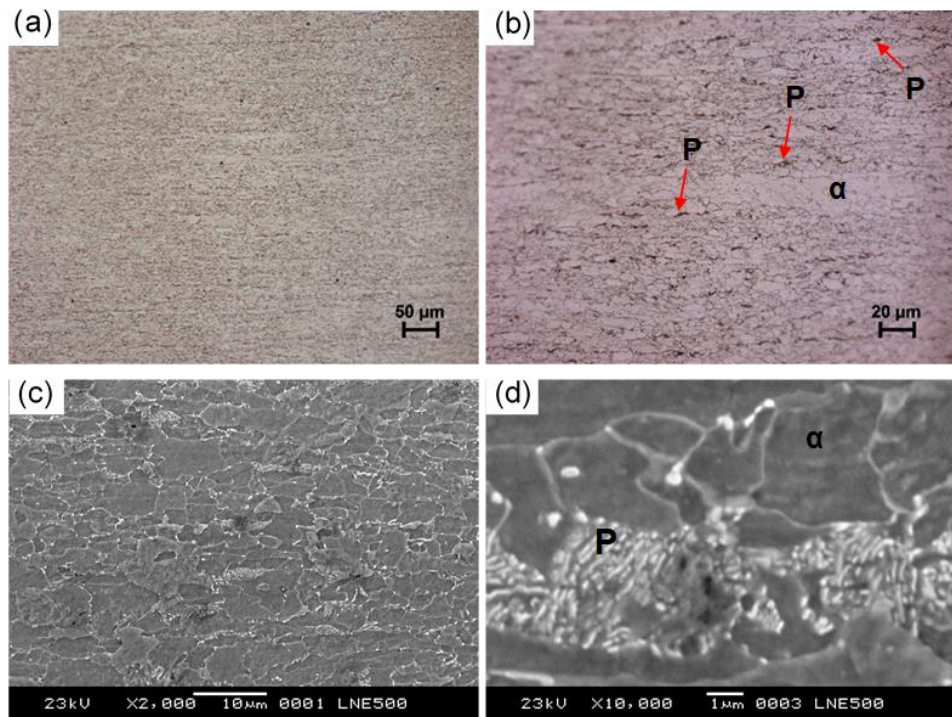


Figure 27: Typical microstructure of the base metal LNE500, optical micrographs (a) (b) and SEM micrographs (c)(d). P: Pearlite, α: allotriomorphic ferrite.

A more detailed investigation of the LNE500 microstructure was carried out by TEM analysis. Figure 28 shows the ferritic matrix and its small grain size. Some of the grain size is lower than 2 μm .

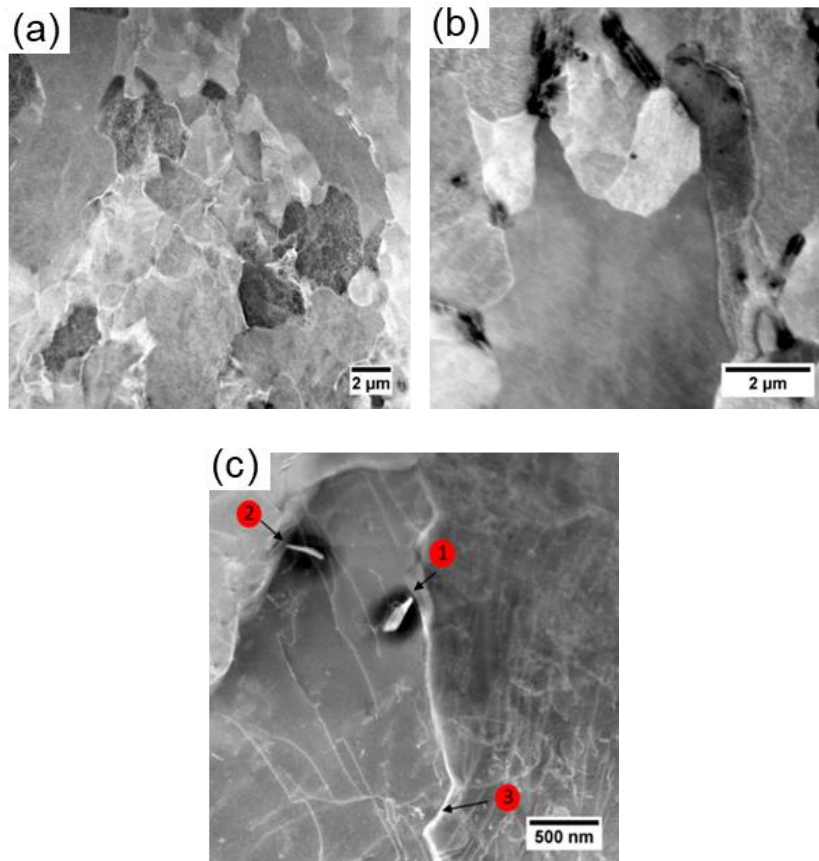


Figure 28: STEM micrographs of LNE500 BM, ferritic matrix with different grain sizes (a)(b), and two precipitates (1 and 2) and ferrite grain boundary (3) (c).

Table 6: Chemical composition of the precipitates and matrix of LNE500 BM. See Figure 28c.

	wt%										
	C	N	O	Si	Mn	Al	S	Ti	Nb	Cu	Fe
1	0.99	-	1.13	-	1.89	0.12	-	-	-	14.67	81.22
2	0.51	-	1.07	-	1.40	0.44	-	-	-	15.49	81.06
3	0.20	0.22	1.17	-	0.84	0.19	-	-	-	19.39	77.92
Matrix	0.40	0.08	1.29	-	0.93	-	-	-	-	15.31	81.97

Precipitates found in TEM micrographs (points 1 and 2 in Figure 28c) were analysed by EDS. They were identified as Fe carbides with large amounts of Cu and Mn as shown in Table 6. The large amount of Cu is related to the signal of the TEM holder. Therefore, BM LNE500 has a near-equiaxed grain structure comprised of

predominant ferrite matrix with small amounts of pearlite. The amount of pearlite is around 7% as determined using Image J® from 3 SEM micrographs.

In order to confirm the microstructure, XRD analyses of the LNE500 BM were conducted. The XRD pattern is shown in Figure 29. Only ferrite peaks were detected by XRD analysis (JCPDS # 00-006-0696).

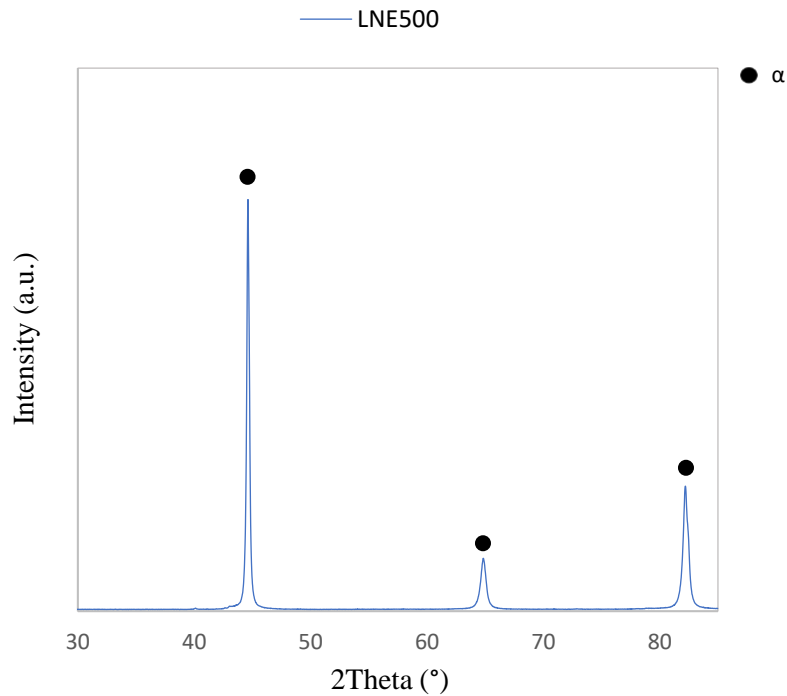


Figure 29: X-ray analysis of base metal LNE500.

4.1.2. AHSS900

The AHSS900 base metal microstructure presents refined constituents. Thin-lath morphology of tempered martensite is shown in Figure 30. Figure 30a and 30b show optical micrographs of the BM. However, the microstructure is too refined to allow obtaining detailed information about the microstructure from the optical micrographs. From the SEM micrograph, shown in Figure 30c some precipitates were detected. Figure 30d shows them in detail.

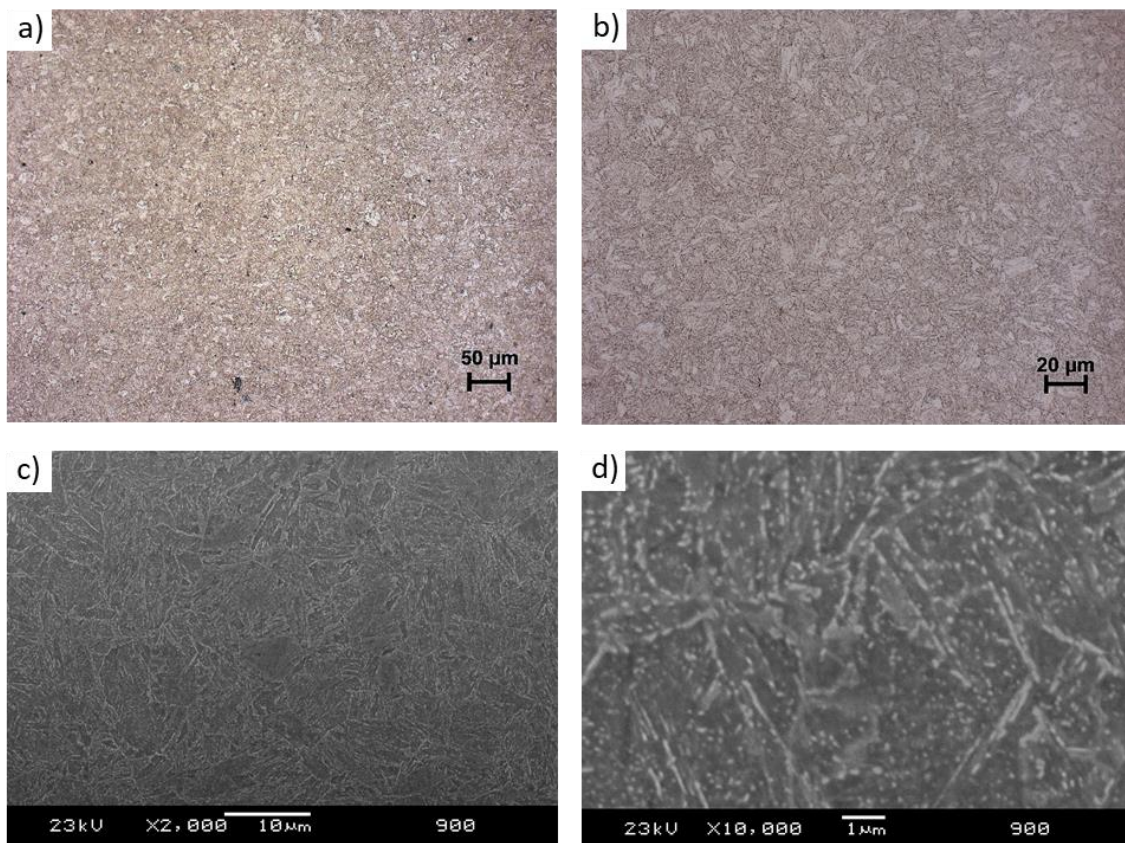


Figure 30: Typical microstructure of the base metal AHSS 900 (a)(b) optical images and (c)(d) SEM images.

The precipitates observed in Figure 30d, were analysed by TEM. The results are presented later on this chapter. It is anticipated here, though, that the precipitates resulting from tempering of martensite are typically cementite.

By carefully examining the optical micrographs, a distinguishable type of precipitate was found on the AHSS900 microstructure as shown in Figure 31. The average size of these precipitates is around 3 μm (Figure 31b), but some of them were found to have dimensions of up to 6 μm (Figure 31a). Their square shape is also a characteristic feature.

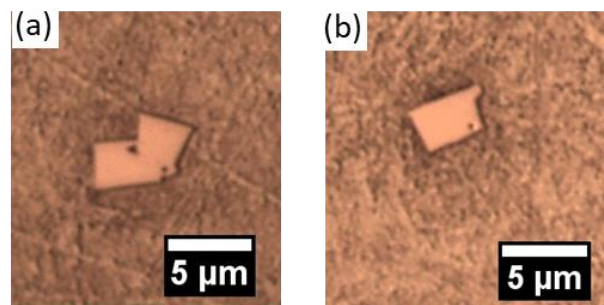


Figure 31: Optical micrographs showing precipitates found on the AHSS 900 BM.

EDS analysis from precipitate in Figure 31a identified that these precipitates as Ti- and Nb-rich carbides and nitrides, as shown in Figure 32.

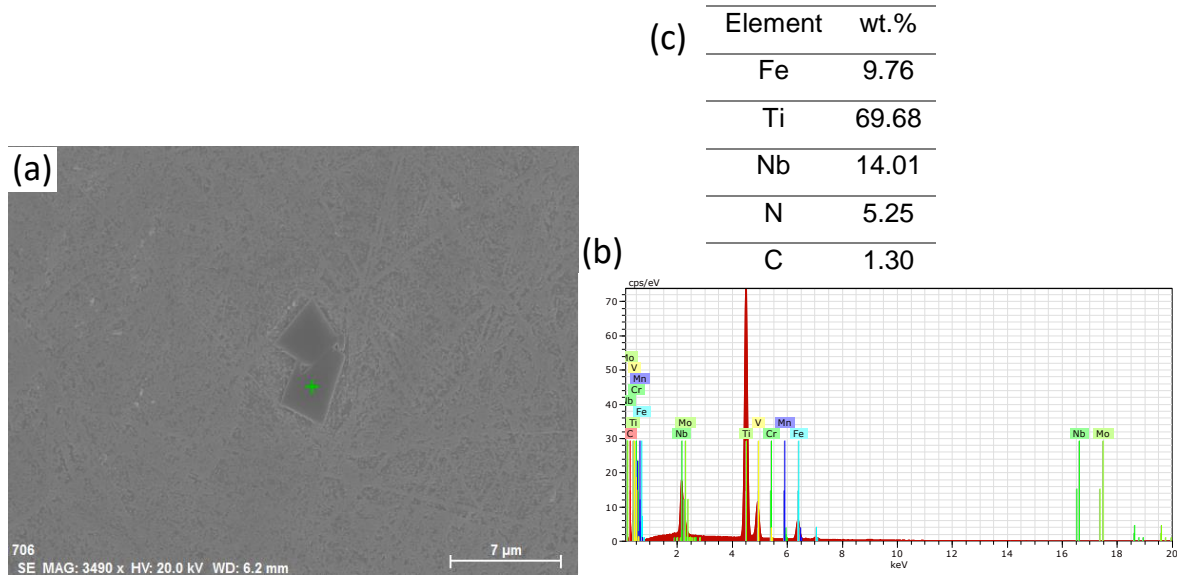


Figure 32: SEM micrographs showing a precipitate found in the AHSS900 BM (a), EDS Spectrum from the precipitate (b) and its chemical composition (c).

These large Ti,Nb(C,N) precipitates are formed upon solidification. Large TiN precipitates ($> 1\mu\text{m}$) increase with increasing titanium content which minimise the amount of nitrogen left in solid solution available for subsequent formation of smaller TiN particles in austenite (SOTO et al., 1999).

Figure 33 shows the XRD pattern of the AHSS900 BM. The X-ray pattern confirmed the microstructure in the AHSS900 BM, consisting of tempered martensite (JCPDS #00-044-1289). The presence of carbides was not identified on XRD pattern and neither retained austenite.

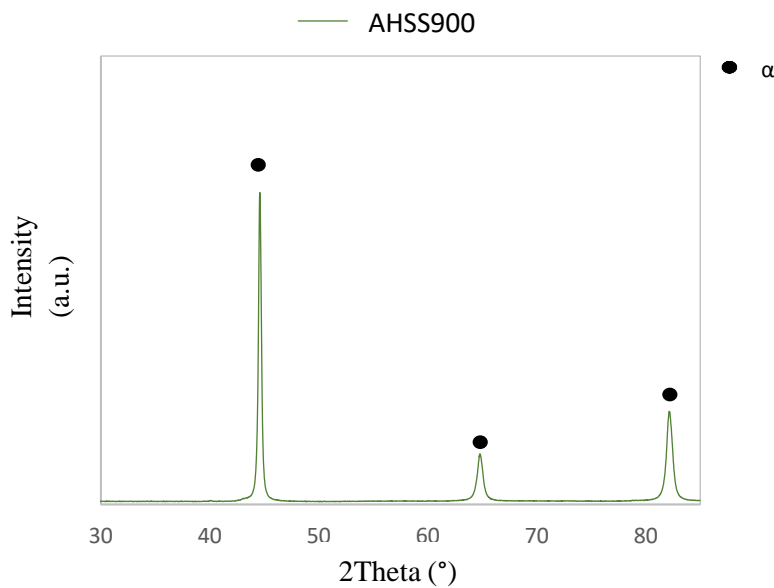


Figure 33: X-ray analysis of base metal AHSS900.

For quenched steels, martensite peak at $2\theta = \sim 82$ degree is characterised as a double peak and also some retained austenite is detected. However, tempering process causes decomposition of retained austenite and the double peak is only detected as a single peak (CHEN et al., 2015; JUNIOR & SANTOS, 2013).

Comparing XRD from LNE500 and AHSS900 BMs, the peaks of ferrite and martensite are coincident. Similar results are found in the literature (TAVARES et al., 2014). Ferrite has a body-centred cubic crystal structure whereas martensite presents a body-centred tetragonal crystal structure. The position of the peaks in the XRD pattern is related to the dimension of the elementary cell. Due to the tempering, the metastable sample (martensitic microstructure) is held isothermally at a temperature where austenite cannot form. During the first stage of tempering, excess carbon in solid solution segregates to defects or forms clusters within the solid solution. It then precipitates. Further annealing leads to stage 2, in which almost all of the excess carbon is precipitated, and the carbides all convert into more stable cementite. Continued tempering then leads to the coarsening of carbides, extensive recovery of the dislocation structure, and finally to the recrystallisation of the ferrite plates into equiaxed grains. Any retained austenite may decompose during this last stage. Therefore, the peak can coincide with ferrite as the structure was recovered during tempering (BHADESHIA, 2017).

TEM was used to fully characterise the microstructure of the base metal. Figure 34 shows two transmission electron micrographs of the AHSS900 BM. Figure 34a shows precipitates dispersed in some grains whereas Figure 34b shows the precipitates within a grain and in its boundaries.

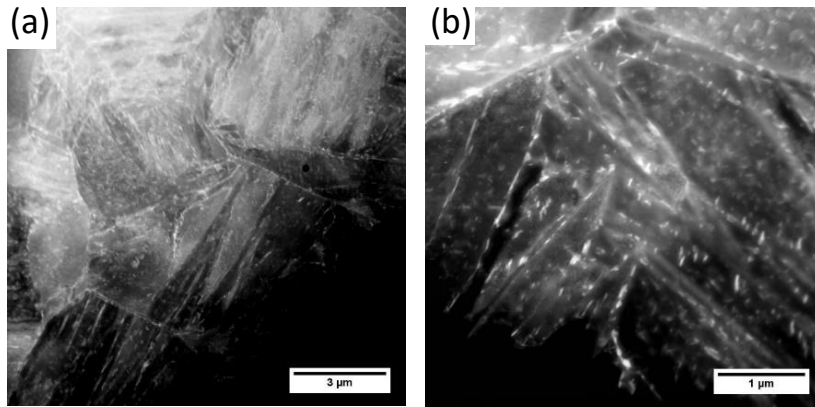


Figure 34: STEM micrographs of AHSS900 showing precipitates dispersed in some grains (a) and within a grain and in its grain boundary (b).

This high amount of precipitates, as also detected by SEM images (see Figure 30d) is a consequence of the tempering process. The AHSS900 BM is a tempered steel processed by TMCP. Other precipitates were identified during TEM analysis. Figure 35 shows the morphology of precipitates in the AHSS900 base metal and EDS mapping analysis for Mn, Fe, Nb, N, Ti and V.

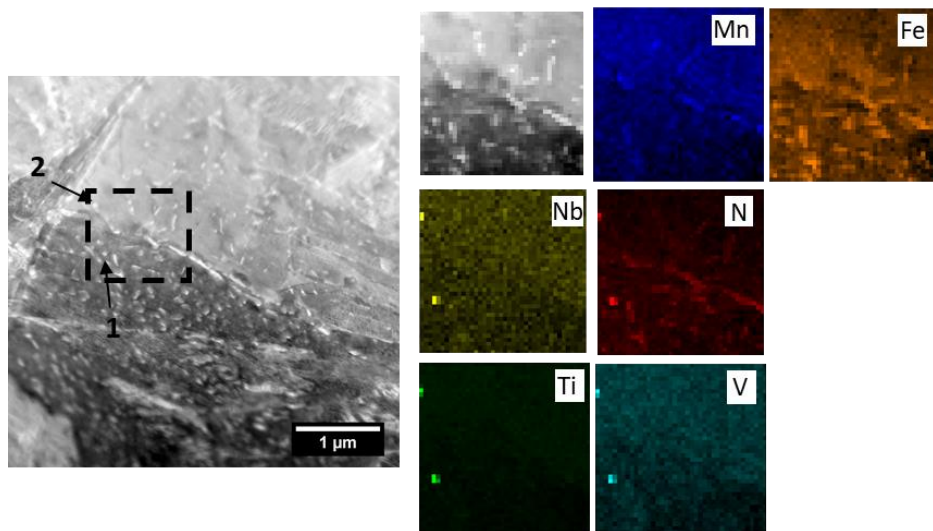


Figure 35: STEM/EDS mapping analysis of small precipitates rich in Ti found on the AHSS900 BM.

The EDS mapping revealed two distinguishing precipitates, named 1 and 2. It is seen they are richer in some alloying elements such as Ti, Nb, V. Their chemical composition is shown in Table 7.

Nanometric precipitates rich in Nb and Ti were also detected in the matrix as shown in Figure 37. EDS mapping analysis shows two distinguishing precipitates rich in Nb, Ti and V. They have a clearly different chemical composition from the big precipitate (named 1) and from the matrix.

Table 9 shows the chemical composition of the precipitates showed in Figure 37. The big precipitate (1) is iron carbide with presence of other elements such as Al, Cr and Si. The nanometric precipitate (2) is carbide rich in Ti, Nb and V.

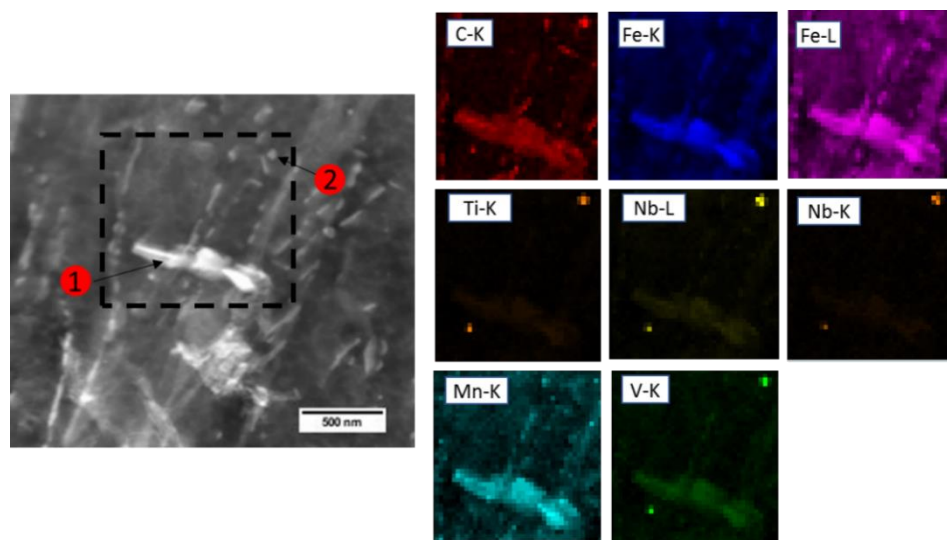


Figure 37: STEM/EDS mapping analysis on the AHSS900 BM, of a large cementite and a nanometric precipitate rich in Ti, Nb and V.

Table 9: Chemical composition of the precipitates and matrix of AHSS900 BM detected in Figure 37.

wt%	C	Mn	Si	Cu	Cr	Al	Mo	Ti	Nb	V	P	Fe
1	4.87	1.36	0.06	3.64	0.31	0.05	-	-	-	-	0.03	88.10
2	4.87	0.51	-	3.73	-	-	-	12.34	8.14	2.55	-	67.83
matrix	0.19	1.26	1.37	2.79	-	-	-	-	-	-	-	94.36

In general, the EDS analysis shows two main precipitates: 1. Big precipitates, uniformly distributed within the matrix (Figure 35b and 35c), characterized as iron carbides with some Mn and Cr; 2. Nanometric precipitates characterized as carbides rich in Ti, Nb, V and B. The volume fraction of iron carbides is higher than that of carbides rich in alloying elements. The smallest precipitates size is around 50 nm.

These nanometric precipitates are the most dominant factor in the strengthening of microalloyed steels (SOTO et al., 1999).

4.1.3. Considerations of BMs microstructures

The base metals studied in this work have different microstructures, mainly due to their chemical compositions and manufacturing process. LNE500 consists of polygonal ferrite and small amount of pearlite, whereas AHSS900 consists of tempered martensite.

Precipitates were detected mainly in the AHSS900 BM. They were characterised as iron carbides and nanometric Ti,Nb (C,N). Tempering at a low temperature relieves the excess of carbon trapped in martensite, by the precipitation of iron carbides. It takes place within the tempered martensite matrix and continuously grows when the tempering temperature and tempering time increase (PHETLAM & UTHAISANGSUK, 2015).

The low fraction of pearlite in the LNE500 is a result of its low C content. Some iron carbides were found in the LNE500 BM. Precipitation of microalloying carbonitride in ferrite is affected by the formation of pearlite. Carbon available in the matrix would be consumed to the formation of pearlite and, thus, it would reduce the precipitation free energy and retard the precipitation process (YONG et al., 2011). This explains the lower carbide content found in LNE500.

4.2. MICROSTRUCTURE OF THE WELDED JOINTS FOR THE LNE500 STEEL

The typical microstructural changes that occur across the neighbouring HAZ as a result of heat dissipation from the weld deposit are illustrated in Figure 38. The characteristic zones associated with welding are a result of the temperature gradient from the weld metal to the unaffected base material. As a consequence, those regions experience heating and cooling cycles whose severities depend on the distance from the fusion boundary.

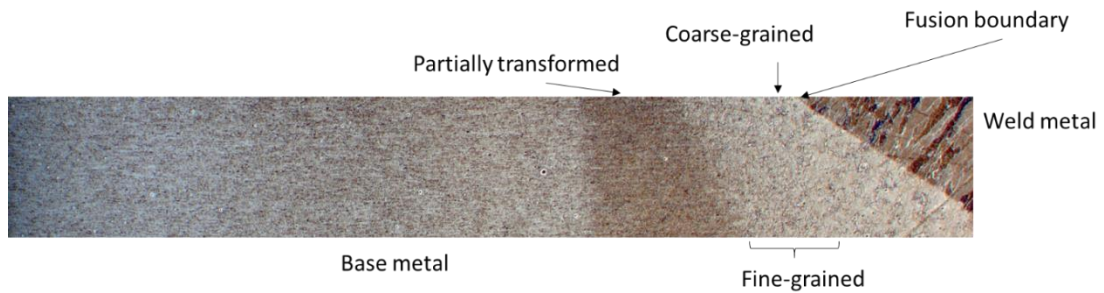


Figure 38: Weld microstructure across the heat-affected zone from sample B.

. The effect of the thermal cycle is especially evident on the grain size which reduces moving away from the fusion boundary (the effect of grain size will be further discussed on section 4.6). More detailed optical micrographs along the welded joint of samples A and B are shown in Figure 39 and Figure 40, respectively.

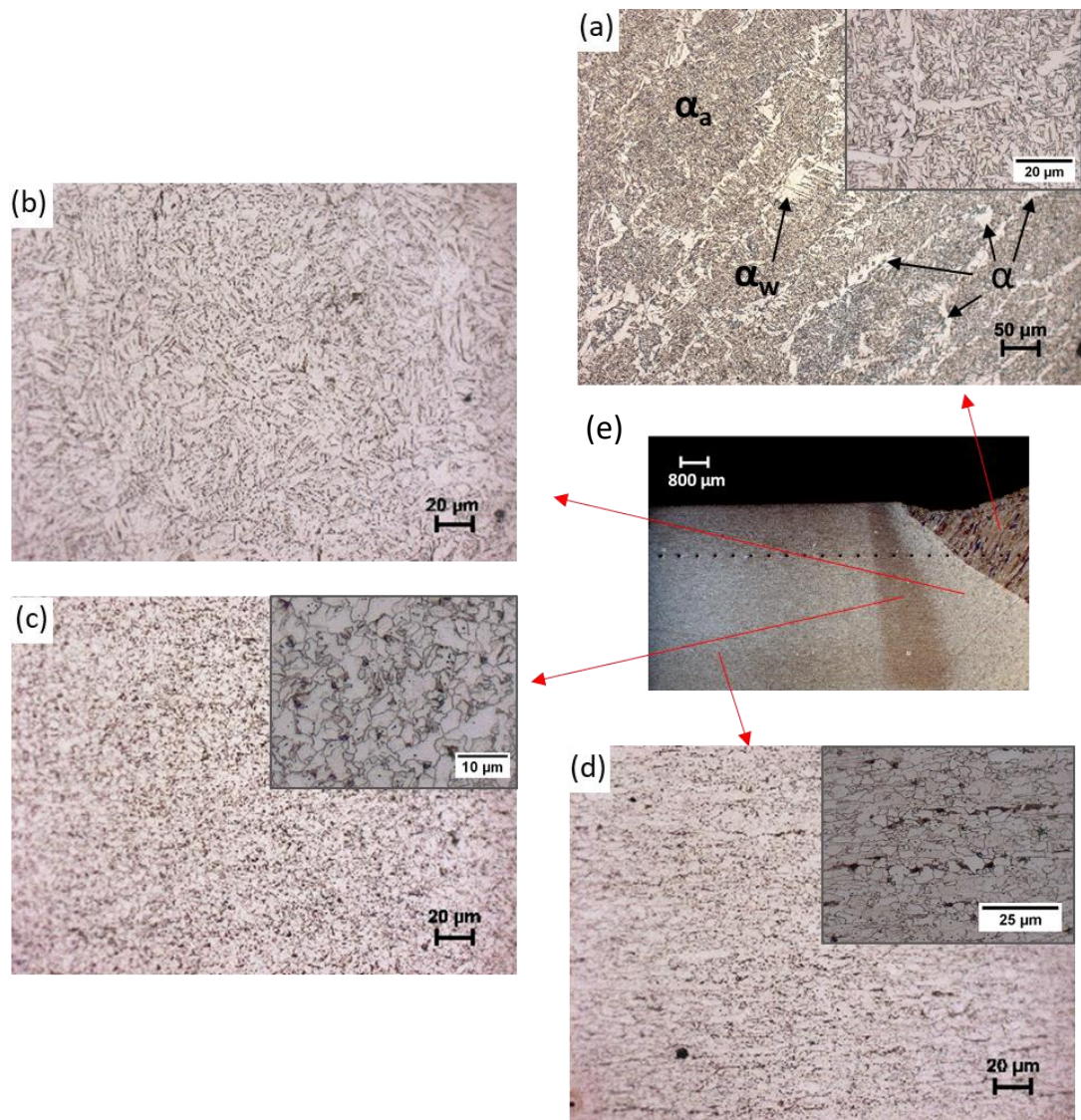


Figure 39: Typical microstructure of the welded joint LNE500 Sample A (500-P-0.72) - (a) WM, (b) coarse-grained HAZ, (c) partially transformed HAZ, (d) BM and (e) macrograph of the welded region.

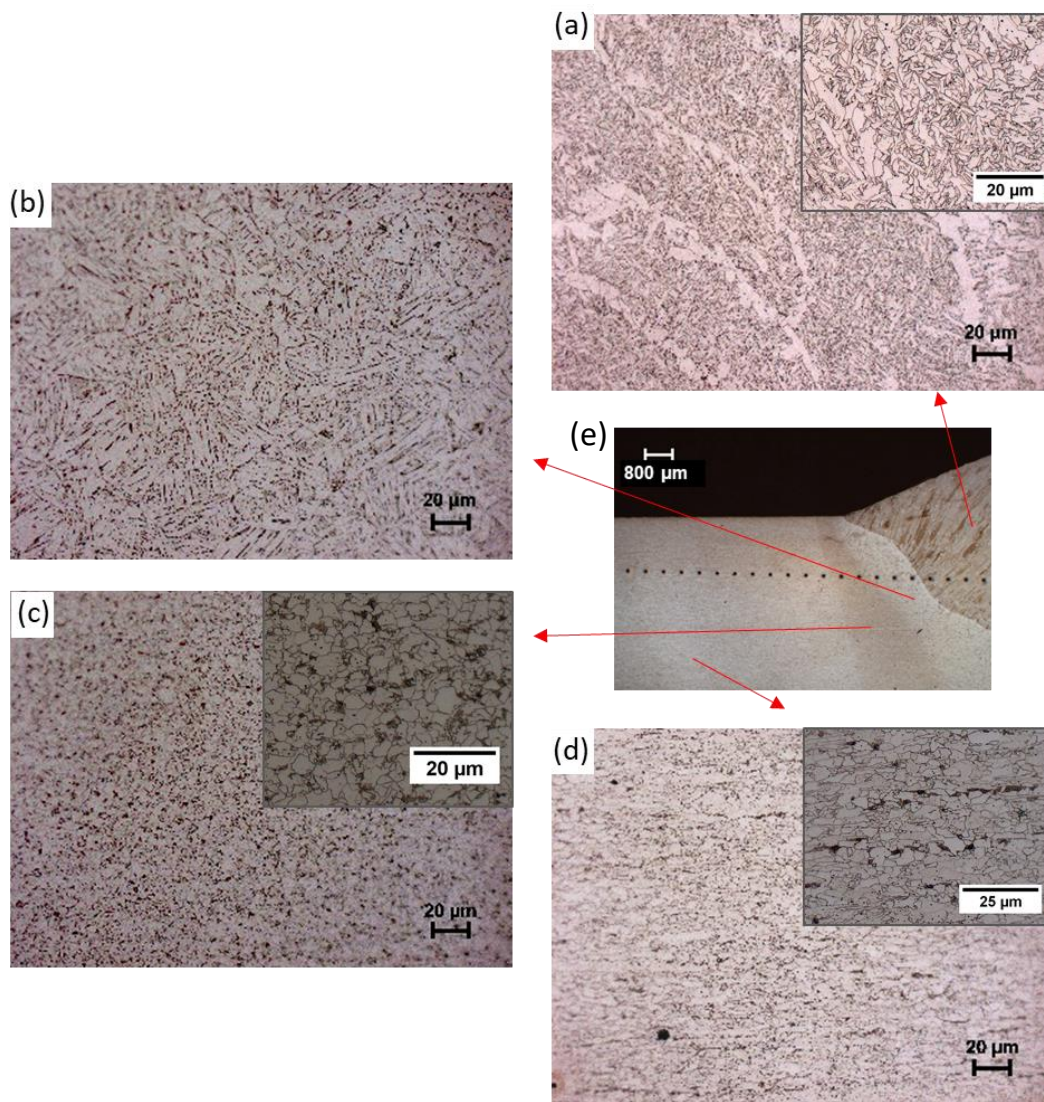


Figure 40: Typical microstructure of the welded joint LNE500 Sample B (500-CMT-0.70) - (a) WM, (b) coarse-grained HAZ, (c) partially transformed HAZ, (d) BM and (e) macrograph of the welded region.

Metallographic analysis allowed for identifying the presence of allotriomorphic ferrite (α), Widmanstätten ferrite (α_w) and acicular ferrite (α_a) in the WM for both samples (all phases are pointed out in Figure 39a). The acicular ferrite exhibits an interlocked morphology consisting of fine ferrite plates with different spatial orientations. The WM microstructure of sample B presented lower volume fraction of α_w and higher volume fraction of α_a than that of the sample A. As the filler material is the same for both welded samples the difference is due to the peak temperature as a consequence of the higher heat and cooling rate.

During solidification, the grain growth in the weld metal occurs epitaxially with respect to the HAZ, which results in a columnar austenitic structure in the weld bead with axes following the direction of maximum heat flow as can be seen in Figure 39a and Figure 40a. The prior austenite grain boundaries appear as light-coloured regions which are transformed into allotriomorphic ferrite during cooling.

Partially transformed HAZ (Figure 39c and Figure 40c) consists of ferrite but compared with BM (Figure 39d and Figure 40d) it is free of banded structures. The coarse-grained HAZ (CGHAZ) (Figure 39b and Figure 40b) consists of granular bainite (this microstructure can be better seen later in Figure 42c and Figure 43b).

The main difference observed between both welded samples is the coarse-grained HAZ. Sample A, welded with higher heat input, suffered an increase in the solidification time and a reduction in the cooling time. These two characteristics increased its grain size in the CGHAZ. Section 4.6 presents the grain size measurement for all welded samples and BM. Comparing the weld section (Figure 39e and Figure 40e), wider HAZ area is observed for sample A (4108.8 μm) than for sample B (3200.4 μm).

The XRD pattern of the CGHAZ and WM of the welded samples A and B are shown in Figure 41a and 41b, respectively. The XRD pattern in Figure 41a confirms the ferrite in the HAZ for both samples (JCPDS #00-006-0696). For the WM the XRD patterns are different for samples A and B. The presence of retained austenite and ferrite peaks are identified for both samples (JCPDS #00-052-0512), but an oxide, containing some Cu, Fe and Mn, was only detected for sample B (JCPDS #01-074-2072). The fraction for each phase is shown in Table 10.

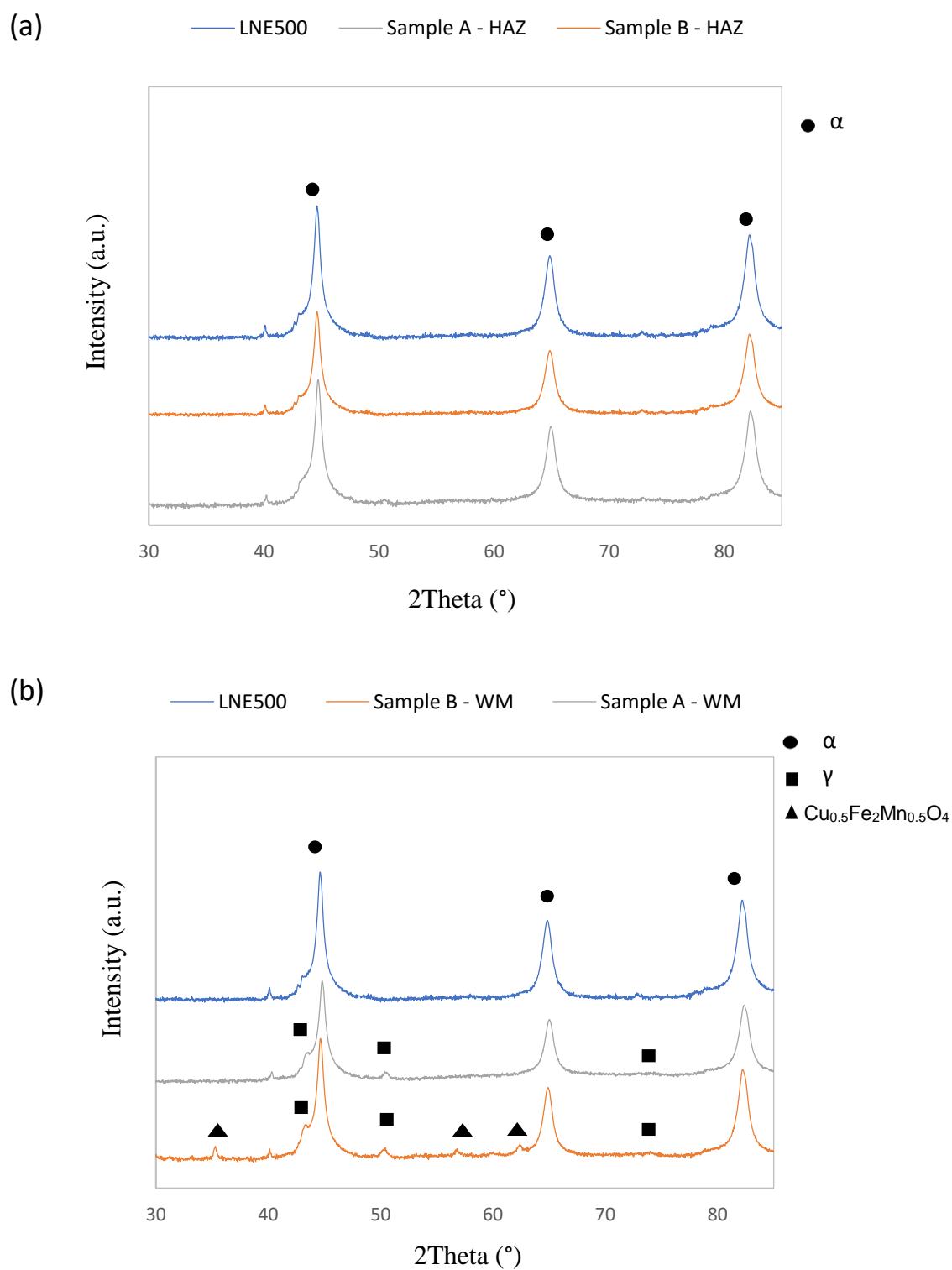


Figure 41: X-ray analysis at the a) CGHAZ; b) WM of samples A and B and LNE500 BM.

Table 10: Fraction of phases in the HAZ and WM

Sample	α /%	γ /%	$\text{Cu}_{0.5}\text{Fe}_2\text{Mn}_{0.5}\text{O}_4$ /%
LNE500	100	-	-
Sample A - HAZ	100	-	-
Sample B - HAZ	100	-	-
Sample A - WM	99.0	1.0	-
Sample B - WM	97.2	1.6	1.2

The formation of acicular ferrite on the WM requires heterogeneous nucleation sites. Later on, in this chapter, these nucleation sites (oxides) were also identified by TEM analysis, not only for sample B but also for sample A. However, XRD only detected the oxide for sample B, which may indicate its higher fraction in the WM of sample B.

Optical microscopy analysis of the microstructure in the HAZ revealed the presence of some precipitates. They are shown in Figure 42 and Figure 43 for samples A and B, respectively. Figure 42a and 42b show orange square shaped precipitates, whereas Figure 42c shows a longer orange rectangular shaped precipitate.

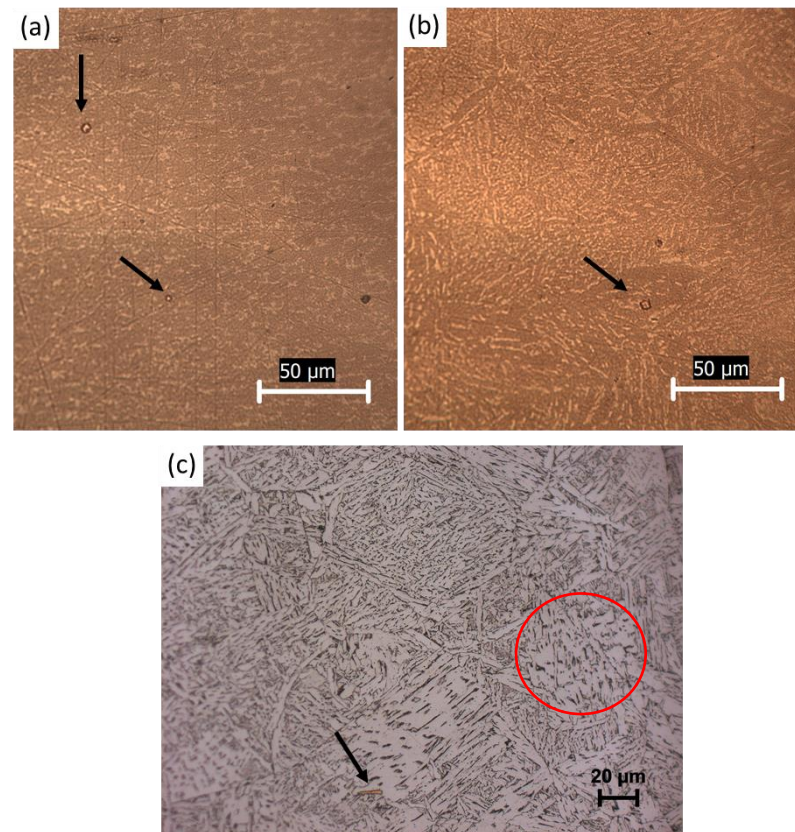


Figure 42: Optical micrographs from HAZ of sample A (500-P-0.72). Arrows indicate small square shaped precipitates – sample was etched with acid picric solution (a-b) and orange long rectangular shaped precipitate – sample was etched with Nital (c). Circle indicates granular bainite.

Similar orange square-shaped precipitates are shown in Figure 43a and 43b for sample B. These precipitates are smaller for sample B (average size around 4 μm) than Sample A (average size around 10 μm). EDS analysis confirmed that these precipitates are Ti,Nb(C,N) (Figure 44).

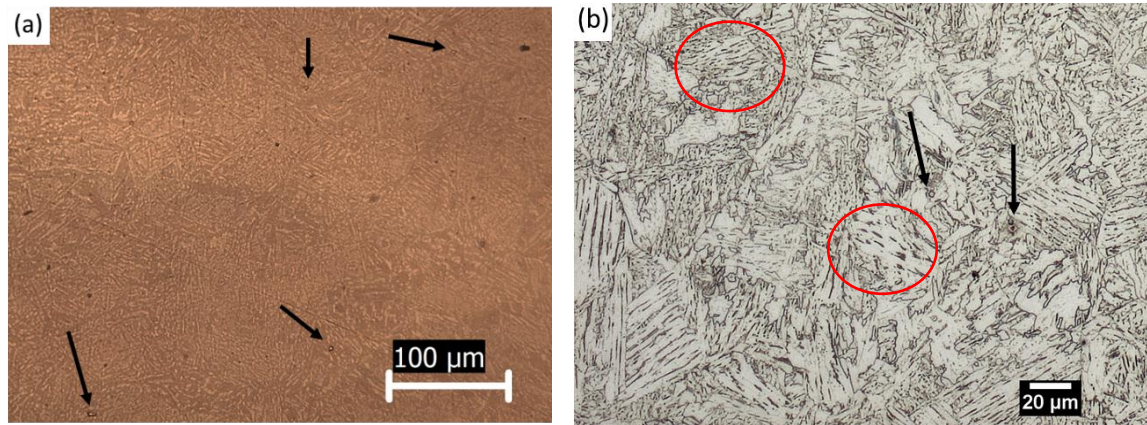
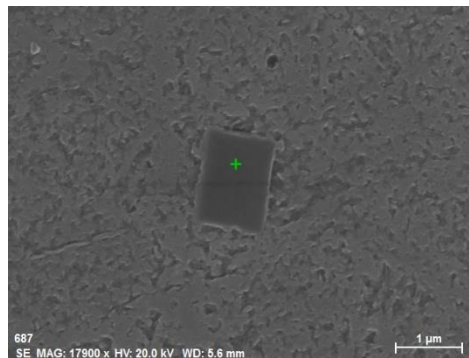


Figure 43: Optical micrographs from HAZ of sample B (500-CMT-0.70). Arrows indicate precipitates. Sample was etched with acid picric solution (a) and with Nital (b). Circles indicate granular bainite.



Element	wt%
Fe	45.42
Ti	38.64
Nb	10.22
N	8.72
C	14.44

Figure 44: SEM micrographs with EDS chemical composition for a typical precipitate found in the HAZ for welded samples from LNE500.

In order to further characterise the type of precipitates present in the HAZ and their chemical composition, TEM analysis was conducted. Figure 45 shows square-shaped precipitates and their chemical composition found on HAZ of sample A. Table 11 shows the chemical composition of regions 1 and 2 of the precipitate showed in Figure 45.

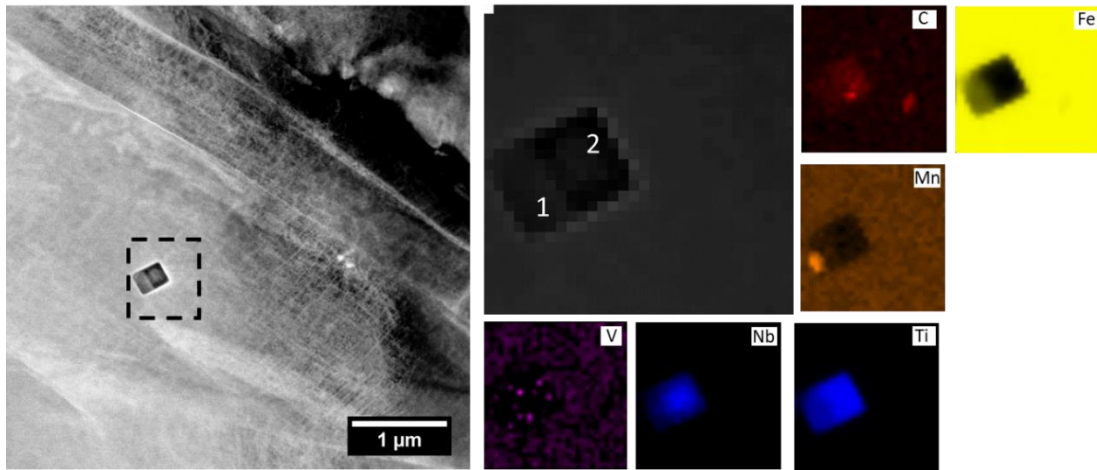


Figure 45: STEM/EDS mapping analysis of a precipitate in the HAZ of sample A (500-P-0.72).

Table 11: Chemical composition of the precipitate in the WM of sample A 500-P-0.72

wt%	C	N	Si	Mn	Al	Ti	Nb	V	Cr	Cu	Fe
Region 1	0.68	6.30	-	2.88	0.08	33.52	3.26	-	0.15	0.42	51.43
Region 2	1.49	5.20	0.06	0.44	0.06	56.01	11.93	0.36	0.04	-	24.32
Matrix	0.85	-	0.09	1.25	0.11	0.28	-	0.09	0.11	0.29	96.75

Figure 45 shows a square-shaped precipitate. By EDS mapping analysis, two distinct regions within this precipitate are identified and named 1 and 2. Region 1 is much richer in Mn (2.88 wt%) and Cr. Vanadium-rich particles can be clearly seen inside the Ti (C,N) along region 1 and 2. Region 2, in turn, is richer in Ti and Nb, according to Table 11. A Square/rectangular-shaped precipitate found on HAZ of sample B is shown in Figure 46. Table 12 shows the chemical composition of different regions of the precipitate showed in Figure 46 and the matrix. The size of the Ti,Nb(C,N) showed in Figure 46 is around 7 μm .

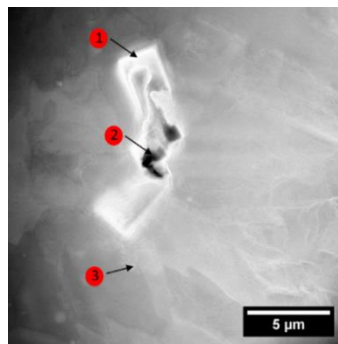


Figure 46: STEM/EDS chemical composition of a precipitate in the HAZ of Sample B (500-CMT-0.70)

Table 12: Chemical composition of the precipitate in the WM of sample B (500-CMT-0.70).

wt%	C	N	O	Si	Mn	Al	S	Ti	Nb	Cu	Fe
1	1.00	8.05	-	-	0.01	-	-	59.19	8.90	-	22.82
2	1.53	13.70	-	-	-	-	-	71.12	4.41	-	8.23
3	0.34	-	-	-	1.59	-	-	-	-	1.97	96.00
Matrix											

The chemical composition of the precipitates found in the HAZ for samples A and B are similar, with Ti content of up to 50 wt% and Nb of up to 10 wt%. All precipitates are chemically heterogeneous.

The microstructure of the weld metal was also studied by TEM. Figure 47 shows non-metallic particles found in the WM of sample A. The chemical composition obtained by EDS analysis of the matrix and the inclusion (shown in Figure 47) is shown in Table 13.

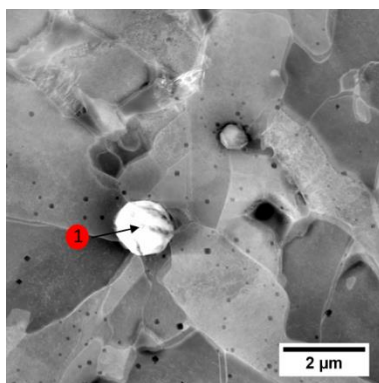


Figure 47: STEM micrographs showing inclusions in the WM of sample A 500-P-0.72.

Table 13: Chemical composition of the inclusions in the WM of sample A 500-P-0.72

wt%	C	N	O	Si	Mn	Al	S	Ti	Nb	P	Cu	Fe
1	0.42	1.88	50.80	8.22	13.11	18.04	0.04	1.23	-	0.06	3.81	2.33
Matrix	0.21	-	0.03	0.30	-	0.29	-	-	-	-	10.30	88.84

Figure 48 shows a TEM micrograph with EDS mapping analysis for a non-metallic inclusion. The EDS mapping analysis show the determination of Mn, O, Cu, Ti, Fe, Al and C. The chemical compositions of the matrix, regions 1 and 2 are shown in Table 14.

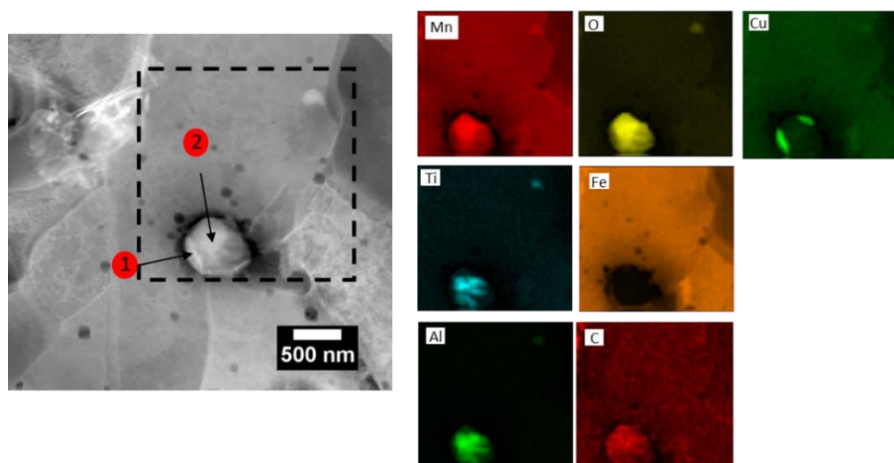


Figure 48: STEM/EDS mapping analysis and chemical composition of the inclusion in the WM of the sample A 500-P-0.72.

Table 14: Chemical composition of the inclusions in the WM of sample A 500-P-0.72

wt%	C	N	O	Si	Mn	Al	S	Ti	Nb	Cu	Fe
Matrix	0.20	-	-	-	-	-	-	-	-	7.62	92.17
1	-	-	31.09	3.16	9.17	5.62	9.76	-	-	32.17	9.00
2	-	-	54.37	2.04	8.31	-	-	5.72	-	2.69	1.62

Figure 49 shows three inclusions of sample B. Their size is around 1 μm . Table 15 shows the chemical composition of the inclusions pointed out in Figure 49.

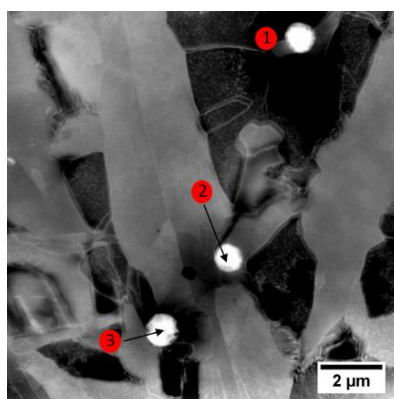


Figure 49: STEM micrographs showing inclusions in the WM of sample B 500-CMT-0.70.

Table 15: Chemical composition of the inclusions in the WM of sample B 500-CMT-0.70.

wt%	C	N	O	Si	Mn	Al	S	Ti	Nb	Cu	V	Fe
1	3.96	-	34.19	9.89	16.86	5.87	0.38	3.34	-	1.99	-	23.47
2	3.69	-	20.37	3.49	12.92	7.13	0.19	1.07	-	1.20	-	49.91
3	0.80	-	39.66	8.24	29.93	14.32	0.12	3.21	-	0.12	-	3.551
Matrix	1.02	-	2.37	0.41	1.24	0.16	0.09	0.11	-	0.39	-	94.15

The chemical compositions of the oxide inclusions for samples A and B are similar. Considering that iron signal is from the steel matrix, the present inclusion would be a mixture of Si, Mn and Al oxide containing a small amount of titanium, sulphur and copper.

As can be clearly seen in Figure 48, oxide inclusions are not homogenous. The region in the centre on the inclusion is richer in Ti, Al, whereas two edges of the spherical inclusion are richer in Cu.

Almost all of the inclusions observed were spherical, with sizes of up to 2.5 μm . Some of them appeared to act as nucleating sites for acicular ferrite, i.e. several ferrite laths look like to be fanned outwards from the inclusions.

A key feature was that sample B showed higher fraction of oxide particles than sample A. This fact was identified in the TEM analyses and also by XRD measurements. These oxides were identified by XRD as $\text{Cu}_{0.5}\text{Fe}_2\text{Mn}_{0.5}\text{O}_4$.

4.4. MICROSTRUCTURE OF THE WELDED JOINT AHSS900.

Figure 50 and Figure 51 show optical micrographs along the welded joint of samples C and D, respectively.

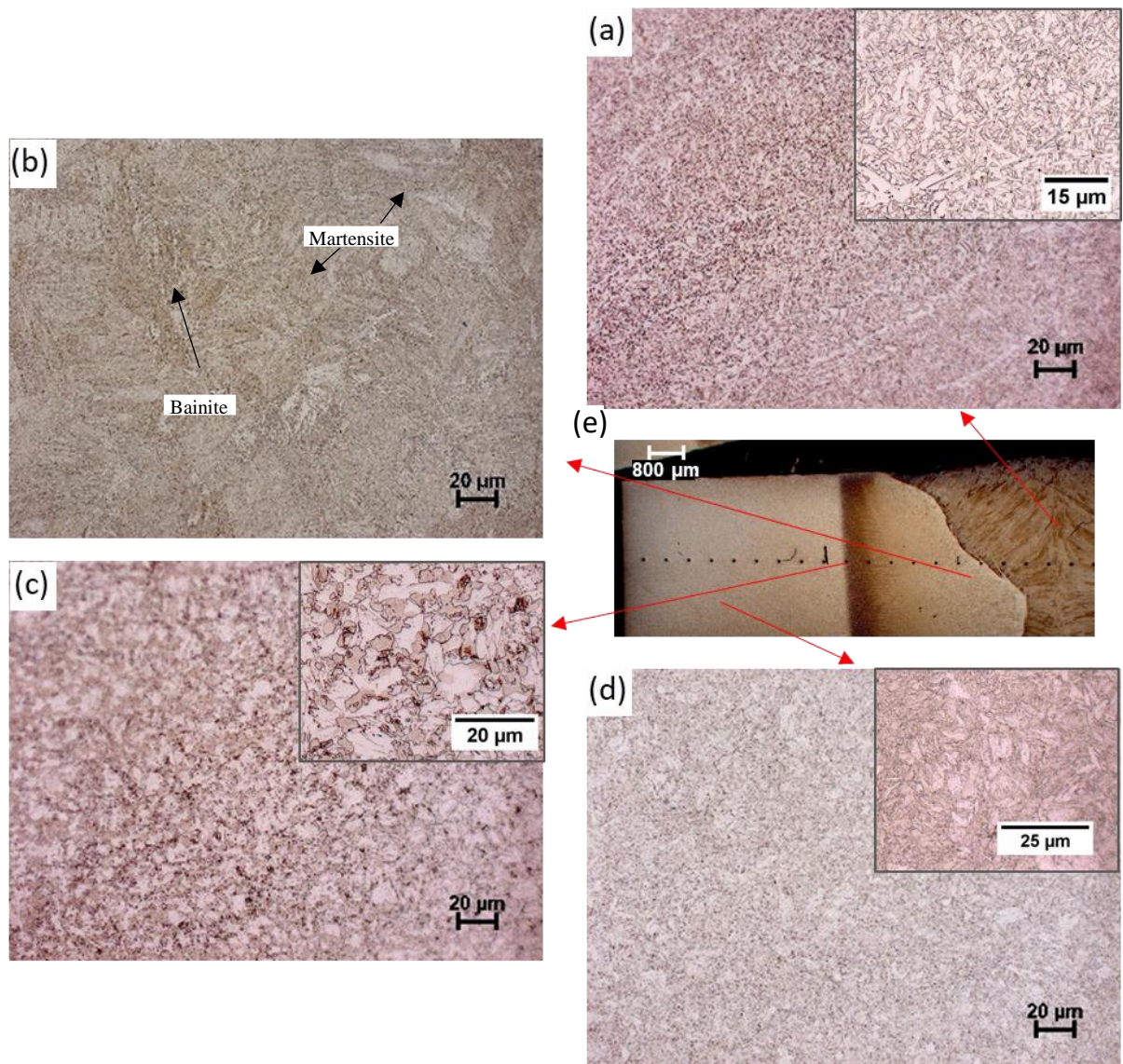


Figure 50: Typical microstructure of the welded joint AHSS900 Sample C (900-CMT-0.31) – (a) WM, (b) coarse-grained HAZ, (c) partially transformed HAZ, (d) BM and (e) macrograph of the welded region.

The microstructure of the WM (Figure 50a and Figure 51a) consists of acicular ferrite (α_a) with interlocked morphology. Both samples showed very similar WM microstructures, however sample D seems to have lower fraction of acicular ferrite, considering visual analysis from optical micrographs.

The CGHAZ primary microstructure consists of lath martensite and granular bainite for both samples. Sample D was subjected to a higher heat input than sample C thus it has a coarser microstructure. Comparing the weld section (Figure 50e and Figure 51e), wider HAZ area is observed for sample D (5399.7 μm) than for sample C (3357.2 μm).

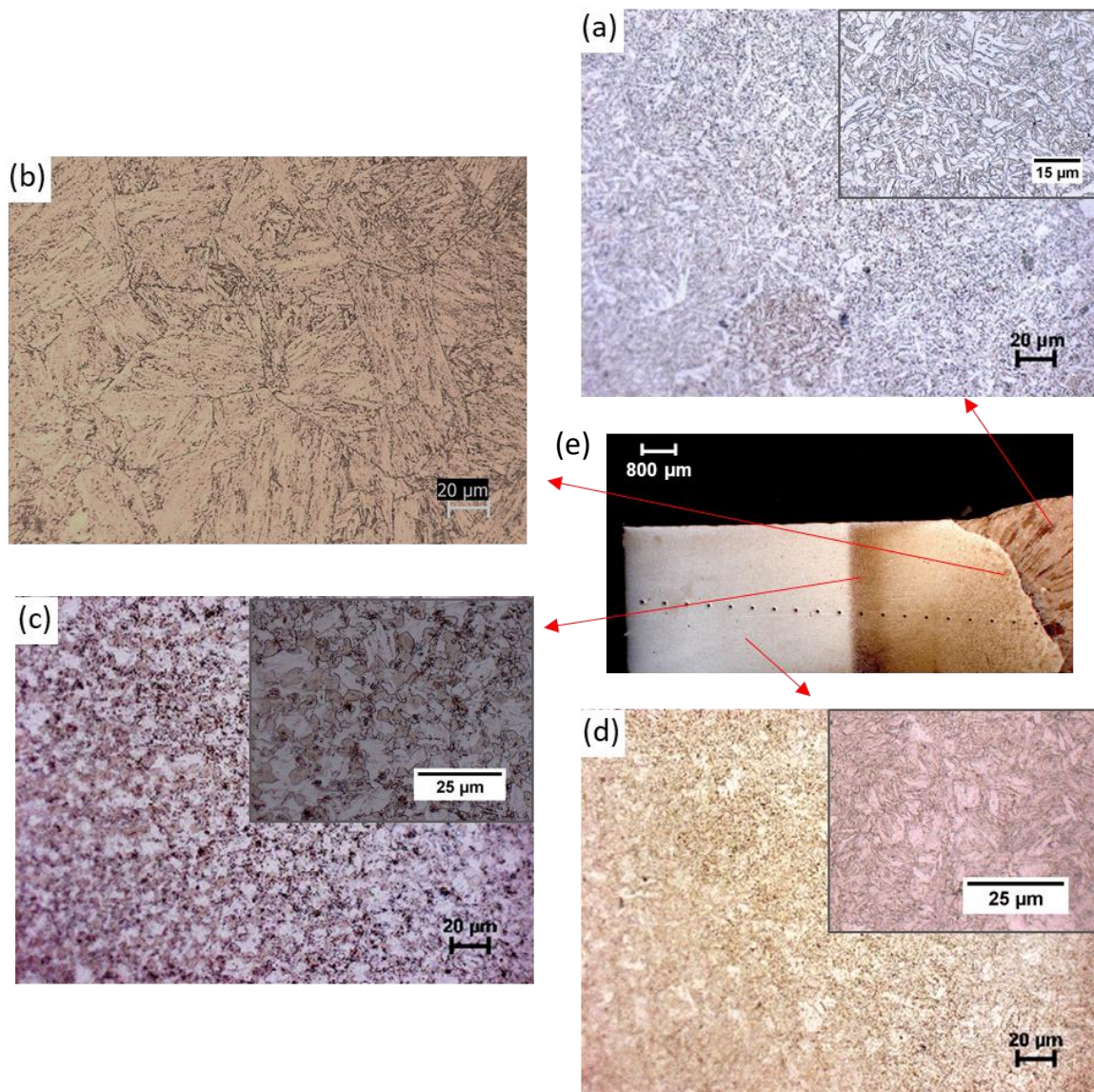


Figure 51: Typical microstructure of the welded joint AHSS900 Sample D (900-CMT-0.47) - (a) WM, (b) coarse-grained HAZ, (c) partially transformed HAZ, (d) BM and (e) macrograph of the welded region.

The microstructure of the partially austenitic HAZ for both samples is different from that of the base metal. Ferrite equiaxed grains can be detected. As this region is formed at a certain distance from the fusion zone, the temperature achieved during

welding cannot lead to a complete austenitization. The small amount of austenite that does form has a large carbon concentration because of the higher solubility of carbon in austenite at lower temperatures (BHADESHIA & HONEYCOMBE, 2017). However, the temperature that this region experienced is high enough to allow recrystallisation from ferrite plates into equiaxed grains.

The XRD pattern of the CGHAZ and WM of the welded samples D and C are shown in Figure 52a and 52b, respectively. The XRD pattern confirms the ferrite in the HAZ for both samples and no difference is detected. The XRD pattern for WM is also identical for samples A and B showing the presence of ferrite and retained austenite. Table 16 summarises the relative fraction of each phase.

Table 16: Summary of the X-ray diffraction analysis

Sample	α /%	γ /%
HSLA900	100	-
Sample C - HAZ	100	-
Sample D - HAZ	100	-
Sample C - WM	98.3	1.7
Sample D - WM	97.6	2.4

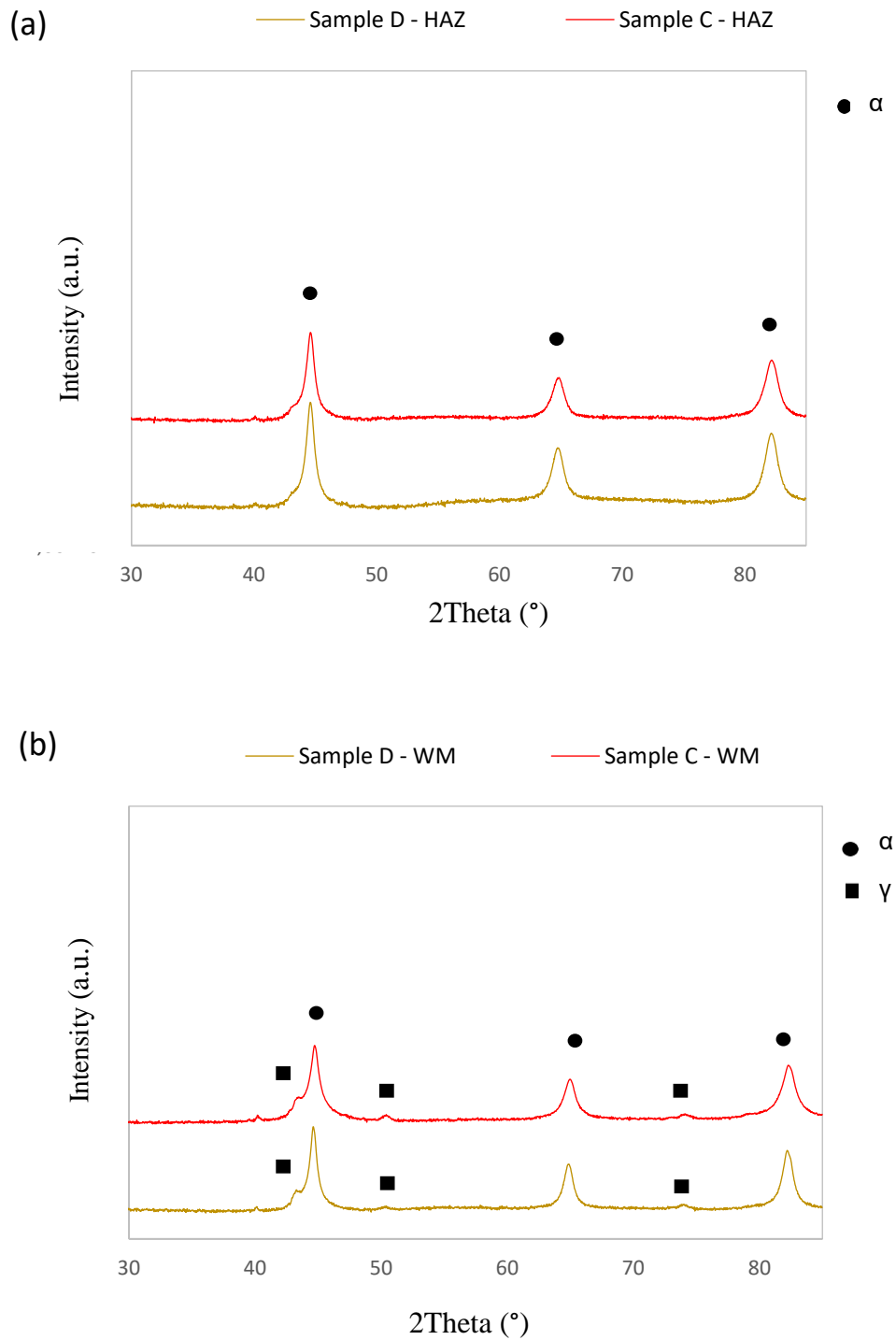


Figure 52: X-ray analysis at the (a) HAZ; (b) WM of Samples C (900-CMT-0.31) and D (900-CMT-0.47).

By the time the weld deposit cools to about 500 °C most of the austenite has been consumed. The small quantity of remaining austenite (around 5%) is enriched in carbon and either transforms to martensite, or into pearlite, which is degenerate because it does not have the opportunity to establish a lamellar structure. Higher heat input - slower cooling rate - favour the formation of pearlite relative to martensite and

some austenite may also be retained to ambient temperature as was detected in both samples. Pearlite and martensite, because of their small volume fractions in the overall microstructure, are called 'microphases' and their identification is not trivial (BHADESHIA & HONEYCOMBE, 2017).

In addition, further examination of the microstructure resulted in the identification of the same type of precipitate found on the base metal, (Ti,Nb(C,N)). These precipitates were also found in the HAZ for both samples, as can be seen in Figure 53 and Figure 54 for sample C and D, respectively. Their size varies, but sample D showed bigger precipitates (average size around 5 μm) than sample C (average size around 3 μm).

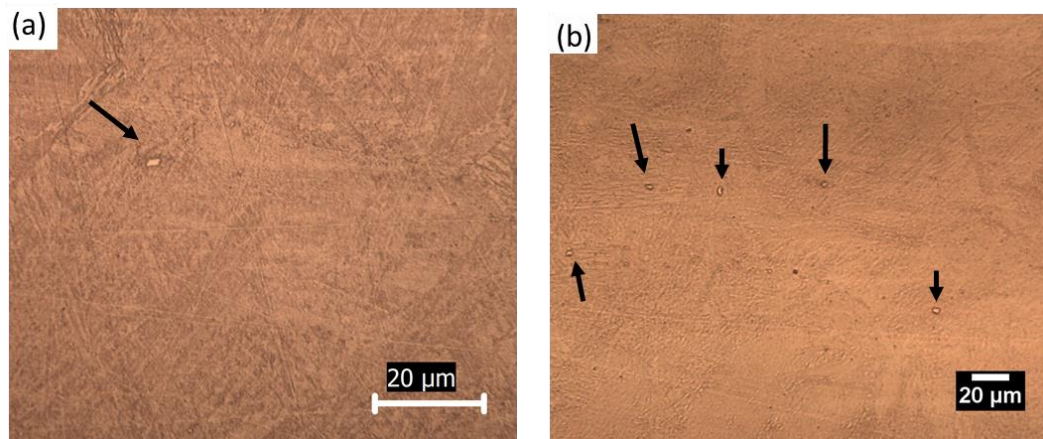


Figure 53: Optical micrographs from HAZ of sample C (900-CMT-0.31) showing the shapes of the precipitates (a) and the large amount of them along the sample (b).

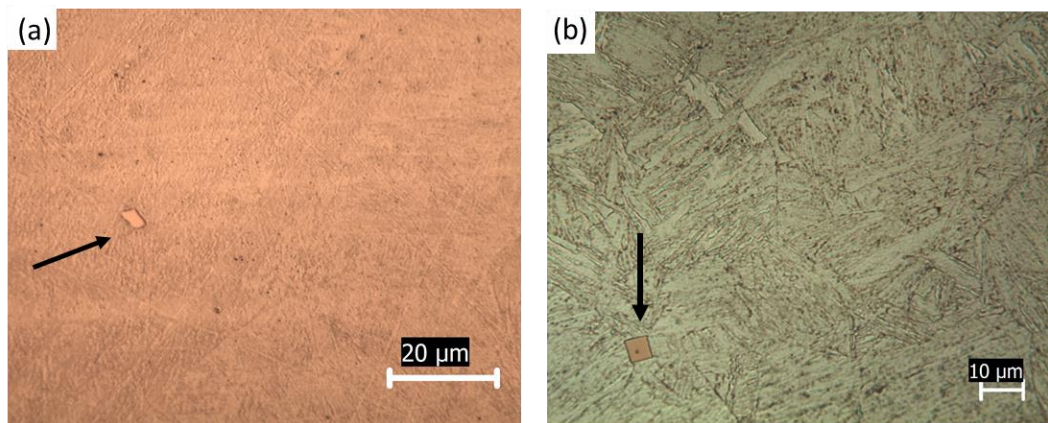


Figure 54: Optical micrographs from HAZ of sample D (900-CMT-0.47) showing the shapes of the precipitates etched with picric acid solution (a) and Nital (b).

The identification of these precipitates was done by SEM/EDS analysis. Figure 55 shows a typical precipitate found in the HAZ for samples C and D. It was identified

as Ti, Nb(C,N) with size of up to 6 μm . TEM analysis of the HAZ for samples C and D was carried out. A typical microstructure is shown in Figure 56.

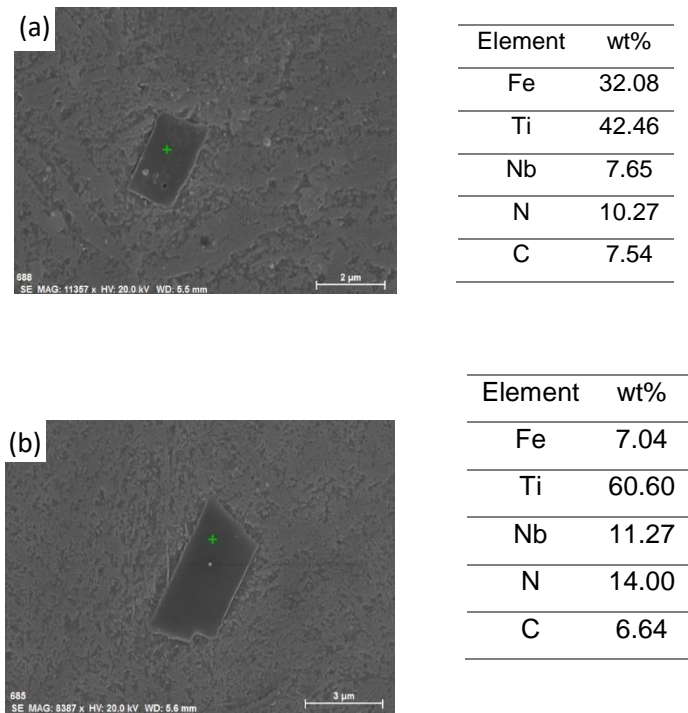


Figure 55: SEM micrographs with EDS chemical composition for typical precipitates found in the HAZ for welded joint (a) sample C and (b) sample D.

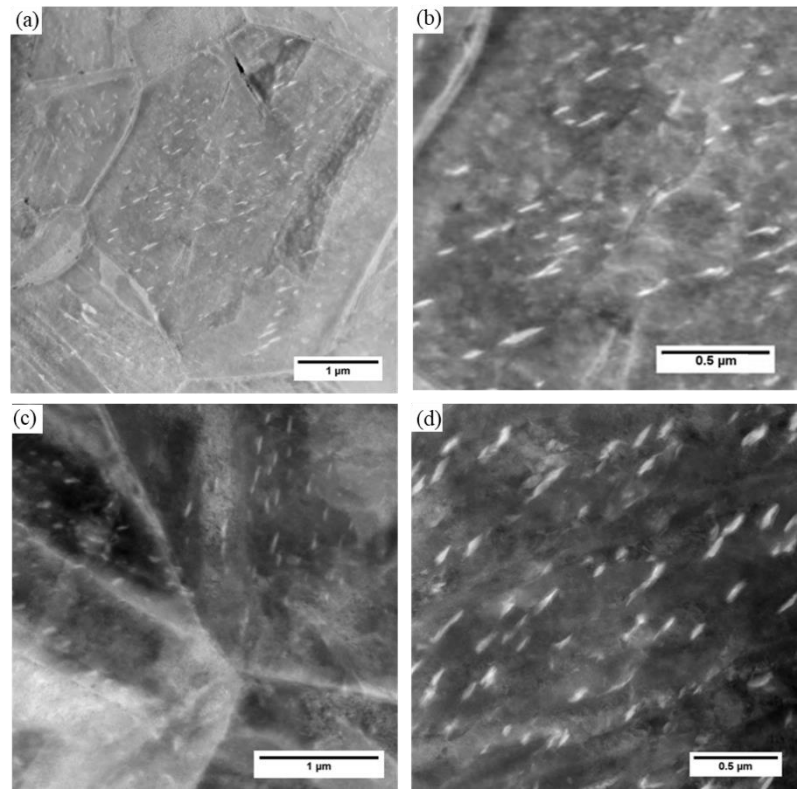


Figure 56: STEM micrograph of HAZ (a-b) sample C (900-CMT-0.31) and (c-d) sample D (900-CMT 0.47).

Two key features can be perceived: i) The presence of oriented plate-shaped nanometric precipitates uniformly distributed within the grain and its boundaries; ii) The average precipitates sizes are 100 nm and 125 nm for samples C and D, respectively.

The elemental composition of the precipitates was analysed by EDS mapping, as shown in Figure 57 and Figure 58 for sample C and Figure 59 for sample D.

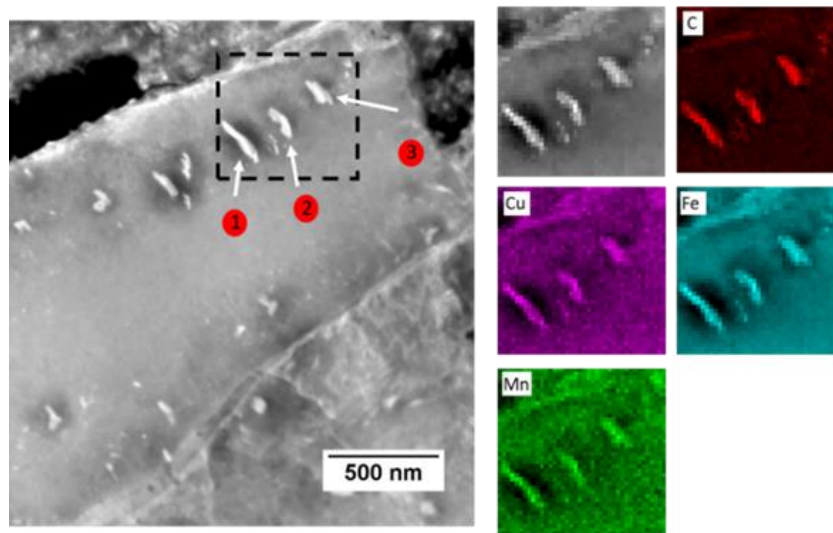


Figure 57: STEM/EDS mapping analysis showing three oriented precipitates in the HAZ of Sample C (900-CMT-0.31).

Table 17 shows the chemical compositions of the three precipitates identified in Figure 57.

Table 17: Chemical composition of the precipitates in the HAZ of sample C (900-CMT-0.31) shown in Figure 57.

wt%	C	N	Si	Mn	Al	S	Ti	Nb	Cu	Fe
1	14.61	-	-	1.01	-	-	-	-	3.56	80.79
2	10.67	-	-	0.45	-	-	-	-	3.00	85.86
3	13.33	-	-	1.31	-	-	-	-	3.10	82.23

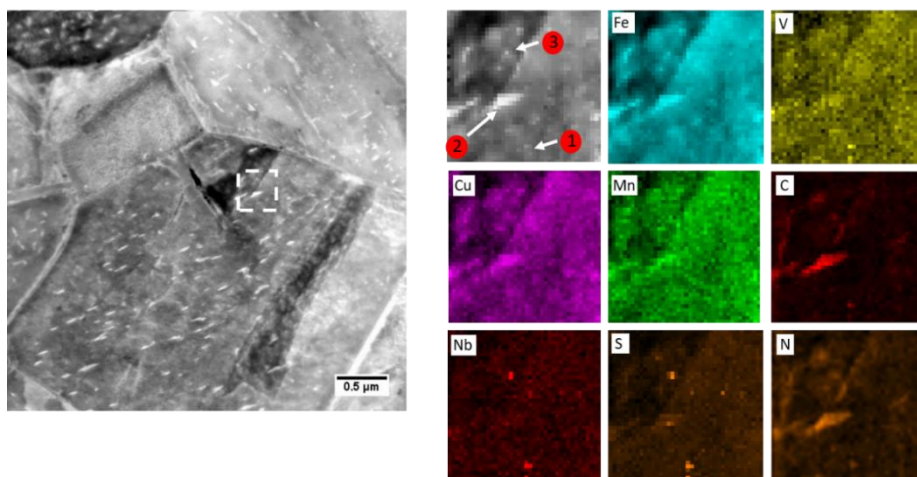


Figure 58: STEM/EDS mapping analysis showing different precipitates within a grain in the HAZ of Sample C (900-CMT-0.31).

The chemical compositions of the three precipitates (named 1, 2 and 3) from Figure 58 are shown in Table 18.

Table 18: Chemical composition of the precipitates in the HAZ of sample C(900-CMT-0.31) shown in Figure 58.

wt%	C	N	Mn	Al	S	Ti	V	Nb	Cu	Fe
1	2.71	0.52	0.87	-	0.08	-	0.04	1.04	2.46	92.27
2	8.52	0.04	0.51	-	-	-	-	-	2.64	89.21
3	4.28	0.53	0.79	-	0.91	-	0.17	1.81	2.92	88.54

The majority of the precipitates are iron carbides with some Mn as shown in Figure 57 (precipitates 1, 2 and 3). Besides, smaller precipitates were also found (Figure 58 – precipitates 1 and 3). The latter are rich in Nb but also contain V and S. With STEM images, the identification of these precipitates is not easy. However, EDS mapping shows clearly the nanometric precipitates. They are spherical, and their size is approximately 15 nm.

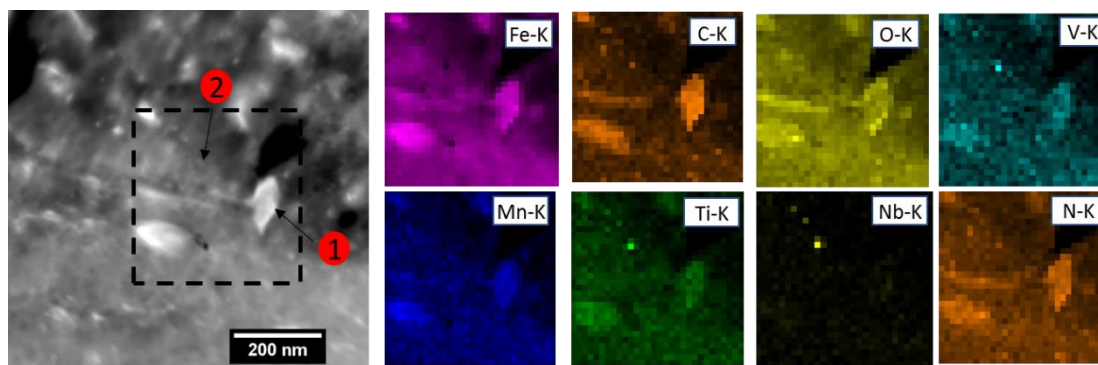


Figure 59: STEM/EDS mapping analysis and chemical composition on HAZ of the sample D (900-CMT-0.47).

The chemical compositions of the two precipitates (named 1 and 2) in Figure 59 are shown in Table 19. Similar iron carbides were found in the HAZ of the sample D. The nanometric particles are rich in Nb and V. Their size is between 10-15 nm.

Table 19: Chemical composition of the precipitates in the HAZ of sample D (900-CMT-0.47) shown in Figure 59.

wt%	C	Mn	Cu	Ti	Nb	V	O	Fe
1	4.81	0.79	-	-	-	-	-	94.39
2	7.22	-	7.56	5.98	18.84	2.75	9.34	48.27

TEM analyses were carried in the WM for samples C and D. The inclusions found are nucleating sites for acicular ferrite as ferrite lath tightly bonded on the inclusion surface as shown in Figure 60a.

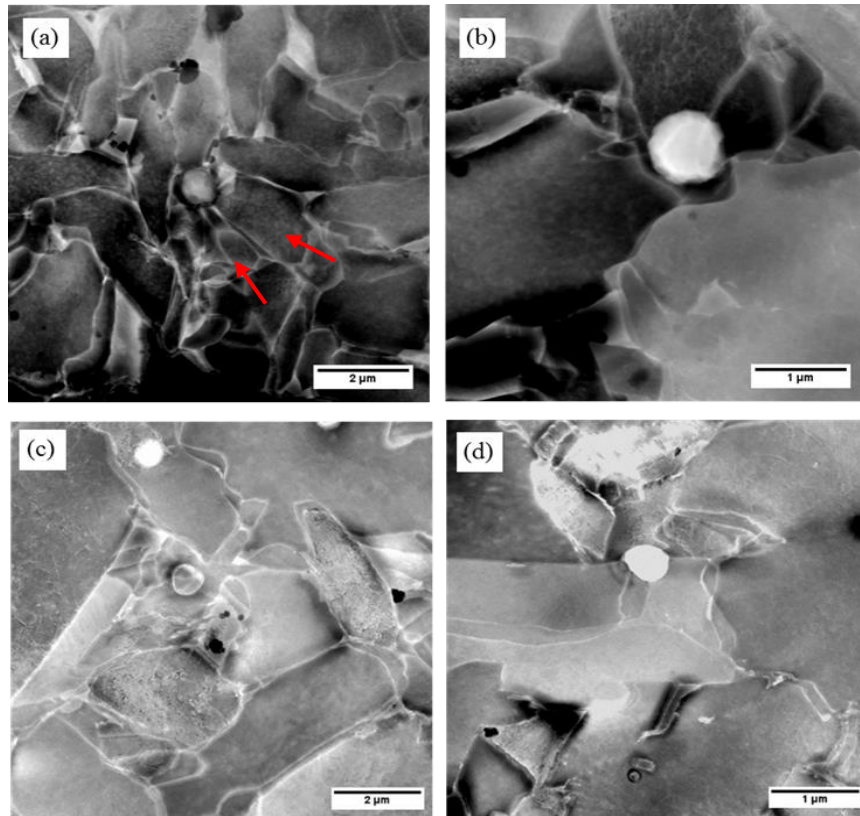


Figure 60: TEM micrographics showing precipitates at the WM, (a)(b) of sample C and (c)(d) for sample D.

Almost all of the inclusions observed were spherical-shaped. Their chemical compositions are shown in Figure 61 and Figure 62 for samples C and D, respectively. The chemical compositions of the two precipitates (named 1 and 2) in Figure 61 are shown in Table 20 and the chemical composition of the precipitate in Figure 62 is shown in Table 21.

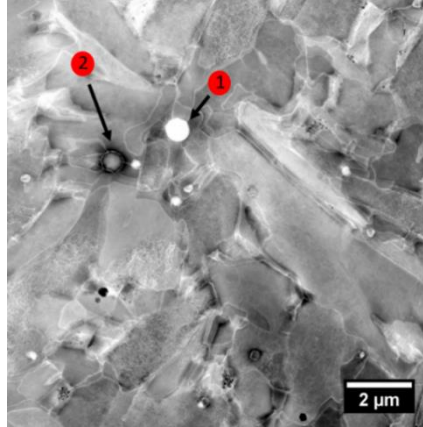


Figure 61: STEM micrograph of precipitates in the WM for Sample C (900-CMT-0.31).

Table 20: Chemical composition of inclusions in the WM of sample C(900-CMT-0.31).

wt%	C	N	O	Si	Mn	Al	S	Ti	V	Nb	Cu	Fe
1	0.56	-	28.75	4.33	5.38	11.56	0.05	0.53	-	-	5.29	43.50
2	0.57	-	52.55	15.59	10.06	14.87	0.17	0.93	-	-	1.79	3.43
Matrix	0.97	-	2.46	1.07	1.47	0.28	0.48	0.09	-	-	7.74	85.38

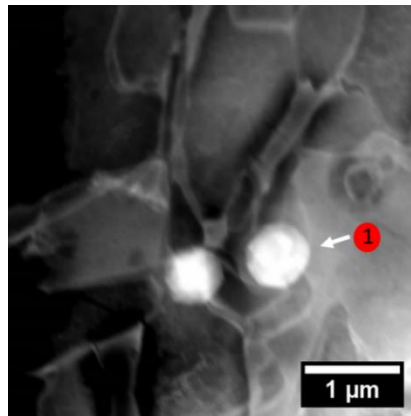


Figure 62: STEM micrograph of precipitates in the WM for Sample D (900-CMT-0.47).

Table 21: Chemical composition of inclusions in the WM of sample D (900-CMT-0.47).

wt%	C	N	O	Si	Mn	Al	S	Ti	V	Nb	Cu	Fe
1	0.43	-	20.22	8.35	17.34	8.31	0.50	1.01	-	0.39	-	43.31
Matrix	0.35	-	0.44	0.76	2.29	0.26	0.29	0.22	-	-	2.00	93.35

The inclusions evaluated by EDS were identified as oxides along with deoxidising elements such as silicon, aluminium and titanium. Sulphur is also detected.

The oxide particles are entrapped in the fusion zone during solidification. Mineral fluxes or inert gas shrouds are employed in order to protect the hot metal

against environmental attack during welding. Such protection is not entirely effective, with the result that the oxide content of the welded joints tends to be much larger than that of wrought steel (BHADESHIA & HONEYCOMBE, 2017).

4.5. DISCUSSION OF THE MICROSTRUCTURE OF THE WELDED JOINTS

The WM microstructure was predominantly comprised of acicular ferrite with small volume fraction of allotriomorphic ferrite and Widmanstätten ferrite on samples A and B. The presence of Widmanstätten ferrite was not observed in samples C and D and the volume fraction of allotriomorphic ferrite was lower than for samples A and B. The illustration of the morphology of phase constituents in WM of a typical low alloy steel weld bead is presented in Figure 63.

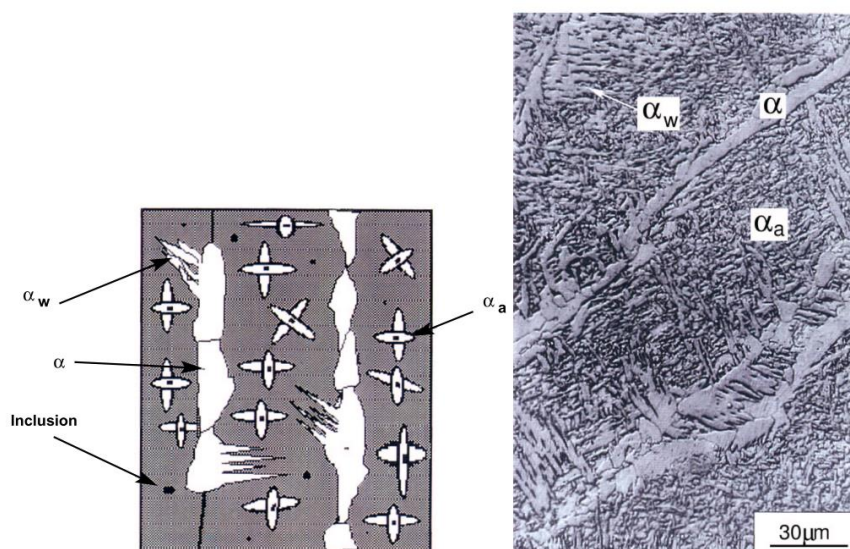


Figure 63: (a) illustration of the morphology of allotriomorphic (α), acicular (α_a), and Widmanstätten ferrite (α_w) (BHADESHIA & SVENSSON, 1993); (b) Scanning micrograph of a weld microstructure (WANG, MA, & LI, 2011).

Allotriomorphic ferrite (α) is the first phase to form during cooling from the austenite phase field and its volume fraction depends mainly on the thickening rate of ferrite allotriomorphs and on the austenite grain size (BHADESHIA, SVENSSON, & GRETOFT, 1985; LEVINE & HILL, 1977). It nucleates at the austenite grain boundaries and grows by a diffusional mechanism. The thickness of the ferrite varies with the square root of time, because the distance over which carbon has to diffuse increases with time. As the temperature decreases, diffusion becomes sluggish and displacive

transformation is kinetically favoured. At relatively low under-cooling, plates of α_w (side-plate ferrite) forms by a displacive mechanism. At further undercooling, bainite may nucleate by the same mechanism as α_w and grows in the form of sheaves of small platelets. Acicular ferrite nucleates intragranularly at inclusions and grows (MIRZAEI et al., 2013). There are usually two kinds of α_w to be found, primary and secondary α_w (BHADESHIA et al., 1985; YANG & CHANG, 1997). Secondary Widmanstätten ferrite nucleates at the allotriomorphic ferrite/austenite boundaries and grows as sets of parallel plates separated by thin layers of austenite, the latter subsequently being retained to ambient temperature or partially transforming to martensite and/or pearlite. On the other hand, primary α_w nucleates directly from austenite grain boundaries which are not covered by allotriomorphic ferrite, although its growth mechanism is identical to that of secondary α_w . However, such difference was not possible to be identified by optical microscopy.

The presence of oxides for all samples were detected by TEM and they showed heterogeneous composition.

These oxides are well-known to promote acicular ferrite in the WM. As the liquid weld pool cools, its solubility of dissolved gases decreases. Reactions between these gases and other elements cause the formation of oxides (BHADESHIA & SVENSSON, 1993).

Lee and collaborators studied the effect of the inclusion size on the nucleation of acicular ferrite in welds. They classified the inclusion into two groups, i.e. the non-nucleant and the nucleant inclusions. The larger the inclusion size was the more ferrite laths could be nucleated (LEE et al., 2000). Mn-Ti-O complex inclusions which exist in liquid can supply a large number of effective heterogeneous nucleation cores resulting in refining crystal microstructure by disturbing the growing direction of columnar crystal (CHEN et al., 2014). However, the final microstructure in the weld metal can be quite complex and depends on a certain number of variables: steel composition, temperature range, prior austenite grain size, and particle density (DÁZ-FUENTES, IZA-MENDIA, & GUTIÉRREZ, 2003). From our TEM micrographs it was noted that some inclusions were non-nucleating sites and other were clearly nucleating sites. No correlation with the size of the oxides particles was observed.

Samples welded with higher heat input presented a decrease of acicular ferrite fraction in the WM. It was identified by comparing samples B with A and C with D. It is suggested in the literature that a reduction in austenite grain size in the WM leads to a replacement of acicular ferrite by bainite. When steels containing appropriate inclusions are welded, the amount of acicular ferrite that forms during the process increases at the expense of bainite. Eventually, at very large heat inputs, the cooling rate decreases so much that larger quantities of α_w are obtained and there is a corresponding reduction in the amount of acicular ferrite (BHADESHIA & SVENSSON, 1993).

The inclusions found in the WM have two major effects on the steel: they serve the desirable role of promoting intragranular nucleation of acicular ferrite plates, leading to a toughness improvement without loss of strength. But they are also responsible for the nucleation of voids during ductile fracture, or the nucleation of cleavage cracks during brittle fracture (BHADESHIA & SVENSSON, 1993).

Even though an apparent higher density of inclusions was found in sample B, it is difficult to assume a conclusion considering the small area studied by TEM analysis. Furthermore, the probability of nucleation is not the same along the WM. An inclusion with continuous cooling behaviour has a bigger probability of nucleating in the region with small fluid-flow velocities, i.e., near fusion/HAZ boundary (HONG et al., 2000). Figure 64 shows a TTT diagram of the formation of different types of oxides in the WM.

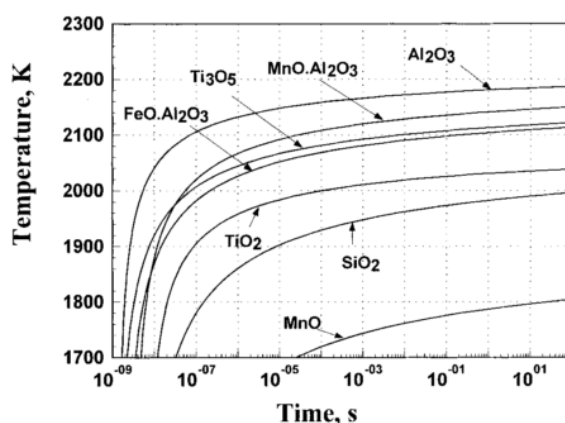


Figure 64: TTT diagram of the formation of different kind of oxide inclusion in a low alloy steels (HONG et al., 2000).

The TTT diagram shows that no oxide inclusion will form above 2200 K. On the other hand, temperatures in the weld pool often reach levels near 2500 K. At these

temperatures, oxide inclusions will dissolve. However, while cooling, the first oxide to form will be Al_2O_3 (HONG et al., 2000).

Therefore, any assumption about the density of inclusion regarding heat input is not trivial and requires further studies.

By TEM analysis, Ti- and Nb-rich nanometric precipitates were identified in the HAZ for all conditions studied in this work. These fine carbo-nitride particles have at least two strengthening effects: 1. Producing dispersion strengthening; 2. Grain refinement, inhibiting grain growth by carbonitride particles. These two effects can happen simultaneously (LAGNEBORG et al., 1999). TiN is stable up to very high temperatures, at which niobium, vanadium and/or aluminium nitrides are dissolved. For this reason, titanium additions to a weldable steel is reported to be useful in restricting grain growth (KARMAKAR et al., 2017; LAGNEBORG et al., 1999). Nb(CN) has also a strengthening effect. Nb in solution promotes the formation of acicular ferrite constituents and shifts austenite decomposition to lower temperatures (MILITZER, FAZELI, & JIA, 2014).

4.6. GRAIN SIZE AND CHEMICAL COMPOSITION MEASUREMENT

Figure 65 shows optical micrographs of the base metals LNE500 and AHSS900 after etching in picric acid solution. This procedure was adopted to reveal the prior austenite grain size.

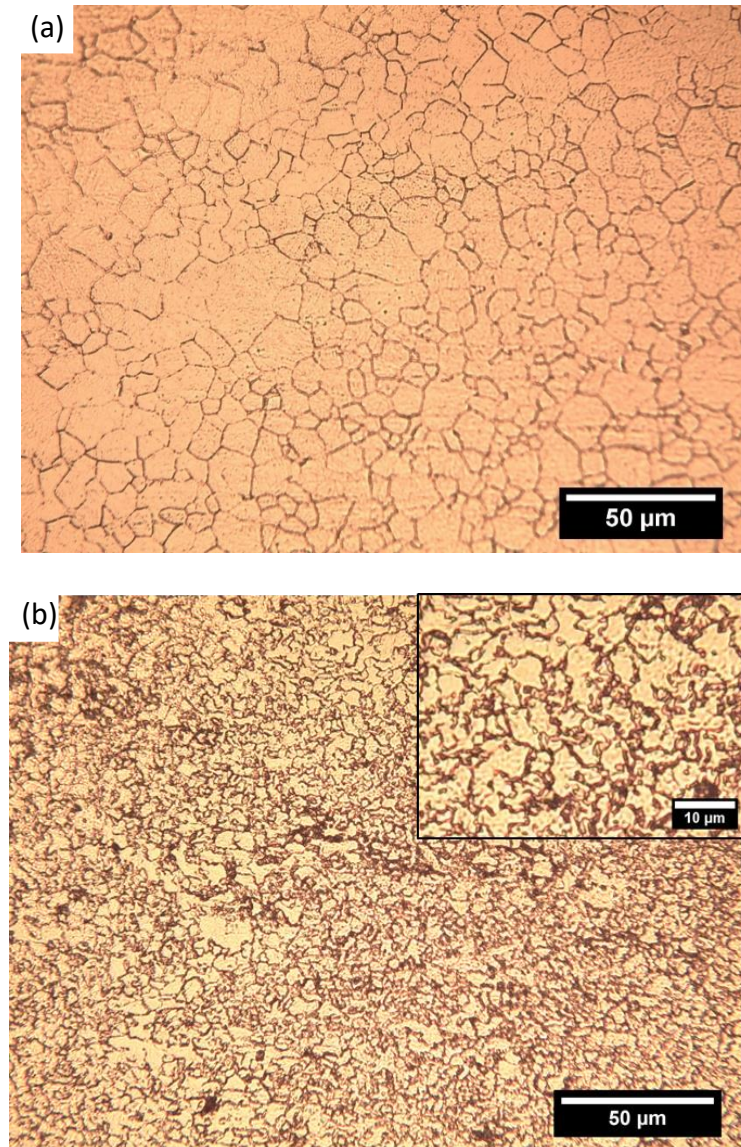


Figure 65: Optical micrographics showing prior austenite grain size of (a) LNE500 steel and (b) AHSS900 steel. Etched with picric acid solution.

Prior austenite grains are clearly observed for both samples. Using the linear intercept method, the average prior austenite grain size of LNE500 and AHSS900 steels are $8.47 \pm 1.26 \mu\text{m}$ and $4.24 \pm 0.60 \mu\text{m}$ respectively.

Figure 66 shows the microstructures of different regions of samples A and B. The main difference between both samples is the grain size in the CGHAZ (Figure 66c and 66d). Figure 66a and 66b, in turn, show that the bigger grains are situated near the fusion zone which is related with the influence of heat input.

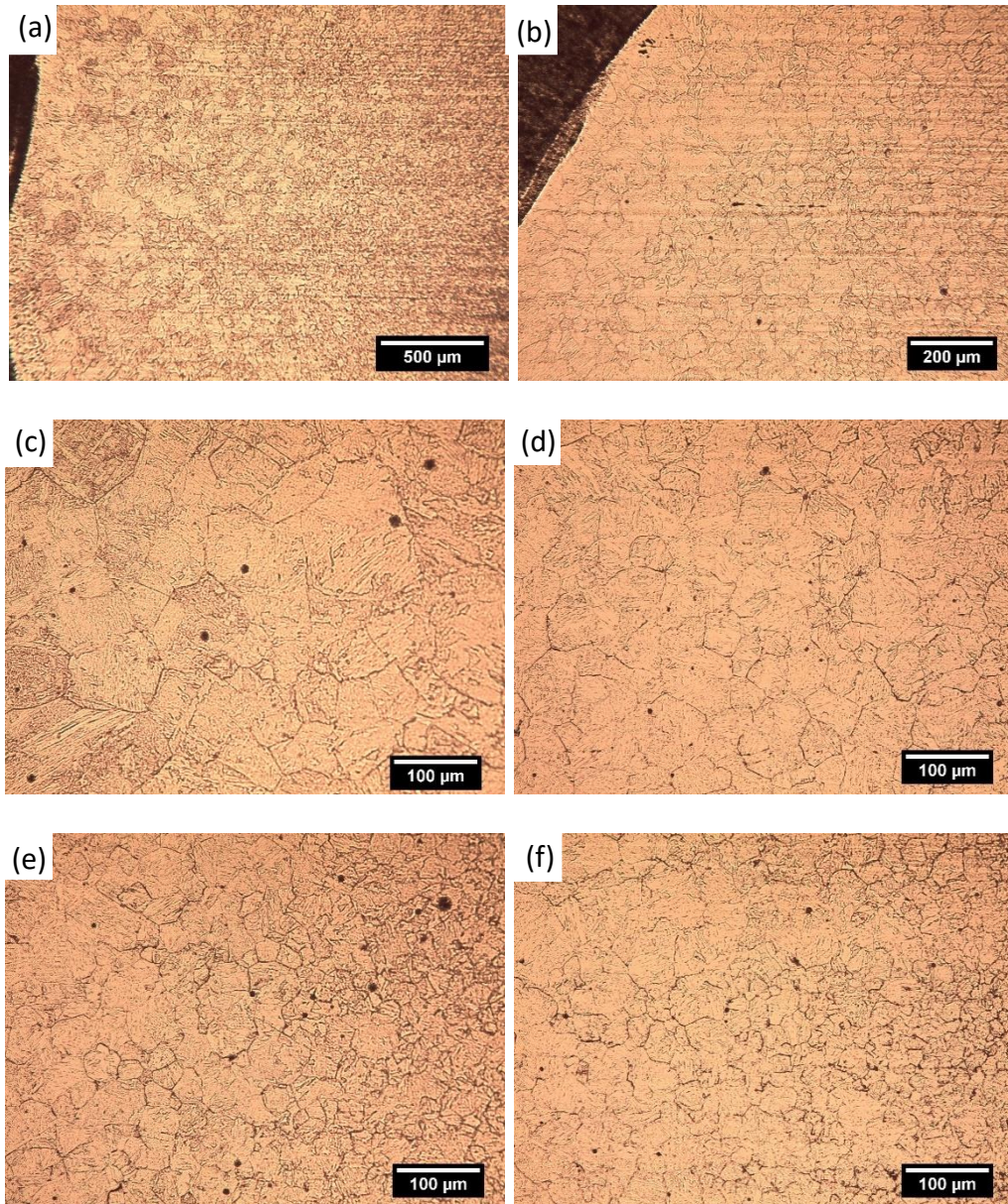


Figure 66: Optical micrographics showing prior austenite grain size sample A (a), (c), (e) and Sample B (b), (d), (f). Etched with picric acid solution. Regions presented are: (a) and (b) interface between WM and HAZ, (c) and (d) CGHAZ and (e) and (f) interface between CGHAZ and fine-grained HAZ.

The grain size decreases as the peak temperature falls monotonically with the distance from the fusion line. The sub HAZ regions after CGHAZ (Figure 66e and f) are essentially fine-grained because of a very short duration of ferrite → austenite matrix transformation processes, hindering the growth of austenite grains (FALAT et al., 2014).

The same behaviour is presented by samples C and D. Figure 67 shows the optical micrographics of different regions for these samples. The visualisation of

austenite grain on the samples C and D is not easy. Notwithstanding, it is possible to observe that sample D, welded with higher heat input, presents wider austenite grain size in CGHAZ and wider prior austenite grain on the boundary between WM and HAZ. The average grain sizes at the interface was $59\text{ }\mu\text{m}$ and $172\text{ }\mu\text{m}$ for samples C and D, respectively.

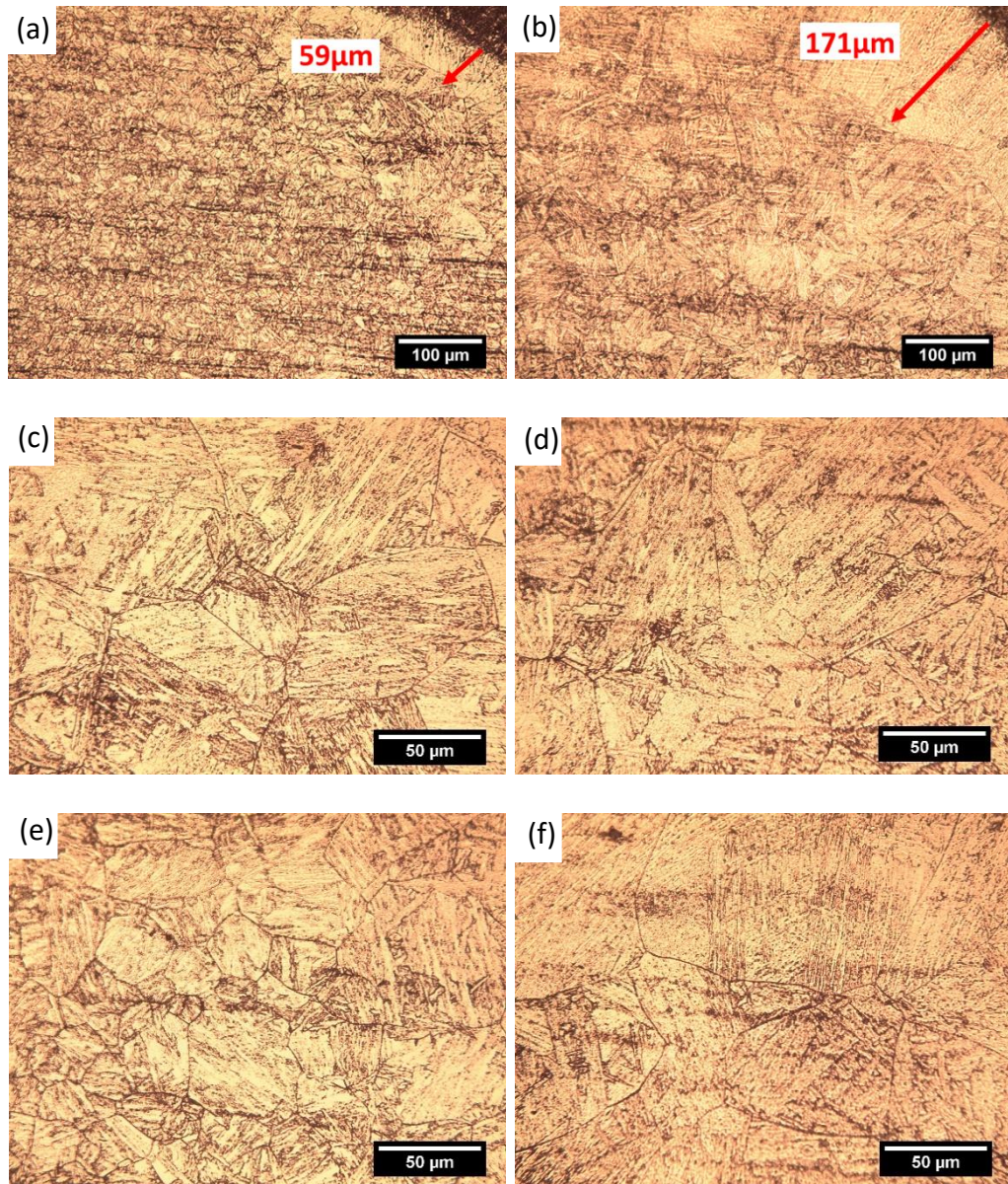


Figure 67: Optical micrographics showing prior austenite grain size sample C (a), (c), (e) and Sample D (b), (d), (f). Etched with picric acid solution. Regions presented are: (a) and (b) interface between WM and HAZ, (c), (d), CGHAZ and (e) and (f) region a bit further from CGHAZ.

The HAZ immediately adjacent to the fusion boundary is heated up to very high temperatures and hence transform completely to austenite. During continuous heating, the peak temperature in the HAZ next to the fusion boundary exceeded the

temperature at which the sample becomes fully austenitic. Consequently, the austenite that forms is annealed during heating, giving rise to a very coarse grain structure (BHADESHIA & HONEYCOMBE, 2017).

The average austenite grain size in the HAZ for all samples and also for the base metals are shown in Figure 68. The results point that a lower heat input yields a more refined microstructure than higher heat input. After experiencing different heating cycles, C and B presented similar prior austenite grain size. It is worthy to pay attention to the fact that samples from LNE500 have different thickness compared with samples from AHSS900 (plate thickness for LNE500 is 6 mm while for AHSS900 thickness is 4 mm). Thus, the nominal heat input may be equal, but the heat cycle experienced by each steel is not the same.

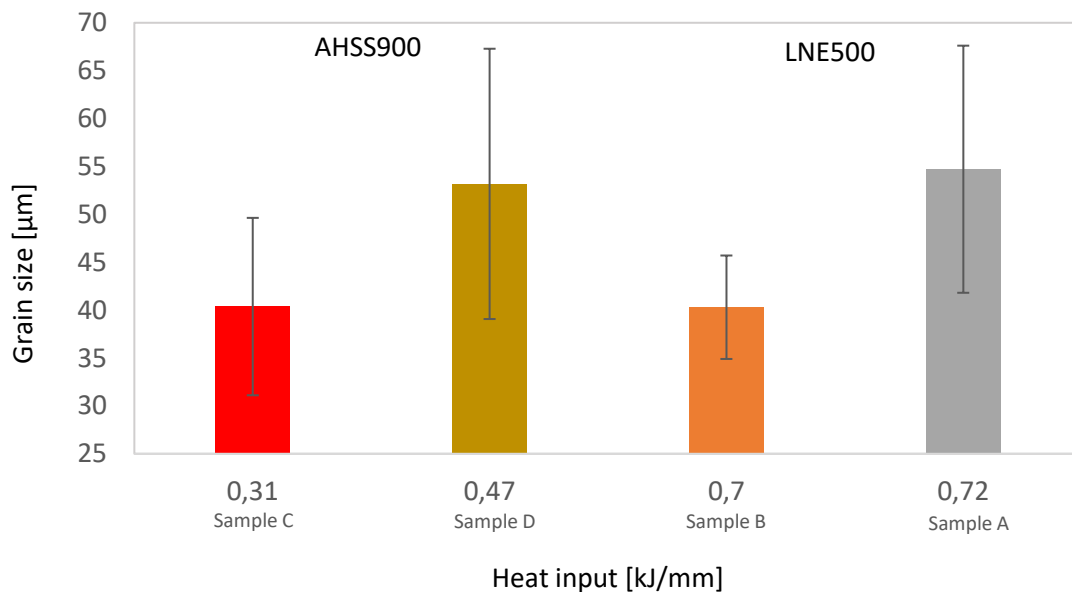
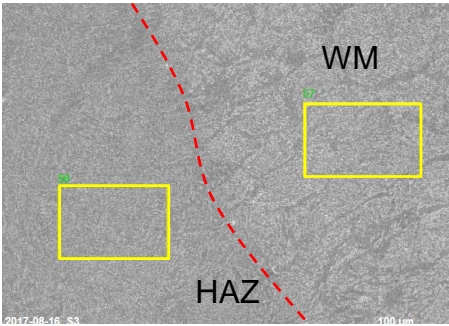


Figure 68: Prior austenite grain size in the CGHAZ versus heat input of the samples A-D.

Finally, chemical composition was studied in order to analyse the difference between WM and HAZ. Table 22 and Table 23 show the mass distribution of elements in the HAZ and WM as obtained by EDS analysis. As expected, it can be observed that the elemental distribution is not homogeneous.

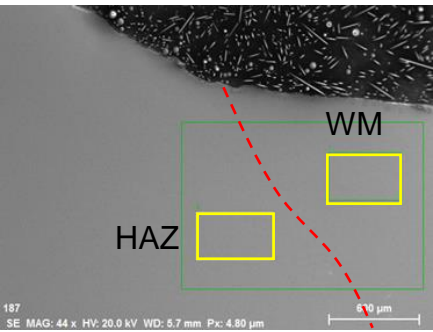
Table 22: Chemical composition at HAZ and WM or LNE500 welded joints



The micrograph shows a cross-section of a welded joint. A dashed red line separates the Heat Affected Zone (HAZ) on the left from the Weld Metal (WM) on the right. Two yellow rectangular boxes are placed in each region, labeled '5' (in HAZ) and '6' (in WM), indicating the locations for chemical composition analysis. The scale bar at the bottom right indicates 400 μm.

Element	wt%			
	Sample A		Sample B	
	500-P-0.72		500-CMT-0.70	
	HAZ	WM	HAZ	WM
Mn	1.39	1.29	1.30	1.39
Cr	0.02	0.02	0.01	0.02
Fe	95.50	95.06	94.84	94.63
Mo	-	-	-	-
C	2.88	3.12	3.51	3.59
Cu	0.03	0.09	0.06	0.02
Si	0.02	0.31	0.04	0.35
Nb	0.07	-	0.09	-

Table 23: Chemical composition at HAZ and WM for AHSS900 welded joint



The micrograph shows a cross-section of an AHSS900 welded joint. A dashed red line separates the Heat Affected Zone (HAZ) on the left from the Weld Metal (WM) on the right. Two yellow rectangular boxes are placed in each region, indicating the locations for chemical composition analysis. The scale bar at the bottom right indicates 60 μm. Technical data at the bottom left: 187 SE MAG: 44 x HV: 20.0 kV WD: 5.7 mm Px: 4.80 μm.

Element	wt%			
	Sample C		Sample D	
	900-CMT-0.31		900-CMT-0.47	
	HAZ	WM	HAZ	WM
Mn	1.43	1.56	1.51	1.56
Cr	0.24	0.12	0.22	0.07
Fe	93.17	93.19	94.31	94.25
Mo	0.23	0.07	0.22	-
C	4.51	4.58	3.62	3.64
Cu	-	0.02	-	0.08
Si	0.18	0.35	0.11	0.38

From Table 22, it can be observed that only silicon and niobium have a significant content differences when the HAZ and WM are compared for sample A and B. Si content is higher in the WM than in the HAZ for both samples and Nb was only found in the HAZ and not in the WM. The other elements such as Cr, Cu, Mn showed similar contents in both regions.

From Table 23, Mn was found in identical amounts in the WM (1.56 wt%) for samples C and D. The chromium content, in turn, was significantly higher in the HAZ than in the WM for both samples. In the HAZ its percentage was 0.24 wt% and 0.22 wt% for samples C and D, respectively, whereas in the WM it was 0.12 wt% for sample C and 0.07 wt% for sample D. A similar result was found for Mo. Its amount in the HAZ was approximately 0.22 wt% for both samples. In the WM, though, it was 0.07 wt% for sample C whereas it was not detected for sample D. Cu was detected in small percentages only in the WM. The silicon content was higher in the WM than in the HAZ for samples C and D.

In general, element concentrations have not varied much between HAZ and WM for samples A and B. Only silicon and niobium contents showed significant differences. Besides, a more severe chemical difference was detected at the welded joints for samples C and D, whose HAZ was richer in Cr and Mo. Likewise samples A and B, the weld metal of samples C and D presented higher Si content than at the HAZ. Therefore, the results indicated that the welded joints C and D showed a more heterogeneous chemical composition. This heterogeneity is more related to the chemical composition of the base material (AHSS900) and filler material than to the heat input. AHSS900 has higher contents of Mo and Cr than the filler material. The filler material, in turn, presents higher Si content. Hence, Si has a significant bearing on the amount of oxygen available to form titanium oxide. It is reported that in wrought steels an increase in the silicon concentration in the molten steel leads to a decrease in the available oxygen concentration and, consequently, promotes the formation of titanium nitrides at the expense of titanium oxides (LEE & PAN, 1993).

4.7. INFLUENCE OF HEAT INPUT ON THE MICROSTRUCTURE

The microstructure of the welded joint showed is affected by the heat input. As expected, austenite grain size of the coarse-grained HAZ increases with higher heat input (higher peak temperature at HAZs). The austenite grain size increases with peak temperature because the mobility of solute atoms, for the austenite grain growth at high temperature, is higher than that at low temperature (GHARIBSHAHIAN et al., 2011). Higher temperature also leads to lower pinning force, thus promoting grain growth. At the fusion zone a large austenite grain size was measured for sample D. Austenite grain size has grown near the fusion line because this zone is the longest over which the temperature for complete austenitizing occurs. Besides, it is known that if the actual heat input is higher, there is an increase in the solidification time and a reduction in the cooling time (QUINTINO et al., 2013). Both characteristics increase the grain size.

In the present work a correlation between austenite grain size and heat input was observed. A difference of heat input of 0.16 kJ/mm in the AHSS900 showed great influence on grain size. Moreover, even though the nominal heat input for sample A = 0.72 kJ/mm was similar to sample B = 0.70 kJ/mm, great changes on the grain sizes were also detected. This great difference between samples A and B is associated with the welding transfer mode. For sample A, it was pulsed transfer whereas for sample B, it was CMT. The sample welded by CMT welding transfer showed finer microstructure, mainly in the CGHAZ, compared with the sample welded with similar heat input by pulsed transfer. Clearly these two different transfer modes do not have the same efficiency as reported by some works. The efficiency value is reported as 85% (PÉPE et al., 2011).

There was found a correlation between heat input and TiN particle size in the HAZ. Samples welded with higher heat input showed larger TiN particles. This behaviour happened with welded joints from LNE500 (Samples A and B) and from AHSS900 (Samples C and D).

TiN has a large stability at high temperatures. Thus, large TiN precipitates do not dissolve during the heating stage of the welding process. Lagneborg and collaborators found that for larger cooling rates, ingots produced a finer precipitation of

TiN and for slower cooling rate coarser TiN was produced (LAGNEBORG et al., 1999). In our study, samples welded with higher heat input suffer slower cooling rate and larger TiN precipitates were found in agreement with the literature. The same tendency was observed by Moon et al. (MOON, LEE, & LEE, 2007).

TiN precipitates limit austenite grain growth in the HAZ and, thereby, limit excessive increases in hardenability or substantial decreases in HAZ strength and toughness (SAMPATH, 2006). However, coarse precipitates are not desired regarding mechanical properties. The TiN precipitates bigger than 1 μm are the most potent crack-forming. Particles coarsen and become large enough to crack, thus providing crack nuclei which may then propagate into the matrix (ECHEVERRÍA & RODRIGUEZ-IBABE, 2003). In a more recent report, large Ti-rich particles at the HAZ, even after the welding thermal cycle, were considered as potential toughness-reducing agents (ZHANG & KANNENGIESSER, 2014). Hence, large TiN particle are not effective in limiting the austenite grain growth.

Regarding NbC particles, certain fraction of them, especially those with a smaller size, is completely dissolved during the heating stage of the welding cycle. The amount of dissolved Nb goes into solution and can precipitate at lower temperatures, restraining the austenite grain growth (DI SCHINO & DI NUNZIO, 2017).

TiN and TiC are typically reported as having square-shaped and spherical morphology, respectively, which agrees with our results. For a low carbon steel with similar chemical composition to the one studied in this thesis (0.054 wt%Ti – 0.045 wt%C), the Ti possible precipitates are M_3C , $\text{Ti}(\text{C},\text{N})$ and $\text{Ti}_4\text{C}_2\text{S}_2$ (Zhou, Kang, & Mao, 2008).

It has been reported that Ti-rich (C,N) precipitates act as nucleation sites for intragranular ferrite. During the heating cycle of the welding process, the core of precipitates consisted of undissolved Ti-rich (C,N) and there is a critical size at which nucleation occurs (SHI et al., 2016).

The precipitation temperature for TiN particles is above 1500°C and that for TiC is between 1150°C and 800°C. During fusion welding, these precipitates limit austenite grain growth in the HAZ (SOTO et al., 1999).

Interestingly, iron carbides found in samples C and D were oriented and uniformly dispersed in the HAZ. With increased heat input their sizes increased and original orientation was not altered. A type of iron carbide that is typically oriented is epsilon (ϵ)-carbide. It tends to adopt a single crystallographic variant in a given plate of lower bainite. ϵ -carbides have their longest axes inclined at about 60° to the growth direction of the ferrite platelets. They transform to cementite on holding at the isothermal transformation temperature. The orientation of the carbides in the HAZ is due to the transformation of ϵ -carbides firstly, and subsequently, into cementite (not losing the orientation). For plain carbon steels, at higher temperatures epsilon carbide formation should become more favourable. However, precipitation of ϵ -carbides is reported to be possible only for steels with carbon content exceeding about 0.55 wt%, For low C content steels, the partitioning of carbon into the austenite depletes the bainitic ferrite too rapidly to permit ϵ -carbide (HSU (ZUYAO XU) & JIN, 2011; KALISH & ROBERTS, 1971). It was reported the presence of (ϵ)-carbides in the HAZ region for a dual-phase and TRIP steels (both steel grades contained around 0.1 to 0.2 wt% carbon and they are microalloyed) after baking that is a heat treatment typically at temperatures in the vicinity of 150°C , during a range from 20 to 30 min (TUMULURU, 2010).

4.8. CONCLUSIONS

It was found that the LNE500 base metal microstructure consists of equiaxed ferrite grains and fine perlite, while AHSS900 microstructure was comprised of tempered martensite.

The microstructure of CGHAZ consisted of lath martensite and granular bainite to samples C and D whereas it was comprised of granular bainite for samples A and B. The WM microstructure was predominantly acicular ferrite with small volume fraction of allotriomorphic ferrite and Widmanstätten ferrite on samples A and B, but no presence of Widmanstätten and lower fraction of allotriomorphic on samples C and D.

Ti- and Nb-rich nanometric precipitates were identified in the HAZ, but also large TiN precipitates were found. The size of the latter was influenced by the heat input. Samples welded with higher heat input showed larger TiN particles in the HAZ.

Oriented and uniformly dispersed iron carbides were also detected in the HAZ of sample C and D. With increased heat input these iron carbides size was increased.

The WM microstructure consisted of mainly acicular ferrite and fine bainite with Al-Si-Mn-Ti oxide inclusions. The acicular ferrite nucleation was seen to originate from some of these inclusions.

There was no obvious effect of heat input on the microstructure of the other sub regions of HAZ.

Austenite grain size was greatly influenced by the heat input mainly at the coarse-grained HAZ. Its size increased with higher heat input. A greater CGHAZ was observed on samples C and D. The width of the grain size in the fusion line was 59 μm for a heat input of 0.31 kJ/mm (sample C) and 171 μm for a heat input of 0.47 kJ/mm (sample D).

Finally, as expected there is chemical difference between HAZ and WM. Silicon content was higher in the WM than in the HAZ for all samples studied. HAZ of samples C and D was richer in Cr than the WM. However, most of this chemical difference between base metals and filler material was related to their chemical composition more than heat input influence.

Chapter 5

5. MECHANICAL PROPERTIES

5.1. MICROHARDNESS

Vickers microhardness measurements for welded samples A and B are illustrated in Figure 69. The hardness measurement started on the BM (X-axis = 0 mm). Other regions of the welded joints (HAZ and WM) are shown in this figure. The dashed line represents the average hardness of the BM = 240 HV.

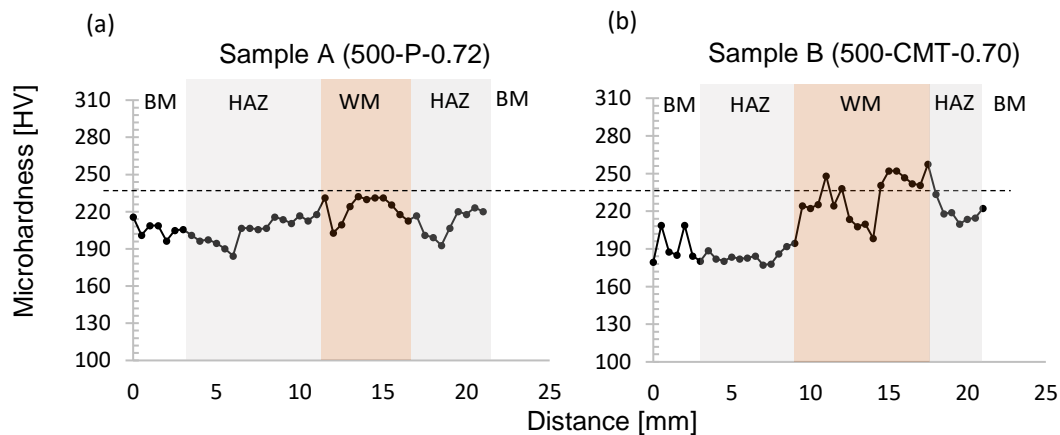


Figure 69: Cross-weld hardness distribution of sample A (a) and sample B (b). Dashed line represents the average hardness value of the LNE500 BM.

Indentations cover some of the BM, HAZ and WM on both sides of the welded joint. The microhardness values of WM for both samples overlap those of the HAZ. However, hardness values for sample B are higher at the WM and there is a drop in the middle of the WM. In general, the scatter seen in the hardness profile reflects the

heterogeneity of the microstructure. Therefore, for the welded joints of samples A and B, the hardness values are slightly higher in WM and are similar for HAZ and BM. No significant effect of heat input on hardness is evident on the profiles of samples A and B.

Microhardness values for the welded joints of samples C and D are shown in Figure 70. The dashed line represents the average hardness of the AHSS900 BM = 340 HV.

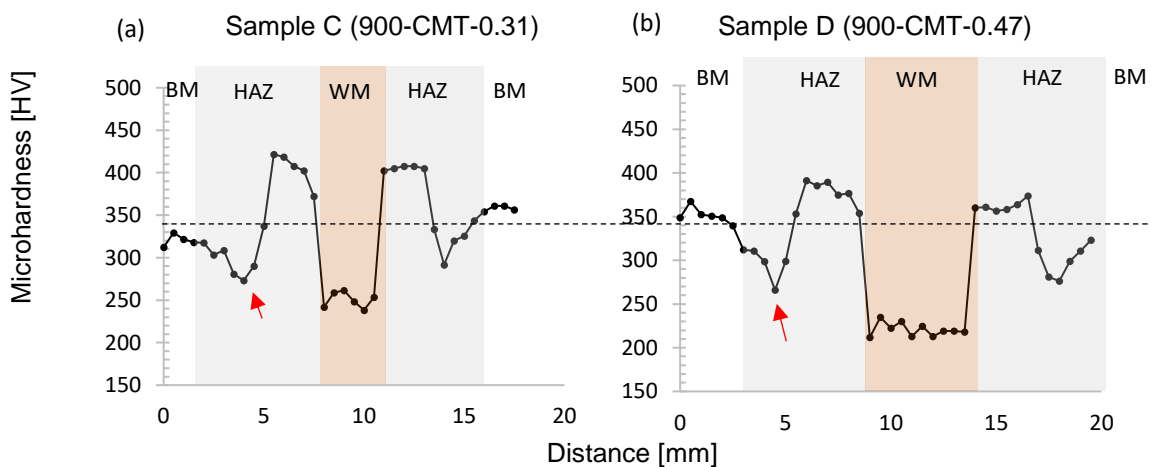


Figure 70: Cross-weld hardness distribution of sample C (a) and sample D (b). Dashed line represents the average hardness value of the AHSS900 BM.

The highest microhardness values of approximately 400 HV were achieved in HAZ and the lowest values, around 250 HV, in the WM. In this respect, these results indicate that samples C and D exhibited hardening in the coarse-grained HAZ. The HAZ microstructure, lath martensite and fine-grained bainite, explains the reason for the higher hardness in this region. At the fine-grained HAZ and partially transformed HAZ there is a decrease of hardness values, forming a softening zone (indicated by the arrow).

There is an evident influence of the heat input on the hardness values as shown in Figure 71. By increasing the heat input, in general, a marked hardness decrease was observed for all samples. This behaviour can be seen for HAZ and WM of samples C and D, and for WM of samples A and B.

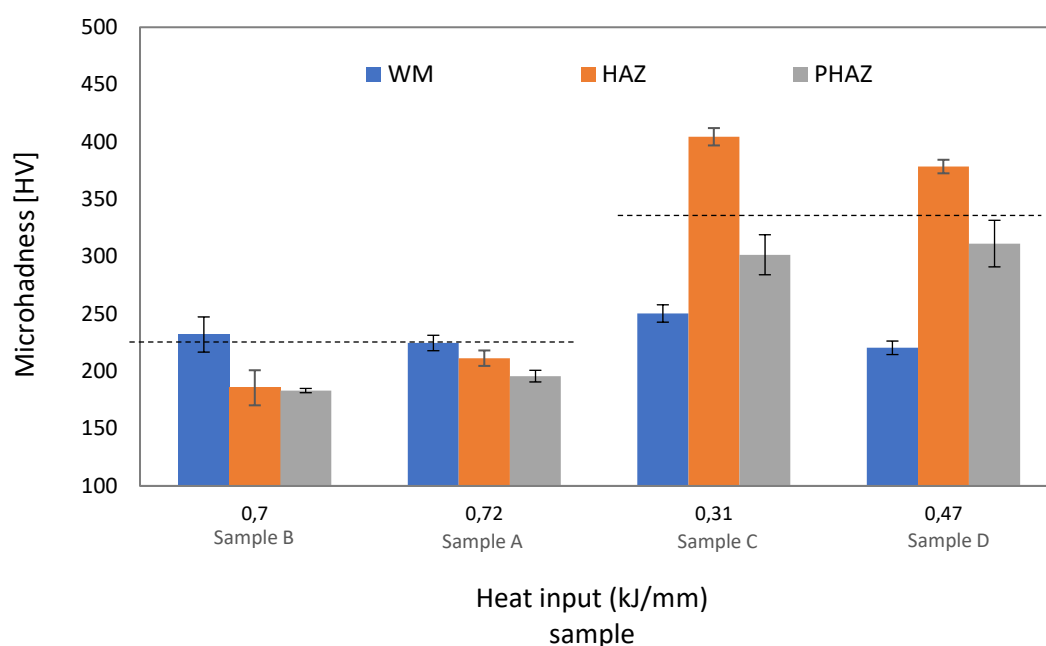


Figure 71: Microhardness versus heat input of the samples A-D in WM, HAZ and PHAZ (Partially transformed HAZ). Dashed lines represent the average hardness value of the base metal AHSS900 (Samples C and D) and LNE500 (Samples A and B).

Regarding samples from the LNE500 BM, the hardness values showed only small variations. HAZ and PHAZ for sample B (lower heat input) showed slightly lower hardness values compared with the same regions for sample A.

Hardness values for samples C and D, in turn, showed high values. By increasing the heat input from 0.31 to 0.47 kJ/mm (reduction of the cooling rate), the HAZ average hardness HAZ decreased from 420 to 375 HV and in the WM from 250 to 225 HV and PHAZ hardness values increased by increasing the heat input.

It is observed that samples A and B (LNE500 BM) showed a more homogeneous microhardness profile and an average low hardness, whereas a clear hardness variation was observed along the welded joint for samples C and D. This effect arises from the compositional and microstructural heterogeneities across the welded joint.

The welded joints of the AHSS900 BM presented higher hardness when compared to the LNE500 BM. This can be associated with their different microstructures. Atta-Agyemang et al. studied the difference between conventional steel and a TMCP steel. They observed that the HAZ of a QT welded steel joint had higher hardness in the coarse-grained heat-affected zone (CGHAZ), reaching 290-317 HV, than a TMCP steel welded joint, which has 230-240 HV. The higher

hardness of the conventional steel is a result of the increased carbon content in the base metal. The lower hardness of the TMCP steel HAZ relative to the base metal was due to the low level of alloying elements and the low carbon content. The lowest hardness in the HAZ of both steels corresponds to the partially transformed HAZ (PHAZ) (ATTA-AGYEMANG et al., 2017). In our study, both steels have low carbon contents and the higher hardness of the AHSS900 relative to the LNE500 is due its higher level of alloying elements and its harder microstructure (tempered martensite).

HAZs from samples C and D were visible to either side of the fusion zone, being harder than either the weld metal or the surrounding base metal. These high hardness values evidence the presence of hard lath martensite packets with high dislocation density.

On the other hand, WM was the region which showed the highest hardness for samples A and B. The low hardness values in the HAZ for these samples when compared to the HAZ of samples C and D can be ascribed to the absence of hard martensite which was confirmed in chapter 4 (Figure 39, Figure 40. Figure 50 and Figure 51).

Regarding the WM hardness, sample C presented the highest value. Its microstructure was characterised by a lower amount of allotriomorphic ferrite and showed no presence of Widmanstätten ferrite, being acicular ferrite the predominant phase. Therefore, acicular ferrite was responsible for the higher hardness values. Acicular ferrite is reported to be the most desirable phase in the weld metal. Its platelets nucleate intragranularly at point sites which consequently avoids the formation of parallel plates. This non-organised microstructure has better mechanical properties and hence, greater resistance to crack propagation (BHADESHIA, 1998).

The softening region in the HAZ of samples C and D corresponds to the fine-grained part of the heat-affected zone (FGHAZ) and partially transformed HAZ. It is known that hardness changes occur due to recovery, coarsening of carbide particles and recrystallisation (BHADESHIA, STRANG, & GOOCH, 1998). The softening happens due to decomposition of martensite to soft products due to over tempering (MOHANDAS, REDDY, & KUMAR, 1999). The fine-grained HAZ is exposed to temperatures typically between 1300 and 910 °C. Figure 72 shows schematically the formation of FGHAZ for a quenched and tempered steel (the case of AHSS900).

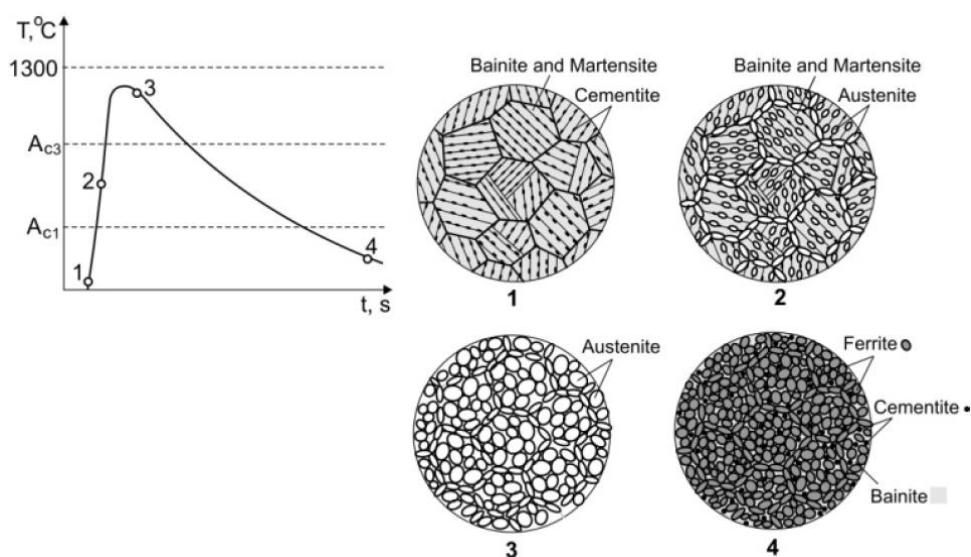


Figure 72: Scheme of FGHAZ for a quenched and tempered steel (PIRINEN, 2013).

During heating ferrite \rightarrow austenite transformation starts; however, austenite does not have time to properly develop, and the grain size remains small. Hence, carbides and nitrides may not be fully dissolved, and the austenite grains nucleate heterogeneously at the boundaries of the prior austenite grains and grow along them (2). At the same time, the nucleation of austenite grains occurs due to cementite dissolution (2). During cooling, austenite \rightarrow ferrite transformation occurs. The large grain boundary area (from the small grains of austenite) tends to promote nucleation of fine ferrite grains (4).

The partially transformed zone reaches temperatures up to 600 °C and does not become fully austenitic. However, the ferrite grain and iron carbides grow.

Therefore, this fine and soft microstructure of FGHAZ and PHAZ is responsible for the softening zone in samples C and D. In general, the extent and degree of softening have been observed to be maximum in GTAW (gas tungsten arc welding) and GMAW (gas metal arc welding), due to their high heat inputs (MOHANDAS et al., 1999). When high-strength low-alloy steels are welded they are prone to softening in the heat-affected zone (HAZ) due to grain growth. As a consequence, mechanical properties decrease (MOHANDAS et al., 1999). Low heat input maintains the fine grain structure, minimising softening, and as an extra benefit, it decreases welding induced distortion which can have a detrimental effect on the construction of final products (CAO et al., 2011; LAGNEBORG et al., 1999).

The highest hardness in the HAZ of samples C and D corresponds to the coarse-grained part of the heat-affected zone (CGHAZ). The evolution of the microstructure is shown in Figure 73.

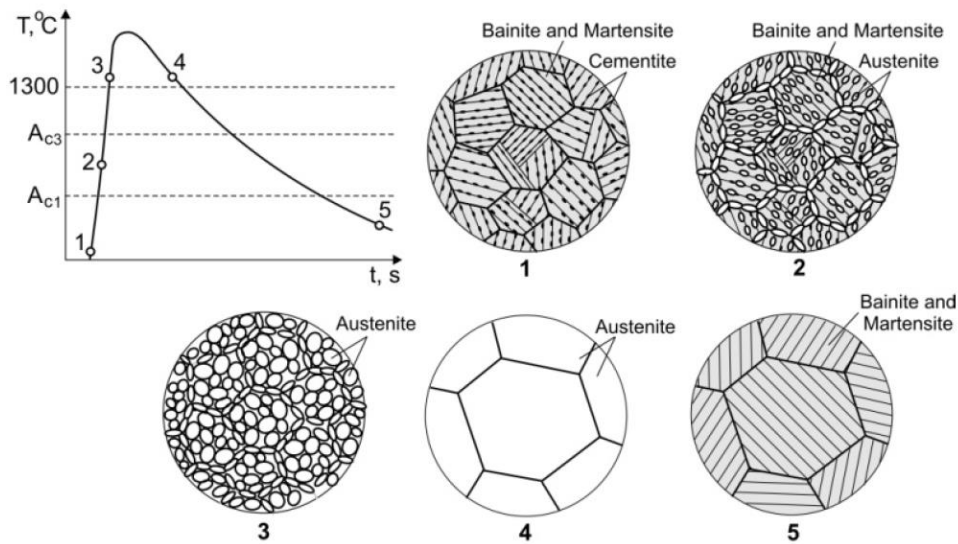


Figure 73: Scheme of CGHAZ for a quenched and tempered steel (PIRINEN, 2013).

From the microstructural analysis carried out in chapter 4, CGHAZ for both samples consisted of lath martensite and fine-grained bainite with large fraction of iron carbides, TiN (with different sizes) and Ti,Nb(C,N) nanoparticles. The presence of hard phase martensite is main reason for the CGHAZ high hardness. Similar results are reported by other authors (MIRZAEI et al., 2013). In fact, according to Yurioka, cited by Loureiro, the maximum hardness of the HAZ should be 444 HV10, if the structure was totally martensitic, and 223 HV10, in the case of non-martensitic structure (LOUREIRO, 2002).

It is well-known that grain size distribution plays an important role in the mechanical properties of welded steels. In Chapter 4, it was showed that austenite grain growth was promoted by increasing heat input. The CGHAZ of sample D presented larger grains than sample C, due to its higher heat input. Hence, sample D hardness was approximately 50 HV lower than that of sample C at the CGHAZ. Moreover, lower heat inputs which have higher cooling rate, lead to the formation of martensitic structure, resulting in higher hardness (MIRZAEI et al., 2013).

It has been reported that any increase in the heat input has an inverse effect on the hardness of welded metal and its HAZ, which is in agreement with our results (GHARIBSHAHYAN et al., 2011).

It is worth noting that the HAZ softening, found on samples C and D is a characteristic from the BM due to thermal cycle to which it is subjected during the welding process. Even if the filler material were replaced by other type of filler metal, this feature would not change. The softened HAZ zone is expected in most TMCP steels, but the variation in hardness values depend on detailed chemistry and steel processing route and the softened zone width will depend on the welding process and procedure (PISARSKI & DOLBY, 2003).

5.2. TENSILE TESTS

Tensile tests were carried out for the as-received base metals and for samples A, B, C and D. The stress-strain curves are shown Figure 74. The constitutive parameters are listed in Table 24.

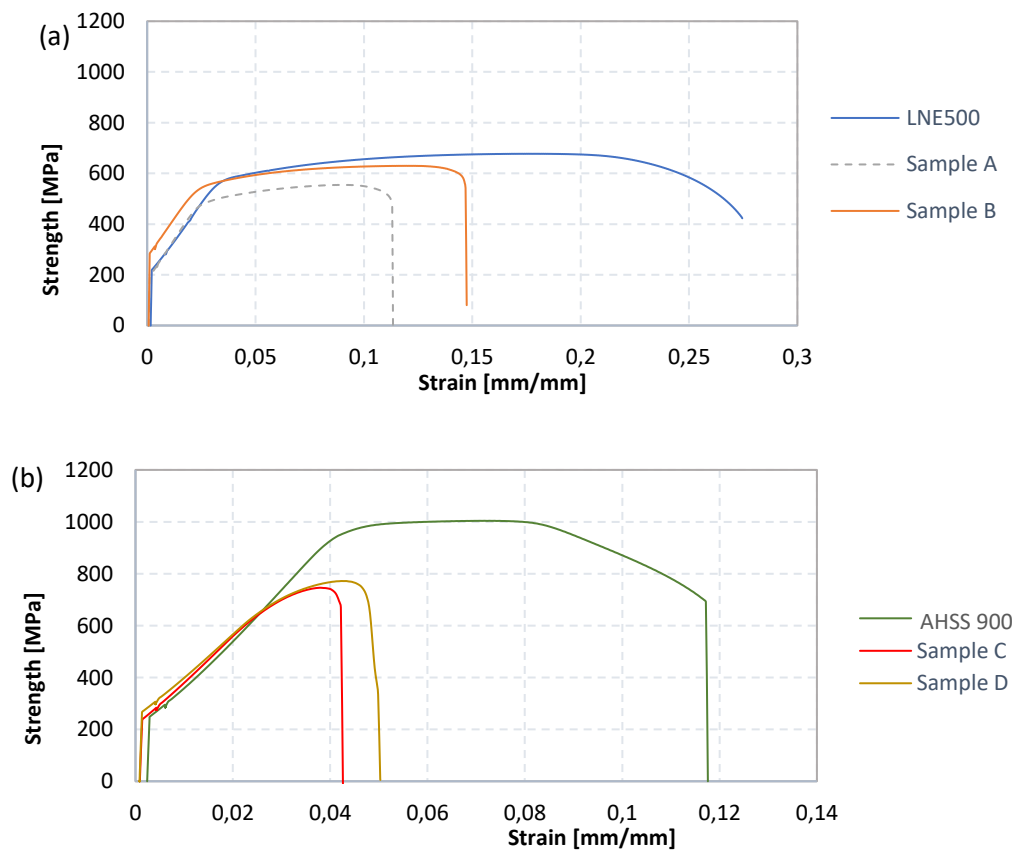


Figure 74: Strength vs. strain profiles of tension tests (a) base metal LNE500 and its welded specimens and (b) base metal AHSS900 and its welded specimens.

Table 24: Mechanical properties of the base metal and welded joints

	Tensile strength (MPa)	Yield strength $\sigma_{y0.2}$ (MPa)	Joint efficiency (%)
LNE 500 BM	677 \pm 22	225 \pm 12	-
Sample A_500-P-0.72	593 \pm 26	225 \pm 46	87.7
Sample B_500-CMT-0.70	597 \pm 52	323 \pm 21	88.2
AHSS900 BM	1018 \pm 20	900 \pm 15	-
Sample C_900-CMT-0.31	732 \pm 42	248 \pm 15	71.9
Sample D_900-CMT-0.47	784 \pm 26	280 \pm 33	77.0

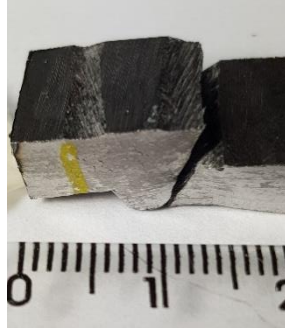
All welded joints showed lower tensile strengths compared to the base metals. The region where fracture happened is shown in Figure 75 for all samples.

Clearly the weakest zone of the welded joints C and D is the weld zone. All welded samples of the AHSS900 BM failed through the weld (Figure 75 e, f, g and h). Despite this fact, the strength of the welded joint D was slightly higher than that of the welded joint C.

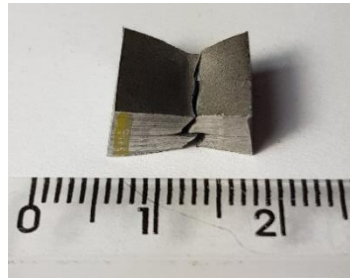
For samples A and B, some failures (50% of them), did happen in the BM as shown in Figure 75b and d. Under these circumstances, the tensile strength was around 630 MPa and yield strength was 360 MPa. Another fact is that for some specimens the failure started from the fusion line between weld and HAZ as shown in Figure 75a. When this happened the break direction was towards the weld at a traditional 45° angle which is the maximum shear-stress plane (CHENG et al., 2008). No failure happened through the weld metal for samples A and B, indicating that this region is not the weakest for the welded joints from the LNE500 steel.

Sample A (500-P-0.72)

(a)



(b)

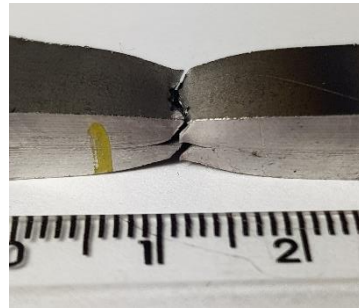


Sample B (500-CMT-0.70)

(c)

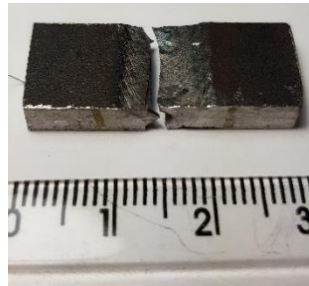


(d)

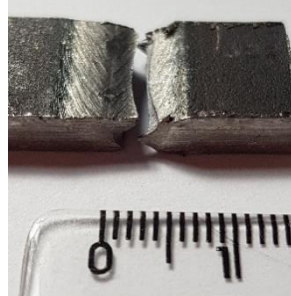


Sample C (900-CMT-0.31)

(e)

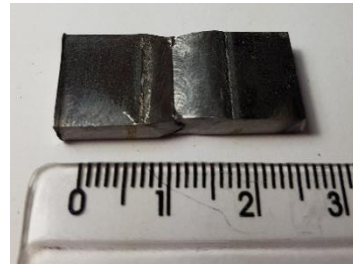


(f)



Sample D (900-CMT-0.47)

(g)



(h)

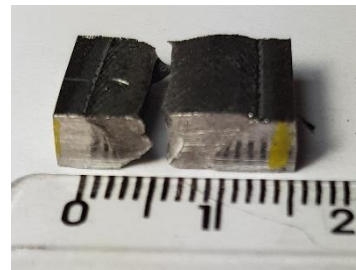


Figure 75: Photograph demonstrating where the failure occurred for sample A (a-b), sample B (c-d), sample C (e-f) and sample D (g-h). Most of the failures happened in the welded joint excepted for (b) and (d).

In order to evaluate the influence of the heat input on the mechanical properties of the different samples the graphical representation in Figure 76 was plotted.

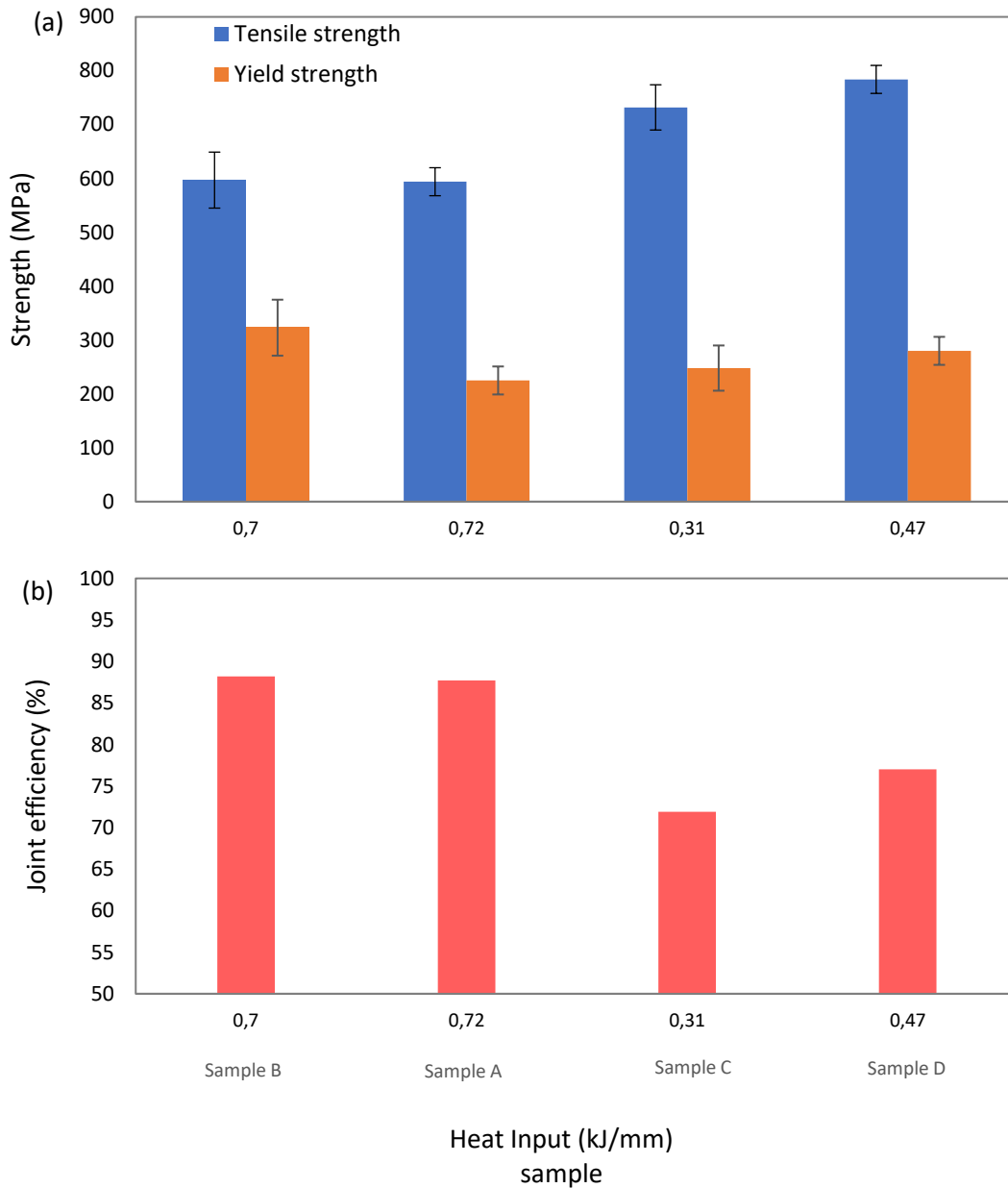


Figure 76: Influence of heat input versus (a) strength and (b) joint efficiency.

Joint efficiency slightly increased with the heat input, as well as the tensile strength and yield strength. The only exception was for sample A whose yield strength decrease compared to sample B.

Tensile tests showed a key feature: weak behaviour of the weld metal. All specimens from AHSS900 showed failure through the weld metal and low tensile and yield strength. This result is due to the undermatching in strength levels between BM

and filler material. By applying the tensile stress, the soft weld metal began to deform before the base metal. For the LNE500 welded joints, failure happened in different parts, including the fusion zone and BM. In the cases where failure started from the fusion zone, the low yield strength of filler material and also possible deformation in the weld bead can be responsible for this event.

For all welded specimens, a decreased plastic deformation was observed relative to the base metal. Sample A showed lower yield strength than sample B. This can be associated with the grain size in the CGHAZ. Recrystallisation in the CGHAZ is known to result in a decrease in the yield strength in many cases, mainly due to a reduction in grain boundary hardening as larger grains are formed. However, this behaviour did not happen for samples C and D. Sample D (higher heat input) showed higher mechanical properties, indicating that for AHSS900, higher heat input increased the mechanical properties. The mismatching between BM and filler material regarding mechanical properties influenced this result. The filler material clearly was the weakest part.

Sample D presented the highest tensile strength values. However, the highest yield strength was achieved by sample B (LNE500). The highest yield strength is correlated to the better match between LNE500 and filler material mechanical properties, whereas the highest tensile strength is more related to the BM properties.

From our results, it is clear that the weld joint is the weakest part of the specimen. The fracture in the welded joint depends on the mismatch in strength between the weld deposit and the parent plate. The worst-case fracture toughness of softened HAZs occurred when the HAZ undermatched in strength both the weld deposit and parent metal. Higher toughness is measured when either the weld metal or the parent steel undermatched the HAZ in strength (PISARSKI & DOLBY, 2003).

It is reported that the lower the weld strength mismatching, the higher the fracture toughness of the HAZ (UMEKUNI & MASUBUCHI, 1997).

Therefore, in the case of AHSS900 BM, a harder filler material may be needed to ensure the same rupture life as the base metal which is also claimed in the literature (BHADESHIA et al., 1998).

Precipitates also affect the mechanical properties of the welded joint. Coarse TiN particles were found on the AHSS900 BM and in the HAZ for all conditions (samples A, B, C and D). Precipitates with sizes ranging from 100 to 300 nm inhibit austenite grain growth at high temperatures through particle pinning whereas smaller precipitates in the range of 50 nm retard or prevent recrystallization of the deformed austenite leading to highly deformed pancaked austenite (NISHIOKA & ICHIKAWA, 2012). All these features increase mechanical properties. However, these precipitates grow up to a specific size may be deleterious to mechanical properties. For example, the TiN precipitates bigger than 1 μm are the most potent crack-forming and they are most effective when located in suitable coarse ferrite grains (or coarse bainitic packets) (ECHEVERRÍA & RODRIGUEZ-IBABE, 2003). These particles coarsen and become large enough to crack, thus providing crack nuclei which may then propagate into the matrix.

TiN precipitates bigger than 1 μm were found in the BM and in the HAZ for all conditions studied in the present work. They may affect the mechanical properties, however their influence was not clear in our study.

5.3. CONCLUSIONS

In general, hardness values in the HAZ and weld zone reduced with increasing of heat input for samples from AHSS900 steel (sample C and D). Whereas hardness profile for samples A and B were more homogeneous and no influence was detected.

The maximum hardness for samples C and D occurred in the CGHAZ which is attributed to its hard microstructure, consisting of lath martensite and bainite. Furthermore, the higher hardness of the weld metal for the samples welded with lower heat input was attributed to martensite formation.

Owing to the hardness measurement profile, samples C and D showed softened HAZ at FGHAZ and PHAZ. The softening is a result of the fine microstructure on these two regions, fine ferrite grain and absence of hard phases such as martensite.

Sample D displayed the highest tensile strength among the welded joints. However, for all welded specimens from AHSS900 BM failures happened at the weld bead, which indicate the weak mechanical properties of the filler material. Therefore, the filler material can be considered inadequate for the AHSS900 BM.

Although a considerable drop in tensile strength and weld being the weakest zone, it has been noticed that by increasing heat input (sample D compared with sample C) better joint efficiency was achieved.

Referring to the tensile test results of the welded joints of LNE500 welded with two heat inputs, average yield strength of 250 MPa and average tensile strength of 600 MPa has been achieved. Higher heat input was, lower yield strength was.

The initial idea was the use the same filler material to weld both high strength steels. However, the results showed that the filler material used is not suitable for the AHSS900 steel. It is known that for a given life, weld must be harder than parent steel (BHADESHIA & HONEYCOMBE, 2017).

The increase of heat input, in general, induced a marked hardness decrease in WM and HAZ. This reduction may be associated to the changes in the microstructure such as grain size. In the WM this behaviour may be due to the increase of the ferrite volume fraction and the microstructural coarsening.

Chapter 6

6. CORROSION BEHAVIOUR

6.1. ELECTROCHEMICAL BEHAVIOUR

6.1.1. Base metals

Electrochemical impedance spectroscopy (EIS) diagrams for the base metals, LNE500 and AHSS900 in the as-received condition in 3.5 wt% NaCl aqueous solution, are shown in Figure 77.

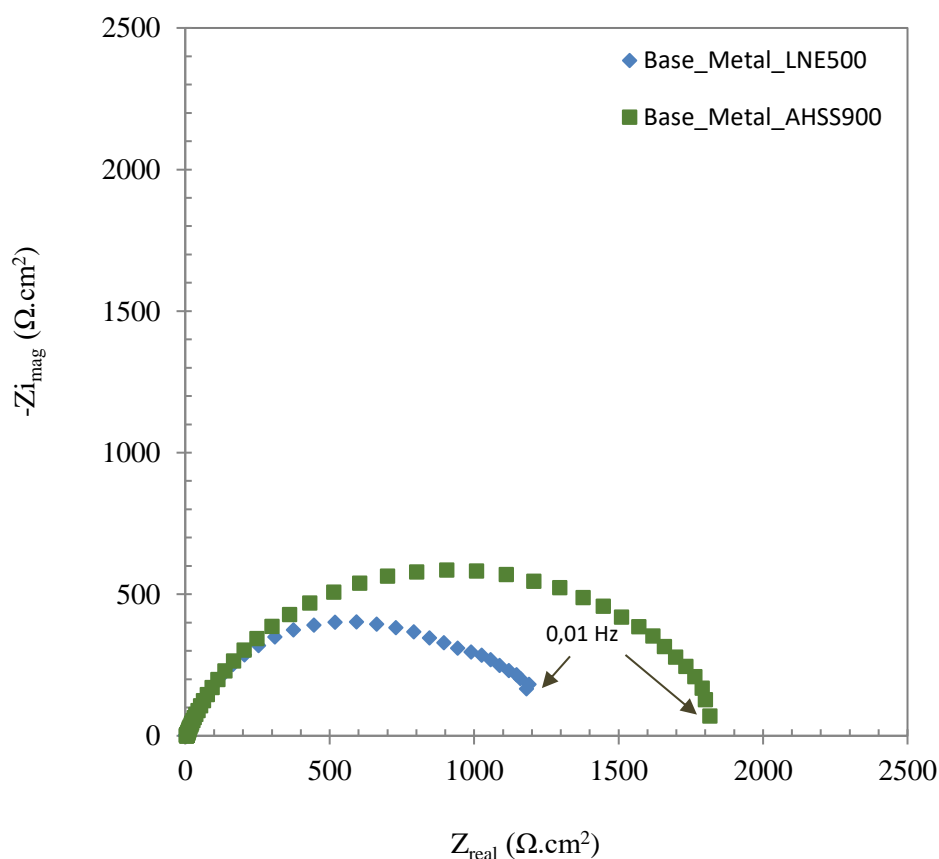


Figure 77: Electrochemical impedance spectra of LNE500 and AHSS900 in 3.5 wt% NaCl.

Nyquist plots (Figure 77) are characterized by one single capacitive loop and imperfect semicircles. The imperfect semicircle diameter for the AHSS900 base metal is larger, which reflects better corrosion resistance of the AHSS900. It is well-known that the size of the capacitive loop in Nyquist plots is related to the magnitude of the charge transfer resistance and, therefore, to the corrosion resistance of the electrode surface (HAMDY, EL-SHENAWEY & EL-BITAR, 2006).

The Bode diagrams of phase angle (a) and impedance modulus (b) versus frequency for the base metals in 3.5 wt% NaCl aqueous solution are shown in Figure 78.

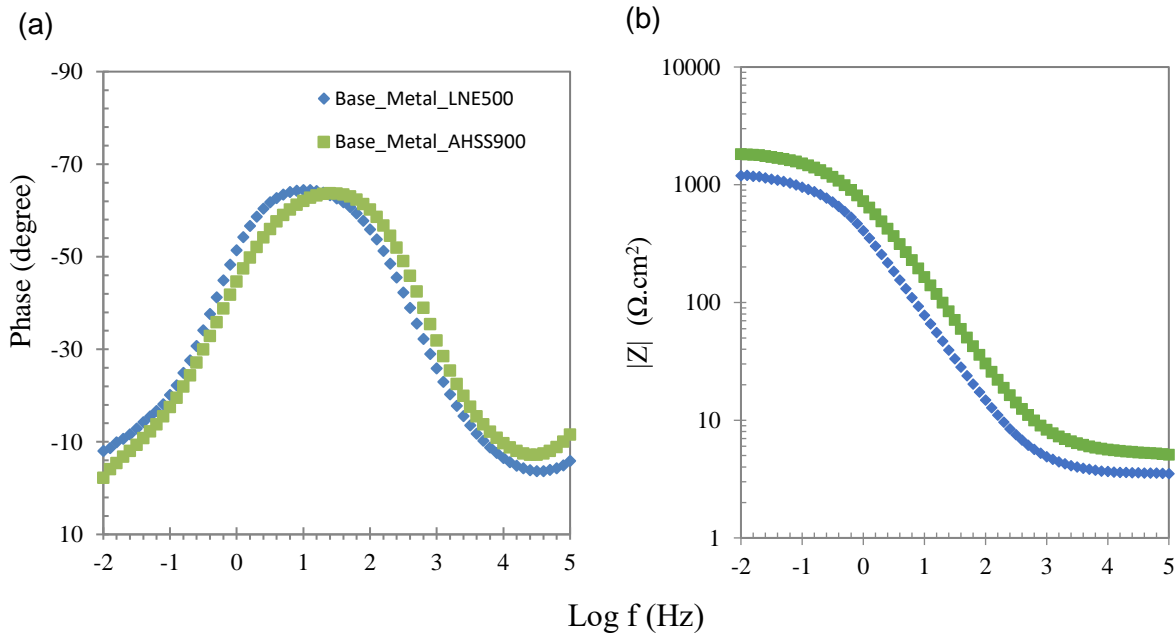


Figure 78: Bode diagram of phase angle (a) and impedance modulus (b) versus logarithm of frequency for the base metals LNE500 and AHSS900 in 3.5 wt% NaCl.

A maximum phase peak identified between 1 - 100 Hz for the samples immersed in 3.5 wt% NaCl (Figure 78). The maximum peak, for LNE500 is shifted to lower frequencies. The peak occurs around -64° for both base metals. The EIS response for LNE500 and AHSS900 is close to that of a pure capacitive behaviour. Indeed, the Bode diagrams and Nyquist diagram indicated higher corrosion resistance of base metal AHSS900 than LNE500. The value of $\log |Z|$ at the lowest frequencies is higher for AHSS900 steel, confirming that it is less prone to corrosion. For a pure capacitor, phase-angle is -90° while for a resistor it is zero (BARSOUKOV & MACDONALD, 2005; FATTAH-ALHOSSEINI & VAFAEIAN, 2015). AHSS900 base metal has a superior corrosion resistance in this solution than LNE500 BM.

Bode diagrams indicated one time constant for the base metals, indicating a free corrosive process on the surface of the electrode. The Nyquist and Bode diagrams show a resistive behaviour at high frequencies, but in the middle to the low frequency domain there was a marked capacitive response.

Potentiodynamic polarisation curves for the base metals in 3.5 wt% NaCl solution at room temperature are shown in Figure 79.

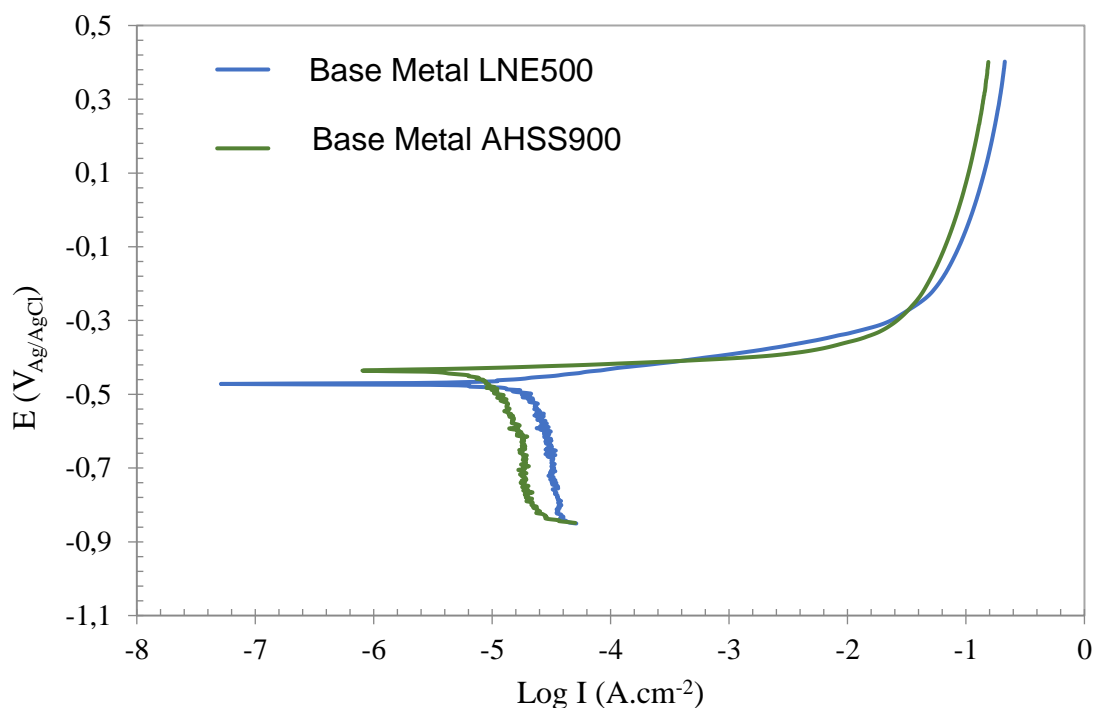


Figure 79: Polarisation curves of base metals in 3.5 wt% NaCl solution.

LNE500 and AHSS900 exhibited typical active corrosion behaviours. This is indicated by the continuous increase of the current density as the applied potential is further increased above E_{corr} . The electrochemical parameters obtained using the Tafel extrapolation method are shown in Table 25.

Table 25: Electrochemical parameters of LNE500 and AHSS900 BMs in 3.5 wt% NaCl obtained using Tafel analysis

Electrolyte 3.5 wt% NaCl		
	E_{corr} (V _{Ag/AgCl})	i_{corr} ($\mu\text{A} \cdot \text{cm}^{-2}$)
LNE500	$-0.44 \pm 0,04$	16.16 ± 2.88
AHSS900	-0.44 ± 0.01	10.00 ± 0.30

Base metals showed the same corrosion potential (E_{corr}) in the 3.5 wt% NaCl solution and AHSS900 lowest corrosion current density (i_{corr}). The corrosion potential can be used to evaluate the stability of the electrode with regard to the onset of corrosion processes. More anodic values of E_{corr} are related to more stable surfaces and i_{corr} values expresses the rate at which the corrosion process takes place at the electrode surface (RÍOS, SOUZA, & ANTUNES, 2016). Therefore, the corrosion process is faster for the LNE500 steel than for the AHSS900 steel.

6.1.2. Welded joints

Nyquist plots of the welded joints (sample A, sample B, sample C and sample D) immersed in 3.5 wt% NaCl solution at room temperature are shown in Figure 80.

Nyquist plots are characterized by one single capacitive loop, with imperfect semicircles for all samples. The imperfect semicircle diameter for samples C and D (AHSS900 BM) is larger than the diameter for samples A and B (LNE500 BM). Therefore, the welded joints of the AHSS900 BM showed higher corrosion resistance than welded joints from the LNE500 BM.

Considering the welded joints of the AHSS900 BM (Figure 80b), the capacitive loop diameter is larger for sample D (welded with higher heat input), which reflects its better corrosion resistance than sample C (welded with lower heat input). Considering the welded joints from the LNE500 steel (Figure 80a) sample B (lower heat input) showed smaller semicircle diameter than sample A. It is worth mentioning that the impedance values are of the same order of magnitude for samples A and B, which evidences that the heat input did not have a remarkable influence on the corrosion behaviour of the LNE500 steel. The same behaviour was observed for the welded joints of the AHSS900 BM.

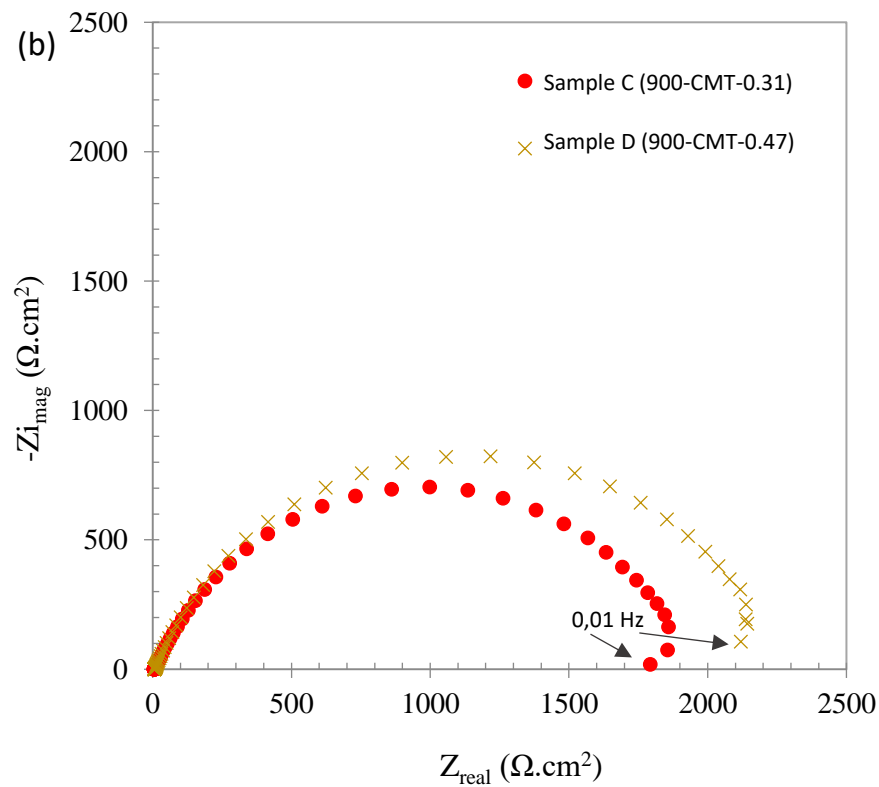
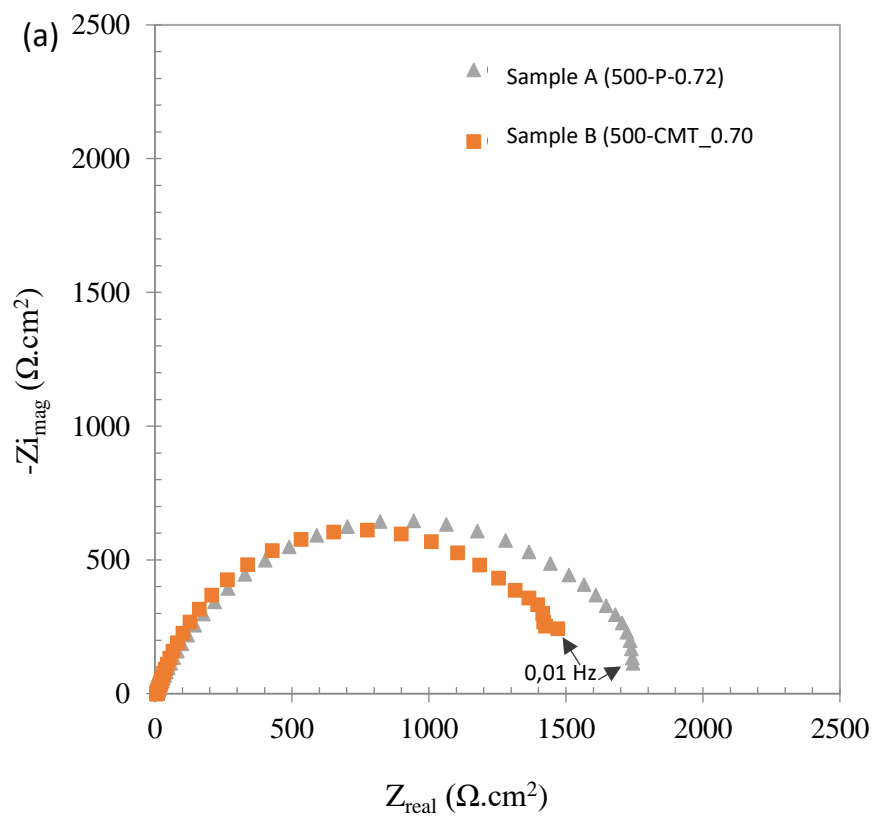


Figure 80: Electrochemical impedance spectra of welded joints samples A and B (a) and for samples C and D (b) in 3.5 wt% NaCl solution.

Bode plots of the welded joints (samples A, B, C and D) immersed in the 3.5 wt% NaCl solution at room temperature are shown in Figure 81.

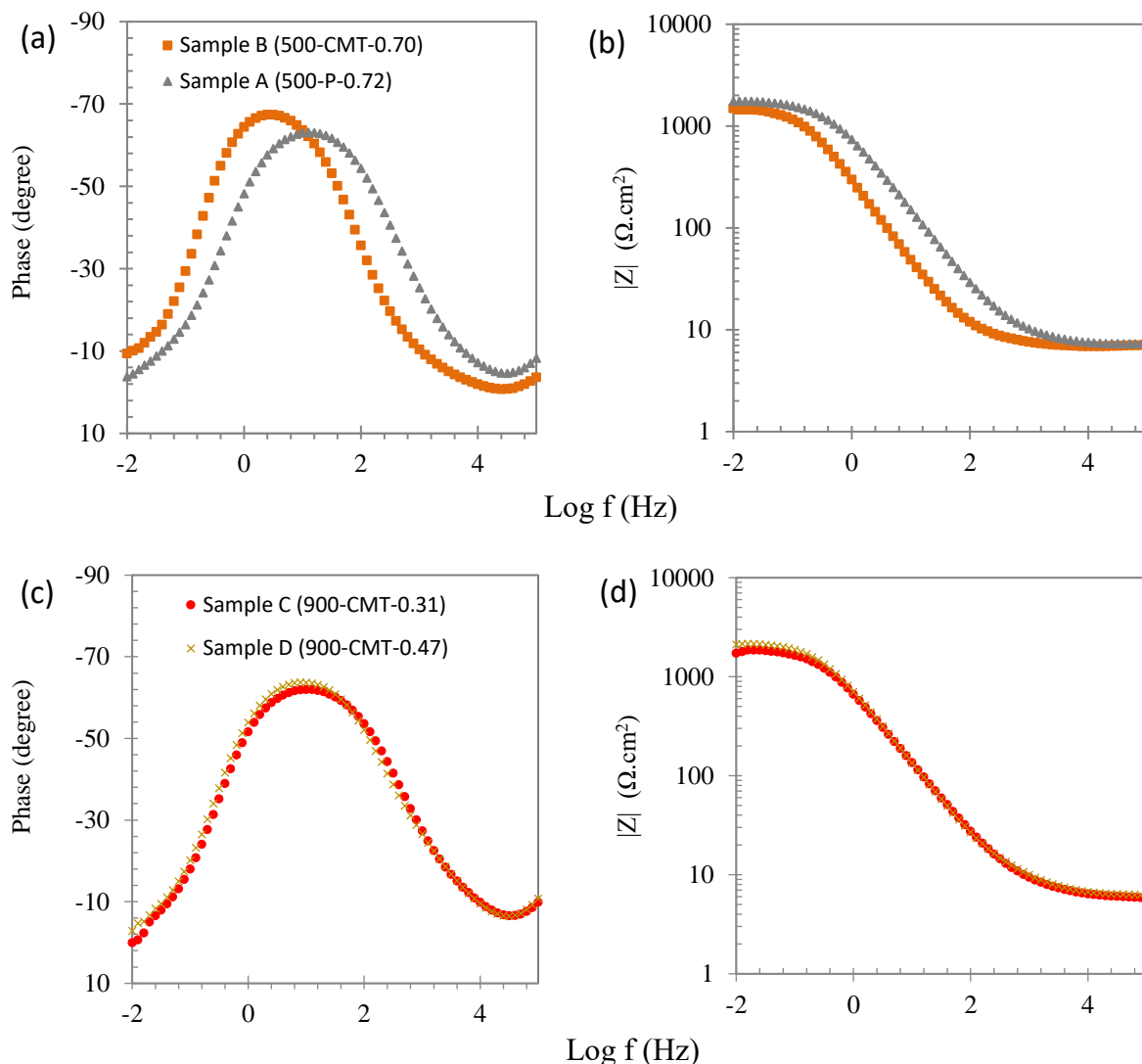


Figure 81: Bode diagram of phase angle (a)(c) and impedance modulus (b)(d) versus logarithm of frequency for the welded joints samples A and B (a)(b) and samples C and D (c)(d) in 3.5 wt% NaCl solution.

A maximum phase peak is observed for sample B which is the sample closer to -90° (pure capacitive behaviour), denoting that this condition had superior corrosion resistance. Samples C and D showed similar plots.

Bode diagrams indicated one time constant for the welded joints, indicating a corrosive process on the surface of electrode. The Nyquist and Bode diagrams show a resistive behaviour at high frequencies, but in the middle to low frequency range domain, there was a marked capacitive response.

The heat input did not show significant influence on the results. As can be seen in the Bode diagrams (Figure 81), the values of $\log |Z|$ are similar for all conditions.

Potentiodynamic polarisation curves of the welded joints in 3.5 wt% NaCl solution at room temperature are shown in Figure 82.

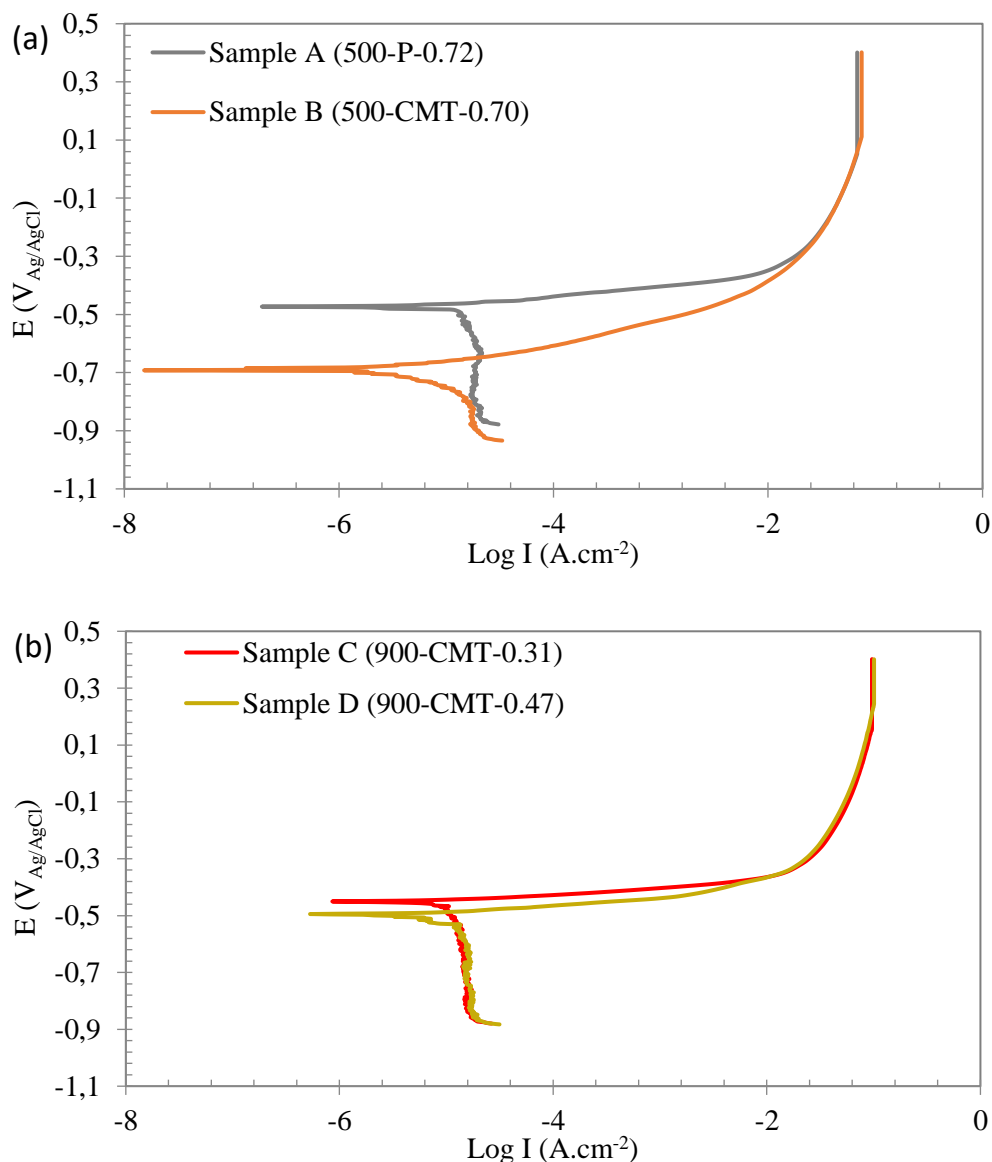


Figure 82: Polarisation curves of welded samples (a) samples A and B and (b) samples C and D in 3.5 wt% NaCl solution.

All conditions exhibited typical active corrosion behaviour. This is indicated by the continuous increase of the current density as the applied potential is further increased above E_{corr} . The potential corrosion, E_{corr} , and current density, i_{corr} , obtained using the Tafel extrapolation, are shown in Table 26.

Table 26: Electrochemical parameters of welded samples in the electrolyte of 3.5 wt% NaCl, obtained using Tafel analysis.

	E_{corr} (V _{Ag/AgCl})	i_{corr} ($\mu\text{A} \cdot \text{cm}^{-2}$)
Sample A (500-P-0.72)	-0.60 ± 0.05	9.32 ± 3.03
Sample B (500-CMT-0.70)	-0.59 ± 0.06	10.11 ± 5.61
Sample C (900-CMT-0.31)	-0.44 ± 0.01	16.20 ± 3.30
Sample D (900-CMT-0.47)	-0.55 ± 0.09	10.00 ± 2.87

Figure 83 displays the i_{corr} and E_{corr} values as a function of the heat input for the different welded joints. it is apparent that both E_{corr} and i_{corr} decrease for higher heat input values.

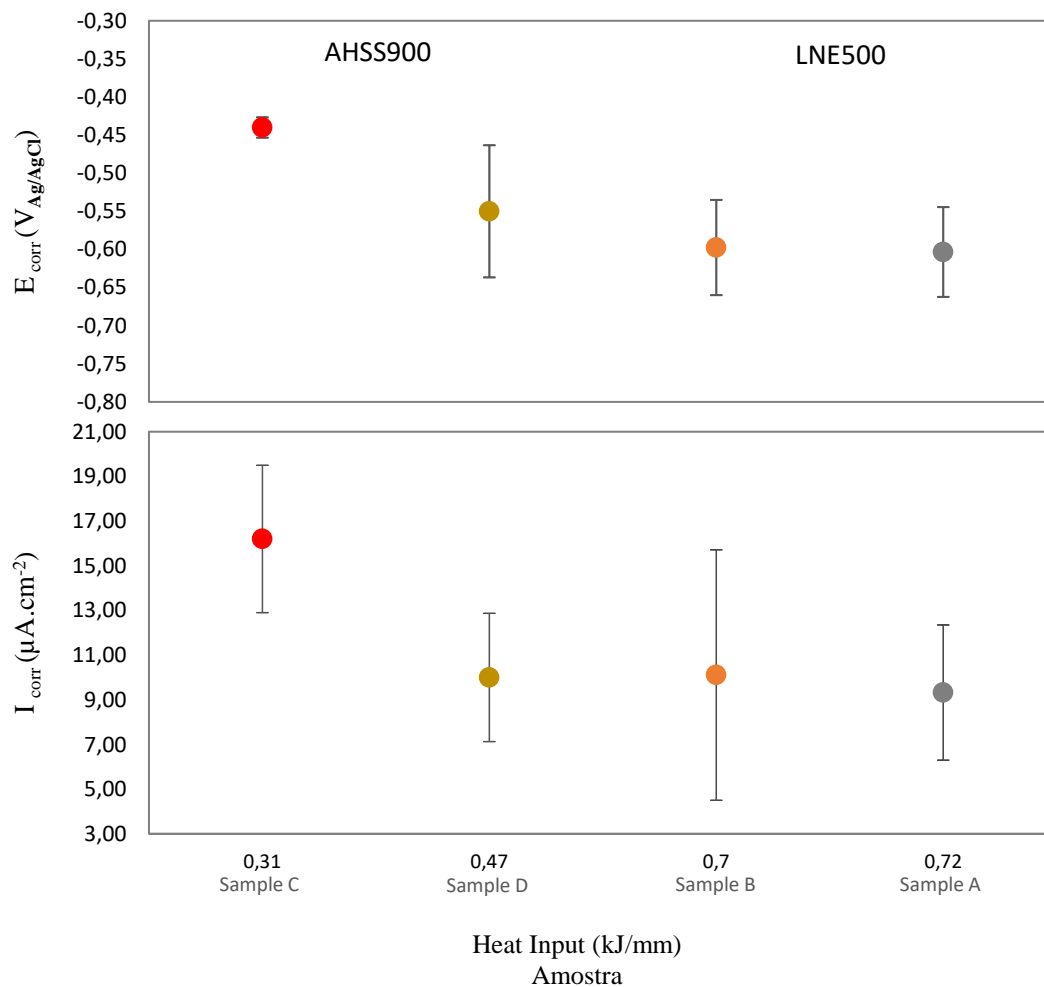


Figure 83: Corrosion potential, E_{corr} , corrosion current density, i_{corr} , extracted from the potentiodynamic curves versus heat input of the samples A-D, in 3.5 wt% NaCl aqueous solution.

Welded joint from AHSS900 BM (samples C and D) showed the highest corrosion potential and current density values. Samples A, B and D showed very similar E_{corr} and i_{corr} values.

It should be emphasised at this point that potential corrosion and current density are in the same orders of magnitude which do not vary significantly, this respect, no clear correlation is in fact observed between the corrosion behaviour and the heat input. Other features have to be considered to explain the corrosion behaviour such as microstructure and chemical composition.

Figure 84 shows its Nyquist diagram for the WM. As detailed in the experimental procedure BM and HAZ were covered to permit the corrosion behaviour of the WM only.

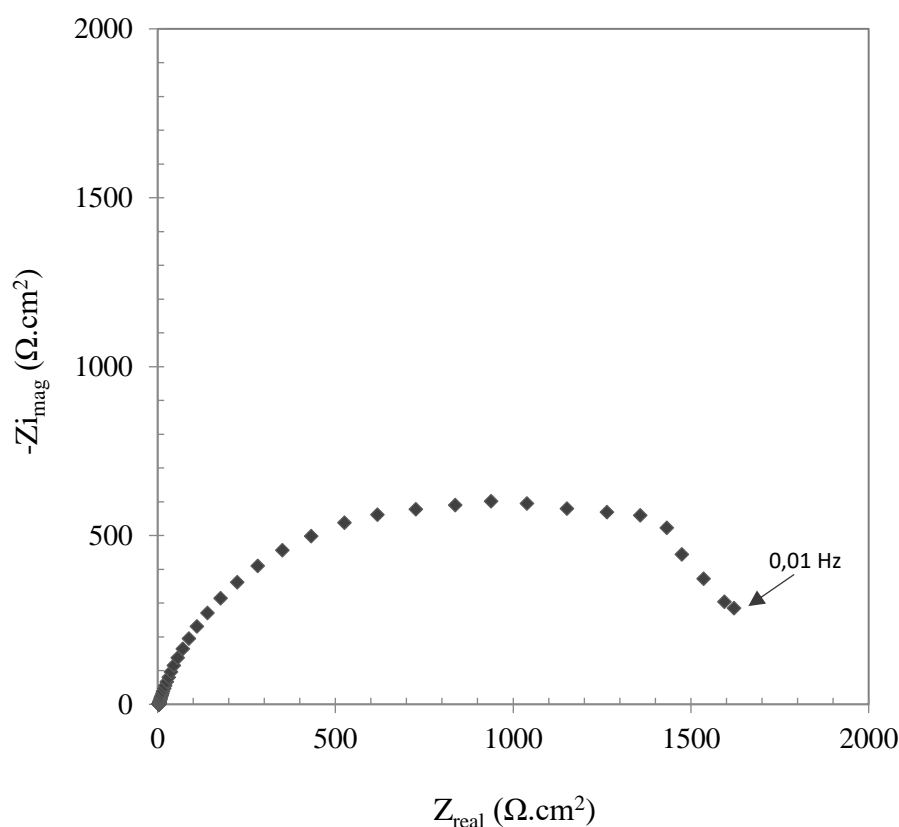


Figure 84: Electrochemical impedance spectra of weld metal in 3.5 wt% NaCl solution.

Nyquist plot for the weld metal is characterized by one single capacitive loop, with imperfect semicircle. The Bode diagrams (phase angle and impedance modulus versus frequency) for the weld metal are shown in Figure 85.

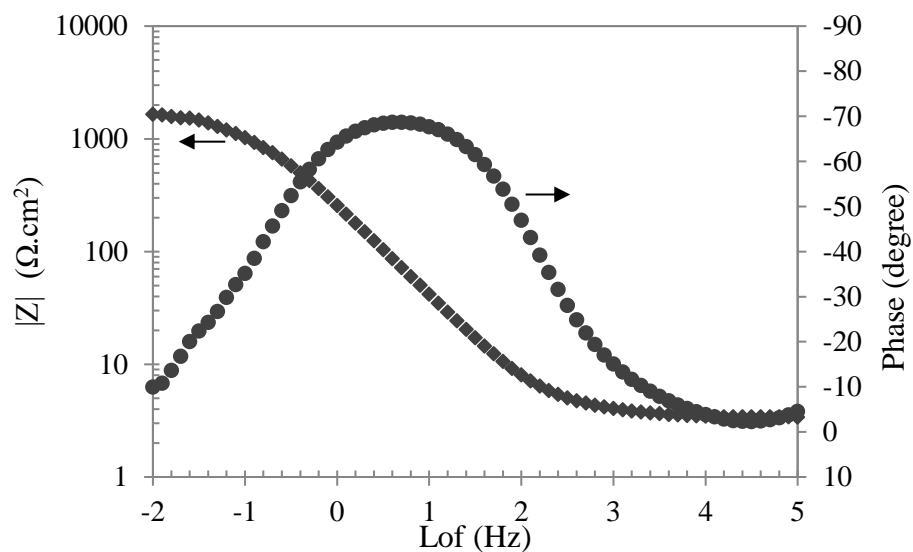


Figure 85: Bode diagram of phase angle and impedance modulus versus logarithm of frequency for the weld metal in 3.5 wt% NaCl solution.

A maximum phase peak is observed around -70° between 1 - 10 Hz. The phase peak has the highest value compared to the welded joints.

Potentiodynamic polarisation curve of the weld metal in 3.5 wt% NaCl solution at room temperature is shown in Figure 86.

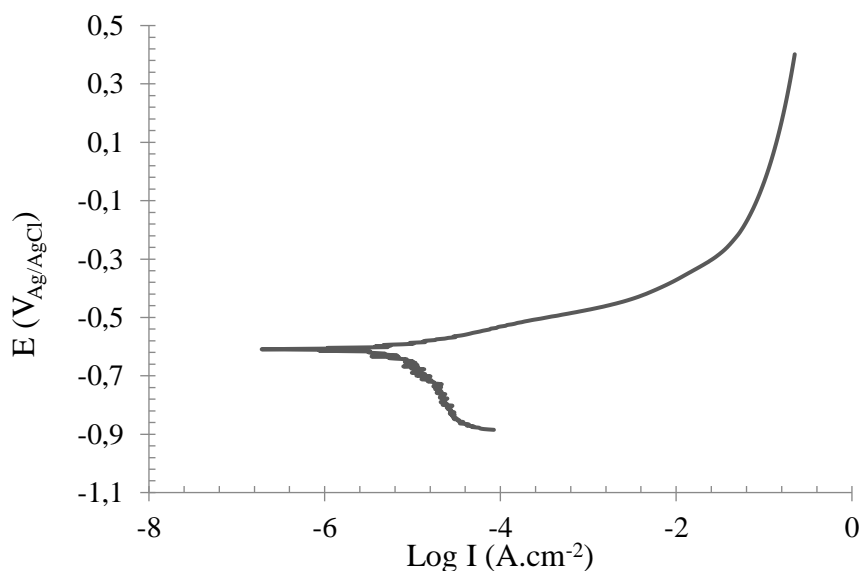


Figure 86: Polarisation curves of weld metal in 3.5 wt% NaCl.

Weld metal exhibited typical active corrosion behaviour. This is indicated by the continuous increase of the current density as the applied potential is further increased

above E_{corr} . Using the Tafel extrapolation, the corrosion potential was determined, $E_{\text{corr}} = -0.61 \text{ V}_{\text{Ag/AgCl}}$ and current density, $i_{\text{corr}} = 6.3 \mu\text{A}/\text{cm}^2$.

E_{corr} and i_{corr} values of the BMs (LNE500 and AHSS900) and weld metal were summarised in Table 27.

Table 27: Electrochemical parameters of LNE500 and AHSS900 and WM, in 3.5 wt% NaCl, using Tafel analysis

Electrolyte 3.5 wt% NaCl		
	$E_{\text{corr}} (\text{V}_{\text{Ag/AgCl}})$	$i_{\text{corr}} (\mu\text{A}.\text{cm}^{-2})$
LNE500	-0.44 ± 0.04	16.16 ± 2.88
AHSS900	-0.44 ± 0.01	10.00 ± 0.30
WM	-0.61 ± 0.06	6.30 ± 1.20

WM showed the smaller value of i_{corr} , indicating the corrosion process happen more slowly on this material compared to LNE500 and AHSS900. WM showed values of E_{corr} more negative which means prone to corrode. WM E_{corr} value is related to its microstructure and chemical composition that will be discussed further in this chapter.

6.2. CONFOCAL LASER SCANNING MICROSCOPY (CLSM)

CLSM images of the different samples were obtained before and after potentiodynamic polarisation tests. A significant depth difference was found between HAZ and weld metal after the corrosion test in 3.5 wt% NaCl aqueous solution. Figure 87 shows the CLSM micrographs before the corrosion test and Figure 88 and Figure 89 show the CLSM micrographs after corrosion product removal from the surfaces of samples A, B, C and D.

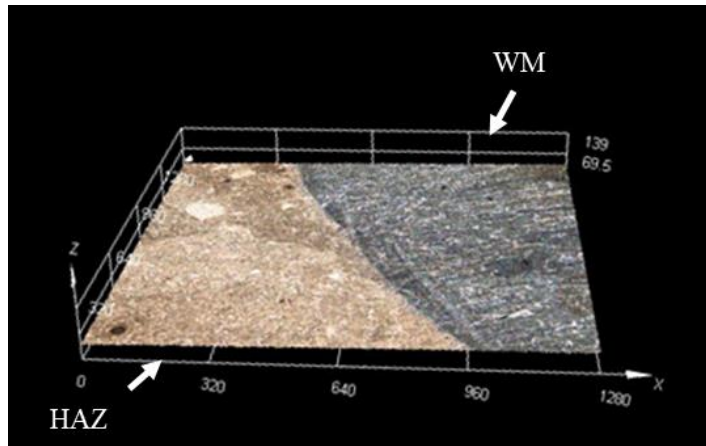


Figure 87: CLSM image of welded joint before corrosion test.

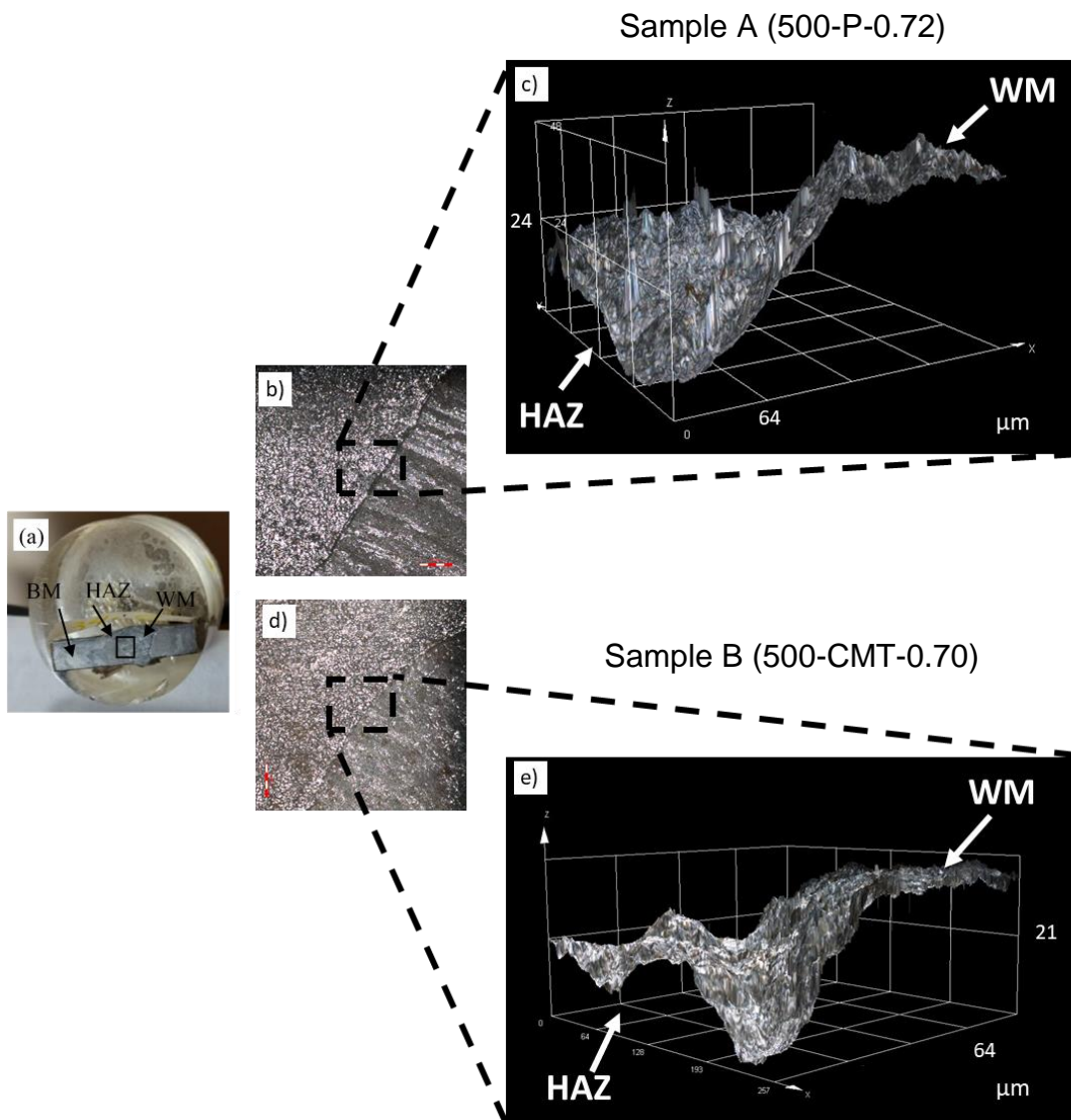


Figure 88: Welded joint after removing the corrosion product a) specimen b) 2D CLSM image c) 3D CLSM image of sample A (LNE500) and d) 2D CLSM image e) 3D CLSM image of Sample B (LNE500).

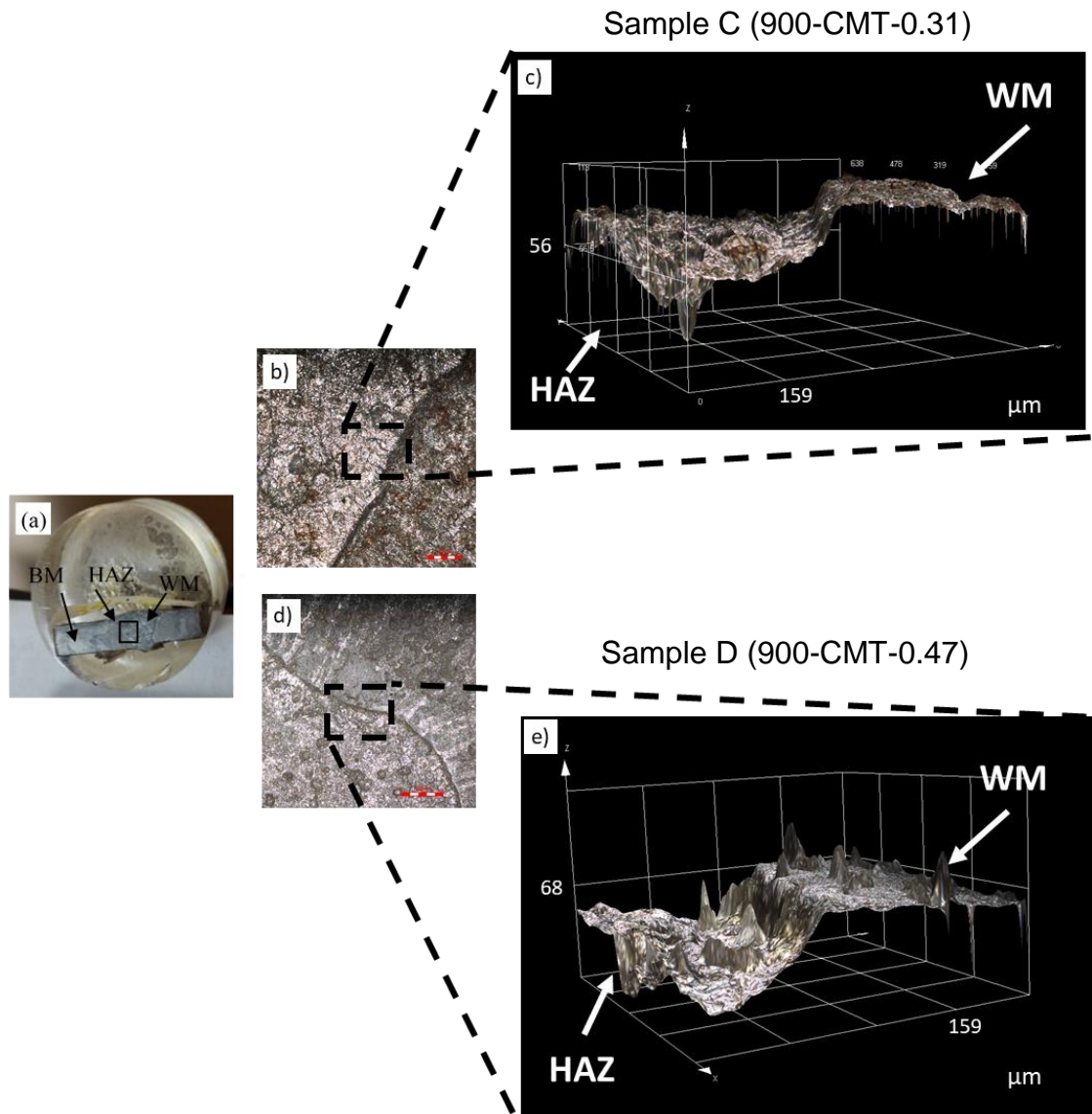


Figure 89: Welded joint after removing the corrosion product a) specimen b) 2D CLSM image c) 3D CLSM image of sample C (AHSS900) and d) 2D CLSM image e) 3D CLSM image of Sample D (AHSS900).

A depth difference was found for all conditions. It was 61.28 and 34.87 μm for samples A and B, and 36.74 and 41.04 μm for samples C and D, respectively. Therefore, sample A was the condition with the biggest depth difference between HAZ and WM.

As shown in Figure 87 this depth difference did not exist before the corrosion test. Therefore, it is to be noted that a galvanic effect existed between the weld metal and the HAZ/parent metal. HAZ was more intensely corroded and so acted as the anode and the weld metal as the cathode of the galvanic couple.

Considering the results from electrochemical techniques, base metal/HAZ showed higher values of i_{corr} which may explain why this region corroded more severely in 3.5 wt% NaCl solution.

The concentration of Cl^- ions was not enough to provoke an intense corrosion and thus no step between HAZ and WM was found.

6.3. SCANNING VIBRATING ELECTRODE TECHNIQUE (SVET)

In order to fully understand the corrosion behaviour of the welded joint, SVET has been used to investigate the onset of the corrosion process. The results were obtained in 0.1 wt% NaCl aqueous solution as mentioned in section 3.10. Preliminary tests indicated that with 3.5 wt% NaCl, the corrosion process happened too fast and its evolution could not be observed.

SVET results for the LNE500 and AHSS900 base metals are shown in Figure 90 and Figure 91, respectively. Surface plots of normal current density i_z were recorded at various times following immersion in 0.1 wt% NaCl (aq) at the open circuit potential are displayed. The photographs showed below the maps were taken after the SVET measurement and show the corrosion products formed during the test. The maps and the photographs are at the same scale.

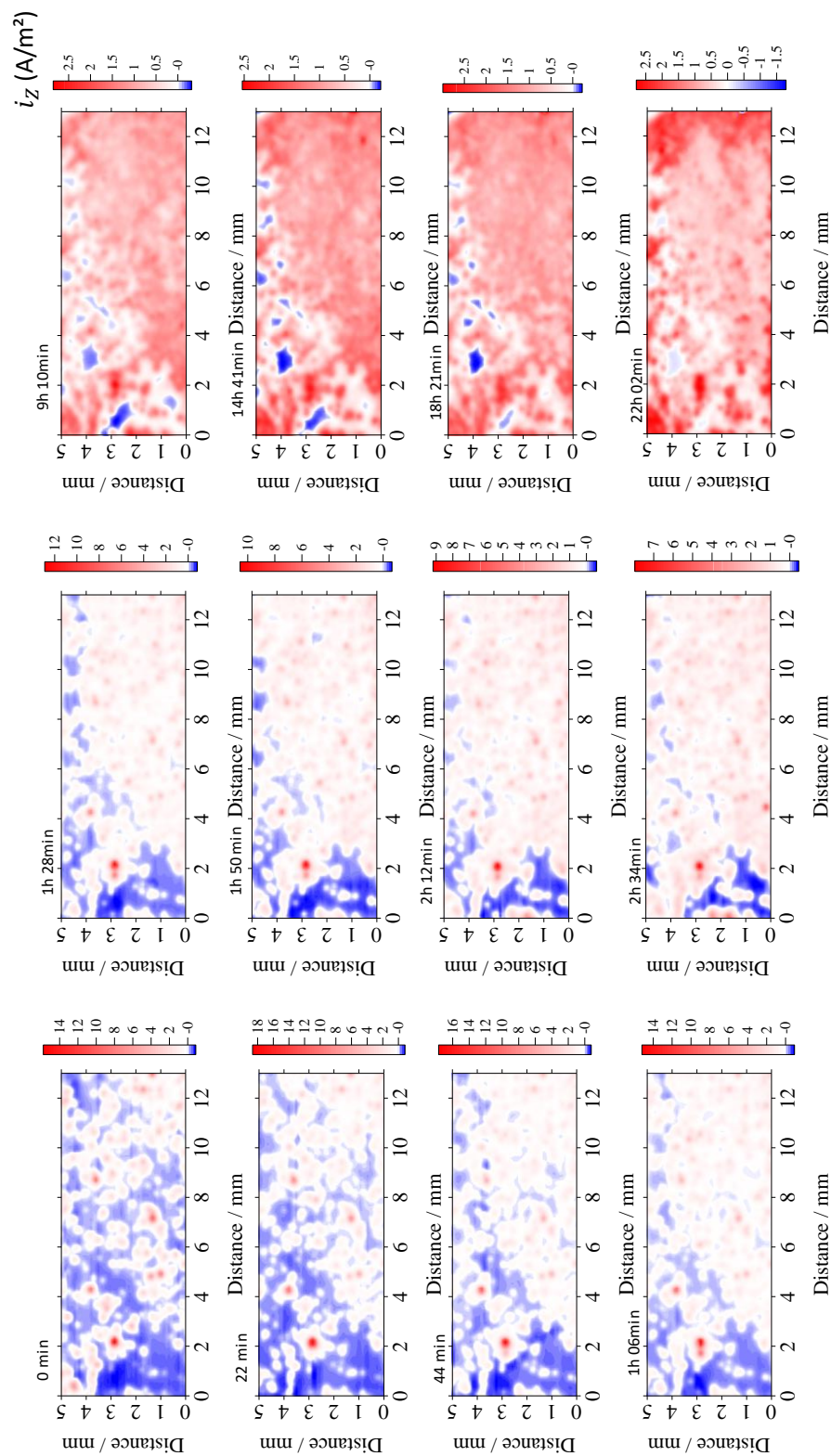


Figure 90: SVET measurements of the LNE500 steel in 0.1 wt% NaCl aqueous solution

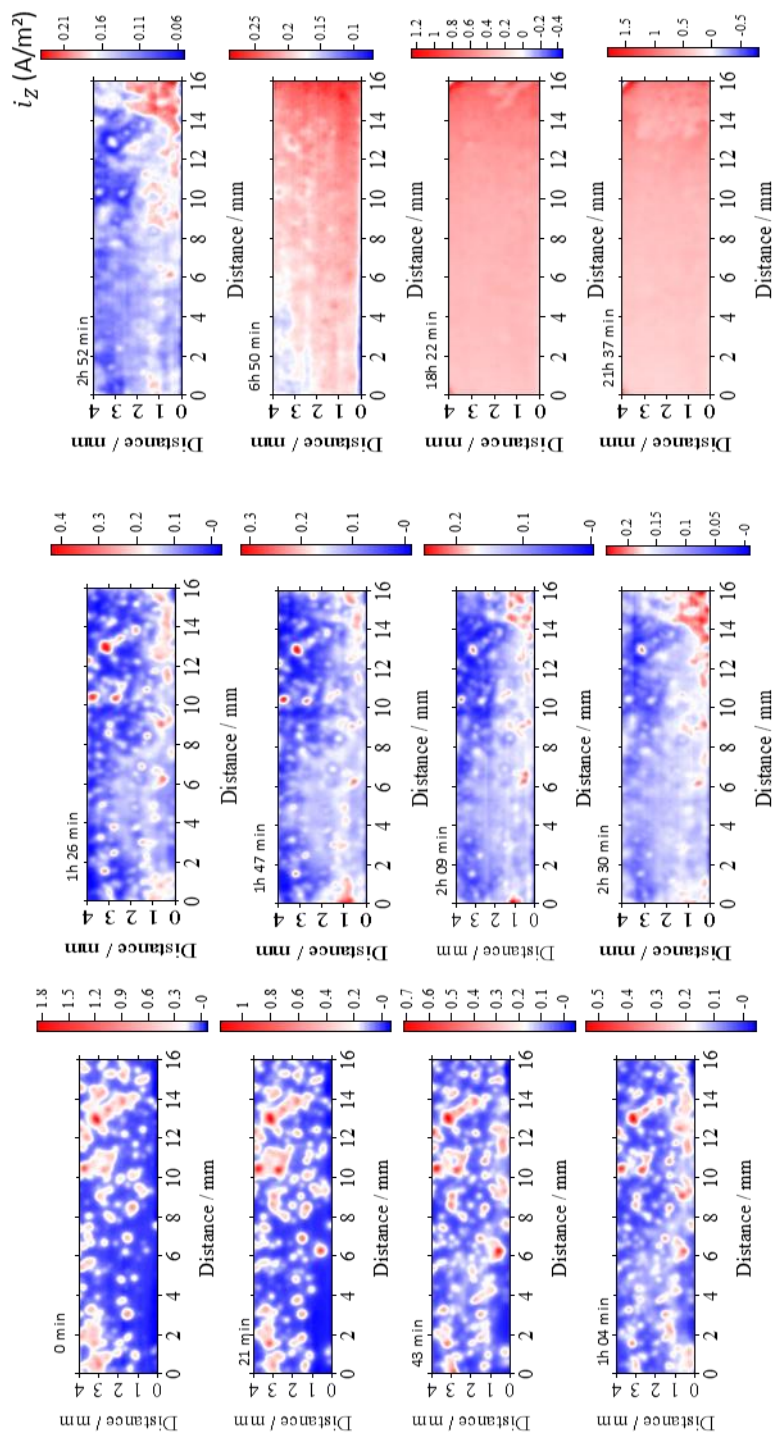


Figure 91: SVET measurements of the AHSS900 steel in 0.1 wt% NaCl aqueous solution.

As can be seen from Figure 90 and Figure 91 in the SVET measurements spatial variation of current density (i_z) is mapped. The blue colour represents negative current densities whilst red colour presents positive current densities. The first scan recorded, for both base metal, captured intense local anodic activity regions (red dots). Subsequent scans show the corrosion expanding along the surface. The SVET-derived current density maps also show that local anodic current decreases significantly with time for the LNE500 BM (Figure 90). For example, anodic i_z values of typically $+2.5 \text{ A/m}^2$ were measured after 10 h immersion, while initially its value was $+16 \text{ A/m}^2$. For the BM AHSS900, anodic i_z values measured were $+1.8 \text{ A/m}^2$ and it decreased to $+0.5 \text{ A/m}^2$ after 1 h. The decrease in the current density is observed due to the corrosion products attached on the surface.

SVET was also carried out on the welded samples A, B, C and D, as can be seen in Figure 92, Figure 93, Figure 94 and Figure 95, respectively. For each sample, two current density maps are shown, the maps were obtained after different immersion times.

(a)

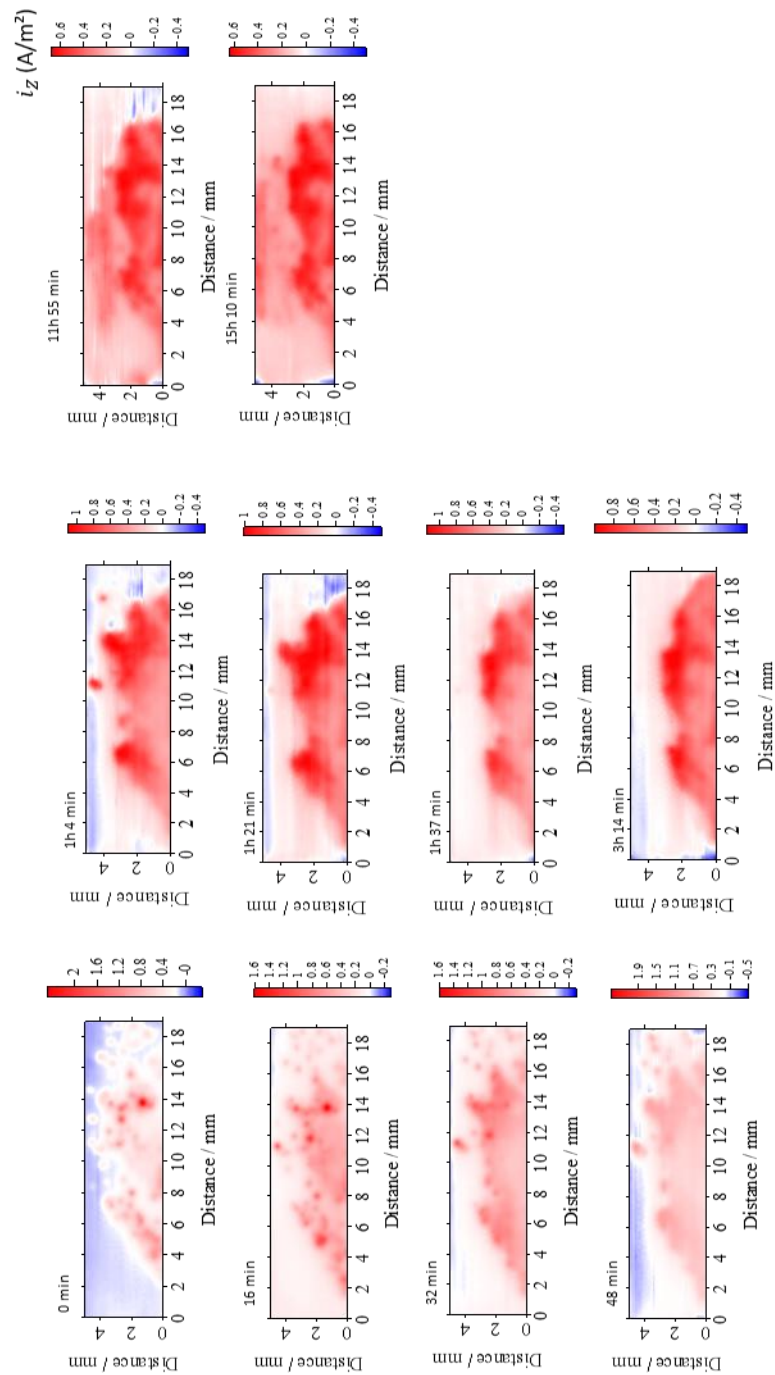


Figure 92: SVET measurements of welded joint Sample A (500-P-0.72) in 0.1 wt %NaCl aqueous solution for specimen 1 (a) and specimen 2 (b).

(b)

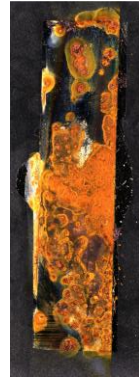
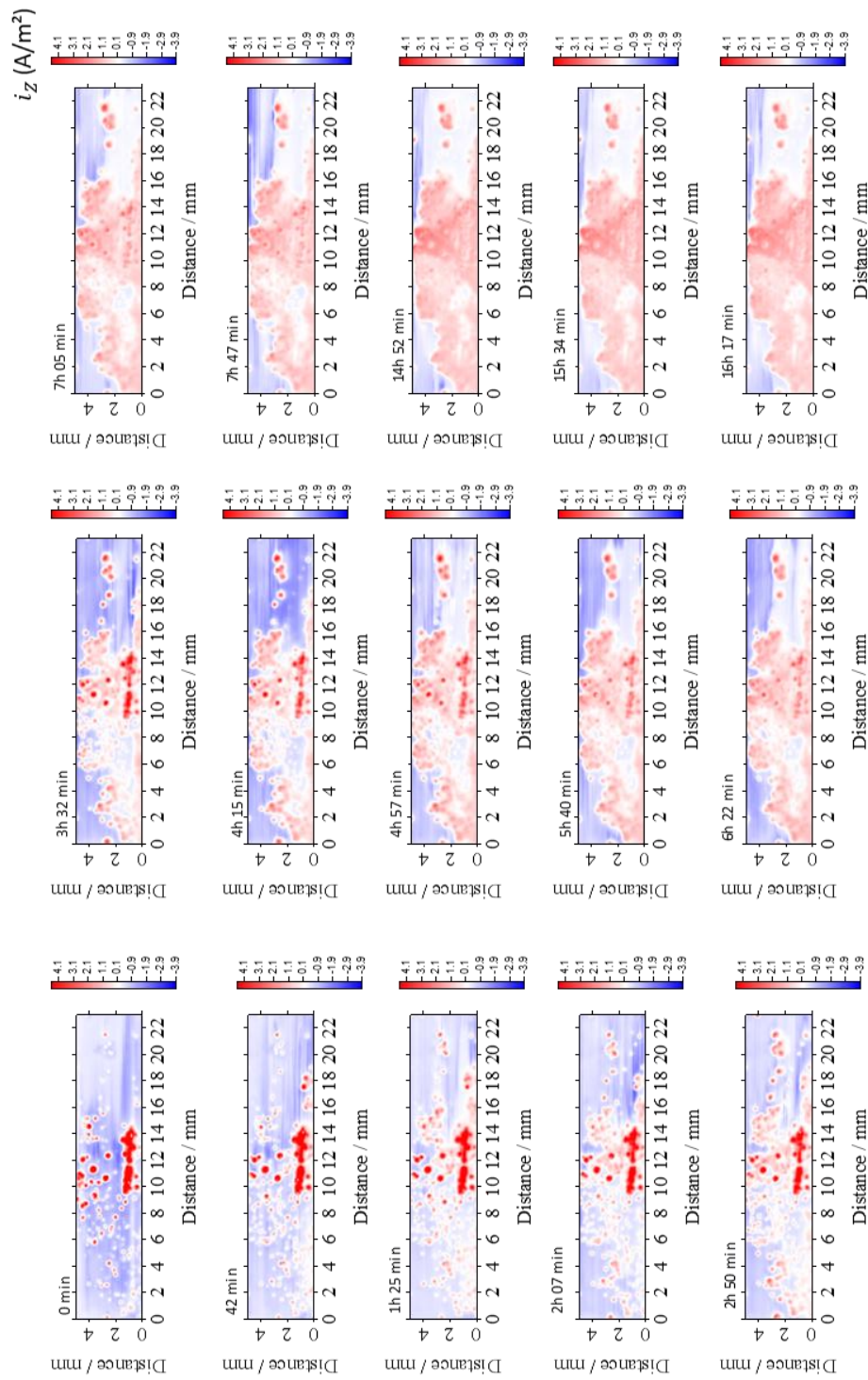


Figure 92: continued

(a)

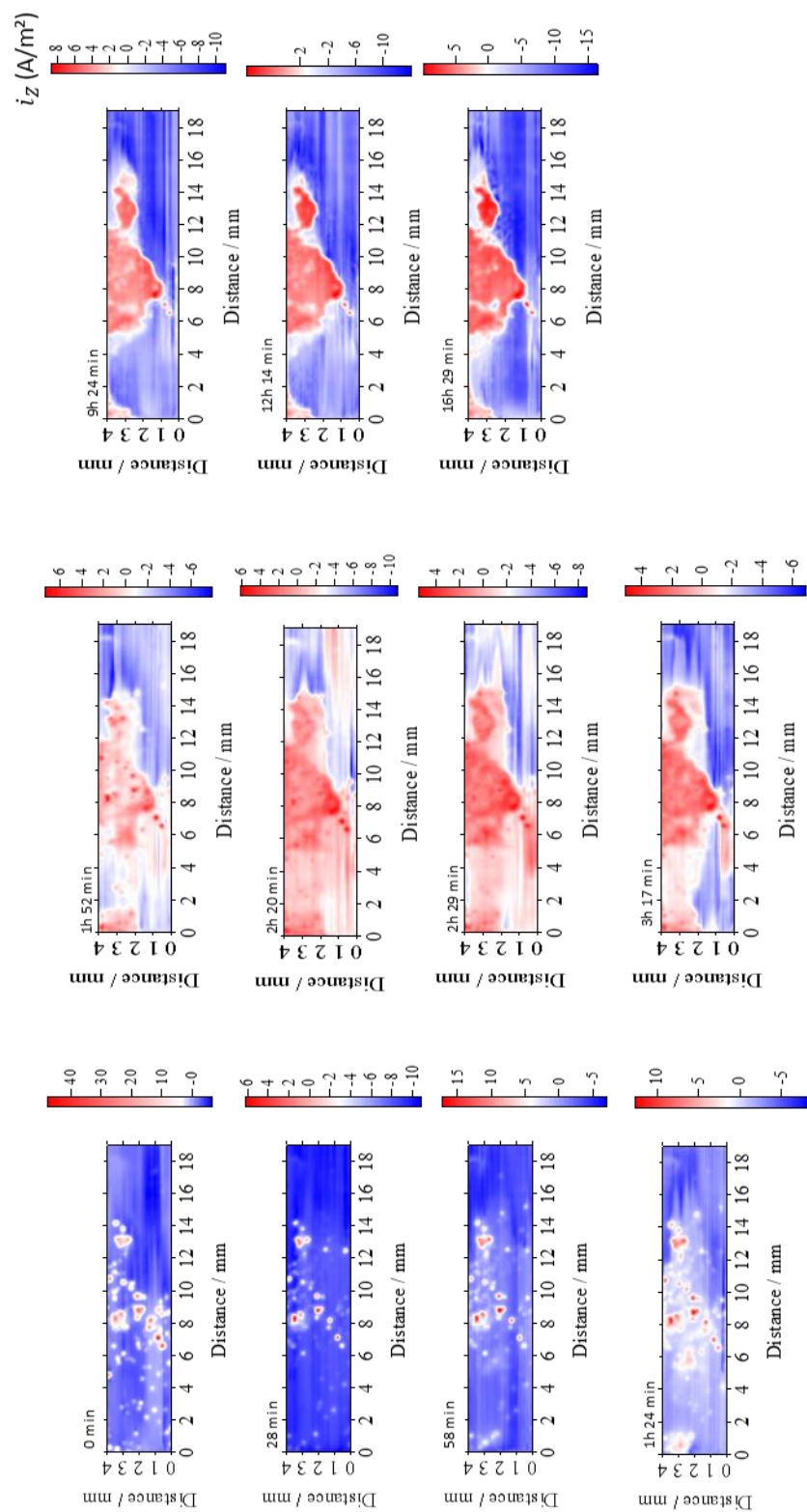


Figure 93: SVET measurements of welded joint Sample B (500-CMT-0.70) in 0.1 wt% NaCl aqueous solution for specimen 1 (a) and specimen 2 (b).

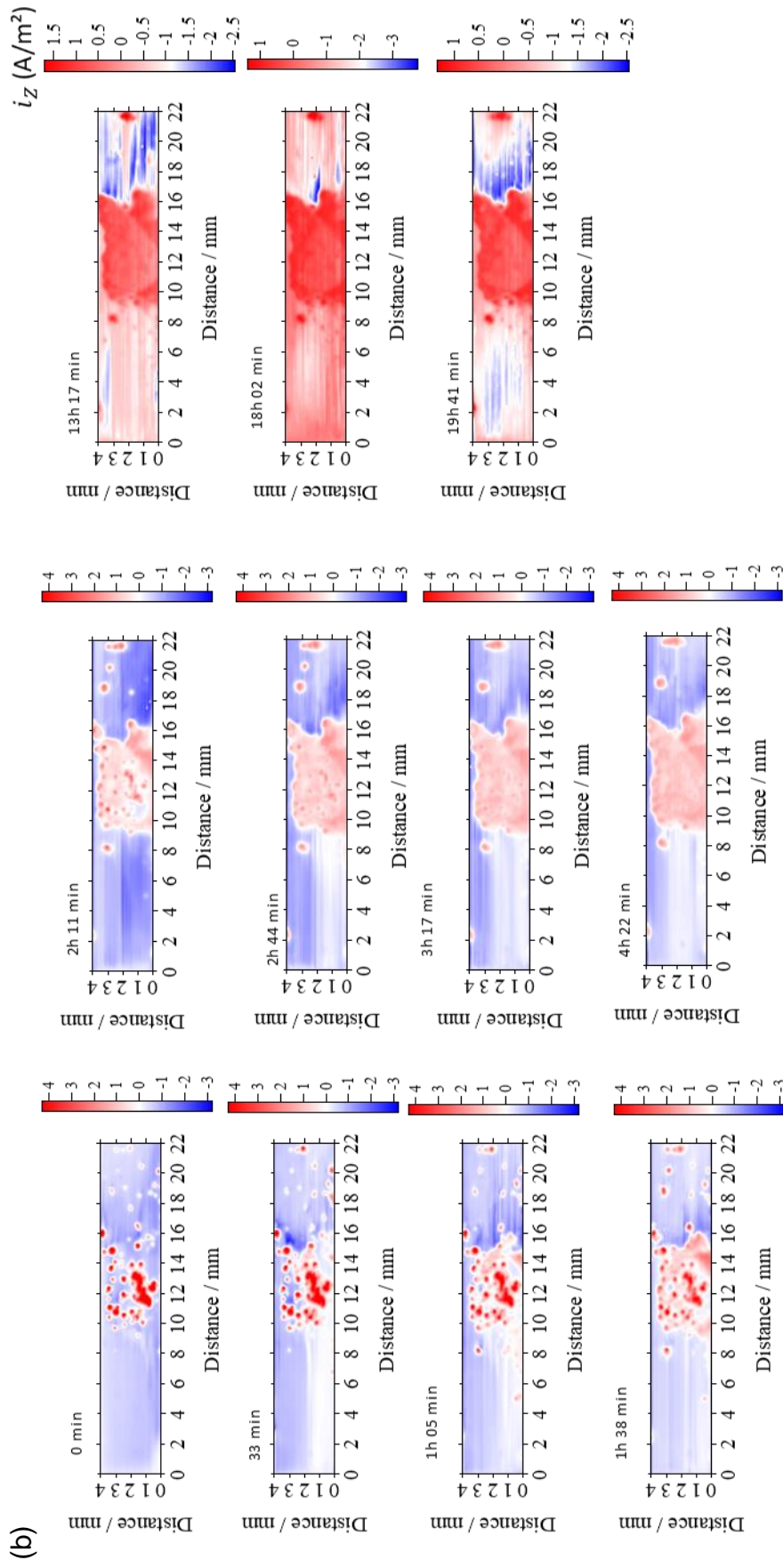


Figure 93: continued.

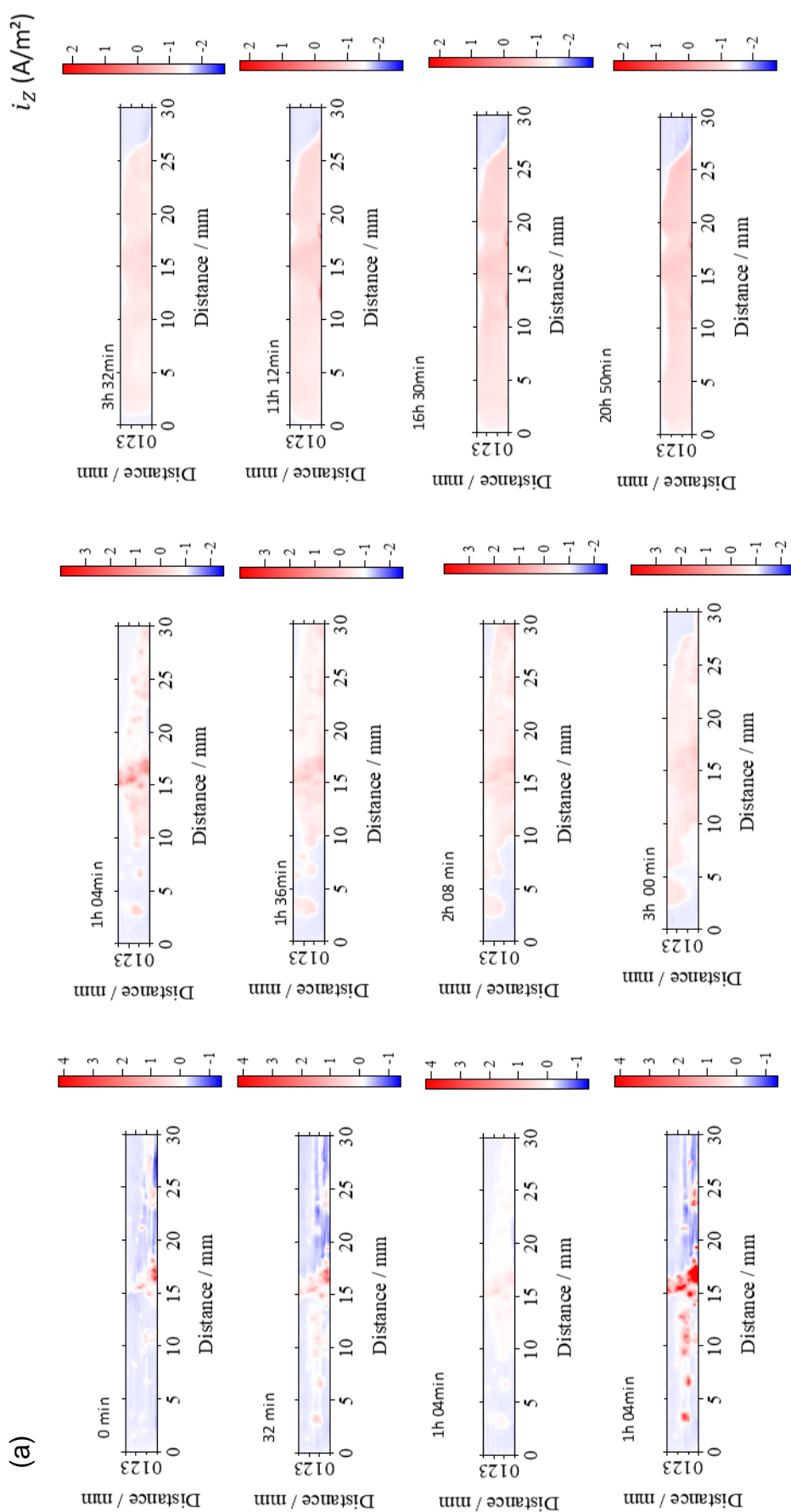


Figure 94: SVET measurements of welded joint Sample C-900-CMT-0.31 in 0.1 wt% NaCl aqueous solution for specimen 1 (a) and specimen 2 (b).

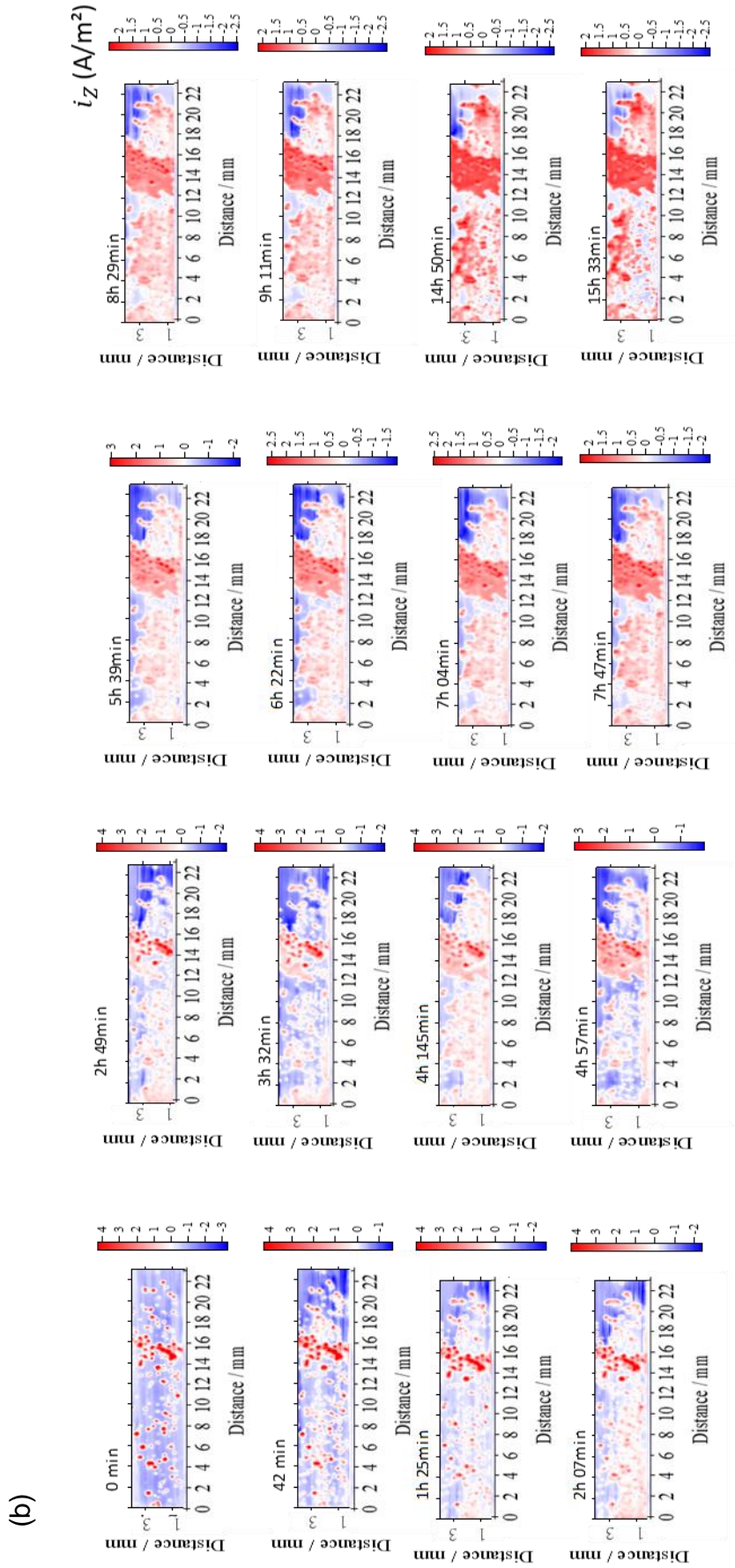
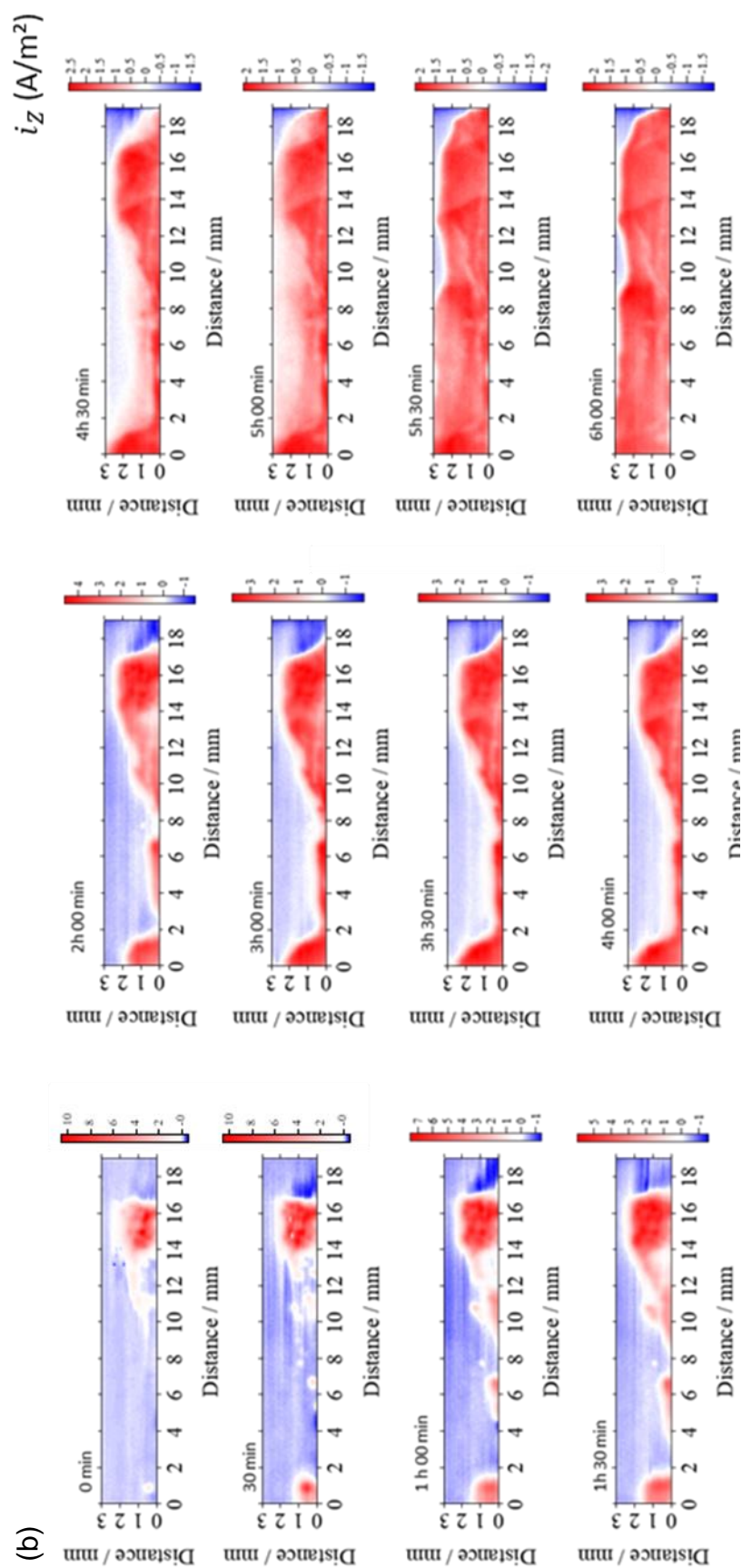


Figure 94: continued.



Figure 95: SVET measurements of welded joint Sample D (900-CMT-0.47) in 0.1 wt% NaCl aqueous solution for specimen 1 (a) and specimen 2 (b).



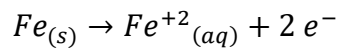
Over the welded surfaces negative (cathodic) and positive (anodic) ionic current densities were detected. In general, all samples showed similar behaviour. Anodic peak current densities were captured initially in the welded metal, representing a region that is preferentially corroded, and BM/HAZ is captured with cathodic peak current densities. After a while, corrosion spreads along the surface of the welded joint.

The higher anodic corrosion currents (in the weld metal), when the measurement begins, is due to carbon steel susceptibility to corrode in chloride media as it does not form a passive layer. The images after SVET measurements reveal an orange oxide film, which is generally composed of iron hydroxides that are poorly protective on iron because it is non-adherent (PAGOTTO et al., 2015).

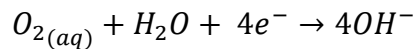
In samples B, C and D (Figure 93b, Figure 94b and Figure 95a), in contrast to the weld metal, the presence of orange oxidation products from iron in the BM/HAZ was not observed. Sample A was the only condition for which oxidation products covered a larger area, more intensely in WM but also in the base metal/HAZ.

For all conditions a galvanic couple was formed, with the weld metal as the anode and base metal as the cathode. The corrosion reactions, anodic reaction in the weld metal and its complement in the base metal, cathodic reaction, are as follows (WANG et al., 2014):

Equation 12: Anodic reaction



Equation 13: Cathodic reaction



It was observed that anodic and cathodic current decreases with time, indicating that the corrosion process is not complete, but the non-adherent oxide on the corroded steel surface hinders corrosion current measurements.

6.4. DISCUSSION

E_{corr} values were similar for both base metals. LNE500 showed higher current density, indicating that its corrosion process happens faster. Corrosion potential is a static indicator of electrochemical corrosion resistance, which reveals corrosion susceptibility. In general, the higher the value is, the better corrosion resistance of the material is (WANG et al. 2011). Therefore, in general the high strength steel AHSS900 has better corrosion resistance. SVET results agreed with this tendency by the higher values of current density of the LNE500 BM.

Regarding chemical composition and microstructure, the base metal AHSS900 was richer in Si, Cr and Mo (see Table 27) and its microstructure is comprised of tempered martensite with a large amount of small iron carbides dispersed within the matrix and some Ti- and Nb-rich carbides and nitrides. LNE500 microstructure consists of polygonal ferrite and some pearlite.

The lower corrosion resistance of LNE500 is associated with its microstructure. Pearlite usually has a non-homogeneous chemical composition. For example, some authors studied the corrosion behaviour of steels with the same Cr content (3%) but different microstructures (martensite – M 3Cr, bainite – B 3Cr and ferrite + pearlite – F+P 3Cr). The M 3Cr steel with small and few CrFe precipitates showed the highest free Cr content, and thus the highest corrosion resistance. The free Cr content of B 3Cr steel was lower than that of martensitic steel, and the corrosion rate of bainitic steel was higher than that of M 3Cr steel. The precipitates found in the bainitic steel were CrMnTi and M_3C , compared with the precipitates in M 3Cr steel, the Cr-containing precipitates were larger. Finally, the Cr-containing precipitates in the P+F 3Cr steel specimen was much greater than those in the other two steel specimens, thus it had the lowest free Cr content. Because of the low free Cr content presented in ferritic and pearlitic steel, the corrosion rates of this steel were the highest (LI et al., 2017). Other studies showed that pearlitic transformations have been concerned with the partitioning of solute. In continuously cooled pearlitic steel, Cr, Mn and V were found to be partitioned to the pearlitic cementite, whereas Si partitioned to ferrite (BAKER, 2009). It is believed that because of elements partitioning, the corrosion process is accelerated (higher values of i_{corr}) for LNE500 than AHSS900. Furthermore, AHSS900

has higher Cr contents and it may have higher free Cr content due to its microstructure (tempered martensite), which improve its corrosion resistance.

In polarisation and EIS measurements, regarding the welded joints, samples C and D (AHSS900 BM) showed higher corrosion potential than welded joints of samples A and B (LNE500 BM). The higher values of corrosion potential for samples C and D is believed to be related to the base metal influence (larger area in the joint) as the AHSS900 base metal showed better corrosion resistance than LNE500. In general, sample A showed the best corrosion resistance.

Key features were found analysing CLSM micrographs. 3D images showed that HAZ was preferentially dissolved (with a clear depth difference) for all conditions, thus acting as the anodic region in the 3.5 wt% NaCl aqueous solution.

SVET has been employed, to map changes in local electrochemical activity over welded joints of samples freely corroding in aqueous 0.1 wt% NaCl electrolyte. Within minutes of immersion, corrosion became initiated. Initially, it can be seen that there is dissolution of small active sites (red dots) specially in the WM, but some amount of red dots were also detected in the BM. These small active sites are believed to be precipitates and inclusions.

The microstructure analysis described in Chapter 4 identified a wide range of precipitates in the HAZ for all samples. Samples A and B was characterised by bainitic ferrite microstructure with the presence of nanometric Ti,Nb(C,N) and TiN precipitates with some Nb with large size (around 10 and 4 μm for samples A and B, respectively). In samples C and D, HAZ was characterised by lath martensite and bainite with the presence of precipitates. A large amount of orientated iron carbide with some Mn, and also nanometric precipitates characterized as carbides and nitrides rich in Nb, V and Ti. Finally, the WM microstructure for all samples was characterised mainly by the presence of acicular ferrite and oxide inclusions, $\text{Cu}_{0.5}\text{Fe}_2\text{Mn}_{0.5}\text{O}_4$ with some Ti, Al, S and Si.

The local electrochemical activity of an inclusion depends on its composition. For example, it has been reported that Si-enriched inclusion has a high electrochemical activity and a galvanic couple forms between the inclusion and the adjacent steel matrix. The preferential dissolution of the Si-enriched inclusion generates a local microvoid, which will continue to dissolve due to its high electrochemical activity (JIN

& CHENG, 2011). Hence, metals with Si content above 0.25% are reported to behave as most un-noble metals i.e. more negative E_{corr} values (PARKINSON et al., 1989). In our study it was verified that WM is rich in Si.

In polarisation and EIS test, HAZ was preferentially dissolved in 3.5 wt% NaCl aqueous solution. It is believed that HAZ/BM microstructures and precipitates are responsible for this galvanic corrosion. The large amount and orientated nature of the iron carbides, with some Mn and Cr, result in depletion of these elements in the precipitate boundary. These precipitates in the HAZ in combination with the heterogeneous microstructure (samples C and D: lath martensite and bainite in CGHAZ + ferrite in FGHAZ + tempered martensite in base metal; Samples A and B: bainitic ferritic in CGHAZ + ferrite in FGHAZ and ferrite and pearlite in the base metal) can give rise to corrosion processes by forming micro-electrochemical cells between the grain boundary and the matrix by increasing the electrochemical reactivity (Garcia et al., 2017).

Chemical composition may also affect the corrosion process. The chemical composition of WM and HAZ was determined as shown in Chapter 4. In summary, for samples A and B (LNE500), a great level of partitioning of Nb and Si was observed between HAZ and WM was observed; Si content was higher in the WM than in the HAZ for both samples, whereas Nb was only found in the HAZ and not in the WM. For samples C and D (AHSS900), chromium and molybdenum contents were significantly higher in the HAZ than in the WM, Cu was detected in small percentages only in the WM and the silicon content was higher in the WM than in the HAZ.

Even though HAZ in samples C and D was found to be richer in Cr, it did not show higher corrosion resistance than the WM. It can be explained because of part of these elements is not in solid solution as confirmed by the chemical composition of the precipitates. Most of them contains some amount of Cr. If these elements are not in solid solution, they lose their effectiveness in increasing corrosion resistance (ALVES, BRETT, & CAVALEIRO, 2001). Moreover, it is found in the literature that the presence of Cr carbides leads to preferential attack in the metal matrix, whereas this effect is less marked for Mo, Ti and Nb carbides (GRABKE, SPIEGEL, & ZAHS, 2004).

After a certain time, it was observed on the SVET map that corrosion spread along the surface and became generalised. As the immersion time evolved, corrosion

processes of regions with high anodic dissolution rate are inhibited to some extent by the corrosion products, decreasing the anodic current density. Corrosion products were observed, and they grew quickly on the steel surface due to the fast reactions between Fe and Cl^- at the initial immersion stage. The corrosion products on the surface can hinder charge transfer between the steel and the electrolyte. This explains the decrease in current density with time observed in SVET maps. Liu et al. compared the corrosion behaviour of HSLA steel in different periods of immersion in seawater. They observed that the corrosion behaviour changed after the first 6 hours of immersion. In the beginning, the corrosion rate increased due to the elements present on the HSLA, such as Cr, Mo, Ni and Al, but the corrosion resistance was improved for longer times due to the formation of a stable corrosion scale (LIU et al., 2014). Cr, Ni and Cu are reported to promote the formation of compact rust layers, which gradually become denser over time and isolate the steel from various corrosion agents, resulting in substantial reduction of the corrosion rate (ZHOU et al., 2013).

The fine size and random distribution of carbon-rich phases is also reported to play a key role in anchoring rust layers. Carbon-rich phases with a fine size and a uniform distribution improve the anchoring process which is beneficial for weathering resistance (GUO et al., 2008). Moreover, on the same study, Guo and collaborators verified that a selective corrosion of large pearlite produces stress in rust layers from initial corrosion products. Films of uniform corrosion products that contain only few cracks tend to form on homogeneous microstructures such as ferrite and bainite and this is advantageous for the formation of compact rust layers during initial corrosion. Khalaj et al. showed that a less continuous and more disordered distribution of carbide particles renders it less efficient in anchoring deposits on the metal surface when exposed to the corrosive solution which decreases the corrosion resistance (KHALAJ & KHALAJ, 2016).

This can be the case of WM in 3.5 wt% NaCl solution. A stable layer is created on the surface which does not occur in the HAZ/BM, or it is less effective, and thus this region is continuously corroded and the depth difference is formed (GUO et al., 2008).

As discussed so far, galvanic corrosion can happen in the welded joint due to local compositional and microstructural differences between the weld metal (WM), heat affected zone (HAZ), and base metal (BM). Preferential weld corrosion (PWC) must be avoided because if the weld is preferentially dissolved, corrosion will be enhanced

by the unfavourable area ratio, a small anodic weld/large cathodic base metal. PWC is usually controlled by using filler materials with the addition of more noble elements such as nickel, chromium, molybdenum, copper, aluminium, and vanadium. These elements decrease the corrosion rate (LU et al., 2016). It is also reported that corrosion rate of the weld metal with alloying elements is lower than that of the weld metal without the alloying elements, indicating corrosion resistance improvement due to the alloying elements (LU et al., 2016).

Recommend design of the alloying elements in the filler metal minimizing carbon steel preferential weld corrosion (LU et al., 2016), is proposed as follows:

- a. Cr: 0.5% (only if the base metal has 0.5%–1% Cr), otherwise <0.5%.
- b. Cu and Ni: $\Delta = 3.8 \times (C_{U_{base}} \text{ (wt.\%)} - \rho \times C_{U_{filler}} \text{ (wt.\%)}) + 1.1 \times (Ni_{base} \text{ (wt.\%)} - \rho \times Ni_{filler} \text{ (wt.\%)}) + 0.3$.

Where ρ is the filler metal deposition rate; positive Δ values indicate that the base metal is the cathode, and negative Δ values indicate that the weld metal is the cathode.

- c. Si: $(\rho \times Si_{filler} \text{ (wt.\%)} - Si_{base} \text{ (wt.\%)}) \leq 10\text{--}20\% (Si_{base} \text{ (wt.\%)})$.
- d. P: $\rho \times (Ni \text{ (wt.\%)} - 5.85 \times P \text{ (wt.\%)})_{filler} > -0.005$
- e. Mn <1.1%, Mo: 0.3%.
- f. The content of carbon in the filler metal is slightly lower than that in the base metal. The content of the other elements in the filler metal is generally close to that in the base metal.

The filler material used in this work presents Cr < 0.5 wt%, Mn > 1.1 wt%, Mo = 0.003 wt% and its carbon content of carbon is slightly higher than that of the base metal. This indicates that PWC could occur. But, as discussed before, it did not happen.

A study investigating the corrosion behaviour of failed welded joint of AISI1518 low carbon pipeline steel showed that the BM (ferrite and perlite) had the highest corrosion resistance in comparison with the HAZ (polygonal ferrite, pearlite, fine bainitic ferrite and martensite) and WM (martensite, acicular ferrite and fine bainitic ferrite phases). They concluded that the presence of local stresses and lattice defects due to the formation of martensite and bainitic ferrite and the galvanic effect between

the phases on the three distinct regions (BM, HAZ and WM) may result in the higher corrosion current density in the HAZ and WM. Their electrochemical investigations were carried out with in the individual regions (parent metal, HAZ and WM) and not in the welded joint as a whole (GHARAVI et al., 2014).

Therefore, it was found that in 3.5 wt% NaCl solution, WM was cathodic with respect to the HAZ. According to all results, it is hypothesized that corrosion started at the WM for both electrolytes (3.5 wt% NaCl for conventional corrosion techniques and 0.1 wt% NaCl solution for SVET). Due to WM higher number of active points (oxides inclusions) and high amount of acicular ferrite. In the 0.1 wt% NaCl solution, as seen in SVET maps, corrosion spread along the surface with time, but started in the WM. On the other hand, in the 3.5 wt% NaCl aqueous solution what happened was: corrosion started in the weld metal, but after a short period of time spread and HAZ/BM, due to their higher i_{corr} relative to the filler material (see Table 27), corroded faster, thus creating the depth difference (see Figure 88 and Figure 89). The corrosion products deposited on the WM may hinder the corrosion process which contributed to the depth difference between HAZ and WM in this electrolyte.

The WM microstructure was mainly comprised of acicular ferrite for all samples. A study, evaluating corrosion behaviour of the heat-affected zone of API-X100, showed that the sample whose microstructure predominantly consisted of acicular ferrite had the highest charge-transfer resistance, compared with martensitic and equiaxed ferritic microstructure (ELIYAN & ALFANTAZI, 2013). It is reported that during the formation of acicular ferrite there is no partitioning of substitutional alloying elements (Si and Mn), which may improve the corrosion resistance of acicular ferrite (BHADESHIA & SVENSSON, 1993). This is in agreement with the results obtained in the present work.

In order to minimise the depth difference found between WM and HAZ, it is suggested that filler material and base metal should be more similar regarding their chemical compositions. If unalloyed weld fillers are used, the weld itself is corroded preferentially and this must be avoided. Alloying elements are added to the coated electrode as a means of modifying or controlling the chemistry of the weld metal (BALAKRISHNAN, 1994).

It is worth to point out that the choice of a more similar chemical composition for the filler with respect to the parent metal may prevent the chemical difference them,

which may limit the galvanic corrosion effect in the welded joint. This strategy was confirmed by Wei et al. in a recent study. The corrosion step (depth difference between HAZ and WM) was reduced from 42 μm to 5 μm only by modifying the weld metal composition (HU et al., 2014).

6.5. CONCLUSIONS

The aim of this Chapter was to study the influence of heat input in the corrosion behaviour by interlinking the corrosion behaviour with the microstructural features in the welded joint. In the light of the present results, it can be concluded that welded joint is characterised by heterogeneous microstructure which results in a galvanic corrosion process between HAZ/BM and WM. Conventionally, in order to protect against weld preferential corrosion, the weld is made nobler than the base metal

Potentiodynamic polarisation tests showed that all steels and their welded samples showed active corrosion behaviours in the NaCl aqueous solution.

The AHSS900 base metal showed higher corrosion resistance than LNE500 BM which is due to the AHSS900 steel high microalloying element and its microstructure tempered martensite.

Heat input did not have a great influence in corrosion behaviour even though a tendency was found which higher heat input led to higher corrosion resistance of the welded joint.

In 3.5 wt% NaCl, WM of all samples acted as cathode of the galvanic couple and HAZ/BM acted as the anode. This is desirable due to the area ratio between BM/HAZ and WM (large anode with respect to the cathode, minimizing the corrosion current density of the anodic region). High amount of active sites (oxides) and the high Si content in the WM may be responsible for initiating corrosion.

The advanced corrosion measurements (SVET) were performed on localised sites on the electrode. The results were presented as a map scan of the specimen surface, corroborating the results obtained from the classical techniques. SVET results indicated that the corrosion starts in the WM and after a certain time it proceeds to HAZ

and BM and become generalised. Moreover, CLSM images show that WM was corroded slower than HAZ due to the depth difference. The E_{corr} and i_{corr} values are in agreement with these findings. WM E_{corr} value was more negative than for the BMs, indicating that the corrosion process is expected to initiate in the WM but due its low i_{corr} value, the corrosion process happens slowly, consequently HAZ corrosion happens faster which create a depth difference.

Chapter 7

7. GENERAL CONCLUSIONS

The effect of the heat input on microstructure, mechanical properties and corrosion behaviour was investigated in this work. Two high strength steels were selected and one filler material.

The general conclusions are as follows.

- 1) The microstructure of the HAZ was found to be coarse grained and changes with distance from the fusion zone. The heat input mainly affected the coarse-grained heat affected zone. By increasing the heat input the prior austenite prior grain size grew. Silicon content was higher in the WM than in the HAZ for all samples studied. HAZ of samples C and D was richer in Cr than the WM. Most of the chemical difference between base metals and filler material was related to their chemical composition more than heat input influence.
- 2) The hardness values of the base metal, weld metal and heat affected zone show a direct correlation with the microstructure. Softening happened in the partially transformed HAZ for AHSS900 welded samples. The weld metal was found to be the weakest part. A suitable consumable (filler) must be selected, allowing the obtainment of welded joints with good mechanical strength.
- 3) In 3.5 wt% NaCl, WM of all samples acted as cathode of the galvanic couple and HAZ/BM acted as the anode. This is desirable due to the area ratio between BM/HAZ and WM (large anode with respect to the cathode, minimizing the corrosion current density of the anodic region). High amount of active sites (oxides), large amount of acicular ferrite and the high Si content in the WM may be responsible for the initiation of corrosion process. The SVET results,

presented as a map scan of the specimen surface, corroborated the results obtained from the classical techniques. SVET results indicated that the corrosion starts in the WM and after a certain time it proceeds to HAZ and BM and become generalised. Moreover, CLSM images show that WM was corroded slower than HAZ due to the depth difference. The E_{corr} and i_{corr} values are in agreement with these findings. WM E_{corr} value was more negative than for the BMs, indicating that the corrosion process is expected to initiate in the WM but due its low i_{corr} value the corrosion process happens slowly, consequently HAZ corrosion happens faster which create a depth difference.

8. FUTURE WORK

A significant amount of work has been performed to characterise the influence of heat input in the microstructure, mechanical properties and corrosion behaviour.

Given the complexity of corrosion process that start on welded specimen surface, it would be beneficial to study of the corrosion behaviour using traditional corrosion techniques in 0.1 wt% NaCl solution.

Mechanical improvement is one of the goals of high strength steels in the automotive industry. As the filler used in this work did not show adequate mechanical properties, a more appropriate filler material need to be studied. After it, the corrosion behaviour must be analysed again.

The author suggests that before SVET measurements a careful identification and mapping of the principal precipitates, i.e., large TiN in the BM and HAZ has to be done, in order to identify and to fully understand the active sites (red points) in SVET maps.

Toughness determination of the welded samples and its correlation with grain size in the coarse-grained HAZ.

9. REFERENCES

- Akid, R., & Mills, D. J. A comparison between conventional macroscopic and novel microscopic scanning electrochemical methods to evaluate galvanic corrosion. *Corrosion Science*. (2001), 43, 1203-1216.
- Alawadhi, K., Aloraier, A. S., Joshi, S., Alsarraf, J., & Swilem, S. Investigation on Preferential Corrosion of Welded Carbon Steel Under Flowing Conditions by EIS. *Journal of Materials Engineering and Performance*. (2013), 22, 2403-2410.
- Alipooramirabad, H., Paradowska, A., Ghomashchi, R., & Reid, M. Investigating the effects of welding process on residual stresses, microstructure and mechanical properties in HSLA steel welds. *Journal of Manufacturing Processes*. (2017), 28, 70-81.
- Alves, V. A., Brett, C. M. A., & Cavaleiro, A. Influence of heat treatment on the corrosion of high speed steel. *Journal of Applied Electrochemistry*. (2001), 31, 65–72.
- American Society for Testing and Materials. ASTM E165/E165M-12 Standard Practice for Liquid Penetrant Examination for General Industry. (2012a).
- American Society for Testing and Materials. ASTM E384: Standard Test Method for Knoop and Vickers Hardness of Materials. (2012b).
- American Society for Testing and Materials. ASTM E112-13: Standard test methods for determining average grain size. (2013a).
- American Society for Testing and Materials. E8/E8M - Standard Test Methods for Tension Testing of Metallic Materials 1 (2013b).
- Angst, U., & Büchler, M. On the applicability of the Stern-Geary relationship to determine instantaneous corrosion rates in macro-cell corrosion. *Materials and Corrosion*. (2015), 66, 1017-1028.
- Atapek, H., & Zor, S. Effect of Tempering Temperature and Microstructure on the Corrosion Behavior of a Tempered Steel. *Protection of Metals and Physical Chemistry of Surfaces*. (2013), 49, 240-246.
- Atta-Agyemang, S.-A., Kesse, M. A., Kah, P., & Martikainen, J. Improvement of strength and toughness: The effect on the weldability of high-strength steels used in offshore structures. *Proceedings of the Institution of Mechanical Engineers, Part B: Journal of Engineering Manufacture*. (2017), 231, 369-376.
- Baker, T. N. Processes, microstructure and properties of vanadium microalloyed steels. *Materials Science and Metallurgy*. (2009), 25, 1083-1107.
- Balakrishnan, K. Metallurgical aspects of corrosion. *Bulletin of Materials Science*. (1994), 17, 671-684.
- Barbaro, F., Zhu, Z., Kuzmikova, L., Li, H., & Jian, H. Weld HAZ Properties in Modern

- High Strength Niobium Pipeline Steels. *HSLA Steels 2015, Microalloying 2015 and Offshore Engineering Steels 2015 Conference Proceedings*. (2015), 453-457.
- Barker, R., Hu, X., Neville, A., & Cushnaghan, S. Assessment of Preferential Weld Corrosion of Carbon Steel Pipework in CO₂-Saturated Flow-Induced Corrosion Environments. *Corrosion*. (2013), 69, 1132-1143.
- Barsoukov, E., & Macdonald, J. R. *Impedance Spectroscopy: Theory, Experiment, and Applications*. (2005) (2nd ed.) 178p.
- Basson, E. Word steel in Figures 2017. *50 worldsteel association*. (2017). <https://www.worldsteel.org/en/dam/jcr:0474d208-9108-4927-ace8-4ac5445c5df8/World+Steel+in+Figures+2017.pdf>, Accessed July 1, 2017.
- Bhadeshia, H. K. D. H. Diffusional formation of ferrite in iron and its alloys. *Progress in Materials Science*. (1985), 29, 321-386.
- Bhadeshia, H. K. D. H. Interpretation of the Microstructure of Steels. (2017). https://www.phase-trans.msm.cam.ac.uk/2008/Steel_Microstructure/SM.html, Accessed August 10, 2016.
- Bhadeshia, H. K. D. H. Tempered martensite. (2017). <https://www.phase-trans.msm.cam.ac.uk/2004/Tempered.Martensite/tempered.martensite.html>, Accessed April 7, 2017.
- Bhadeshia, H. K. D. H., & Honeycombe, R. W. K. *Steels: microstructure and properties*. (2017) (4th ed.).
- Bhadeshia, H. K. D. H., Svensson, L. E., & Gretoft, B. A model for the development of microstructure in low-alloy steel (Fe-Mn-Si-C) weld deposits. *Acta Metallurgica*. (1985), 33, 1271-1283.
- Bhadeshia, H. K. D. H., & Svensson, L. E. Modelling the Evolution of Microstructure in Steel Weld Metal. *Mathematical Modelling of Weld Phenomena*. (1993), 109-182.
- Bhadeshia, H. K. D. H., Strang, A., & Gooch, D. J. Ferritic power plant steels: remanent life assessment and the approach to equilibrium. *International Materials Reviews*. (1998), 43, 45-68.
- Bhattacharya, D. N. Modern Niobium microalloyed steels for the automotive industry. *HSLA Steels 2015, Microalloying 2015 and Offshore Engineering Steels 2015 Conference Proceedings*. (2016), 71-83.
- Bogucki, R., Mazur, M., & Pytel, S. The influence of molybdenum on stress corrosion in Ultra Low Carbon Steels with copper addition. *Archives of Foundry Engineering*. (2010), 10, 219-224.
- Bokati, K. S., Dehghanian, C., & Box, P. O. Corrosion Inhibition of Sodium Phosphate for Coarse and Near Ultrafine-Grain Mild steel surface. *Journal of Ultrafine Grained and Nanostructured Materials*. (2017), 50, 33-42.
- Bolmsjo, G., Olsson, M., & Cederberg, P. Robotic arc welding - trends and developments for higher autonomy. *Industrial Robot: An International Journal*. (2002), 29, 98-104.
- Cao, X., Wanjara, P., Huang, J., Munro, C., & Nolting, A. Hybrid fiber laser – Arc welding of thick section high strength low alloy steel. *Materials and Design*. (2011),

32, 3399-3413.

- Chang, B., & Park, S. Electrochemical Impedance Spectroscopy. *Annual review of analytical chemistry*. (2010), 3, 207-229.
- Chen, C., Xue, H., Peng, H., Yan, L., Zhi, L., & Wang, S. Inclusions and Microstructure of Steel Weld Deposits with Nanosize Titanium Oxide Addition. *Journal of Nanomaterials*. (2014), 2014. 1-7.
- Chen, J., Lv, M., Liu, Z., & Wang, G-D. Combination of ductility and toughness by the design of fine ferrite/tempered martensite-austenite microstructure in a low carbon medium manganese alloyed steel plate. *Materials Science and Engineering A*. (2015), 648, 51-56.
- Cheng, S., Milligan, W. W., Wang, X. L., Choo, H., & Liaw, P. K. Compressive and tensile deformation behavior of consolidated Fe. *Materials Science and Engineering A*. (2008), 493, 226-231.
- Cho, K., Redkin, K. V., Hua, M., Garcia, C. I., & DeArdo, A. J. Recent Development of Nb-Containing DP590, DP780 and DP980 Steels for Production on Continuous Galvanizing Lines. *Advanced Steels: The Recent Scenario in Steel Science and Technology*. (2011), (1st ed.), 177–185.
- Choi, Y., Shim, J., & Kim, J. Effects of Cr, Cu, Ni and Ca on the corrosion behavior of low carbon steel in synthetic tap water. *Journal of Alloys and Compounds*. (2005), 391, 162-169.
- Dáz-Fuentes, M., Iza-Mendia, A., & Gutiérrez, I. Analysis of different acicular ferrite microstructures in low-carbon steels by electron backscattered diffraction. Study of their toughness behavior. *Metallurgical and Materials Transactions A*. (2003), 34, 2505-2516.
- Di Schino, A., & Di Nunzio, P. E. Effect of Nb microalloying on the heat affected zone microstructure of girth welded joints. *Materials Letters*. (2017), 186, 86-89.
- German Institute for Standardization. DIN-EN-ISO-5817. Welding-Fusion-welded joints in steel, nickel, titanium and their alloys (beam welding excluded)- Quality levels for imperfections (2006).
- Dong, H., Xingjun Sun, Cao, W., Liu, Z., Wang, M., Weng, Y., & Abstract. On the Performance Improvement of Steels through M3 Structure Control. In *Advanced Steels: The Recent Scenario in Steel Science and Technology*. (2011), (1st ed.), 35-57.
- Drillet, J., Valle, N., & Lung, T. Nanometric Scale Investigation of Phase Transformations in Advanced Steels for Automotive Application. *Metallurgical and Materials Transactions A*. (2012), 43, 4947-4956.
- Echeverría, A., & Rodríguez-Ibabe, J. M. The role of grain size in brittle particle induced fracture of steels. *Materials Science and Engineering A*. (2003), 346, 149-158.
- Eliyan, F. F., & Alfantazi, A. Corrosion of the Heat-Affected Zones (HAZs) of API-X100 pipeline steel in dilute bicarbonate solutions at 90 °C – An electrochemical evaluation. *Corrosion Science*. (2013), 74, 297-307.
- Facco G.G. Effect of Cooling Rate and Coiling Temperature on the Final Microstructure

of HSLA Steels After HSM and/or Laboratory TMP Processing (2005). 86pp. Dissertation (Master of Science in Materials Science and Engineering), University of Pittsburgh. Pennsylvania State, 2005.

- Falat, L., Ciripová, L., Kepic, J., Buršík, J., & Podstranská, I. Correlation between microstructure and creep performance of martensitic/austenitic transition weldment in dependence of its post-weld heat treatment. *Engineering Failure Analysis*. (2014), 40, 141-152.
- Fattah-alhosseini, A., & Vafaeian, S. Comparison of electrochemical behavior between coarse-grained and fine-grained AISI 430 ferritic stainless steel by Mott–Schottky analysis and EIS measurements. *Journal of Alloys and Compounds*. (2015), 639, 301-307.
- Fernández-Pérez, B. M., González-Guzmán, J. A., González, S., & Souto, R. M. Impedance Spectroscopy Investigation of the Corrosion Resistance of a Waterborne Acrylic Coating Containing Active Electrochemical Pigments for the Protection of Carbon Steel. *International Journal of Electrochemical Science*. (2014), 9, 2067-2079.
- Fronius. Cold Metal Transfer. (2014) http://www.fronius.com/cps/rde/xchg/SID-B0C6E4CC-0B1EFADC/fronius_international/hs.xsl/79_23609_ENG_HTML.htm#.U8Kn-bHwoJ, Accessed April 20, 2017.
- Garcia, M. P., Mantovani, G. L., Vasant Kumar, R., & Antunes, R. A. Corrosion Behavior of Metal Active Gas Welded Joints of a High-Strength Steel for Automotive Application. *Journal of Materials Engineering and Performance*. (2017), 26, 4718-4731.
- Geng, S., Sun, J., Guo, L., & Wang, H. Evolution of microstructure and corrosion behavior in 2205 duplex stainless steel GTA-welding joint. *Journal of Manufacturing Processes*. (2015), 19, 32-37.
- Gery, D., Long, H., & Maropoulos, P. Effects of welding speed, energy input and heat source distribution on temperature variations in butt joint welding. *Journal of Materials Processing Technology*. (2005), 167, 393-401.
- Gharavi, F., Matori, K. A., Yunus, R., Othman, N. K., & Fadaeifard, F. Corrosion behavior of Al6061 alloy weldment produced by friction stir welding process. *Journal of Materials Research and Technology*. (2014), 4, 314-322.
- Gharibshahiyan, E., Raouf, A. H., Parvin, N., & Rahimian, M. The effect of microstructure on hardness and toughness of low carbon welded steel using inert gas welding. *Materials & Design*. (2011), 32, 2042-2048.
- Grabke, H. J., Spiegel, M., & Zahs, A. Role of alloying elements and carbides in the chlorine-induced corrosion of steels and alloys. *Materials Research*. (2004), 7, 89-95.
- Greene, N. D., & Leonard, R. B. Comparison of Potentiostatic Anodic Polarization Methods. *Electrochimica Acta*. (1964), 9, 45-54.
- Grzybicki, M., & Jakubowski, J. Comparative tests of steel car body sheet welds made using CMT and MIG/MAG methods. *Welding International*. (2013), 27, 610-615.

- Guo, J., Yang, S., Shang, C., Wang, Y., & He, X. Influence of carbon content and microstructure on corrosion behaviour of low alloy steels in a Cl containing environment. *Corrosion Science*. (2008), 51, 242-251.
- Han, Y., Shi, J., Xu, L., Cao, W. Q., & Dong, H. Effect of hot rolling temperature on grain size and precipitation hardening in a Ti-microalloyed low-carbon martensitic steel. *Materials Science & Engineering A*. (2012), 553, 192-199.
- Hamdy, A.S., El-Shenawy, E., El-Bitar, T. Electrochemical Impedance Spectroscopy Study of the Corrosion Behavior of Some Niobium Bearing Stainless Steels in 3.5% NaCl. *International Journal of Electrochemical Science*. (2006), 1, 171-180.
- Hemmingsen, T., Hovdan, H., Sanni, P., & Aagotnes, N. O. The influence of electrolyte reduction potential on weld corrosion. *Electrochimica Acta*. (2002), 47, 3949-3955.
- Hong, T., Debroy, T., Babu, S. S., & David, S. a. Modeling of inclusion growth and dissolution in the weld pool. *Metallurgical and Materials Transactions B*. (2000), 31(1), 161-169.
- Hsu (Zuyao Xu), T. Y., & Jin, X. Ultra-high Strength Steel Treated by Using Quenching–Partitioning–Tempering Process. In *Advanced Steels: The Recent Scenario in Steel Science and Technology*. (2011), (1st ed.), 67-73.
- Hu, J., Du, L., Wang, J., & Sun, Q. Cooling process and mechanical properties design of hot-rolled low carbon high strength microalloyed steel for automotive wheel usage. *Materials and Design*. (2014), 53, 332-337.
- u, J., Du, L.-X., Wang, J.-J., Xie, H., Gao, C.-R., & Misra, R. D. K. High toughness in the intercritically reheated coarse-grained (ICRCG) heat-affected zone (HAZ) of low carbon microalloyed steel. *Materials Science and Engineering A*. (2014), 590, 323-328.
- Huang, V. M., Wu, S.-L., Orazem, M. E., Pébère, N., Tribollet, B., & Vivier, V. Local electrochemical impedance spectroscopy: A review and some recent developments. *Electrochimica Acta*. (2011), 56, 8048-8057.
- Hulka, K. The role of niobium in low carbon bainitic HSLA steel. *Proceedings of the 1st international conference on super-high strength steels*. (2005), 1-12.
- Hutchinson, B., Komenda, J., Rohrer, G. S., & Beladi, H. Heat affected zone microstructures and their influence on toughness in two microalloyed HSLA steels. *Acta Materialia*. (2015), 97, 380-391.
- Isaacs, H. S. The measurement of the galvanic corrosion of soldered copper using the scanning vibrating electrode technique. *Corrosion Science*. (1988), 28, 547-558.
- Javidan, F., Heidarpour, A., Zhao, X., & Fallahi, H. Fundamental behaviour of high strength and ultra-high strength steel subjected to low cycle structural damage. *Engineering Structures*. (2017), 143, 427-440.
- Jin, T. Y., & Cheng, Y. F. In situ characterization by localized electrochemical impedance spectroscopy of the electrochemical activity of microscopic inclusions in an X100 steel. *Corrosion Science*. (2011), 53, 850-853.
- Junior, J. A. da C., & Santos, D. B. Effect of tempering temperature on isothermal decomposition product formed below Ms. *Journal of Materials Research and*

Technology. (2013), 2, 93-99.

- Kaçar, R., & Kökemli, K. Effect of controlled atmosphere on the MIG-MAG arc weldment properties. *Materials & Design*. (2005), 26, 508-516.
- Kah, P., Latifi, H., Suoranta, R., Martikainen, J., & Pirinen, M. Usability of arc types in industrial welding. *International Journal of Mechanical and Materials Engineering*. (2014), 9, 1-12.
- Kah, P., & Martikainen, J. Current trends in welding processes and materials: Improve in effectiveness. *Reviews on Advanced Materials Science*. (2012), 30, 189-200.
- Kah, P., & Martikainen, J. Influence of shielding gases in the welding of metals. *International Journal of Advanced Manufacturing Technology*. (2013), 64, 1411-1421.
- Kajimoto, Z. P., Wolyneć, S., & Chagas, H. C. IR drop compensation for corrosion rate determination of carbon steel in acid solutions. *Corrosion Science*. (1985), 25, 35-41.
- Kalish, D., & Roberts, E. M. On the distribution of carbon in martensite. *Metallurgical Transactions*. (1971), 2, 2783-2790.
- Karmakar, A., Biswas, S., Mukherjee, A., Chakrabarti, D., & Kumar, V. Effect of composition microstructure, precipitation and strengthening of Nb-microalloyed steel. *Materials Science & Engineering A*. (2017), 690, 158-169.
- Kastensson, Å. Developing lightweight concepts in the automotive industry: Taking on the environmental challenge with the SÅNätt project. *Journal of Cleaner Production*. (2014), 66, 337-346.
- Khalaj, G., & Khalaj, M.-J. Investigating the corrosion of the Heat-Affected Zones (HAZs) of API- X70 pipeline steels in aerated carbonate solution by electrochemical methods. *International Journal of Pressure Vessels and Piping*. (2016), 145, 1-12.
- Kim, H.-J., Keoleian, G. A., & Skerlos, S. J. Economic Assessment of Greenhouse Gas Emissions Reduction by Vehicle Lightweighting Using Aluminum and High-Strength Steel. *Journal of Industrial Ecology*. (2010), 15, 64-80.
- Korczak, P. Influence of controlled rolling condition on microstructure and mechanical properties of low carbon micro-alloyed steels. *Journal of Materials Processing Technology*. (2004), 157, 553-556.
- Kumar, S., & Nath, S. K. Effect of heat input on impact toughness in transition temperature region of weld CGHAZ of a HY 85 steel. *Journal of Materials Processing Technology*. (2016), 236, 216-224.
- Lagneborg, R., Siwecki, T., Zajac, S., & Hutchinson, B. The Role Of Vanadium In Microalloyed Steels. *The Scandinavian Journal of Metallurgy*. (1999).
- Lee, J. L., & Pan, Y. T. Effect of silicon content on microstructure and toughness of simulated heat affected zone in titanium killed steels. *Metallurgical Transactions A*. (1993), 8, 236-244.
- Lee, T.-K., Kim, H. J., Kang, B. Y., & Hwang, S. K. Effect of Inclusion Size on the Nucleation of Acicular Ferrite in Welds. *ISIJ International*. (2000), 40, 1260-1268.

- Levine, E., & Hill, D. C. Structure-Property Relationships in Low C Weld Metal. *Metallurgical Transactiona A*. (1977), 8, 1453-1463.
- Li, W., Xu, L., Qiao, L., & Li, J. Effect of free Cr content on corrosion behavior of 3Cr steels in a CO₂ environment. *Applied Surface Science*. (2017), 425, 32-45.
- Li, Y., Wang, F., & Liu, G. Grain Size Effect on the Electrochemical Corrosion Behavior of Surface Nanocrystallized Low-Carbon Steel. *Corrosion*. (2004), 60, 891-896.
- Liu, C., & Bhole, S. D. Challenges and developments in pipeline weldability and mechanical properties. *Science and Technology of Welding and Joining*. (2013), 18, 169-181.
- Liu, W., Pan, H., Li, L., Lv, H., Wu, Z., Cao, F., & Zhu, J. Corrosion behavior of the high strength low alloy steel joined by vertical electro-gas welding and submerged arc welding methods. *Journal of Manufacturing Processes*. (2017), 25, 418-425.
- Liu, W., Zhou, Q., Li, L., Wu, Z., Cao, F., & Gao, Z. Effect of alloy element on corrosion behavior of the huge crude oil storage tank steel in seawater. *Journal of alloys and Compounds*. (2014), 598, 198-204.
- López, D. A., Pérez, T., & Simison, S. N. The influence of microstructure and chemical composition of carbon and low alloy steels in CO₂ corrosion . A state-of-the-art appraisal. *Materials & Design*. (2003), 24, 561-575.
- Loureiro, A. J. R. Effect of heat input on plastic deformation of undermatched welds. *Journal of Materials Processing Technology*. (2002), 128, 240-249.
- Lu, Y., Jing, H., Han, Y., Feng, Z., & Xu, L. Recommend design of filler metal to minimize carbon steel weld metal preferential corrosion in CO₂-saturated oilfield produced water. *Applied Surface Science*. (2016), 389, 609-622.
- Lumsden, J. B. Classic Paper in Corrosion Science and Engineering. *Corrosion*. (2006), 62, 843-855.
- Mayyas, A., Qattawi, A., Omar, M., & Shan, D. Design for sustainability in automotive industry: A comprehensive review. *Renewable and Sustainable Energy Reviews*. (2012), 16, 1845-1862.
- Mayyas, A., Shen, Q., Mayyas, A., Shan, D., Qattawi, A., & Omar, M. Using Quality Function Deployment and Analytical Hierarchy Process for material selection of Body-In-White. *Materials and Design*. (2011), 32, 2771-2782.
- McCafferty, E. Validation of corrosion rates measured by the Tafel extrapolation method. *Corrosion Science*. (2005), 47, 3202-3215.
- McCafferty, E. *Introduction to Corrosion Science*. (2010). Springer.
- Mercedes-Benz Brazil. <https://www.mercedes-benz.com.br/> Accessed January 10, 2017.
- Militzer, M., Fazeli, F., & Jia, T. Effect of niobium and molybdenum on phase transformations in advanced low-carbon steels. In *Fundamentals and Applications of Mo and Nb Alloying in High Performance Steels*. (2014) (1st ed.), 23-36.
- Mirzaei, M., Arabi Jeshvaghani, R., Yazdipour, A., & Zangeneh-Madar, K. Study of welding velocity and pulse frequency on microstructure and mechanical properties

of pulsed gas metal arc welded high strength low alloy steel. *Materials and Design*. (2013), 51, 709-713.

Mohammed, G., Ishak, M., Aqida, S., & Abdulhadi, H. Effects of Heat Input on Microstructure, Corrosion and Mechanical Characteristics of Welded Austenitic and Duplex Stainless Steels: A Review. *Metals*. (2017), 7, 1-18.

Mohandas, T., Reddy, G. M., & Kumar, B. S. Heat-affected zone softening in high-strength low alloy steels. *Journal of Material Processing Technology*. (1999), 88, 284-294.

Mohrbacher, H. Synergies of niobium and boron microalloying in molybdenum based bainitic and martensitic steels. *Fundamentals and Applications of Mo and Nb Alloying in High Performance Steels*. (2014), (1st ed.), 83-108.

Mohrbacher, H. Innovative manufacturing technology enabling light weighting with steel in commercial vehicles. *Advanced Manufacturing*. (2015), 3, 3-18.

Moon, J., Lee, J., & Lee, C. Prediction for the austenite grain size in the presence of growing particles in the weld HAZ of Ti-microalloyed steel. *Materials Science and Engineering A*. (2007), 459, 40-46.

Mourad, A.-H. I., Khourshid, A., & Sharef, T. Gas tungsten arc and laser beam welding processes effects on duplex stainless steel 2205 properties. *Materials Science and Engineering: A*. (2012), 549, 105-113.

Nam, N. D., & Kim, J. G. Effect of niobium on the corrosion behaviour of low alloy steel in sulfuric acid solution. *Corrosion Science*. (2010), 52, 3377-3384.

Nie, Y., Shang, C. jia, You, Y., Li, X. cheng, Cao, J. ping, & He, X. lai. 960 MPa Grade High Performance Weldable Structural Steel Plate Processed by Using TMCP. *Journal of Iron and Steel Research International*. (2010), 17, 63-66.

Nishioka, K., & Ichikawa, K. Progress in thermomechanical control of steel plates and their commercialization. *Science and Technology of Advanced Materials*. (2012), 1, 023001, 1-20.

Nowacki, J., Sajek, A., & Matkowski, P. The influence of welding heat input on the microstructure of joints of S1100QL steel in one-pass welding. *Archives of Civil and Mechanical Engineering*. (2016), 16, 777-783.

Ogawa, K., Sawaragi, Y., Otsuka, N., Hirata, H., Natori, A., & Matsumo, S. Mechanical and corrosion properties of High strength 18% Cr austenitic stainless steel weldment for boiler. *ISIJ International*. (1995), 35, 1258-1264.

Orazem, M. E., & Tribollet, B. *Electrochemical Impedance Spectroscopy*. Wiley. (2008) (1st ed.).

Oryshchenko, A. S., & Khlusova, E. I. High-Strength Steels: Control of Structure and Properties. In Y. Weng, H. Dong, & Y. Gan (Eds.), *Advanced Steels: The Recent Scenario in Steel Science and Technology*. (2011), (1st ed.), 59-65.

Pagotto, J. F., Montemor, M. F., Recio, F. J., Motheo, A. J., Simões, A. M., & Herrasti, P. Visualisation of the galvanic effects at welds on carbon steel. *Journal of the Brazilian Chemical Society*. (2015), 26, 667-675.

Pandit, A. S. *Theory of the Pearlite Transformation in Steels*. (2011).180pp.

- Dissertation (Doctor of Philosophy in Natural Sciences), University of Cambridge. Cambridge, 2011.
- Parkinson, L. D., Malik, L., Mitrovic-Scepanovic, V., & Brigham, R. J. Evaluation of Shielded Metal Arc Welding Consumables for Repair of Weld-Zone Corrosion. *Canadian metallurgical quarterly*. (1989), 28, 135-144
- Pépe, N., Egerland, S., Colegrove, P. A., Yapp, D., Leonhartsberger, A., & Scotti, A. Measuring the process efficiency of controlled gas metal arc welding processes. *Science and Technology of Welding and Joining*. (2011), 16, 412-417.
- Phetlam, M., & Uthaisangsuk, V. Microstructure based flow stress modeling for quenched and tempered low alloy steel. *Materials & Design*. (2015), 82, 189-199.
- Pirinen, M. The Effects of Welding Heat Input on the Usability of High Strength Steels in Welded Structures (2013). Dissertation (Doctor of Philosophy in Natural Sciences). Lappeenranta University of Technology. Lappeenranta, 2013.
- Pisarski, H. G., & Dolby, R. E. The significance of softened HAZs in high strength structural steels. *Welding in the World*. (2003), 47, 32-40.
- Podder, A. S. Tempering of a Mixture of Bainite and Retained Austenite. (2011). 198pp. Dissertation (Doctor of Philosophy in Natural Sciences), University of Cambridge. Cambridge, 2011.
- Poorqasemi, E., Abootalebi, O., Peikari, M., & Haqdar, F. Investigating accuracy of the Tafel extrapolation method in HCl solutions. *Corrosion Science*. (2009), 51, 1043-1054.
- Pourbaix, M., Vandervelden, F. Intensiostatic and potentiostatic methods. Their use to predetermine the circumstances for corrosion or non-corrosion of metals and alloys. *Corrosion Science*. (1965), 5, 81-111.
- Quintino, L., Liskevich, O., Vilarinho, L., & Scotti, A. Heat input in full penetration welds in gas metal arc welding (GMAW). *The International Journal of Advanced Manufacturing Technology*. (2013), 68, 2833-2840.
- Ramos-jaime, D., López-juárez, I., & Perez, P. Effect of process parameters on robotic GMAW bead area estimation. *Procedia Technology*. (2013), 7, 398-405.
- Ríos, C. T., Souza, J. S., & Antunes, R. A. Preparation and characterization of the structure and corrosion alloy. *Journal of Alloys and Compounds journal*. (2016), 682, 412-417.
- Reichert, J. M. Structure and properties of complex transformation products in Nb/Mo-microalloyed steels. (2016). 173pp. Dissertation (Doctor of Philosophy in Natural Sciences), The University of British Columbia, 2016.
- Sampath, K. An Understanding of HSLA-65 Plate Steels. *Journal of Materials Engineering and Performance*. (2006), 15, 32-40.
- Sato, K., Inazumi, T., Yoshitake, A., & Liu, S. D. Effect of material properties of advanced high strength steels on bending crash performance of hat-shaped structure. *International Journal of Impact Engineering*. (2013), 54, 1-10.
- Schorghuber, M. Cold-Metal-Transfer Welding Process and Welding Installation. US 2009/0026188 A1. January 29, 2009. United States.

- Shen, Y. F., & Zuo, L. High-Strength Low-Alloy Steel Strengthened By Multiply nanoscale microstructures. *HSLA Steels 2015, Microalloying 2015 & Offshore Engineering Steels 2015 Conference Proceedings*. (2016), 187-193.
- Shi, Z., Chai, X., Chai, F., Su, H., Pan, T., Wang, Q., ... Yang, C. The mechanism of intragranular ferrite formed on Ti-rich (Ti,V)(C,N) precipitates in the coarse heat affected zone of a V-N-Ti microalloyed steel. *Materials Letters*. (2016), 175, 266-270.
- Shome, M. Effect of heat-input on austenite grain size in the heat-affected zone of HSLA-100 steel. *Materials Science and Engineering A*. (2007), 445-446, 454-460.
- Stern, M., & Geary, A. L. Electrochemical Polarization. I. A theoretical Analysis of the Shape of Polarization Curves. *Journal of The Electrochemical Society*. (1957), 104, 56-63.
- Soto, R., Saikaly, W., Bano, X., Issartel, C., Rigaut, G., & Charai, A. Statistical and theoretical analysis of precipitates in dual-phase steels microalloyed with titanium and their effect on mechanical properties. *Acta Materialia*. (1999), 47, 3475-3481.
- Suban, M., & Tusek, J. Dependence of melting rate in MIG/MAG welding on the type of shielding gas used. *Journal of Materials Processing Technology*. (2001), 119, 185-192.
- Svensson, L. E., Karlsson, L., & Söder, R. Welding enabling light weight design of heavy vehicle chassis. *Science and Technology of Welding and Joining*. (2015), 20, 473-482.
- Tavares, S. S. M., Pardal, J. M., Silva, M. R. da, & Oliveira, C. A. S. de. Martensitic transformation induced by cold deformation of lean duplex stainless steel Uns S32304. *Materials Research*. (2014), 17, 381-385.
- Thaulow, C., Paauw, A. J., & Guttormsen, K. The Heat-Affected Zone Toughness of Low-Carbon Microalloyed Steels. *Welding Research Supplement*. (1987), September, 266-279.
- Tsay, L. W., Chi, M. Y., Wu, Y. F., Wu, J. K., & Lin, D. Y. Hydrogen embrittlement susceptibility and permeability of two ultra-high strength steels. *Corrosion Science*. (2006), 48, 1926-1938.
- Tumuluru M. Effects of baking on the structure and properties of resistance spot welds in 780 MPa dual-phase and TRIP steels. *Welding journal*. (2010), 89, 91-100.
- Ujiro, T., Satoh, S., Staehle, R. W., & Smyrl, W. H. Effect of alloying Cu on the corrosion resistance of stainless steels in chloride media. *Corrosion Science*. (2001), 43, 2185-2200.
- Umekuni, A., & Masubuchi, K. Usefulness of Undermatched Welds for High-Strength Steels. *Welding research supplement*. (1997), (July), 256-263.
- Ushioda, K., Takahashi, J., Takebayashi, S., Maeda, D., Hayashi, K., & Abe, Y. R. Challenges Toward the Further Strengthening of Sheet Steel. In *Advanced Steels: The Recent Scenario in Steel Science and Technology*. (2011), (1st ed.), 229-240.
- Varol, F., Ferik, E., Ozsarac, U., & Aslanlar, S. Influence of current intensity and heat input in Metal Inert Gas-brazed joints of TRIP 800 thin zinc coated steel plates.

- Materials and Design*. (2013), 52, 1099-1105.
- Wagner, C., & Traud, W. On the Interpretation of Corrosion Processes Through the Superposition of Electrochemical Partial Processes and on the Potential of Mixed Electrodes. *Z. Elektrochem.* (1938), 62, 844-855.
- Wagoner, R. H., Lim, H., & Lee, M. Advanced Issues in springback. *International Journal of Plasticity*. (2013), 45, 3-20.
- Wainer, E., Brandi, S. D., & Mello, F. D. H. *Soldagem: processos e metalurgia*. (1992).(1st ed.).
- Wang, L. W., Liu, Z. Y., Cui, Z. Y., Du, C. W., Wang, X. H., & Li, X. G. In situ corrosion characterization of simulated weld heat affected zone on API X80 pipeline steel. *Corrosion Science*. (2014), 85, 401-410.
- Wang, S., Ma, Q., & Li, Y. Characterization of microstructure, mechanical properties and corrosion resistance of dissimilar welded joint between 2205 duplex stainless steel and 16MnR. *Materials and Design*. (2011), 32, 831-837.
- Wang, X.-N., Zhang, S.-H., Zhou, J., Zhang, M., Chen, C.-J., Misra, R. D. K., & A. Effect of heat input on microstructure and properties of hybrid fiber laser-arc weld joints of the 800 MPa hot-rolled Nb-Ti-Mo microalloyed steels. *Optics and Lasers in Engineering journal*. (2017), 91, 86-96.
- Williams, G., & McMurray, H. N. Localized Corrosion of Magnesium in Chloride-Containing Electrolyte Studied by a Scanning Vibrating Electrode Technique. *Journal of the Electrochemical Society*. (2008), 155, 340-349.
- Wong, Y., & Ling, S. An investigation of dynamical metal transfer in GMAW-Effects of argon shielding gas. *Journal of Materials Processing Techonoly*. (2014), 214, 106-111.
- Woo, Y., Weon, S., Jong, S., Hong, S., & Soo, C. Development of Ti and Mo micro-alloyed hot-rolled high strength sheet steel by controlling thermomechanical controlled processing schedule. *Materials Science & Engineering A*. (2013), 565, 430-438.
- Wu, Q., Zhang, Z., Dong, X., & Yan, J. Corrosion behavior of low-alloy steel containing 1% Cr in CO₂ environment. *Corrosion Science*. (2013), 75, 400-408.
- Xia, Y., Luo, X., Zhong, X., Zhou, H., Wang, C., & Shi, J. In-situ TEM observation of cementite coarsening behavior of 5Mn steel during tempering. *Journal of Iron and Steel Research International*. (2016), 23, 442-446.
- Xu, Q., Gao, K., Lv, W., & Pang, X. Effects of alloyed Cr and Cu on the corrosion behavior of low-alloy steel in a simulated groundwater solution. *Corrosion Science*. (2016), 102, 114-124.
- Xue, F., Xu, L. Y., Jing, H. Y., & Han, Y. D. Corrosion behavior of mechanical clad pipe welded joints in CO₂-saturated seawater under high temperature and high pressure. *Materials and Corrosion*. (2013), 64, 544-549.
- Yang, J., & Chang, L. The effect of stress on the Widmanstätten ferrite transformation. *Materials Science and Engineering: A*. (1997), 223, 158-167.
- Yang, J. R., & Huang, C. Y. The effect of niobium additions on the microstructural

morphology in the heat-affected zone of low-carbon steels. *Fundamentals and Applications of Mo and Nb Alloying in High Performance Steels*. (2014), (1st ed.), 63-82.

Yi, L., Yan, Z., Xiaojian, X., Yang, Z., & Rui, W. Effect of welding heat input to metal droplet transfer characterized by structure-borne acoustic emission signals detected in GMAW. *Measurement*. (2015), 70, 75-82.

Yong, Q., Sun, X., Yang, G., & Zhang, Z. Solution and Precipitation of Secondary Phase in Steels: Phenomenon, Theory and Practice. In *Advanced Steels: The Recent Scenario in Steel Science and Technology*. (2011), (1st ed.), 109-117.

Yousefieh, M., Shamanian, M., & Saatchi, A. Influence of Heat Input in Pulsed Current GTAW Process on Microstructure and Corrosion Resistance of Duplex Stainless Steel Welds. *Journal of Iron and Steel Research International*. (2011), 18(9), 65-69.

Zhang, L., & Kannengiesser, T. Austenite grain growth and microstructure control in simulated heat affected zones of microalloyed HSLA steel. *Materials Science & Engineering A*. (2014), A 613, 326-335.

Zhang, X. Development and outlook of advanced high strength steel in Ansteel. In *Advanced Steels: The Recent Scenario in Steel Science and Technology*. (2011), (1st ed.), 15-18.

Zhao, W., Zou, Y., Matsuda, K., & Zou, Z. Corrosion behavior of reheated CGHAZ of X80 pipeline steel in H₂S-containing environments. *Materials & Design*. (2016), 99, 44-56.

Zou, F., Isaacs, H. S., & Thierry, D. Interpretation of AC surface current density by deconvolution of potential differences in solution. *Corrosion Science*. (2000), 42, 1149-1167.

Zhou, J., Kang, Y., & Mao, X. Precipitation characteristic of high strength steels microalloyed with titanium produced by compact strip production. *Journal of University of Science and Technology Beijing*. (2008), 15, 389-395.

Zhou, Y., Chen, J., Xu, Y., & Liu, Z. Effects of Cr, Ni and Cu on the Corrosion Behavior of Low Carbon Microalloying Steel in a Cl⁻ Containing Environment. *Journal of Materials Science and Technology*. (2013), 29, 168-174.